



**HAL**  
open science

# Elastin-like polypeptides conjugated to hydrophobic molecules : towards nanoparticles and hydrogels for biomedicine

Tingting Zhang

► **To cite this version:**

Tingting Zhang. Elastin-like polypeptides conjugated to hydrophobic molecules : towards nanoparticles and hydrogels for biomedicine. Polymers. Université de Bordeaux, 2022. English. NNT : 2022BORD0203 . tel-04114468

**HAL Id: tel-04114468**

**<https://theses.hal.science/tel-04114468>**

Submitted on 2 Jun 2023

**HAL** is a multi-disciplinary open access archive for the deposit and dissemination of scientific research documents, whether they are published or not. The documents may come from teaching and research institutions in France or abroad, or from public or private research centers.

L'archive ouverte pluridisciplinaire **HAL**, est destinée au dépôt et à la diffusion de documents scientifiques de niveau recherche, publiés ou non, émanant des établissements d'enseignement et de recherche français ou étrangers, des laboratoires publics ou privés.

THÈSE PRÉSENTÉE  
POUR OBTENIR LE GRADE DE  
**DOCTEUR DE**  
**L'UNIVERSITÉ DE BORDEAUX**

ÉCOLE DOCTORALE DES SCIENCES CHIMIQUES

SPÉCIALITÉ : POLYMÈRES

Par Tingting ZHANG

**Elastin-like polypeptides conjugated to hydrophobic molecules:  
towards nanoparticles and hydrogels for biomedicine**

Sous la direction de : Prof. Bertrand GARBAY

Soutenue le 5 juillet 2022

Membres du jury :

M. NOTTELET, Benjamin	Professeur, Université de Montpellier	Président
Mme MINGOTAUD, Anne Françoise	Chargée de recherche CNRS, Université Paul Sabatier	Rapporteur
Mme CHAN-SENG, Delphine	Chargée de recherche CNRS, Institut Charles Sandron	Rapporteur
M. GARBAY, Bertrand	Professeur, Institut Polytechnique de Bordeaux	Directeur
M. PERUCH, Frédéric	Directeur de recherche CNRS, Université de Bordeaux	Invité



## **Acknowledgements**

The work of this thesis was conducted under the supervision of Professor Bertrand Garbay in the “Laboratoire de Chimie des Polymeres Organiques” (LCPO, UMR 5629) in Pessac, France. The project was supported by the China Scholarship Council (CSC) and the University of Bordeaux, which I thank for their financial support.

I would like to thank my thesis supervisor Prof. Bertrand Garbay. He patiently guided my work and helped me solve problems quickly. It has been an honor to be guided by him and a pleasure to have been in the working environment of quality established in the laboratory.

I am also very thankful to the members of my thesis committee, Dr. Anne Françoise Mingotaud, Dr. Delphine Chan-Seng, and Prof. Benjamin Nottelet for having accepted to participate in the evaluation process of my thesis.

I would particularly like to thank Dr Frédéric Peruch for his direction on the chemistry part, and the Associate Professors Christophe Schatz and Jean-François Le Meins for their many relevant comments on my work. Their serious attitude towards science greatly influenced my scientific horizon.

I would also like to thank Prof. Sebastien Lecommandoux for his help in applying for CSC founding.

I thank permanent people from LCPO Dr. Elisabeth Garager, Dr. Olivier Sandre, Asst. Prof. Angela Mutschler, Dr. Colin Bonduelle, Prof. Stéphane Carlotti, Prof. Daniel Taton, and Prof. Stéphane Grelier for their advice on my thesis.

I would like to thank all the engineers: Anne-Laure Wirotius, Amelie Vax-Weber, Paul Marque, Emmanuel Ibarboure, Cedric Le Coz, Sylvain Bourasseau, Loic Petrault, Nina Lavenette, Frederique Ham-Pichavant, and Melanie Bousquet for supporting the use of the equipment and sample analysis.

I thank my PhD and Post-Doc colleagues from LCPO for their help: Tim Delas, David Lansade, Qilei Song, Coralie Lebleu, Florian Aubrit, Pierre Lalanne, Martin Fauquignon, Anouk Martin, Nadia Mahmoudi, Clemence Schvartzman, Peter McMichael, Chloe Pascouau, Pablo Gomez Argudo,

Jeremy Mehats, Mohamed Zaky, Assia Stiti, Dijwar Yilmaz, Clemence Casenave, Leslie Dubrana, Sifan Ji, Dongxu Zhou, Yelin Hou, Diana Kazaryan, Mostofa Badreldin, Elise Courtecuisse.

I would also like to thank my Chinese friends who are also studying in Bordeaux.

I want to thank my partner, my parents and elder brother, who love me a lot and give me tremendous spiritual support.

# Table of contents

<b>List of abbreviations</b>	<b>1</b>
<b>Introduction générale et résumé en Français</b>	<b>5</b>
<b>Chapter 1. Bibliography</b>	<b>23</b>
<b>1.1. Introduction</b>	<b>23</b>
<b>1.2. Natural elastin</b>	<b>26</b>
<b>1.3. Elastin-like polypeptides (ELPs)</b>	<b>28</b>
<b>1.3.1. Introduction</b>	<b>28</b>
<b>1.3.2. Role of the “guest” residue</b>	<b>29</b>
<b>1.3.3. Factors influencing the Tt value</b>	<b>32</b>
<b>1.3.4. Production and purification of ELP</b>	<b>34</b>
<b>1.3.5. Immune-response to ELP</b>	<b>39</b>
<b>1.4. ELPs as tools for biological applications</b>	<b>43</b>
<b>1.4.1. Tag for protein purification</b>	<b>43</b>
<b>1.4.2. ELP-based nanoparticles for biomedical applications</b>	<b>44</b>
<b>1.4.2.1. Introduction</b>	<b>44</b>
<b>1.4.2.2. Nanoparticles of ELPs and ELP-drug conjugates</b>	<b>45</b>
<b>1.4.2.3. ELP for Drug Depot</b>	<b>50</b>
<b>1.4.2.4. ELP for hydrogels</b>	<b>52</b>
<b>1.4.2.5. ELPs for nucleic acid encapsulation</b>	<b>54</b>
<b>1.4.2.6. ELP conjugated with polymers, sugars and lipids</b>	<b>55</b>
<b>1.5. Conclusion</b>	<b>59</b>
<b>References</b>	<b>60</b>
<b>Chapter 2. Coupling of natural rubber and Elastin-like polypeptide</b>	<b>75</b>
<b>2.1. Introduction</b>	<b>75</b>
<b>2.2. Results and discussion</b>	<b>76</b>
<b>2.2.1. Synthesis and purification of I20-<i>b</i>-PI</b>	<b>76</b>
<b>2.2.1.1. Synthesis, purification and characterization of ELP I20</b>	<b>77</b>
<b>2.2.1.2. Synthesis of polyisoprene-maleimide (PIMAL)</b>	<b>78</b>
<b>2.2.1.3. Screening for a solvent capable of solubilizing both I20 and PIMAL</b>	<b>84</b>
<b>2.2.1.4. Synthesis of I20-<i>b</i>-PI</b>	<b>87</b>
<b>2.2.1.5. Purification of PI-<i>b</i>-I20</b>	<b>88</b>
<b>2.2.2. Characterization of I20-<i>b</i>-PI</b>	<b>92</b>

2.2.2.1. Size exclusion chromatography	92
2.2.2.2. Infrared spectroscopy	93
2.2.2.3. NMR analyses	93
2.2.2.4. Circular dichroism analyses	94
2.2.3. Self-assembly of I20- <i>b</i> -PI in aqueous solvent	96
2.2.3.1. Determination of the critical aggregation concentration (CAC)	96
2.2.3.2. Characterization of the nanoparticles by dynamic light scattering (DLS)	97
2.2.3.3. Morphology of I20- <i>b</i> -PI nanoparticles	101
2.2.3.4. Encapsulation and release of the hydrophobic dye Nile red	103
2.2.4. Conclusion	102
2.3. Experimental procedures	105
2.3.1. Production and purification of ELP I20	107
2.3.2. Synthesis of maleimide end-functionalized PI	108
2.3.2.1. Synthesis of heterotelechelic keto/aldehyde PI (PIEG)	108
2.3.2.2. Synthesis of heterotelechelic keto/hydroxyl PI (PI-OH)	108
2.3.2.3. Synthesis of Maleimidohexanoic Chloride	109
2.3.2.4. Synthesis of N-polyisoprene-maleimide (PIMAL)	109
2.3.3. Synthesis and purification of the I20- <i>block</i> -PI copolymer (I20- <i>b</i> -PI)	110
2.3.4. Self-assembly of I20- <i>block</i> -PI copolymer in aqueous solution	110
2.3.5. Methods	111
2.3.6. Materials	114
2.4. References	115
<b>Chapter 3. Lipid-Elastin like peptide hybrid polymer self-assembly</b>	<b>119</b>
3.1. Introduction	119
3.2. Results and discussion	122
3.2.1. Synthesis and purification of ELP-FAs	122
3.2.2. Characterization of ELP-FAs	125
3.2.2.1. Reversed-Phase-High Performance Liquid Chromatography (RP-HPLC)	125
3.2.2.2. Mass-spectrometry analyses	127
3.2.2.3. Circular-dichroism analyses	130
3.2.2.4. Turbidimetry analyses for determination of cloud point	132
3.2.3. Solution self-assembly of ELP-FAs	137
3.2.3.1. Determination of the critical aggregation concentration	137
3.2.3.2. Determination of the size of the self-assembled material by DLS	140
3.2.3.3. Effect of salts on self-assembly of ELP-FAs	147
3.2.3.4. Morphology of ELP-FAs micelles	153

3.2.4. Encapsulation and release of a hydrophobic molecule	154
3.2.5. Obtention of ELP-FA micelles compatible with a medical application	156
3.2.6. Conclusions	159
3.3. Experimental section	160
3.3.1. Materials	160
3.3.2. Production and purification of ELPs	160
3.3.3. Synthesis of ELP-FAs	161
3.3.4. Methods	162
3.4. Supplementary figures	165
3.5. References	180
<b>Chapter 4. Physical hydrogel based on C16-ELP-C16 triblock</b>	<b>185</b>
4.1. Introduction	185
4.2. Results and discussion	189
4.2.1. Construction of MxK producing clones	188
4.2.2. Production and purification of MxK and MxC polypeptides	196
4.2.3. Synthesis and characterization of FA-ELP-FA	198
4.2.4. Cloud point determination of FA-ELP-FA	204
4.2.5. Characterization of FA-ELP-FA by DLS	206
4.2.6. Hydrogel formation and characterization	209
4.3. Conclusions and perspectives	217
4.4. Experimental section	221
4.4.1. Materials	221
4.4.2. Construction of MxK clones	221
4.4.3. Production of MxK and M40C	223
4.4.4. Acylation of the ELPs	224
4.4.5. Oxidization of M40C	224
4.4.6. Methods	225
4.5. References	227
<b>Conclusions and perspectives</b>	<b>229</b>



## List of abbreviation

Ala (A)	Alanine
AFM	Atomic Force Microscopy
BMP	Bone Morphogenetic Protein
BSA	Bovine Serum Albumin
CAC	Critical Aggregation Concentration
CD	Circular Dichroism
CMC	Critical Micelle Concentration
CMT	Critical Micelle Temperature
CPs	Chimeric Polypeptides
Cys	Cysteine
<i>D</i>	Dispersity
DCM	Dichloromethane
DCR	Derived Count Rate
DIPEA	N,N-Diisopropylethylamine
DLS	Dynamic Light Scattering
DMF	N,N-dimethylformamide
ECM	Extracellular Matrix
ELISA	Enzyme-linked Immunosorbent Assay
ELP	Elastin-Like Polypeptide
EPR	Enhanced Permeability and Retention
FA	Fatty Acid
FT-IR	Fourier Transform Infrared Spectroscopy
Gly (G)	Glycine
GLP-1	Glucagon-Like Peptide-1
GRAVY	Grand Average of Hydropathy
HA	Hyaluronic Acid
HCTU	O-(1H-6-Chorobenzotriazole-1-yl)-1,1,3,3-tetramethyluronium hexafluorophosphate
HPMA	N-(2-hydroxypropyl)methacrylamide
HSQC	Heteronuclear Single Quantum Coherence

Ile (I)	Isoleucine
IPTG	Isopropyl $\beta$ -D-thiogalactopyranoside
ITC	Inverse Transition Cycling
Leu (L)	Leucine
Lys (K)	Lysine
MALDI	Matrix-assisted Laser Desorption/Ionization
mAB	Monoclonal Antibody
m-CPBA	3-chloroperoxybenzoic acid
Met (M)	Methionine
NGR	Asp-Gly-Arg tripeptide
NMR	Nuclear Magnetic Resonance
NMT	N-myristoyltransferase
NR	Nature Rubber
OD	Optical Density
OERCA	Overlap Extension Rolling Circle Amplification
PBS	Phosphate Buffer Saline
PCR	Polymerase Chain Reaction
PEG	Polyethylene Glycol
PDI	Polydispersity Index
Phe (F)	Phenylalanine
PI	1,4-cis polyisoprene
PIEG	Heterotelechelic keto/aldehyde PI
PIOH	Heterotelechelic keto/hydroxyl PI
PIMAL	Polyisoprene-maleimide
PLP	Proteolipid Protein
POx	Poly(2-oxazoline)s
Pre-RDL	Recursive Directional Ligation by Plasmid Reconstruction
Pro (P)	Proline
PTFE	Polytetrafluoroethylene
PTX	Paclitaxel
PTMC	Poly(trimethylene carbonate)

RDL	Plasmid Directional Ligation
RE	Restriction Endonuclease
RFU	Relative Fluorescence Units
RGD	Arg-Gly-Asp tripeptide
R <sub>H</sub>	Hydrodynamic Radius
RP-HPLC	Reversed-phase High Performance Liquid Chromatography
RT	Room Temperature
SDS-PAGE	Sodium Dodecyl Sulfate PolyAcrylamide Gel Electrophoresis
SEC	Size Exclusion Chromatography
SF	Silk Fibroin
TCEP	Tris(2-carboxyethyl) phosphine hydrochloride
T <sub>cp</sub>	Cloud-Point Temperature
TEA	Triethylamine
TEM	Transmission Electron Microscopy
T <sub>g</sub>	Glass transition Temperature
TGS	Tris/Glycine/SDS
THF	Tetrahydrofuran
THPC	Tetrakis (hydroxymethyl)phosphonium chloride
Tris	Tris hydroxymethyl aminomethane
T <sub>t</sub>	Transition temperature
Tyr (Y)	Tyrosine
Val (V)	Valine
Uv/vis	Ultraviolet/visible



## Introduction générale et résumé en Français

Les polypeptides sont d'un grand intérêt pour les applications médicales telles que la délivrance de médicaments et l'ingénierie tissulaire. Ils sont en effet de par leur nature biodégradables et biocompatibles, et ils peuvent être conçus pour ne pas être immunogènes. En outre, il est possible d'y introduire des motifs d'adhésion cellulaire afin d'améliorer leur interaction avec les tissus biologiques. C'est à notre avis le grand avantage des biomatériaux à base de polypeptides par rapport à ceux constitués par des polymères de synthèse qui sont en effet inertes par rapport aux tissus biologiques environnant.

Les polypeptides naturels présentant les meilleures caractéristiques pour servir de base aux développements de système de délivrance de médicaments ou d'hydrogels sont ceux qui possèdent également des propriétés physiques particulières telles qu'une capacité d'autoassemblage, une bonne résistance mécanique et une variation de ces propriétés en fonction des conditions environnementales (température, pH, concentration saline, etc.). A ce titre les protéines naturelles les plus utilisées vont être les collagènes, les élastines et les soies d'araignée ou de vers. Ces protéines sont extraites de tissus biologiques ce qui pose certains problèmes. Le collagène est par exemple purifié de cadavres d'animaux ou de cultures de fibroblastes, ce qui soulève des questions de sécurité biologique. L'élastine peut également être extraite de tissus d'animaux, mais les fibres étant insolubles des traitements chimiques drastiques doivent être utilisés. L'élastine ainsi purifiée est en outre très hétérogène en taille et présente des propriétés physiques variables. Les soies d'araignées ne peuvent pas être récoltées en grande quantité car l'élevage intensif de ces insectes est rendu impossible à cause de leur caractère agressif. La production recombinante est donc une alternative mais elle reste très difficile à mettre en œuvre. Ces chaînes polypeptidiques sont de taille très élevées (70 à 400 kDa) ce qui entraîne des rendements de production très faibles, elles doivent parfois subir des modifications post-traductionnelles comme l'hydroxylation des prolines pour le collagène, et surtout elles sont constituées par des motifs peptidiques hautement répétés ce qui pose le problème de la stabilité des séquences géniques dans les systèmes d'expression bactériens. C'est pourquoi depuis plusieurs années les chercheurs ont développé des systèmes simplifiés où les polypeptides produits sont de taille raisonnable (< 70 kDa) et contiennent un nombre limité des motifs répétés initialement présents dans la protéine naturelle. Bien entendu ces

polypeptides simplifiés possèdent certaines des caractéristiques physiques des protéines initiales, mais pas toutes.

Les premiers polypeptides à base de motif d'élastine, ou elastin-like polypeptides (ELPs) en anglais, ont été conçus dans les années 1970 par Dan Urry et ses collègues<sup>1</sup>. Ils sont constitués de répétitions d'un des motifs hydrophobes de l'élastine, le pentapeptide VPGXG, dans lequel l'acide aminé X appelé résidu invité peut varier. Ces ELPs sont produits par voie recombinante et le nombre de répétition du pentapeptide peut varier entre 2 et 200. Les techniques de biologie moléculaire permettent également de produire des polypeptides associant plusieurs blocs d'ELPs qui peuvent varier en taille et/ou en composition en incluant des résidus invités hydrophiles (Arg, Lys, Asp etc.) ou hydrophobes (Leu, Ile, Trp etc.). Il est donc possible d'obtenir des ELPs contenant des blocs hydrophiles et hydrophobes, alternés ou pas. L'intérêt principal de ces ELPs, outre leur biocompatibilité et qu'ils sont biosourcés, et qu'ils ont conservés les caractéristiques de coacervation de l'élastine naturelle. Ils sont en effet solubles en tampon aqueux à une température inférieure à leur température de transition de phase (Tt ou T<sub>cp</sub>) et coacervent quand la température du milieu dépasse cette Tt. De nombreux travaux ont montré que cette valeur de Tt dépend de facteurs intrinsèques à l'ELP, tels que sa taille<sup>2,3</sup>, la nature du résidu X<sup>4,5</sup>, mais également de la concentration en polypeptide<sup>3</sup> et de la salinité du milieu<sup>6</sup>.

La synthèse d'ELPs constitués de différents blocs hydrophiles et hydrophobes a largement été utilisée pour produire une variété de biomatériaux allant de nanoparticules pour la délivrance de médicaments, à la fabrication d'hydrogels pour la médecine régénératrice en passant par la fabrication d'organelles artificiels pour les cellules artificielles. Une des principales limitations de l'utilisation des ELPs pour ces approches, outre leur coût de production comparé aux polymères de synthèse, vient du fait que les blocs d'ELPs hydrophobes restent encore relativement hydratés même quand ils sont placés à une température supérieure à leur température de transition (Tt). Ainsi, le rapport hydrophobe/hydrophile obtenu avec des multiblocs d'ELPs est souvent trop faible pour permettre une bonne stabilité des nanoparticules en conditions physiologiques (pH, température, concentrations en sels), et donc pour encapsuler efficacement les médicaments hydrophobes. De même, lorsque des hydrogels à base d'ELPs sont produits, leur élaboration nécessite l'utilisation d'agents de pontages car le seul mécanisme de coacervation ne permet

pas d'obtenir des hydrogels dont les caractéristiques physiques sont compatibles avec des applications biologiques.

Une des solutions pour augmenter la balance hydrophobe/hydrophile de composés à base d'ELPs est donc de leur greffer des groupements hydrophobes tels que des lipides. Lorsque cette thèse a débuté, il y avait très peu d'exemples d'ELP-lipides dans la littérature. Les premiers travaux ont été publiés en 2018 par le groupe de Chilkoti. Pour obtenir des ELPs conjugués à du myristate ou du cholestérol ils ont utilisé une approche extrêmement élégante de lipidation *in vivo* pendant la synthèse de l'ELP recombinant<sup>7-9</sup>. Cela leur a permis de montrer que les ELP-lipides obtenus s'autoassemblaient pour former des micelles stables qui pouvaient encapsuler efficacement des drogues hydrophobes. En revanche, cette approche était limitée pour deux raisons. La première était que les rendements en ELP-lipides purifiés étaient extrêmement faibles, de l'ordre de quelques mg/l de culture, ce qui limitait fortement leur intérêt pour des applications thérapeutiques. Ainsi, l'utilisation de ces ELP-lipides pour faire des hydrogels était complètement exclue. La seconde raison venait de la spécificité des enzymes utilisés pour greffer les lipides sur les ELPs, qui restreignait au myristate et au cholestérol les substrats utilisables. C'est pourquoi nous avons choisi d'utiliser une autre stratégie. Nous avons produit les ELPs par voie recombinante de manière classique, ce qui permettait d'obtenir des rendements entre 100 et 300 mg d'ELPs purifiés par litre de culture. Nous avons ensuite greffé les molécules hydrophobes (polyisoprène et acides gras) par des techniques de conjugaison chimique. Bien entendu, cela a nécessité un plus grand nombre d'étapes de synthèses que la lipidation *in vivo*, notamment dans le cas du polyisoprène, mais les rendements d'ELPs conjugués purifiés étaient sans commune mesure avec ceux obtenus par le groupe de Chilkoti. De plus, nous avons été capables de greffer une grande variété de molécules hydrophobes ce qui nous a permis d'étudier l'effet de leur structure sur l'autoassemblage des ELP-lipides et sur leur capacité à encapsuler des petites molécules hydrophobes.

Notre premier projet a consisté au greffage d'une molécule de polyisoprène (PI) à l'extrémité d'une molécule d'ELP de manière à obtenir un dibloc ELP-*b*-PI. Nous avons choisi le PI car c'est un polymère naturel issu du caoutchouc et parce que le Dr. Frédéric Peruch s'intéressait depuis plusieurs années à ce matériel et notamment à la possibilité de le coupler à des protéines. L'ELP I20 utilisé était un petit polypeptide hydrophobe de séquence MW(VPGIG)<sub>20</sub>C, la cystéine C-terminale étant nécessaire au greffage de la molécule de PI.

Les étapes chimiques effectuées pour obtenir le dibloc ELP-*b*-PI sont montrés dans le schéma 1.

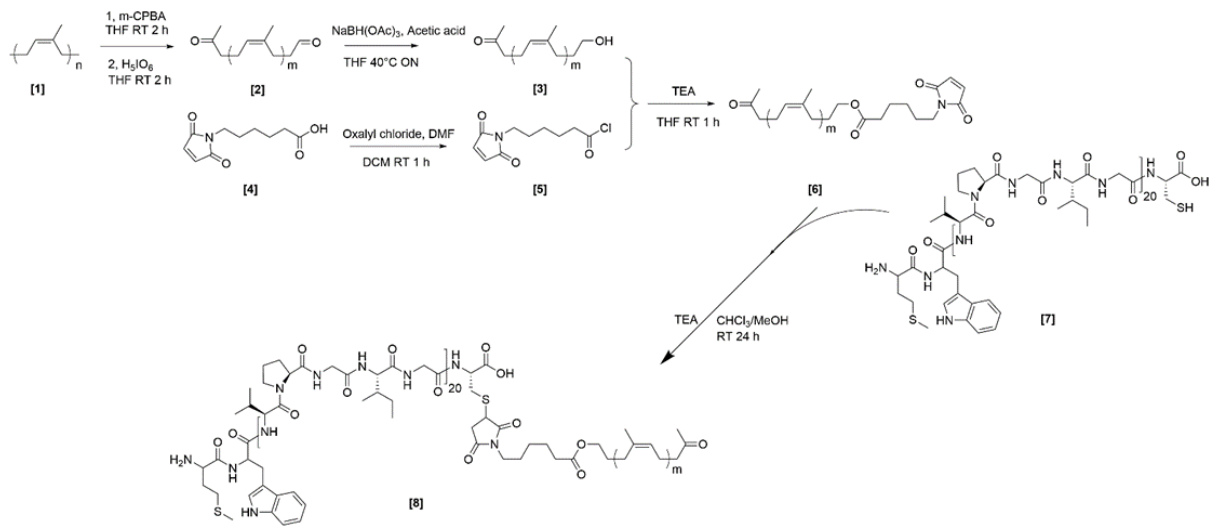


**Schéma 1. Synthèse du dibloc I20-*b*-PI. 1 : époxydation et hydrolyse contrôlée du caoutchouc naturel pour obtenir le céto/aldéhyde PI (PIEG) ; 2 : réduction des extrémités aldéhydiques de PIEG pour obtenir le céto/hydroxyle PI (PIOH) ; 3 : conversion de l'acide maléimidohexanoïque (MalOH) en une forme chlorure d'acide (MalCl) ; 4 : greffage du groupe Maléimide sur le PIOH pour obtenir le polyisoprène-maléimide (PIMAL) ; 5 : Réaction d'addition de Michael entre le groupement maléimide du PIMAL et la cystéine N-terminale de l'ELP I20.**

Le produit de synthèse ELP-*b*-PI a ensuite été purifié pour éliminer le PIMAL et l'ELP qui n'avaient pas réagi. Nous avons ensuite caractérisé le produit purifié par chromatographie d'exclusion stérique et spectroscopie infrarouge (Fig. 1)

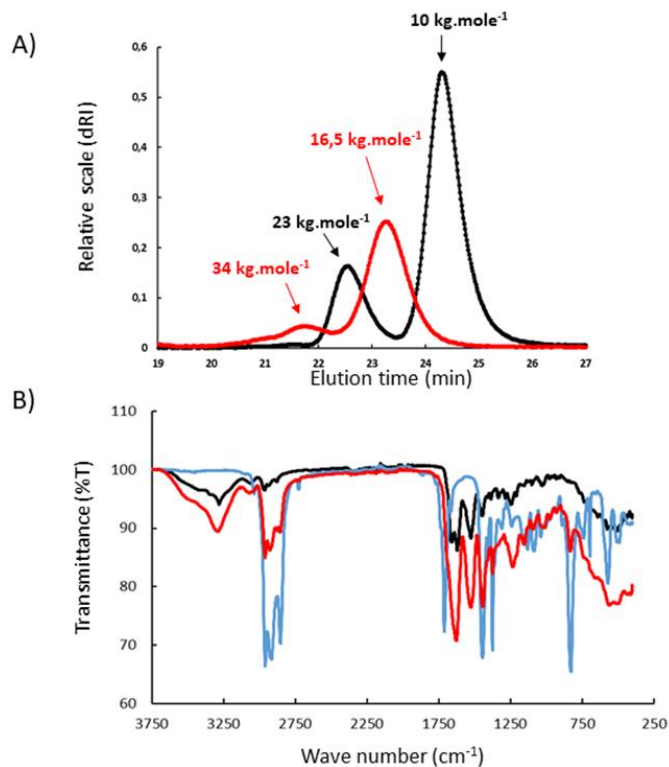


**Figure 2. A) Chromatogramme d'exclusion stérique de l'ELP I20 (en noir) et du dibloc I20-*b*-PI (en rouge). B) Spectres infrarouges. Les traces correspondant à I20 (noir), au PIMAL (bleu) et au dibloc I20-*b*-PI (rouge) ont été superposées pour comparaison.**

Les résultats de chromatographie par exclusion stérique de l'ELP I20 montre la présence de deux pics correspondant au monomère et au dimère formé par un pont disulfure intermoléculaire entre deux cystéines. Dans le cas du dibloc, nous observons bien un pic majeur de taille 16.5 kg/mole qui correspond au greffage d'une molécule de PI sur une molécule d'ELP, ainsi qu'un second pic de faible abondance qui pourrait correspondre à un dimère. L'étude du spectre infrarouge confirme également le succès du couplage du PI sur l'ELP.

Nous avons ensuite utilisé la technique de nanoprecipitation pour former des nanoparticules d'I20-*b*-PI (Fig. 3).

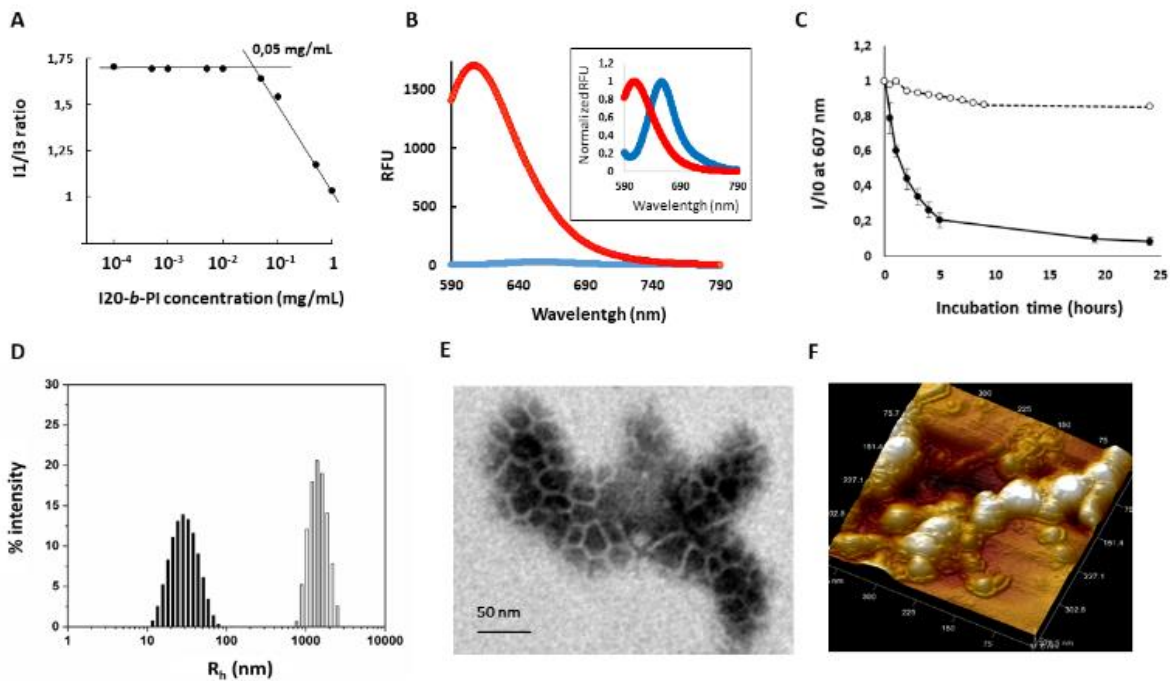


**Figure 3. Caractérisation des nanoparticules I20-*b*-PI.** A) Mesure de la CAC calculée en mesurant le rapport des intensités de fluorescence du pyrène (10  $\mu$ M) à 373 nm et 385 nm. B) Encapsulation du rouge du Nil. Fluorescence dans l'eau (bleu), et en présence de nanoparticules I20-*b*-PI (rouge). Les données relatives à la valeur maximale de chaque échantillon sont présentées dans l'encart. C). Libération du rouge du Nil par les nanoparticules. 1 mL de particules chargées de rouge du Nil (0,27 mg/mL) ont été placés dans un dispositif de dialyse et incubés dans 1 L d'eau à 20 °C. L'émission de fluorescence à 607 nm a été mesurée à différents temps. Les données sont la moyenne de trois expériences indépendantes  $\pm$  SD ( $\bullet$ ). Comme témoin, la fluorescence d'une suspension de particules chargées en rouge du Nil à la même concentration (0,27 mg/mL) a été mesurée pendant 24 h ( $\circ$ ). D) Analyse DLS des particules obtenues par nanoprécipitation. Les barres noires représentent le résultat obtenu dans l'eau. Les barres grises représentent le résultat obtenu en PBS. E) Images TEM de nanoparticules I20-*b*-PI. F) Images AFM de nanoparticules I20-*b*-PI.

Nous avons mesuré une valeur de concentration d'agrégation critique (CAC) de 3,5  $\mu$ M. La taille des nanoparticules formées dans l'eau a été évaluée par diffusion dynamique de la lumière (DLS) et par les techniques d'imagerie de microscopie électronique en transmission (TEM) et de microscopie de force atomique (AFM). Le rayon hydrodynamique des particules ( $R_H$ ) mesuré par DLS était d'environ 40 nm. Des valeurs similaires ont été mesurées par les

techniques de microscopie, celles-ci ayant en outre permis de montrer que les nanoparticules d'I20-*b*-PI étaient sphériques. En revanche l'ajout de sels dans le milieu provoquait leur agrégation en particules micrométriques, très vraisemblablement en raison de la déshydratation des ELPs I20 de surface. Nous avons ensuite évalué la capacité des nanoparticules à encapsuler une molécule hydrophobe, le rouge du Nil. Les mesures de fluorescence nous ont permis de montrer qu'après encapsulation, le rouge du Nil pouvait être libéré des nanoparticules en quelques heures.

Dans ce travail publié dans la revue *Polymer Chemistry*<sup>10</sup>, nous avons couplé avec succès du poly(1,4-*cis*-isoprène) obtenu à partir de caoutchouc naturel et un polypeptide de type élastine produit par voie recombinante. Concernant les applications biomédicales potentielles de ce matériau, on ne pourra pas l'utiliser pour la délivrance de médicaments par injection dans la circulation sanguine. En effet, les nanoparticules s'agrégeraient rapidement du fait de la concentration saline du sérum humain (autour de 150 mM de NaCl) et seraient donc rapidement éliminées de l'organisme. De plus, l'injection dans les veines de particules agrégées peut déclencher une forte réponse immunologique indésirable<sup>11</sup>. Cependant, l'agrégation peut être un avantage pour d'autres applications telles que le dépôt de médicament hydrophobe par injection dans des tissus humains. Après encapsulation d'un médicament hydrophobe dans les particules d'I20-*b*-PI et injection, la concentration saline du sérum déclenchera leur agrégation rapide au site d'injection sous-cutanée ou intramusculaire. Cela conduira à la formation d'un dépôt qui libérera progressivement le médicament encapsulé qui pourrait être un anticancéreux, un antibiotique hydrophobe, ou même un antigène à des fins de vaccination.

Cette étude a donc montré que le biomatériau I20-*b*-PI est intéressant pour certaines applications biomédicales mais limité dans son utilisation en raison de sa forte hydrophobicité et de sa tendance à s'agréger lorsqu'il est placé dans une solution contenant des concentrations physiologiques en sels. Pour contourner ce problème, nous pourrions utiliser un bloc ELP plus hydrophile, mais il sera compliqué de trouver un solvant qui permettra la solubilisation simultanée de l'ELP hydrophile et du PI très hydrophobe avant la réaction de couplage.

Dans notre quête pour obtenir des nanoparticules capables d'encapsuler des médicaments hydrophobes et qui ne s'agrègent pas dans des tampons salins, nous avons choisi de construire des protéolipides diblocs constitués d'ELPs plutôt hydrophiles et de lipides courts comme les acides gras (fatty acids, FA) naturels.

Notre objectif a été d'obtenir une bibliothèque de 15 ELP-FAs, différant par la longueur du bloc d'ELP et la nature de l'acide gras. Les séquences des ELPs étaient MW[(VPGVG)(VPGMG)(VPGVG)<sub>2</sub>]<sub>5,10,20</sub>, et différaient donc par le nombre de répétitions pentapeptidiques (de 20 à 80). Par souci de clarté, ces ELPs seront appelés respectivement M20, M40 et M80. Nous avons sélectionné différents FAs parmi ceux abondants dans les phospholipides membranaires<sup>12</sup>. Les acides myristique (C14:0), palmitique (C16:0) et stéarique (C18:0) ont été choisis pour évaluer l'influence de la longueur de la chaîne hydrophobe sur les propriétés d'auto-assemblage, tandis que les acides oléique (C18:1) et linoléique (C18:2) ont été étudiés pour évaluer l'effet du degré d'insaturation. La réaction chimique pour obtenir les conjugués est montrée dans le schéma 2.

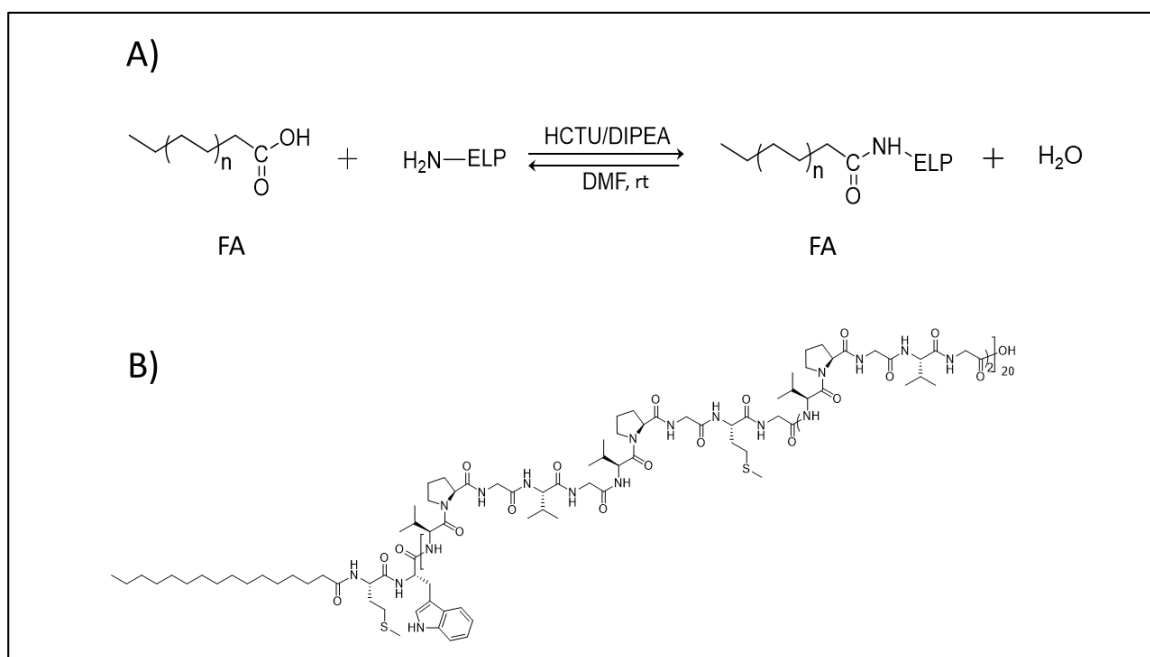


**Schéma 2. A) Réaction de condensation entre un acide gras et l'ELP. B) Exemple de structure, ici celle du M20-C16.**

Après leur synthèse et leur purification, différentes techniques ont été utilisées pour caractériser les ELP-FAs (Fig. 4).

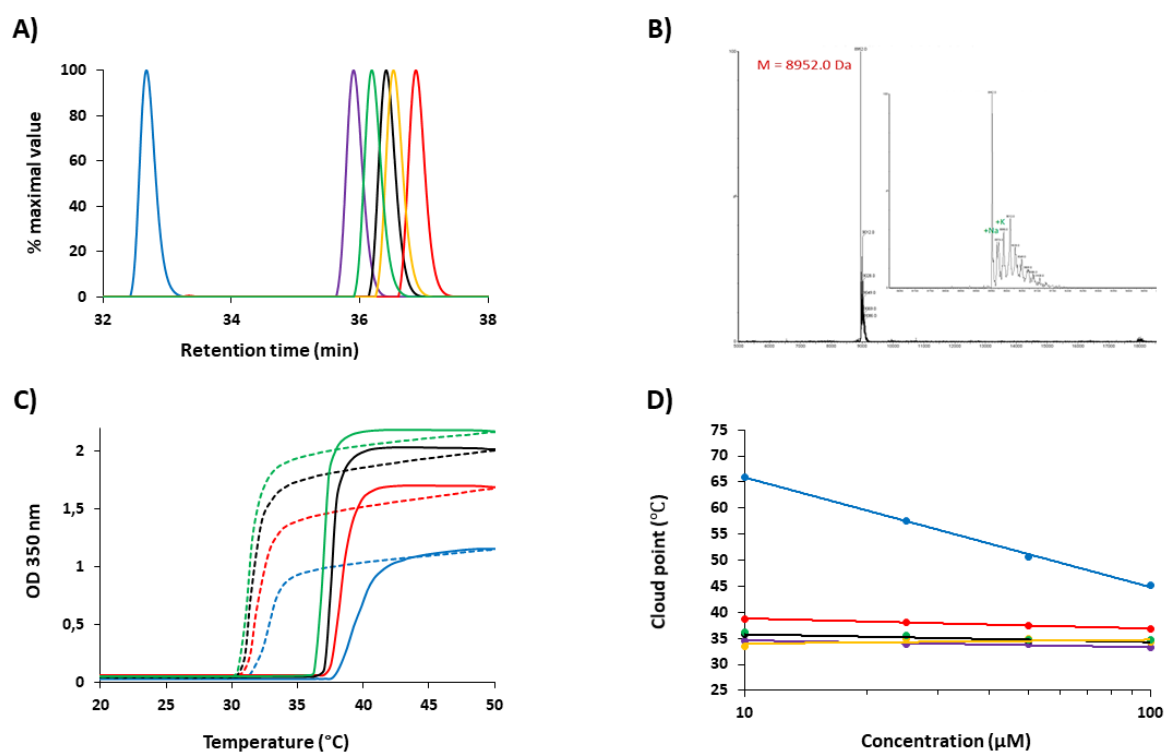


**Figure 4. Caractérisation des ELP-FAs. A) Analyse RP-HPLC des M20 (bleu), M20-C14 (violet), M20-C16 (noir), M20-C18 (rouge), M20-C18:1 (orange) et M20-C18:2 (vert). B) Spectre ESI-MS du M20-C18. L'encart représente le spectre ESI déconvolué. C) Mesure de la T<sub>cp</sub> par turbidimétrie du M20-C18 en tampon PBS (lignes pleines pour les rampes de chauffage, lignes pointillées pour les rampes de refroidissement). Les concentrations des échantillons étaient de 100  $\mu$ M (vert), 50  $\mu$ M (noir), 25  $\mu$ M (rouge) et 10  $\mu$ M (bleu). D) Relation entre la T<sub>cp</sub> et la concentration des ELPs M20 (bleu), M20-C14 (violet), M20-C16 (noir), M20-C18 (rouge), M20-C18:1 (orange) et M20-C18:2 (vert).**

Les analyses par RP-HPLC ont montré que les temps de rétention des conjugués ELP-FAs ont été significativement augmentés par rapport à ceux des ELPs non modifiés. De plus on peut voir que l'étape de purification a été efficace, comme en témoigne l'absence de quantité significative d'ELPs non modifiés dans les conjugués (pureté > 96 %). Les analyses de spectrométrie de masse ont confirmé la réussite des couplages, avec des décalages de +210, +238, +266, +264 et +262 Da après acylation des ELPs par respectivement le C14, le C16, le C18, le C18:1 et le C18:2.

Une étude par dichroïsme circulaire a montré que la structure secondaire des l'ELP-FAs variait avec la température comme c'était le cas pour les ELPs. Ainsi, l'acylation d'un ELP par

des acides gras ne modifie pas significativement sa structure secondaire, que ce soit à une température au-dessous ou au-dessus de la température de point trouble ( $T_{cp}$ ), la thermosensibilité étant donc conservée. En revanche, nous avons montré que l'acylation des ELPs entraînait une forte diminution des valeurs de  $T_{cp}$ , quelle que soit la nature de l'acide gras. Une autre observation a été que l'acylation des ELPs réduit l'effet de dépendance de la  $T_{cp}$  avec la concentration en polymère. Ceci s'explique par le fait que la  $T_{cp}$  des ELP-FAs ne correspond pas à la coacervation de monomères en agrégats, mais plutôt à l'agrégation de micelles déjà présentes à basse température. Ainsi, comme suggéré par le groupe de Chilkoti, l'agrégation serait contrôlée par la concentration locale en ELP à la surface des micelles et non par la concentration totale du conjugué en solution<sup>13</sup>.

Les ELP-FAs s'auto-assemblent spontanément en micelles en milieu aqueux, nous avons étudié leurs caractéristiques (Fig. 5).

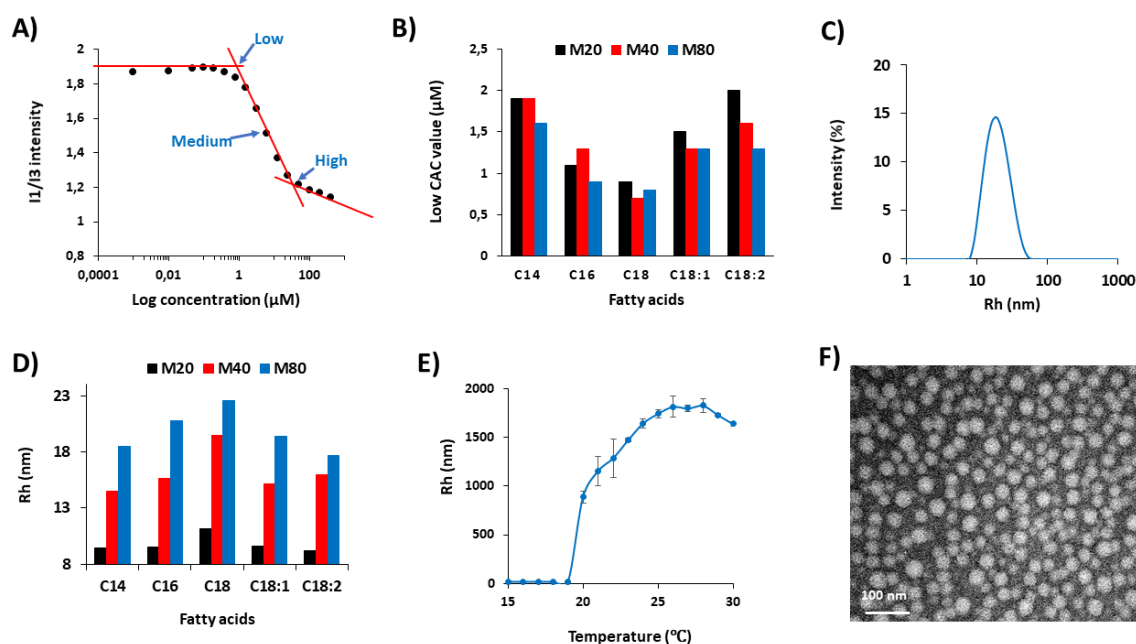


**Figure 5. Caractérisation des micelles d'ELP-FAs.** A) Calcul de la CMC en tampon PBS du M80-C16. B) Valeurs de la CMC pour les M20-FAs (noir), M40-FAs (rouge) et M80-FAs (bleu). C) Analyse par DLS des micelles de M80-C16 à 15°C en tampon PBS. D) Valeurs du rayon hydrodynamique  $R_H$  des 15 ELP-FAs. E) Une solution de M80-C16 à 1 mg/ml (29  $\mu$ M) a été incubée dans du tampon PBS, et les mesures DLS ont été enregistrées entre 15 et 30 °C. Pour chaque valeur, les données sont la moyenne de trois mesures  $\pm$  SD. F) Image de TEM des micelles M40-C16.

Nous avons montré que plus la longueur de la chaîne d'acides gras saturés augmente, plus la valeur de CMC diminue, les valeurs les plus faibles ayant toujours été mesurées avec le C18 quelle que soit la taille de l'ELP. La présence d'insaturation dans la chaîne C18 a entraîné une augmentation de la CMC, cette augmentation étant proportionnelle au niveau d'insaturation. Nous avons également montré que la taille de l'ELP influence également la CMC. Dans la plupart des cas, la valeur CMC la plus basse pour un FA donné a été obtenue avec l'ELP M80, et la plus élevée avec l'ELP M20. Cependant, les différences de valeurs de CMC entre deux ELPs acylés par le même FA étaient beaucoup plus faibles que celles entre les ELPs acylés par différents FAs. Ainsi, la principale force motrice pour l'auto-assemblage de l'ELP-FA à 15 ° C, c'est-à-dire en dessous de la température d'agrégation, provient clairement de l'hydrophobicité du FA.

Pour les 15 ELP-FAs étudiés, une seule population homogène d'objets a été détectée par DLS à 15°C en tampon PBS. La taille des micelles augmentait proportionnellement à la longueur de la chaîne carbonée. Au contraire, lorsqu'une ou deux insaturations étaient présentes le  $R_H$  diminuait. Cela peut s'expliquer par le fait que les doubles liaisons introduisant une courbure de la chaîne acyle, la longueur totale est diminuée. Toutefois nos résultats montrent que la taille des micelles dépend principalement de la masse moléculaire de l'ELP. Le  $R_H$  des micelles des M20-FAs était d'environ 10 nm, compris entre 14 et 18 nm pour les M40-FAs et entre 18 et 23 nm pour les M80-FAs. De plus, pour un FA donné les micelles obtenues avec le conjugué M80 étaient toujours les plus grosses et les micelles du conjugué M20 les plus petites. Des images de microscopie ont ensuite montré que les micelles d'ELP-FAs étaient sphériques.

Nous avons enfin évalué la capacité des micelles à encapsuler et libérer le rouge du Nil. Notre objectif principal était d'étudier le rôle de la longueur de la chaîne acyle gras. Nous nous sommes donc concentrés sur les M80-FAs car nous avons précédemment montré qu'ils formaient des nanoparticules plus grosses que les M40-FAs et M20-FAs, et pouvaient donc encapsuler davantage de molécules hydrophobes. Cette expérience a montré que la longueur de chaîne des acides gras est un facteur important pour l'encapsulation du rouge de Nil dans les micelles, les efficacités d'encapsulation étant respectivement de 20%, 31% et 44 % pour les M80-C14, M80-C16 et M80-C18. Les expériences de relargage ont ensuite montré que la cinétique de libération du rouge de Nil était assez similaire pour les micelles de M80-C14 et M80-C16, avec une libération rapide de 70 à 80 % du contenu pendant les cinq premières

heures, alors que la libération était plus lente avec les micelles de M80-C18, 35 % de fluorescence étant encore détecté dans cet échantillon après 24 h de dialyse. Au final ces expériences ont démontré qu'il sera possible d'affiner la composition des ELP-FAs afin d'obtenir des micelles capables d'encapsuler différentes quantités de médicaments hydrophobes, et de les relarguer selon différentes cinétiques.

Nous avons donc réussi à conjuguer cinq acides gras naturels sur trois polypeptides de type élastine en utilisant un protocole simple qui peut être facilement utilisé pour produire de plus grandes quantités. Ces composés biosourcés ont été caractérisés et leur auto-assemblage étudié. Nous avons montré que les micelles formées étaient stables dans le PBS à une température inférieure à la  $T_{cp}$ , et que cette  $T_{cp}$  dépendait principalement des caractéristiques de l'ELP telles que sa masse moléculaire et/ou son hydrophobicité. La taille des micelles, avec un rayon hydrodynamique compris entre 9 et 22 nm, peut être ajustée en modifiant soit le fragment ELP et/ou la longueur ou la saturation de la chaîne des acides gras. Ces micelles peuvent encapsuler de petites molécules hydrophobes. L'efficacité de l'encapsulation et la cinétique de libération du médicament peuvent être ajustées en modifiant la conception moléculaire de l'ELP-FA.

Dans le dernier chapitre nous avons réfléchi aux moyens d'utiliser nos micelles d'ELP-FAs pour former des hydrogels. Habituellement, les hydrogels à base d'ELPs sont obtenus par réticulation chimique, enzymatique ou par irradiation  $\gamma$ . Ils ont de bonnes propriétés rhéologiques mais contiennent souvent des composants chimiques nécessaires à la réaction de réticulation qui sont peu biocompatibles. De plus, ces hydrogels ne sont pas réversibles car leur intégrité est maintenue par des liaisons covalentes. Pour certaines applications thérapeutiques, les hydrogels physiques sont plus adaptés en raison de leurs propriétés d'auto-réparation. Ces hydrogels physiques sont généralement constitués de polymères associatifs, également appelés polymères téléchéliques, qui sont des copolymères triblocs de type BAB avec un squelette hydrophile (bloc A) et deux groupements hydrophobes (blocs B). Ils s'associent en milieu aqueux dans des « micelles de fleurs » : lorsque la concentration augmente et que les micelles commencent à interagir, les greffons hydrophobes se rassemblent pour créer des microdomaines, ce qui conduit à la formation d'un réseau physique 3D. Ce processus est illustré dans la figure 6.

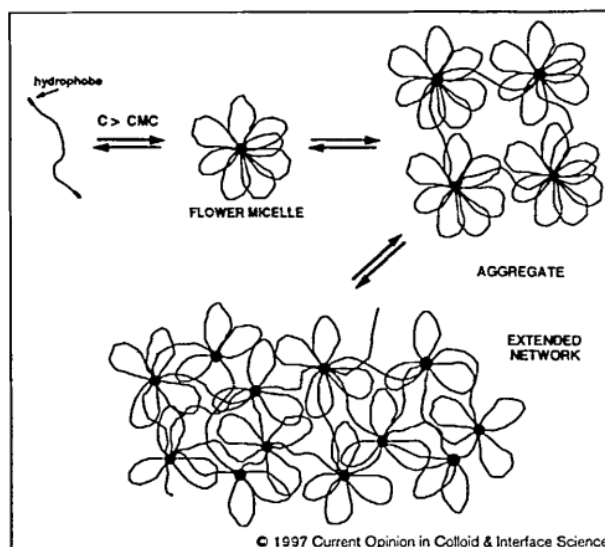


**Figure 6. Représentation de l'association de copolymères triblocs de type BAB selon Winnik et Yetka<sup>14</sup>.**

Pour obtenir des triblocs BAB, nous avons utilisé deux stratégies. Dans la première, nous avons introduit par mutagenèse dirigée une lysine en C-terminal dans la séquence des ELPs de la série Mx utilisés dans le chapitre précédent. Ces nouveaux ELPs contenaient donc deux amines primaires, celle de la méthionine N-terminale et celle de la chaîne latérale de la lysine à l'extrémité C-terminale. Après production et purification de ces ELPs, nous les avons acylés avec l'acide palmitique grâce à la réaction de conjugaison précédemment décrite. Dans la seconde stratégie, nous avons acylé l'amine primaire N-terminale d'ELPs qui possédaient une cystéine en position C-terminale. En condition oxydante, ces FA-ELPCs pouvaient donc former des dimères par formation d'un pont disulfure intermoléculaire ce qui conduisait à la création de triblocs FA-ELPC-CELP-FA.

Dans un premier temps nous avons procédé aux étapes de mutagenèse dirigée pour obtenir les clones permettant l'expression des ELPs M20K, M40K, M60K et M80K. En parallèle, nous avons défini les conditions d'oxydation qui permettaient d'obtenir des dimères de M40C sans oxyder les résidus méthionines présents dans la séquence. Après acylation, les triblocs FA-MxK-FA et FA-ELPC-CELP-FA ont été purifiés et analysés par RP-HPLC. Leur  $T_{cp}$  a été déterminée par turbidimétrie et la taille des micelles évaluée par DLS en conditions diluées (1 mg/ml). A une température inférieure à la  $T_{cp}$ , la taille des micelles en tampon Tris variait entre 8 et 16 nm, le  $R_H$  étant dépendant de la taille du bloc ELP. L'ajout de sel dans le milieu provoquant l'agrégation des micelles, la formation des hydrogels physique a été réalisée dans

de l'eau. Pour former ces hydrogels, nous avons utilisé une concentration finale en tribloc de 5%, soit 50 mg/ml. Des hydrogels ont été obtenus avec 5 % de M80K palmitoylé et 5 % de dimères de M40C palmitoylé, ce qui montrait l'importance de la taille du bloc hydrophile. Les études rhéologiques ont montré que les hydrogels de M80K palmitoylé avaient un caractère de fluide viscoélastique, alors que les hydrogels de dimères de M40C palmitoylé avaient les caractéristiques attendues pour un hydrogel physique (Figure 7).

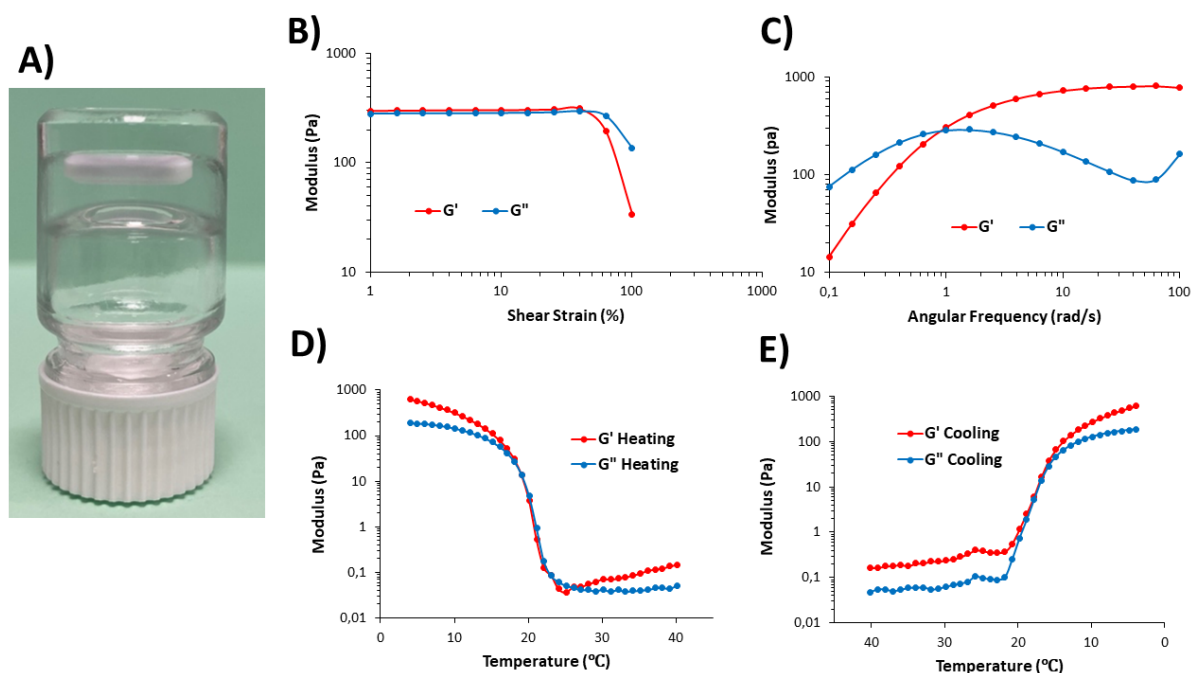


**Figure 7. Paramètres rhéologiques du gel C16-M40C-CM40-C16 à 4°C. A) Photo du gel obtenu avec 5% de conjugué dans de l'eau. B) Module élastique (G' en rouge) et module de perte (G'' en bleu) en fonction de la contrainte de cisaillement à 1 rad/s. C) Module élastique (G') et module de perte (G'') en fonction de la fréquence. D) et E) Module élastique (G') et module de perte (G'') en fonction du chauffage (D) ou du refroidissement (E) de l'échantillon. La fréquence angulaire était de 10 rad/s.**

Nous avons ensuite étudié le comportement de cet hydrogel physique en fonction de la température. A basse température, nous avons mesuré des valeurs de G' et G'' de 630 et 190 Pa. Lors du chauffage, les deux modules ont diminué progressivement jusqu'à 18°C puis ont chuté à des valeurs inférieures à 1 Pa indiquant une rupture du gel. Lors du refroidissement de l'échantillon, nous avons observé une tendance similaire : des valeurs basses inférieures à 1 Pa pour les deux modules entre 40 et 22°C, puis une forte augmentation jusqu'à ce que la température atteigne 16°C. A cette température, la valeur de G' devient supérieure à celle de

G" indiquant la formation de l'hydrogel. La dissociation du gel observée à température supérieure à 18-20°C peut s'expliquer par le fait que le bloc ELP subit une transition vers un caractère plus hydrophobe. La structure micellaire en forme de fleur est alors perdue en raison de l'agrégation des ELPs dans la couronne et les connexions préexistantes entre les différentes micelles sont alors rompues.

En utilisant ces dimères M40C palmitoylés nous avons obtenu des hydrogels physiques aux propriétés intéressantes : (i) ils sont hautement transparents, ce qui est une caractéristique recherchée pour des applications thérapeutiques telles que les implants intraoculaires ; (ii) ils possèdent des propriétés d'auto-réparation qui peuvent intéresser l'ingénierie tissulaire ; (iii) ils peuvent être dissociés soit par incubation avec un agent réducteur qui va casser les ponts disulfures et donc générer des micelles identiques à celles décrites pour le M40-C16, soit en augmentant la température du milieu. Ces gels pourraient être améliorés pour modifier la température à laquelle ils se dissocient. En effet, l'idéal serait qu'ils ne se dissocient pas en dessous de la température physiologique. La température de dissociation dépendant de la T<sub>cp</sub> de l'ELP, notre objectif sera de l'augmenter soit en oxydant les méthionines du M40C, soit en alkylant ces mêmes méthionines comme cela a déjà été réalisé avec succès dans notre laboratoire<sup>15</sup>.

En conclusion, les travaux de cette thèse ont montré l'intérêt des ELPs conjugués à des groupements hydrophobes pour générer des nanoparticules capables d'encapsuler des molécules hydrophobes, ou pour former des hydrogels physiques. Les propriétés de ces nanoparticules et hydrogels peuvent être ajustées en jouant sur la taille et la composition de l'ELP et/ou sur la nature du groupement hydrophobe (lipide, acide gras, polyisoprène, etc.). Les méthodes de production des ELPs par voie recombinante sont bien établies et pourront être industrialisées si nécessaire. Les réactions de couplage que nous avons utilisées sont relativement simples, notamment pour la conjugaison des acides gras, ce qui permettra également un changement d'échelle pour la production des ELP-FAs.

Les développements futurs pourront se faire dans deux directions. Pour la délivrance de médicaments, il serait par exemple intéressant que les micelles d'ELP-FAs soient capables de délivrer leur contenu dans des types cellulaires déterminés. Pour introduire cette spécificité, on pourrait imaginer de greffer à une des extrémités de l'ELP un motif peptidique ou glucidique qui se lierait à un récepteur cellulaire donné. En ce qui concerne les hydrogels, hormis le fait

de développer des composés qui permettront d'obtenir des hydrogels stables dans des conditions physiologiques (température, concentrations en sels, etc.), il faudra évaluer leur biocompatibilité et leur capacité à permettre l'adhésion cellulaire. Pour ce dernier point, nous pensons que la nature même de nos triblocs FA-ELP-FA sera favorable puisque les acides gras qui assurent la cohésion du gel en se connectant entre deux micelles pourront également s'insérer dans les membranes des cellules environnantes pour améliorer leur adhésion.

## Bibliographie

- 1 D. W. Urry, M. M. Long, B. A. Cox, T. Ohnishi, L. W. Mitchell and M. Jacobs, *Biochimica et Biophysica Acta (BBA) - Protein Structure*, 1974, **371**, 597–602.
- 2 D. W. Urry, B. Haynes and R. D. Harris, *Biochemical and Biophysical Research Communications*, 1986, **141**, 749–755.
- 3 D. E. Meyer and A. Chilkoti, *Biomacromolecules*, 2004, **5**, 846–851.
- 4 D. W. Urry, *Progress in Biophysics and Molecular Biology*, 1992, **57**, 23–57.
- 5 D. W. Urry, T. L. Trapane and K. U. Prasad, *Biopolymers*, 1985, **24**, 2345–2356.
- 6 Y. Cho, Y. Zhang, T. Christensen, L. B. Sagle, A. Chilkoti and P. S. Cremer, *Journal of Physical Chemistry B*, 2008, **112**, 13765–13771.
- 7 K. M. Luginbuhl, D. Mozhdzhi, M. Dzuricky, P. Yousefpour, F. C. Huang, N. R. Mayne, K. L. Buehne and A. Chilkoti, *Angewandte Chemie - International Edition*, 2017, **56**, 13979–13984.
- 8 D. Mozhdzhi, K. M. Luginbuhl, M. Dzuricky, S. A. Costa, S. Xiong, F. C. Huang, M. M. Lewis, S. R. Zelenetz, C. D. Colby and A. Chilkoti, *J Am Chem Soc*, 2019, **141**, 945–951.
- 9 D. Mozhdzhi, K. M. Luginbuhl, J. R. Simon, M. Dzuricky, R. Berger, H. S. Varol, F. C. Huang, K. L. Buehne, N. R. Mayne, I. Weitzhandler, M. Bonn, S. H. Parekh and A. Chilkoti, *Nat Chem*, 2018, **10**, 496–505.

- 10 T. Zhang, F. Peruch, A. L. Wirotius, E. Ibarboure, F. Rosu, C. Schatz and B. Garbay, *Polymer Chemistry*, 2021, **12**, 6030–6039.
- 11 E. M. Moussa, J. P. Panchal, B. S. Moorthy, J. S. Blum, M. K. Joubert, L. O. Narhi and E. M. Topp, *J Pharm Sci*, 2016, **105**, 417–430.
- 12 S. K. Abbott, P. L. Else, T. A. Atkins and A. J. Hulbert, *Biochimica et Biophysica Acta (BBA) - Biomembranes*, 2012, **1818**, 1309–1317.
- 13 J. R. McDaniel, J. Bhattacharyya, K. B. Vargo, W. Hassouneh, D. A. Hammer and A. Chilkoti, *Angewandte Chemie International Edition*, 2013, **52**, 1683–1687.
- 14 M. A. Winnik and A. Yekta, *Current Opinion in Colloid & Interface Science*, 1997, **2**, 424–436.
- 15 J. R. Kramer, R. Petitdemange, L. Bataille, K. Bathany, A.-L. Wirotius, B. Garbay, T. J. Deming, E. Garanger and S. Lecommandoux, *ACS Macro Letters*, 2015, **4**, 1283–1286.



# Chapter 1. Bibliography

## 1.1. Introduction

In 20<sup>th</sup> century, drugs were administered in pill form, where drug molecules were released immediately in water, without control<sup>1</sup>. This results in rapid clearance of small-molecule drugs from the circulation, inconvenient dosing regimens, and dose-dependent side effects. The Nobel laureate Paul Ehrlich developed the concept of ‘control drug delivery’, which aim to deliver drugs to specific targets while avoiding off-target toxicity<sup>2</sup>. Since 1950s, researchers have focused first on drug diffusion, dissolution, and pharmacokinetics, then on increasing circulation time and local drug release<sup>3,4</sup>. Liposomal amphotericin B was the first drug delivery system, approved by FDA in 1990<sup>5</sup>. Synthetic materials or polymers as drug carriers achieved slow renal excretion by increasing their molar mass, but it can lead to uncontrolled stereochemistry or molar mass and trigger immunogenic or toxic degradation products<sup>6-8</sup>. Therefore, natural materials such as lipids, polysaccharides, nucleic acids, and proteins<sup>9</sup> are favored by researchers.

Protein-based materials are biocompatible and their degradation products, amino acids, are nontoxic<sup>10</sup>. Both biopolymers based on consensus sequence from naturally derived proteins and *de novo* designed polypeptides are used for biomedical applications<sup>1,11</sup>. These two approaches provide near-absolute control over the sequence, self-assembly, stimuli-responsiveness, and dispersity of the carrier, which cannot be matched by synthetic polymers<sup>12</sup>. As shown in Figure 1, recombinant polypeptides can be: (i) introduced active functional groups for chemical modification and drug conjugation; (ii) used to create fusion proteins by recombinant technologies<sup>10,13</sup>; (iii) designed according to the application<sup>14</sup>; (iv) designed to responds to variety of stimuli, including temperature, pH, oxidative conditions, or the presence of specific biomolecules<sup>15,16</sup>; (v) engineered to self-assemble into a variety of architectures ranging from nanomaterials to hydrogels to porous scaffolds<sup>17</sup>.

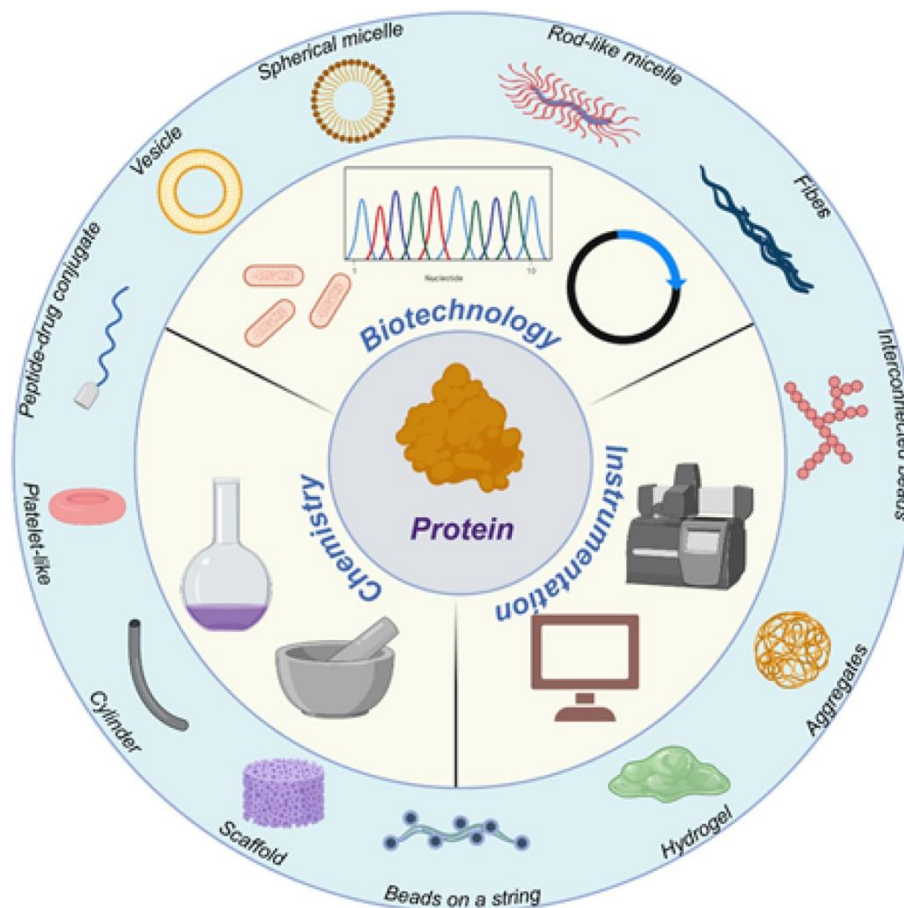


**Figure 1. Recent advances in the engineering of the peptide-based biomaterials as delivery vehicles. Adapted from Varanko and collaborators<sup>18</sup>**

Generally, drug delivery systems are designed to overcome the pathophysiological and translational challenges. Hydrophobic drugs with low aqueous solubility can be administered systemically by combining them with surfactants, which however pose health risks<sup>19</sup>. Therefore, hydrophobic drugs should be encapsulated to improve solubility. The size of the drug, its charge and hydrophobicity determine its half-circulation time. For example, molecules under 60 kDa or 6 nm diameter are rapidly cleared from blood circulation. Drug encapsulation prevents clearance by renal filtration and degradation by serum enzymes or macrophages<sup>20,21</sup>. Encapsulation increases drug accumulation by passive targeting, including increased permeation by the enhanced permeability and retention (EPR) effect, and active targeting by binding to cell receptors<sup>22,23</sup>. Indeed, to transport the drugs into the tissue, drug carriers can be loaded with penetrating peptides or modified to tune their physicochemical properties<sup>24</sup>. Directing the drug to the subcellular site of its molecular action<sup>25–28</sup>, and modulate its release kinetic<sup>29</sup> are also current challenges.

Proteins such as silk, keratin, albumin, collagen, elastin, resilin, and others are widely used in biomedicine.

Silk is a fibrous protein produced from silkworms such as *Bombyx mori* and spiders. The one used in biomedical applications comes from *Bombyx mori* because it is available in large quantities at a reasonable cost. It consists of two major proteins, sericin (which may cause an immunogenic response) and silk fibroin (SF)<sup>30,31</sup>. SF contains a light chain of 26 kDa linked to a 390 kDa heavy chain by a single disulfide bond. The heavy chain consists of alternating hydrophilic and hydrophobic blocks, the hydrophobic blocks being responsible for the  $\beta$ -sheet structure. SF is biocompatible, biodegradable and non-immunogenic<sup>32</sup>. It can self-assemble into various structures ranging from nanoparticles to hydrogels by modulating the organization of its  $\beta$ -sheets<sup>32,33</sup>. Its structure can be changed by external stimuli such as pH<sup>34</sup>, salt concentration<sup>34</sup> or other co-solvent<sup>35,36</sup>. SF can be chemically modified<sup>37</sup>, and recombinant DNA technology was used to modify its sequence<sup>38-40</sup>. For instance, Numata and colleagues recombinantly synthesized silk-based block copolymers with poly(L-lysine) domains for gene delivery<sup>41</sup>. The SF has also been used for the administration of injectable<sup>42</sup> and conjugated<sup>43</sup> drug.

Keratin is a protein with a fibrous structure containing a high content of cysteine which gives it particular mechanical and chemical characteristics. When the cystine content is high, hard keratins are formed, while soft keratin can be obtained when the cystine content is lower. It is therefore oxidation-reduction reactions that regulate the characteristics of the fibers<sup>44</sup>. Keratin has several characteristics that make it a good candidate for biomedical applications. It is negatively charged and therefore the electrostatic interaction of keratin nanoparticles or hydrogels with a positively charged drug can provide sustained release of said drug<sup>45-47</sup>. It is also pH sensitive due to the large number of carboxyl groups. At acidic pH, protonation of carboxyl groups leads to a higher proportion of  $\beta$ -sheets in the sequence, resulting in pH-sensitive hydrogels<sup>48,49</sup>. Finally, its composition rich in cysteine allows it to be sensitive to oxidation-reduction by regulating the content of disulfide bridges, a characteristic widely used for drug release<sup>50-52</sup>. Thus, its sensitivity to changes in glutathione concentration has been used to deliver chemotherapy drugs to metastatic cancer cells<sup>46</sup>.

Albumin, the most abundant protein in human plasma, can serve as a carrier for drugs. Bovine serum albumin<sup>53-57</sup> and human serum albumin transports small hydrophobic molecules such as

hormones and fatty acids, and therefore can bind hydrophobic drugs<sup>58</sup>. It is biodegradable and has no known systemic toxicity. Additionally, it has an exceptionally long half-life of 19 days in humans and animals because it bypasses the body's clearance and degradation systems<sup>59–62</sup>.

Collagen is the most abundant protein in mammals, and is found in skin, hair, ligaments, tendons, cartilage, bone, and placenta<sup>63,64</sup>. It is the main component of the extracellular matrix (ECM) and connective tissue. Collagen has a broad spectrum of functions, including cell adhesion, cell migration, tissue scaffolding, and repair<sup>63</sup>. The triple helix structure of collagen is comprised by three interlocking polypeptide chains, each chain containing repetitions of the sequence Gly-X-Y, where X and Y are Proline (Pro) and hydroxyproline, respectively<sup>18</sup>. Collagen has been used for drug delivery and tissue engineering, thanks to its self-assembly properties, its ability to form hydrogels, its biodegradability and its reactivity to external stimuli<sup>65,66</sup>. However, the collagen currently used is purified from biological tissues or cell cultures, which poses biosafety concerns. Therefore, several groups developed collagen-mimetic peptide or collagen-like peptides<sup>67,68</sup>. It has been shown that these collagen mimics can self-assemble through cysteine knot<sup>69</sup> or through  $\pi$ - $\pi$  interactions after introduction of aromatic amino acids in their sequence<sup>70,71</sup>. They can also be conjugated with lipids to interact with hydrophobic drugs<sup>72,73</sup>.

Finally, elastin is also a natural protein that has interesting properties both for the delivery of drugs and for the formation of hydrogels. This is detailed below.

## 1.2. Natural elastin

Elastin is the protein responsible for the elastic properties of vertebrate tissues. In humans, elastin synthesis begins in the 3–4-month-old fetus and continues through early adulthood. Then, its synthesis stops, and no renewal of the degraded elastin fibers is possible. Elastin is abundant in human lung (30% of dry weight), skin (2–4% of dry weight), elastic ligaments (70% of dry weight) and blood vessel (50% of dry weight)<sup>74–77</sup>. It contributes to the elastic behavior, the organ being able to deform under the action of an external force. This deformity occurs when a joint flexes and distorts the ligaments and overlying skin, when the lung is dilated during breathing, and when blood pressure pulses pass through vessels and arteries<sup>78</sup>.

The biosynthesis pathway is shown in Figure 2. After transcription of the tropoelastin gene, the corresponding transcript is translated in the rough endoplasmic reticulum<sup>79,80</sup>. As soon as the

protein is synthesized, a specific chaperone protein, galactoselectin also called elastin-binding protein, binds to newly synthesized tropoelastin molecules to prevent their intracellular aggregation<sup>81,82</sup>. Following Golgi secretion, the extracellular tropoelastin dissociated from its chaperone which interacts with the microfibrils galactosugars present in the extracellular space. The chaperone is then recycled by the surrounding cells, and the tropoelastin molecules starts to aggregate together and to interact with microfibrils. Then, the lysyl residues of tropoelastin are deaminated and oxidized by lysyl oxidase in the presence of  $\text{Cu}^{2+}$ <sup>74,83</sup>. Oxidized lysines react with each other and with non-oxidized lysines to create interchain covalent bonds.

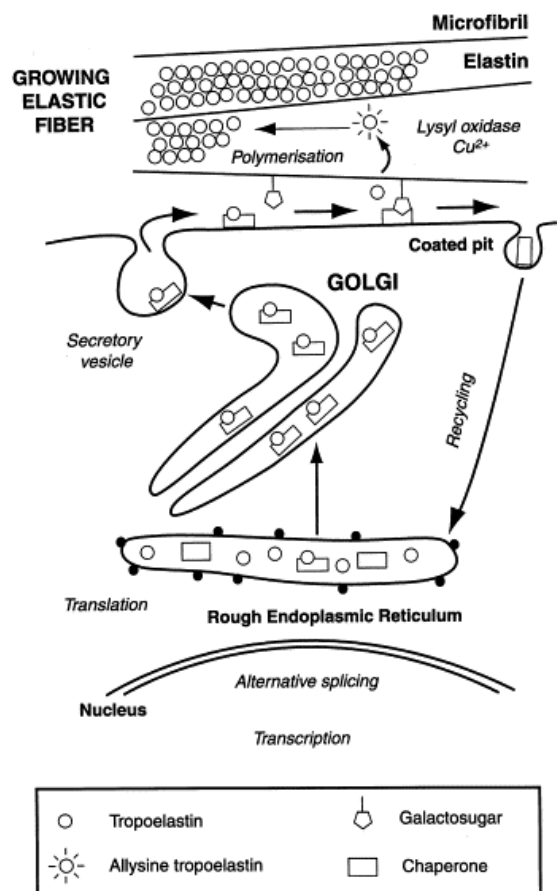


**Figure 2. Schematic description of elastin deposition. From Debelle and Tamburo<sup>80</sup>**

Thus, native elastin is an insoluble polymer composed by several tropoelastin monomers covalently bound by cross-linking. It is a very stable protein, its half-life having been estimated at around 70 years in humans. Part of this stability comes from its conformation<sup>84</sup>. Elastin belongs to the family of intrinsically disordered proteins, which is a generic term used for proteins lacking a cooperatively folded structure under native conditions<sup>76,84,85</sup>. Tropoelastin is made of two types of domains, hydrophobic ones with many Gly, Val, Ala and Pro residues

and hydrophilic domains with Lys and Ala residues which are important for crosslinking<sup>86</sup>. The driving force of elastic properties, which is the spontaneous recoil of stretched elastin, is entropic in nature<sup>87</sup>. Indeed, all the energy is stored in the polypeptide backbone when the molecule is stretched and can be recovered during relaxation. The glass transition temperature ( $T_g$ ) is also a characteristic of elastin. At 30% of hydration, this  $T_g$  is about 30°C, below body temperature<sup>88</sup>. In addition, elastin undergoes a phase transition called coacervation. It is soluble in aqueous solution at ambient temperature, but aggregates because of interactions between hydrophobic domains when temperature is raised<sup>89</sup>.

### 1.3. Elastin-like polypeptides (ELPs)

#### 1.3.1. Introduction

The concept of elastin-like polypeptide was raised by Dan W. Urry and his colleagues in the early seventies<sup>90,91</sup>. They synthesized polymers that consisted of repeats of one of the hydrophobic pentapeptide units of human elastin, VPGVG, and showed that these synthetic polypeptides coacervate above a specific temperature similarly to natural tropoelastin. This transition temperature ( $T_t$ ) is also called the cloud-point temperature ( $T_{cp}$ ). A schematic representation of the ELP thermosensitivity is shown in Figure 3.

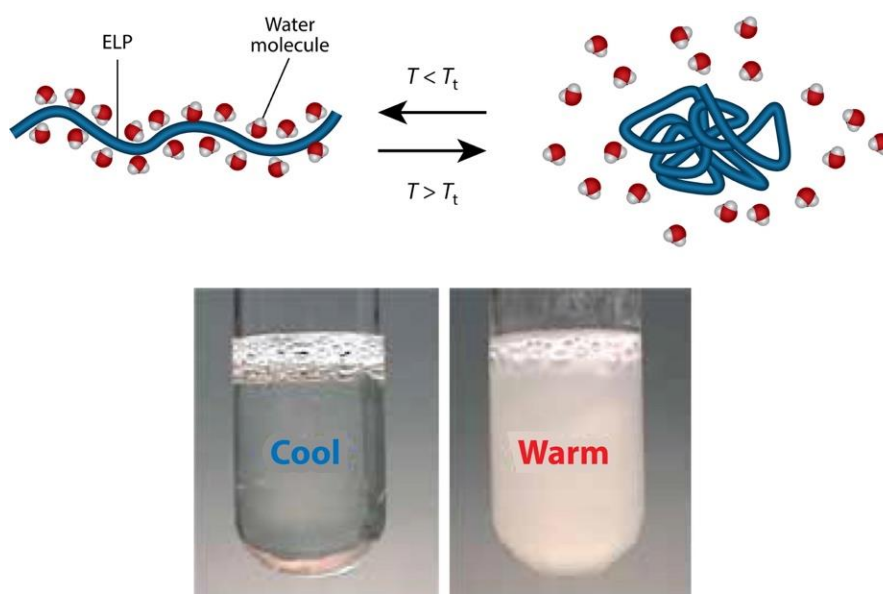


**Figure 3. ELP thermosensitivity. Adapted from Varanko and collaborators<sup>92</sup>.**

At temperatures below its Tt, the ELP is hydrated and fully soluble, appearing as an optically transparent solution. As the temperature is raised above the Tt, the ELP coacervates and phase separates, appearing as cloudy solution. As the temperature is lowered below the Tt the ELP re-solubilizes<sup>92</sup>. At low temperature, the ELP is in a disordered state and fully hydrated. The increase of temperature above the Tt results in a disorder of the hydrophobic hydration of the polymer<sup>93-95</sup> and structural changes towards type-II  $\beta$ -turns, type-I  $\beta$ -turns, and  $\beta$ -strands, leading to their aggregation<sup>96,97</sup>. When the temperature is raised above Tt, the positive entropy that occurs from ordered water to bulk water is larger than the negative entropy caused by polymer ordering. Despite folded phase separation, the product still contains 63% water and 37% polymers by weight<sup>98</sup>.

The Tt value of ELP is usually detected with Uv/vis spectrophotometer at 350 nm with a narrow temperature window (1-2°C). The point where the absorption increases significantly is the Tt value. This transition can also be measured by differential scanning calorimetry and by dielectric relaxation methods<sup>99,100</sup>.

### **1.3.2. Role of the “guest” residue**

ELPs are made of multiple repeats of Val-Pro-Gly-Xaa-Gly pentapeptides, where the guest residue (Xaa) can be any natural amino acid except proline<sup>99</sup>. Other position substitutions, such as a single substitution of an alanine for a glycine residue at the third position of the VPAVG repeat sequence transforms the mechanical behavior of the ELP from elastomeric to plastic<sup>101,102</sup>.

A schematic representation of the canonic pentapeptide sequence is shown in Figure 4.

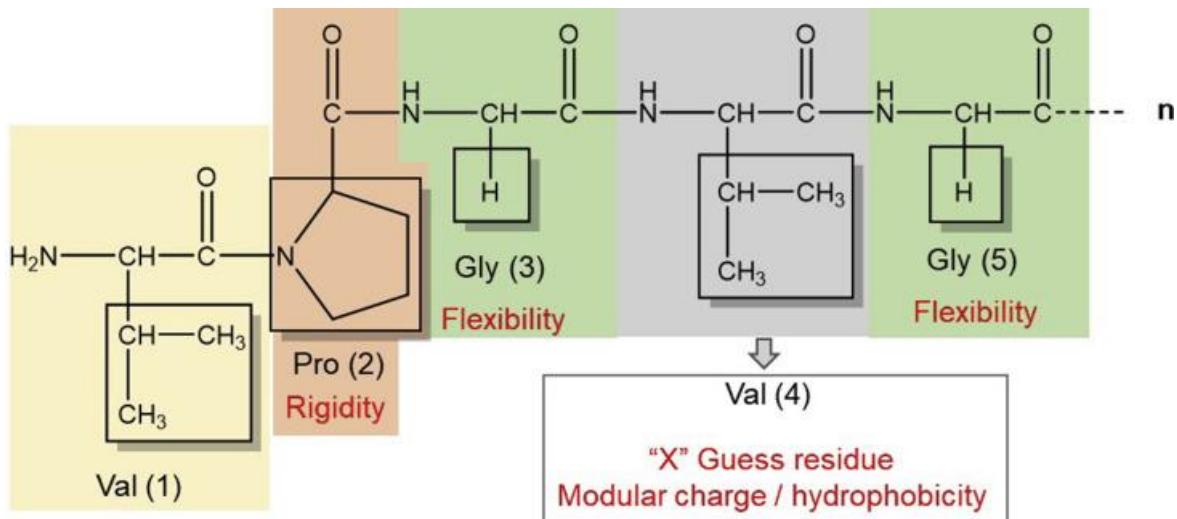


**Figure 4. Pentapeptide unit of Elastin-like polypeptide. Adapted from Quintanilla-Sierra and collaborators<sup>76</sup>.**

Urry and colleagues proposed that there is one type II  $\beta$ -turn per pentapeptide with adjacent proline and glycine residues at the corner of the bend, stabilized by a hydrogen bond connecting the C=O group of the first valine to the NH of the guest residue. The repetition of this conformational motif gives rise to structures called  $\beta$ -spirals, the  $\beta$ -turns acting as spacers between the turns of the spiral<sup>103</sup>. The cyclic structure of proline gives it a more rigid conformation than those of other amino acids. Indeed, it does not contain amide hydrogen atoms at physiological pH, and its dihedral angle phi is restricted. Proline is therefore unable to form stabilizing hydrogen bonds in secondary structures. Therefore, proline breaks the classical secondary structures such as  $\alpha$ -helices and  $\beta$ -turns.

On another hand, the disordered structure of ELPs at  $T^{\circ} < T_t$  is the consequence of the high proline and glycine content in the ELP backbone, with a compositional threshold of  $(2 \text{ Pro} + \text{Gly}) \geq 0.6$ , thus meaning that the percentage of proline is more decisive than that of glycine<sup>104</sup>. However, glycine plays also a role in the fact that ELP are disordered and hydrated at low temperature. The absence of a side chain on the glycine residues allows ELP to adopt different conformation in aqueous solution, and therefore a higher entropy which disadvantages the formation of ordered structures<sup>85,105</sup>.

Dan Urry's group first pointed out that the ELP transition temperature is inversely related to the average residue hydrophobicity<sup>106</sup>. Using differential scanning calorimetry, they compared the  $T_t$  value of poly(VPGVG) and poly(IPGVG) and demonstrated that an increase in hydrophobicity leads to a decrease in  $T_t$ . They explained that poly(IPGVG) contains  $\beta$ -

branching which provide important hydrophobic interactions during folding caused by the  $\text{CH}_2$  moiety of each pentamer<sup>107</sup>. Then, they studied the impact of the hydrophobicity of residue X on the value of  $T_t$  using an ELP of sequence  $[f_v(\text{GVGVP}), f_x(\text{GXGVP})]$ , where  $f_v$  and  $f_x$  are molar fractions (Figure 5).

At a fixed value of  $f_x$  of 0.2, they showed that the value of  $T_t$  is directly correlated with the nature of the residue X, the hydrophobic amino acids such as Tyr, Phe, Leu or Ile decreasing the  $T_t$  compared to the residue Val, whereas the incorporation of hydrophilic amino acids like Asp or Lys increases  $T_t$  (Fig. 5A)<sup>108</sup>. In addition, they showed that there is a linear relationship between the  $T_t$  value and the molar ratio ( $f_x$ ) of the pentapeptide containing the X residue (Fig. 5B). Urry later developed a thermodynamic model for the relationship between the X residue and the  $T_t$  that fits the experimental data<sup>109</sup>.

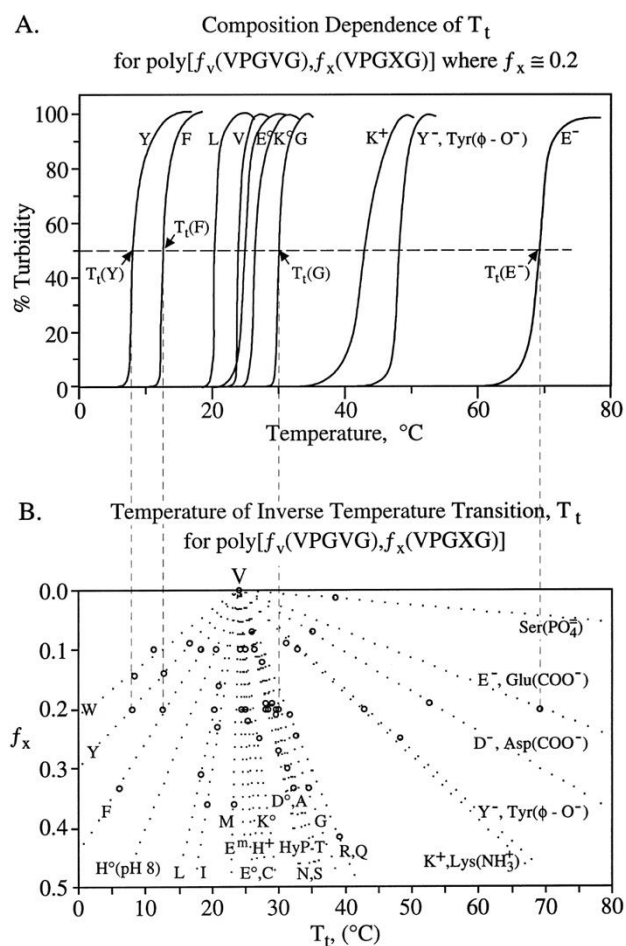


**Figure 5. (A) Transition temperatures of poly $[f_v(\text{VPGVG}), f_x(\text{VPGXG})]$  for  $f_x = 0.2$  with different X-residues. (B) Plots of  $T_t$  versus  $f_x$  for all the amino acid residues. Adapted from Urry<sup>99</sup>**

Interestingly, Rodriguez-Cabello's group investigated if the  $T_t$  depends only on its overall polarity, or if in the case of ELPs made up of alternating hydrophobic and hydrophilic blocks the spatial organization is important. They recombinantly expressed di- and triblock ELP copolymers made of hydrophilic and hydrophobic blocks. By changing the arrangement and the length of the blocks while keeping the average polarity constant, they demonstrated that the sequence plays a key role in the behavior of ELPs, and therefore that the prediction of  $T_t$  based only on the average polarity and the mass molecular is only applicable to regular homopolymers<sup>110</sup>. A model was also created by Ashutosh Chikoti's group to predict the  $T_t$  of a given ELP. The objective was to be able to elaborate the sequence of the ELP to reach a target  $T_t$  before the stage of recombinant production. The ELPs used in this study were poly (Val-Pro-Gly-Xaa-Gly), with Xaa = Ala or Val<sup>111</sup>.

### 1.3.3. Factors influencing the $T_t$ value

Meyer and Chilkoti developed a model to represent the variation of  $T_t$  value as a function of ELP concentration and ELP size<sup>112</sup>. They used three ELP libraries with different guest residues and polypeptide length. The experimental data were obtained by turbidimetry and used to establish a model (Figure 6).

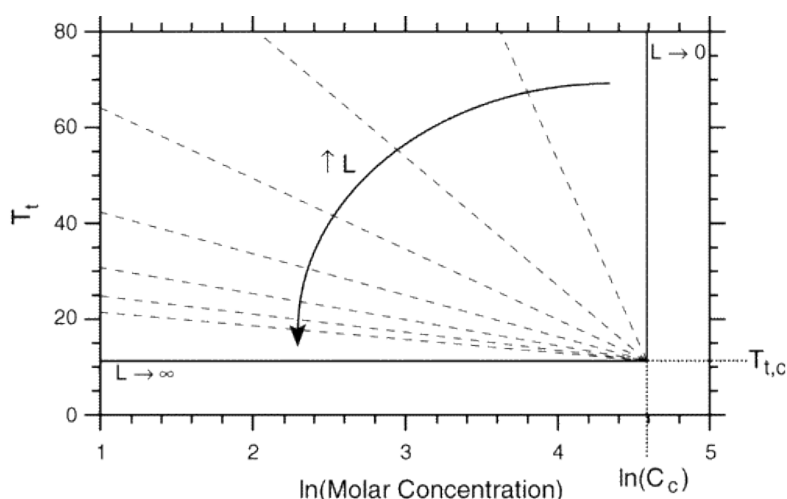


**Figure 6. Model that describes the variation of  $T_t$  as a function of ELP chain length ( $L$ ) and ELP concentration. Adapted from Meyer and Chilkoti<sup>112</sup>.**

They showed that for a given ELP sequence, the Tt decreases with increasing concentration and with increasing size of the polypeptide. Figure 6 also showed that for a given ELP library, all the lines converge to a single point which is defined by a common Tt and concentration.

The results of this study are fundamental for anyone wishing to use ELPs for therapeutic applications. Indeed, they demonstrate a very strong effect of ELP concentration on Tt. Thus, if ELPs are injected to use their coacervation properties, their dilution after injection could lead to a strong increase in Tt and therefore prevent their aggregation at physiological temperature. To combat this phenomenon, the solution lies in the use of large ELPs, which are less sensitive to the effect of dilution. However, the difficulty is to produce ELPs of very high molecular mass (> 100 kDa).

The salt concentration of the medium in which the ELP is dissolved also affects the Tt value. Tirrell and colleagues measured the Tt of the (VPGIG)<sub>40</sub> in the presence of various concentrations of salts including KCl, NaCl, K<sub>2</sub>SO<sub>4</sub>, or KI<sup>113</sup>. They showed that the Tt linearly decrease with increasing concentrations of KCl, NaCl and K<sub>2</sub>SO<sub>4</sub>. They also showed that the nature of ions plays was important. Salting-out ions facilitate ordered forms, whereas salting-in ions favor random structures.

The chemical modification of the amino acids of an ELP chain can also modify the Tt. A good example is the oxidation of ELPs containing methionine<sup>114</sup>. It was demonstrated that incubation of the ELP (VPGMG)<sub>40</sub> with 30% H<sub>2</sub>O<sub>2</sub> at 0°C for 30 min led to the selective oxidation of methionine to sulfoxide. This resulted in an increase of the Tt from 25°C to 55°C. However, further oxidation of ELP with harsher oxidation conditions led to the appearance of sulfone instead of sulfoxides, which resulted in a decrease in Tt from 55°C to 43°C.

Several pH responsive ELPs were also developed, such as the ELP ([VPGVG]<sub>2</sub>-VPGE-[VPGVG]<sub>2</sub>)<sub>n</sub><sup>100</sup>. At pH 3.5, the  $\gamma$ -carboxylic of glutamic acid is in the protonated state and the authors measured a Tt of 30°C. When pH of the solution was increased to 8.0, a negative charge appeared on the carboxylate and the Tt increased to 85°C.

Light-sensitive ELPs were also designed. They are azobenzene derivatives of (VPGVG). In the dark, the *p*-phenylazobenzene adopted a *trans* isomer conformation which is apolar. After UV irradiation, the *cis* isomer becomes more abundant, and since it is somewhat more polar, this increases the Tt<sup>100</sup>.

In conclusion, several factors can determine the Tt of an ELP. Some are intrinsic to the polypeptide sequence, such as the molecular weight, the nature of residue X, the presence of ionizable or oxidizable groups, and others depend on the environment such as salts and ELP concentration. Therefore, although many studies have been devoted to the development of models for predicting Tt values, none have been able to consider all possible variables. This is of course problematic for researchers who would like to design an ELP for a specific therapeutic application. General rules can be followed but ultimately the true Tt will be determined experimentally on the purified ELP after a tedious process of cloning and production.

#### **1.3.4. Production and purification of ELP**

In the pioneering work of Urry ELPs were produced by solid phase peptide synthesis. However, this technique is complicated and time-consuming, only small-sized ELPs can be obtained, and the production yields are rather low. Thus, the recombinant expression of ELP was quickly considered. Another advantage of recombinant expression is the perfect control of the sequence and size of the polypeptide.

The expression process of a recombinant ELP can be summarized in three successive steps: design of the monomer and construction of the plasmid, recombinant expression in bacteria or eukaryotic cells, and then purification (Fig. 7).

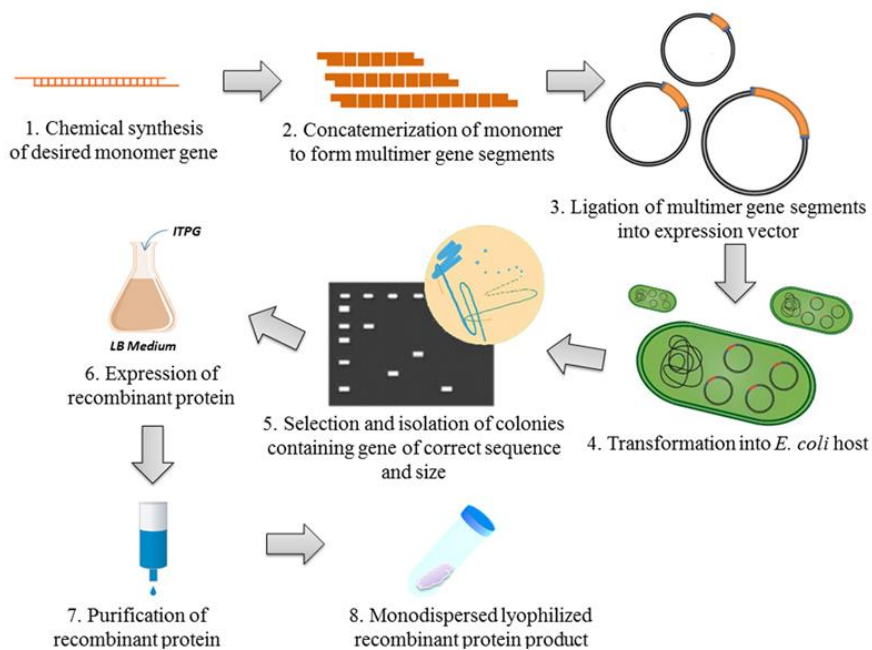


**Figure 7. General biosynthesis scheme of genetically engineered protein using recombinant DNA technology. Adapted from Huang and collaborators<sup>115</sup>.**

The first recombinant elastomeric polypeptide G-(VPGVP)<sub>19</sub>-VPGV was produced in *Escherichia coli* using the vector pGEX-3X<sup>116</sup>. Briefly, a *gst*-G-(VPGVG)<sub>19</sub>-VPGV fusion protein was expressed after induction by 1 mM isopropyl β-D- thiogalactopyranoside (IPTG). After cell lysis by sonication, the fusion protein was affinity purified and cleaved with protease factor Xa to separate the *gst*-tag from the ELP moiety. The ELP was finally recovered by ammonium precipitation, dialyzed and characterized by SDS-PAGE and NMR. Although successful, the yield of purified ELP was very low, around 1 mg/L of culture. In the following years, efforts were made to improve the production and purification processes.

Several strategies have been developed for the construction of ELP clones. One of the most used methods is called recursive plasmid directional ligation (RDL)<sup>117</sup>. As shown in Figure 8, a plasmid “B”, containing two restriction endonuclease (RE) sites, is first obtained by ligation with an oligonucleotide cassette encoding a small ELP sequence (usually 10 to 20 repetitions). Then, part of plasmid B is digested with RE1 and RE2 to obtain the ELP insert, while the other part of plasmid B is only digested by RE1 yielding a linear plasmid with the ELP sequence at one of its extremities. After ligation of this linear plasmid with the purified ELP insert (step C

in Fig. 8), it is possible to obtain a new plasmid containing an ELP sequence twice as large. This cycle can be repeated to obtain multiple repetitions of the initial ELP sequence.

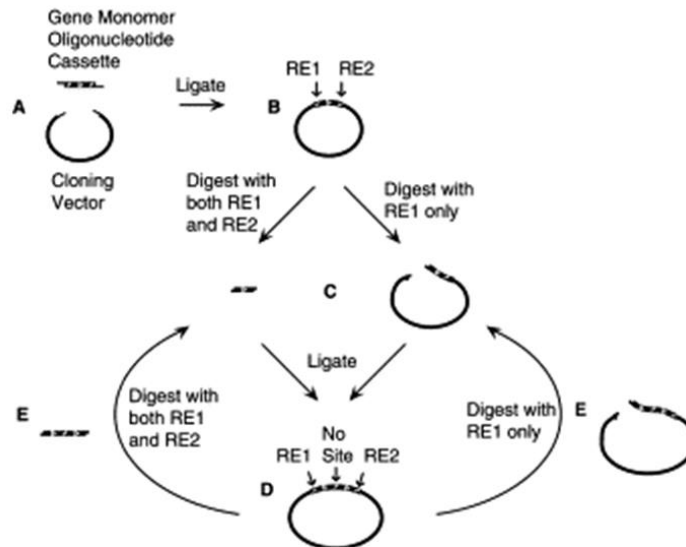


**Figure 8. Schematic representation of the RDL process. RE1 and RE2 are restriction endonucleases sites. Adapted from Chilkoti and collaborators<sup>117</sup>.**

Certain constraints exist, such as the fact that the initial ELP sequence must contain specific sites for RE1 and RE2. This quite often results in the insertion of unwanted extra amino acids between the repeating units of the ELP. In addition, cloning efficiency is limited due to vector or insert self-ligation events. Finally, the RDL was designed for pUC vectors that are not suitable for expression, requiring subsequent subcloning into an expression plasmid.

Based on RDL, Ashutosh Chikoti's group introduced recursive directional ligation by plasmid reconstruction (PRe-RDL)<sup>118</sup>. In this technique, two halves of the parent plasmid, each containing the desired oligomer, are ligated together to create the same plasmid backbone but containing two ELP units (Fig. 9). PRe-RDL is applicable to any arbitrary DNA sequence and has no extraneous peptide oligomers at the junctions between repeats because it uses type II endonucleases. The main advantages of PRe-RDL are that self-ligation and circularization are prevented, and the modular design of PRe-RDL is suitable for the rapid generation of any repetitive peptide sequence of a specified length. It can also be used to join blocks of different lengths and sequences in a predetermined order.

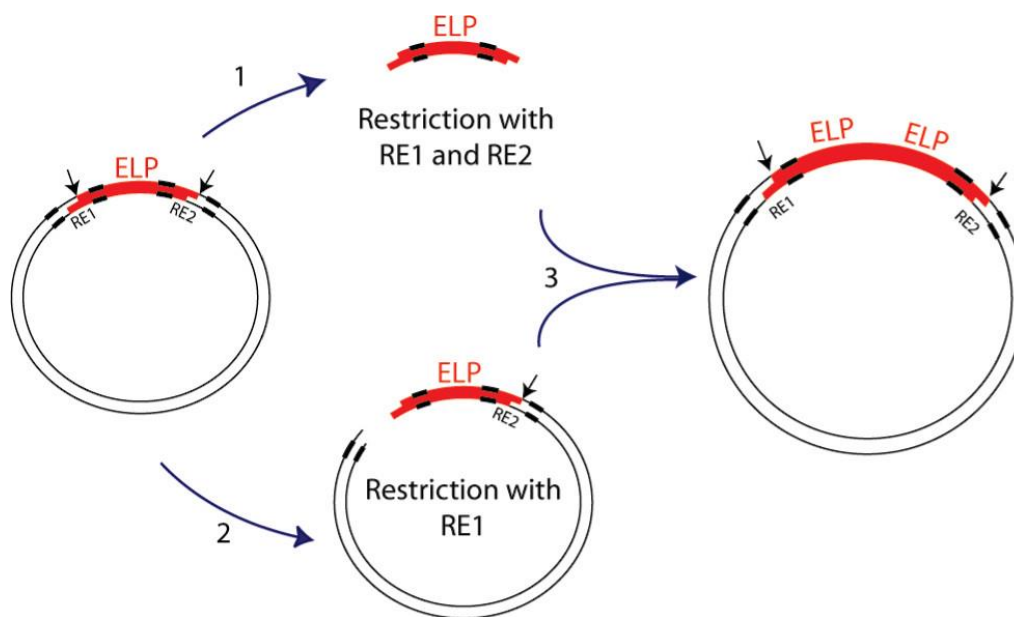


**Figure 9. Recursive directional ligation. The bold areas on the vector represent the endonuclease recognition sequence, the black arrows indicate the location of the cleavage site. From McDaniel and collaborators<sup>118</sup>.**

More recently, Ashutosh Chilkoti's group designed another method called "overlap extension rolling circle amplification" (OERCA). OERCA is a robust method for highly parallel synthesis of genes encoding repetitive protein polymers<sup>119</sup>.

Recombinant expression of ELPs usually occurs in *E. coli*<sup>113,120,121</sup>, as these polypeptides do not require specific post-translational modifications to be active. Nevertheless, the successful expression of recombinant ELPs in yeast<sup>122-124</sup>, fungus<sup>125</sup>, and plants<sup>126,127</sup> has been published. Most groups involved in the production of ELP use the classical pET T7-lac vector system. Briefly, a clone is grown in culture medium to an OD of between 0.5 and 1. Then IPTG is added to the medium to trigger expression of the recombinant ELP which will last for several hours. The cells are recovered by centrifugation, resuspended in an appropriate buffer (water or PBS) and lysed by sonication. After removal of soluble debris by centrifugation, the soluble fraction is used in the purification process.

The ELP purification process takes advantage of the fact that they are thermosensitive. By heating the solution, the ELP will precipitate, and the contaminating soluble host cell proteins will be eliminated in the supernatant by centrifugation. After addition of cold buffer, the ELP will solubilize but not the insoluble contaminating proteins. After a new centrifugation, the

purified ELP will be recovered in the supernatant. This technique is called inverse transition cycling or ITC (Fig. 10).

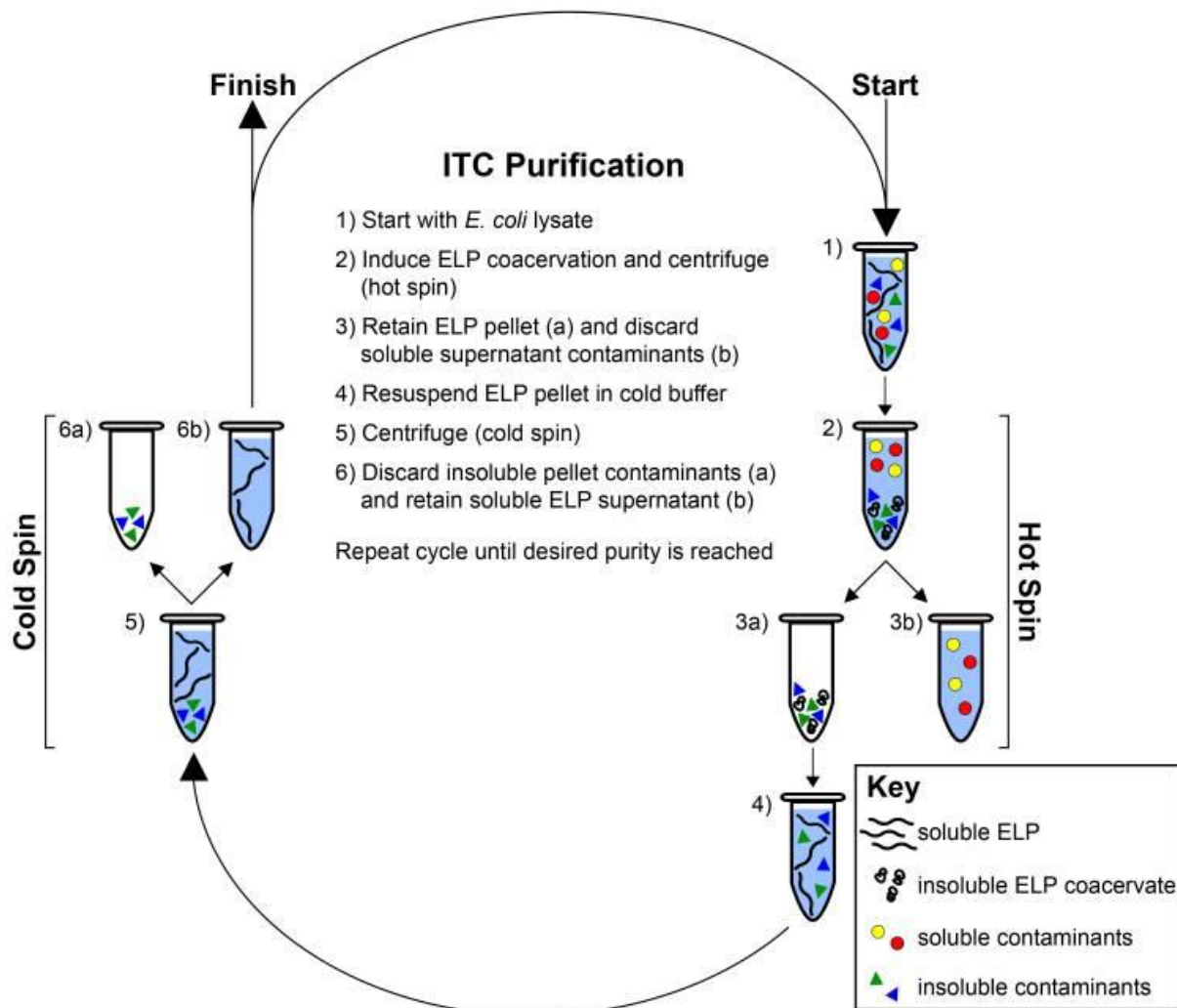


**Figure 10. Inverse transition cycling.** From MacEwan and collaborators<sup>120</sup>.

Compared to conventional processes used to purify recombinant proteins such as chromatography, ITC has several advantages: there is no need for expensive purification machines, the whole process is carried out in aqueous buffers, and it can be easily scaled up<sup>120</sup>. However, there is also one limit. It came from the Tt of the ELP to be produced. If the Tt of the ELP is high, above 60°C, the heating step will be difficult to achieve. Few centrifuges can run at temperatures above 60°C, and incubation of the ELP sample at such a high temperature could result in oxidation of Met or Lys residues if present in the sequence. Even for ELPs with a lower Tt, this can be a problem. As we have already said, the Tt depends on the concentration of ELP. During the first ITCs, the polypeptide is generally diluted in the homogenate and therefore high temperatures must be used to trigger its precipitation, with all the side effects

described above. To circumvent this problem, high concentration of salts could be used to lower the Tt of the sample. However, when producing small hydrophilic ELPs other purification methods should be considered.

### **1.3.5. Immune-response to ELP**

In most articles published on ELPs, it is written that they are biocompatible, biodegradable, and non-immunogenic. These arguments are used for a variety of distinct ELPs, which differ in composition. This is quite surprising, and it is interesting to know where it comes from.

An argument often employed is that ELPs are biocompatible and non-immunogenic because they are derived from the sequence of the human elastin. From a biological point of view, this is a somewhat simplistic reasoning. Indeed, under certain circumstances natural elastin can be degraded into highly immunogenic peptides that can trigger devastating autoimmune responses, such as in systemic sclerosis<sup>128</sup> or in thoracic aortic aneurysm and dissection in smokers<sup>129</sup>.

Fortunately, during the last 35 years several studies were conducted to evaluate the biocompatibility and immunogenicity of these biopolymers. Although rare when compared to the wealth of literature devoted to ELPs, they gave important information.

The first *in vivo* report was obtained with different ELPs that were synthesized chemically and crosslinked before implantation in animals. In 1986, Wood and colleagues<sup>130</sup> chemically synthesized the VPGVG pentapeptide and obtained polymeric forms up to 240 repetitions. These polymers were crosslinked by  $\gamma$ -irradiation and implanted into rabbit muscles. Biocompatibility of the material was simply assessed by radiography of the zone of implantation to detect any strong sign of necrosis, and by histological examination of the surrounding tissues after sacrifice of the animal. Fibrous tissue capsules with active phagocytic cell infiltration were detected around the implants, but the authors said that this mild inflammatory response was similar to that observed with bovine collagen implants or biodegradable suture (PLA-PGA). The same material was later extensively studied for its mutagenicity, acute systemic toxicity, systemic antigenicity, dermal sensitization and pyrogenicity<sup>131</sup>. All these tests gave negative results, except for the muscle implantation in which a slight irritation was observed. Importantly, the lack of immunogenicity was based on the observation that the intraperitoneal injection into Guinea pig did not lead to anaphylactic signs (sick animals), but no immunoglobulins dosage was performed.

The inflammatory response after subcutaneous and intravitreal injections of poly-(VPAVG) particles was evaluated by Rodriguez-Cabello's group<sup>132</sup>. After subcutaneous injection in rats, they showed that the polymer did not induce more cytotoxicity or inflammatory response than the PBS control. After intraocular injection of poly(VPAVG) microparticles, the anterior and posterior segment of the eyes were examined. At first, no significant differences were observed between the eyes from the experimental group and the control group in terms of edema or hemorrhages. However, histopathologic studies showed that among the 11 eyes treated with the poly(VPAVG) microparticles, two showed a marked inflammatory response with monocytic and lymphocytic cell infiltrations, and moderate or low inflammation signs were seen in four more eyes. No inflammatory signs were noticed in the eyes belonging to the control group (n=3). The authors concluded that the inflammatory response detected after the intravitreal injections of poly-(VPAVG) was more likely linked to fibroblastic activation than to immune response.

In 1998, Wei and colleagues sought to identify potentially immunogenic epitopes on human tropoelastin<sup>133</sup>. They hydrolyzed the protein, injected the corresponding peptides into rabbits and mice to obtain respectively polyclonal and monoclonal antibodies, and then they performed immunoassays. In parallel, they synthesized a series of overlapping hexapeptides along the sequence covering exons 2–7 and 23–36 from the N-terminus to the C-terminus, advancing one amino acid residue each time. These synthetic peptides were used to identify the epitopes by competitive ELISA. They demonstrated that none of the antibody raised could react with the hexapeptide VGVAPG, confirming the previous result obtained by Rodriguez-Cabello's group<sup>132</sup>. However, most of the immunological response was directed toward epitopes present in the hydrophobic sequences that are traditionally selected for ELP synthesis (see table below). Indeed, one of the most employed ELP pentapeptide motif (VPGVG) is present in several of the peptide that elicited an immune response.

Interestingly, when small peptides (GVGVVP, VPGVG, VPGG) were used in the competitive ELISA, they did not inhibit the binding of the antibodies, strongly suggesting that only larger peptides containing these motifs, such as LGGVPGVG as an example, could be immunogenic.

The importance of the nature of the guest residue X in the pentapeptide VPGXG was revealed in another study. Briefly, biomaterials made of either poly(VPGVG) or poly[3(VPGVG), (VPGFG)] were evaluated for their capacity to prevent postoperative fibrous scarring in rabbits.

The material made of poly(VPGVG) elicited an insignificant inflammatory reaction without fibrous membrane formation around the implantation site. On the contrary, the biomaterial made of poly[3(VPGVG), (VPGFG)] caused slight inflammation, and the rapid formation of a dense fibrous membrane around the implant. The authors attributed the difference in the inflammatory response to the presence the amino acid phenylalanine (F) in the copolymer whereas valine was the only guest residue in the polymer<sup>134</sup>.

**Table 1: Sequences of human tropoelastin which react with antibodies (position of the sequence in the tropoelastin molecule is indicated inbrackets). From Wei and collaborators<sup>133</sup>.**

Antibody	Ala-Lys sequences	Hydrophobic and other sequences
mAb A2.1 mAb G8.1 mAb A7.1	AA <del>AA</del> YKAAK [74–80, exon 6]	AAGLGAGIPG [547–554, exon 26] GLGAGLGA [49–54, exon 5]
pAb $\alpha$ E(L)	AAKAAQFGL [670–676, exon 29]  PAAAAKAAKYGAAG [705–716, exons 31–32]	LGGVPGVG [87–92, exon 7] GVVVGAGPA [654–659, exons 28–29] GLGGLGVGG [683–689, exon 30] GVPGVGGGLGG [693–700, exon 30] AAGLGGVVLGGAGQFPLGGVAARPGFGLSP [716–742, exons 32–33] GGACLKACG [748–755, exon 36]
pAb $\alpha$ E(S)	AAAKAAAK [464–469, exon 23] AAKYGAAV [629–634, exons 27–28] AAAKAAAK [655–670, exon 29]	GAFPAVTF [55–60, exon 6] PGVGLAPG [497–502, exon 24]  ACLGKACG [750–755, exon 36]
pAb L85%	AAKAQLRA [539–544, exon 25]  AKAAQFGL [671–676, exon 29]	VGLAPGVG [499–504, exon 24] PSSSQHLP [605–610, exon 26A] GVGIPGGVVGAGPA [648–659, exons 28–29] LGGLGVGG [684–689, exon 30] PGVGGGLGGI [695–701, exon 30] GGACLKACG [748–755, exon 36]
pAb TE	VADAAAAAYK [71–77, exon 6]	AVTFPGAL [59–64, exon 6] GAGLGGVP [84–89, exon 7] VGGLGVSA [93–98, exon 7] AAGLGGLG [681–686, exon 30] AAGLGGVL [716–721, exon 32] GQFPLGGVA [727–733, exons 32–33] SPIFPGGA [743–748, exon 33]

In depth evaluation of the biocompatibility and immunogenicity of ELP biomaterials was evaluated in 2018 by the group of Epstein<sup>135</sup>. The three ELPs tested, ranging between 107 and 112 kDa, were composites containing alternate units of the hydrophilic bloc [(VPGVG)<sub>2</sub>(VPGEG)(VPGVG)<sub>2</sub>]<sub>5</sub> and of the hydrophobic bloc (VPGIG)<sub>20</sub>. Two of them also contained an elastase sensitive sequence (VPGAG)<sub>3</sub>. In addition, each ELP contains one bioactive sequence corresponding to either the adhesion sequence RGD, or the bone morphogenetic proteins BMP2 and BMP7. Incubation of these ELP with mouse splenocytes did not induce cell proliferation or cytokine production. Hydrogels were obtained by incubating the ELP at a T° above their Tt, and were implanted for seven days into mice peritoneal. No significant inflammatory response was detected with the ELP containing the RGD sequence,

as evidenced by a level of interleukins (IL-1 $\beta$ , IL-2 and IL-4) comparable to sham controls (same surgery but no hydrogel implanted). However, a marked increase in IL-4 production was seen for the BMP2 and BMP7-containing hydrogels. Subcutaneous implantation of the hydrogels showed that only mild inflammation and fibrosis were detected, similarly to those observed for the sham controls. Nevertheless, measurements of the mRNA levels by RT-qPCR of several pro-inflammatory genes revealed higher expression levels when compared to sham controls. Similar results were obtained for genes involved in wound healing and fibrosis. Once again, the BMP2 and BMP7-containing hydrogels triggered more inflammation than the ELP-RGD. Finally, it was shown that the ELP-hydrogels led to a marked increase in ELP-specific immunoglobulins (IgG1 and IgE isotypes) titers at days 21 and 56 post-implantation. The conclusion of the authors was therefore that the mice had developed an immune response to the ELPs.

Finally, the proof that ELPs can be immunogenic comes from a recent study from MacKay's group<sup>136</sup>. They were able to obtain two monoclonal antibodies (mABs) against the soluble ELP MG(VPGAG)<sub>192</sub>Y, which has a high Tt (55°C). These mABs were identified as IgM subclass. Of course, to obtain a good immune response the authors boosted the immunization process by using the ELP in combination with Freund's adjuvant and Granulocyte-macrophage colony-stimulating factor. One of the purified mAB was highly specific, with no cross-reactivity with other proteins, and surprisingly showed high specificity in western blot experiments for several other ELPs that contain different guest residues (serine, isoleucine, valine), strongly suggesting that the epitope GVPG was indeed the target of this mAB. Another interesting finding of this study is that ELP diblocks that forms micelles, or ELPs which coacervate at body temperature did not raise an immune response with the same experimental protocol. This suggests that only the injection of a soluble ELP could trigger an immune response, a hypothesis that might explain why crosslinked material of VPAVG did not trigger immune response in earlier studies<sup>132,133</sup>

In conclusion, this literature survey showed that the ELPs are not highly immunogenic when used in mammals, as expected for polymers derived from a human protein that is highly conserved in vertebrates. Nevertheless, it appears that some ELPs can be more immunogenic than others, depending on their size, amino acid composition (guest residue) and solubility in biological fluids at body temperature. Interestingly, it seems that the aggregated forms of ELP

(coacervates or crosslinked forms) are less immunogenic than the soluble monomeric forms, which is good news for therapeutic applications with hydrogels.

## 1.4. ELPs as tools for biological applications

### 1.4.1. Tag for protein purification

Owing to their ease of purification by the ITC method, ELP has been used as purification tag for other recombinant proteins. Specific expression plasmids were developed where the gene of interest can be inserted in fusion with an ELP sequence. Usually, a peptide linker containing a specific protease site is added between the two coding sequences. After recombinant expression of the fusion protein containing the ELP tag, its purification is carried out by several ITC cycles, avoiding the tedious chromatography steps usually required at this stage. Next, the purified fusion protein is incubated with protease to separate the ELP tag from the protein of interest, and the ELP is finally removed by further ITC steps (Fig. 11)

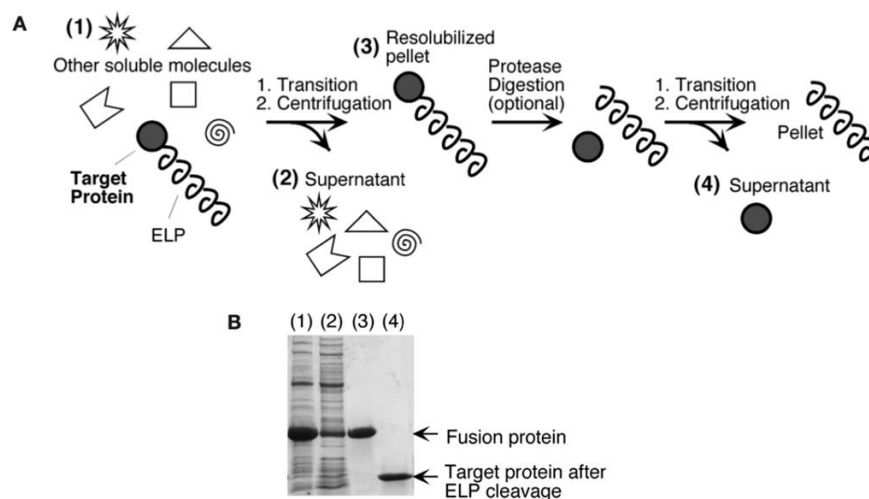


**Figure 11. Protein purification using an ELP tag. From Meyer and collaborators<sup>137</sup>.**

This technique was first developed by Meyer and Chikoti<sup>138</sup>. They demonstrated that the thioredoxin-ELP90 fusion protein had a transition temperature close to that of ELP, which allowed purification by ITC. They also showed that thioredoxin and the activity of thioredoxin thus purified retained its enzymatic activity. They also used ELP tags of different length and

showed that the yields of purified thioredoxin was dependent on the length of ELP tag, smaller ones (9 KDa) being four times more efficient than larger (35 KDa)<sup>137</sup>.

The use of ELP tags to purify recombinant proteins, however, has certain limitations. The first is the thermosensitivity of the protein of interest. As an example, this approach cannot be used to purify temperature-sensitive enzymes because they will be heat inactivated during the "hot steps" of ITC. Additionally, if the recombinant protein is very hydrophilic, the Tt of the fusion protein may be much higher than that of the ELP-tag preventing purification of the fusion protein at reasonable temperatures<sup>139</sup>.

## **1.4.2. ELP-based nanoparticles for biomedical applications**

### **1.4.2.1. Introduction**

Nanotechnology is widely used to develop new tools for cancer diagnosis and treatment. The use of nanocarriers for drug delivery has several advantages. First, nanoparticles can be passively target through the EPR effect to reduce the toxicity and improve efficacy. The EPR effect is the phenomenon by which nanoparticles of size less than 200 nm would have the possibility of penetrating specifically into the tumor tissue. Indeed, tumor growth depending on the nutritional supply of blood and oxygen, it leads to a disorganization of the local vascular tissue which results in greater permeability. Nanoparticles can therefore passively target tumors. Another characteristic of tumors is the lack of effective lymphatic drainage, which promotes the accumulation of nanocarriers. Second, nanoparticles composed of organic or inorganic materials can increase the solubility and biocompatibility of hydrophobic drugs. Most of these drugs show effective activity *in vitro* but are rapidly cleared from the bloodstream due to their poor solubility. Their encapsulation in nanoparticles considerably increases their effectiveness *in vivo*. Third, nanoparticles can be engineered to do active targeting by decorating their surface with antibodies, aptamers, or other cell receptor ligand (peptides, vitamins, and carbohydrates). The targeting of certain cell types makes it possible to accumulate larger quantities of drugs there, and therefore to reduce the doses administered to the patient, thereby reducing the side effects of the treatment. This active targeting can also limit multidrug resistance caused in particular by the expression of membrane transporters expressed on the surface of cancer cells. Fourth, nanoparticles bound to targeting agents or other proteins may also evade detection by the immune system, thereby increasing their half-life in serum. For example, surface coating

of nanoparticles with PEG prevents binding of serum proteins that typically lead to particle degradation by macrophages.

In conclusion, drug-loaded nanoparticles for cancer treatment should (i) be easy to synthesize in a few steps with high yield and purity; (ii) self-assemble into monodisperse nanoparticles with a size less than 100-150 nm; (iii) allow the encapsulation of various drugs; (iv) exhibit favorable pharmacokinetics, tumor-targeted accumulation, efficient drug release with controllable and tunable kinetics; (v) degrade into non-toxic compounds which can be eliminated from the body without undesirable toxicity.

#### 1.4.2.2. Nanoparticles of ELPs and ELP-drug conjugates

Several studies have been conducted to develop ELP nanoparticles capable of encapsulating therapeutic molecules. The first hydrophilic-hydrophobic diblock ELP nanoparticles were developed by Conticello's group<sup>140</sup>. The diblock sequence was G[VPGGG(IPGAG)<sub>4</sub>]<sub>14</sub>-VPGEG[VPGFG(IPGVG)<sub>4</sub>]<sub>16</sub>-VPGPFG. It formed spherical or cylindrical particles with a hydrophobic core and a hydrophilic corona. Due to the ionizable residues in the sequence, the size and shape of the self-assembled nanoparticles were sensitive to pH. Similar pH-sensitive ELP diblock nanoparticles have also been developed by the Chilkoti group to improve tumor penetration<sup>141</sup>. The VPG[VG<sub>7</sub>A<sub>8</sub>]<sub>80</sub>-VPG[VH<sub>4</sub>]<sub>100</sub> diblock self-assembles at 37°C into spherical micelles thanks to stabilization by Zn<sup>2+</sup> ions. These micelles dissociate into ELP unimers when the pH changes from 7.4 to 6.4, the pKa of histidine being close to the physiological pH, which leads to better penetration of tumors compared to micelles whose blocks are insensitive to pH<sup>141</sup>. Researchers were also interested in developing thermosensitive nanoparticles based on ELP diblock. The objective is to associate two ELP segments with two distinct Tts: one below 37°C for the hydrophobic ELP, and the other above 37°C for the hydrophilic block. Therefore, both blocks will be soluble in aqueous media at low temperature but will self-assemble into micelles when placed at 37°C due to hydrophobic block aggregation. An example is shown in Figure 12. A series of ELP block polymers, named ELP<sub>BC</sub> ([V<sub>1</sub>A<sub>8</sub>G<sub>7</sub>]<sub>n</sub>)[V<sub>5</sub>]<sub>n</sub>) with different length and different hydrophobic/hydrophilic ratio were genetically synthesized by recursive directional ligation<sup>142</sup>. Tt#1 was controlled by the length of the hydrophobic block, while Tt#2 was dependent on the hydrophilic block. They showed that for a hydrophobic/hydrophilic ratio varying between 0.5 and 2, these ELP<sub>BC</sub> existed in solution in the form of monomers, spherical micelles or aggregates depending on the temperature of the solution. They then selected two ELP<sub>BSC</sub> (ELP-64/60 and ELP-96/60) that formed micelles between 37°C and 42°C and grafted

the cell-specific ligand Asp-Gly-Arg (NGR) peptide. They demonstrated that cell uptake was improved at 42°C when the diblock was self-assembled into micelles, and that the presence of NGR increased cell internalization efficiency by 3.5 times.

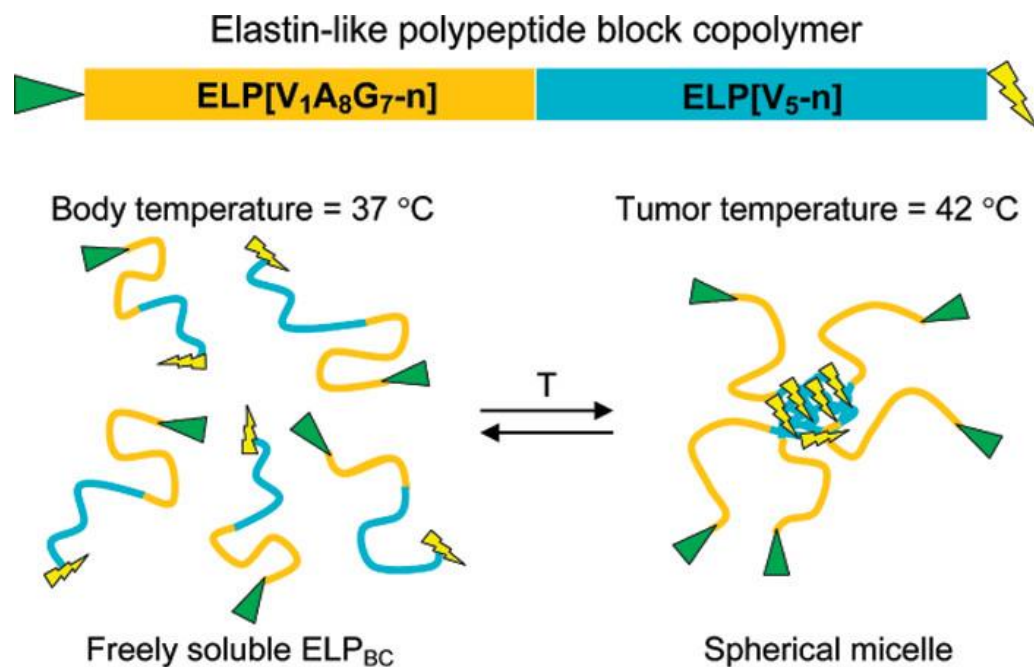


**Figure 12. Temperature triggered self-assembly of an ELP<sub>BC</sub> diblock that forms multivalent spherical micelles. Adapted from Dreher and collaborators<sup>142</sup>**

Similar works were conducted by the group of MacKay. They fused an adenovirus5 button domain to an ELP (VPGSG)<sub>48</sub>(VPGIG)<sub>48</sub>Y diblock, and demonstrated that after self-assembly, the nanoparticles were taken up *in vivo* by hepatocytes<sup>143</sup> and lacrimal gland<sup>144</sup>.

Other structures than micelles such as vesicles can be obtained by combining hydrophilic and hydrophobic ELP blocks and by modifying the arrangement and the length of the blocks<sup>145</sup>.

Recombinant Arg5-ELP diblocks were also expressed in *E. coli* and purified. They contain Cys at their N terminus to allow conjugation with fluorescent probes<sup>146</sup>. These diblocks formed micelles when heated, with a critical micelle temperature (CMT) of 39°C. They showed that above this temperature, the formation of micelles causes a local increase in the concentration of arginine on the surface, considerably increasing absorption by the cells. At lower temperatures, the micelles dissociate into monomers and their arginine concentration is no longer sufficient to allow their cellular internalization (Fig; 13).

The tripeptide RGD was also grafted to ELPs to enhance their intracellular uptake through interaction with integrins<sup>147</sup>. It was shown that the multivalent presentation of the RGD motif by a nanoscale scaffold led to greater cell binding/uptake when compared to presentation of the same ligand by large polydisperse aggregate.

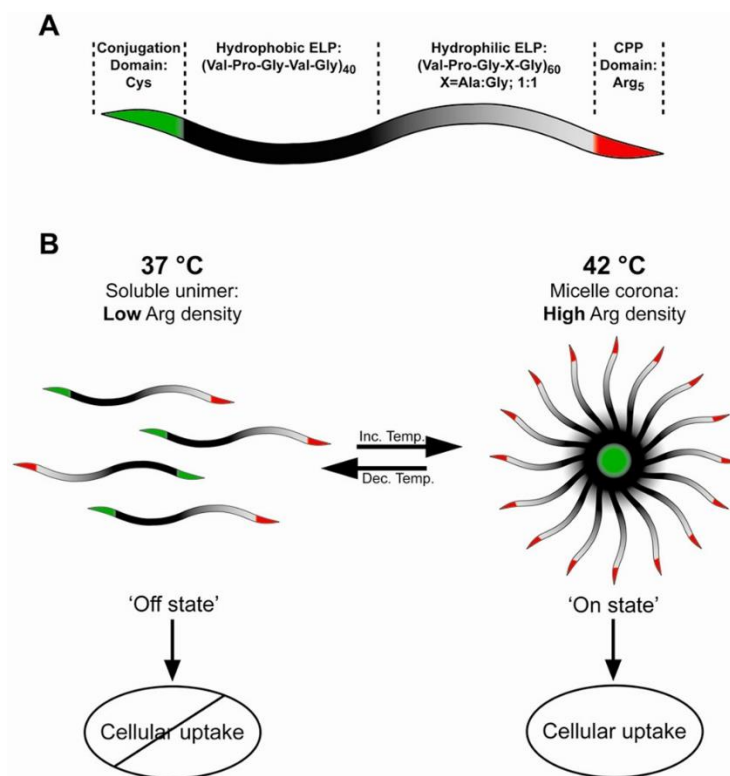


**Figure 13. Controlled cellular uptake by modulation of local Arg density is achieved by temperature-triggered micelle assembly of a genetically encoded Arg5-ELP<sub>BC</sub>.** A) Structure of the ELP diblocks. B) Effect of temperature on self-assembly. Adapted from MacEwan and Chilkoti<sup>146</sup>

Other works have used drug conjugation on ELPs to enhance therapeutic effects<sup>148,149</sup>. This type of approach had previously been used in particular to graft the anti-cancer drug doxorubicin onto (PEG)<sup>150,151</sup>, N-(2-hydroxypropyl)methacrylamide (HPMA)<sup>152–155</sup>, albumin<sup>156</sup>, and transferrin<sup>157</sup>. It has been shown that these conjugates can self-assemble into nanoparticles that enhance anti-cancer activity and reduce off-target toxicity<sup>158,159</sup>. This approach could be also useful to treat other diseases, such as bacterial infections. Indeed, several bacteria like *Staphylococcus aureus* and *Pseudomonas aeruginosa* can form biofilms that render them highly resistant to antibiotic treatments. Most antibiotics are in fact incapable

of penetrating the structure of biofilms. To circumvent this problem, the antibiotic can be encapsulated in liposomes which will penetrate more easily into the structure of the biofilm. For example, heat-sensitive liposomes based on DPPC, DSPE-PEG, cholesterol, and a fatty acid-conjugated ELP have been shown to encapsulate antibiotics and deliver them into *S. aureus* and *P. aeruginosa* biofilms<sup>160</sup>.

Chilkoti's group reported the first ELP-based chimeric polypeptides (CPs) to which drugs had been conjugated that self-assembled into quasi-monodisperse nanoparticles less than 100 nm in size<sup>161</sup>. These CPs consist of two segments, a hydrophilic, biodegradable ELP and a short segment for the attachment of drugs through a pH-labile linker (Fig. 14).

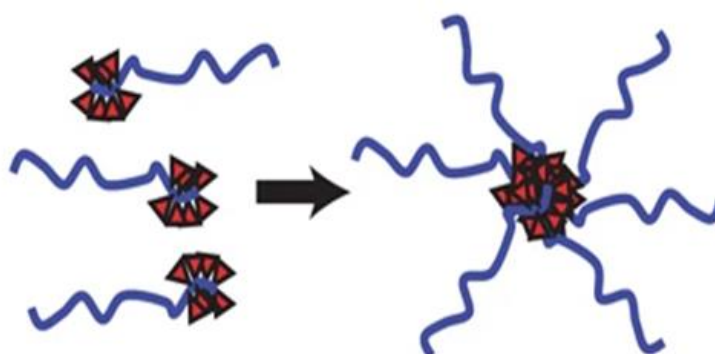


**Figure 14. Structure of CP-dox conjugation. The hydrophobic-drug block triggers self-assembly of CP nanoparticles with a drug-rich (red triangles) core surrounded by a hydrophilic polypeptide corona (blue chains). Adapted from MacKay and collaborators<sup>161</sup>.**

The ELP sequence was repetitions of the pentapeptide Val-Pro-Gly-Xaa-Gly, where Xaa = Val/Ala/Gly [1:8:7]. The Tts of these ELPs were higher than 37°C. A short peptide segment (Gly-Gly-Cys)<sub>8</sub> was appended at the C-terminal end of polypeptide to provide doxorubicine attachment sites. The ELP-Dox self-assembled into spherical nanoparticles with R<sub>H</sub> around 20 nm, and critical aggregation concentration below 3 μM. The liberation of free drug from the CP-Dox nanoparticles requires the pH-dependent of hydrazone bond cleavage. Indeed, the hydrazone bond was stable at pH 7.4, and no significant release of free drug was observed over 24 h. In contrast, at pH 5.0, doxorubicin was released with a first-order half-life of 4.9 ± 0.5 h, and a maximum release of 68 ± 3% of the initial amount of Dox was measured after 24 h.

This result is similar to those obtained for other polymeric hydrazones<sup>162</sup>. It was later showed that the aggregation temperature can be tune to 38-40°C by playing either with the ELP composition, or the ELP length<sup>163</sup>.

*In vivo* studies demonstrated that drug concentration in the tumor was 3.5-fold higher with ELP-dox than with dox alone, leading to an improved lifetime for treated mice (66 days versus 21 days)<sup>161</sup>. Other ELP-dox have also been created by conjugation using other pH-sensitive bonds such as active hydrazones and maleimides<sup>164</sup>.

Conjugation of a hydrophobic drug to an ELP results in a decrease in Tt value, with overall hydrophobicity increasing. More interestingly, it appeared that the Tts of the conjugates were then no longer dependent on the concentration, contrary to what is observed for the ELPs. This was attributed to the fact that the formation of the nanoparticles triggered an increase in the local ELP concentration in the corona<sup>165</sup>. This last characteristic is of major importance. Indeed, in the case of micelles made up of ELP diblocks, the formation of micelles is triggered by the aggregation of the hydrophobic segment when it is placed at a temperature above its Tt. This Tt being dependent on the diblock concentration, it will increase rapidly when the diblock concentration decreases after injection. Consequently, the micelles will disassemble and the encapsulated drug will be rapidly released. In the case of ELP-drug conjugates, this is no longer a problem because the Tt is independent of the concentration.

To better understand the formation of these ELP-drug conjugates, an ELP ((VPGXG)<sub>160</sub>, X = V/A/G [1:8:7]) containing a C(GGC)<sub>7</sub> linker at its C-terminal end was conjugated with a series of compounds of different hydrophobicity (LogD from -1 to 4). They showed that compounds with a LogD greater than 1.5 conferred sufficient amphiphilicity to ELP-drug conjugates to allow self-assembly into nanoparticles, with the conjugated compound forming the hydrophobic core<sup>163</sup>. This was also the case for CP-paclitaxel (PTX, LogD = 4.95)<sup>166</sup>, and CP-Niclosamide (LogD = 4.48)<sup>167</sup>. For compounds with LogD values below 1.5, self-assembly of ELP-drug conjugates can be achieved by adding a hydrophobic peptide segment into the ELP sequence. For instance, (VPGAG)<sub>160</sub>-(YG)<sub>6</sub>-(CGG)<sub>8</sub> conjugated with maleimide derivatives compounds (LogD from -1 to 1.38) self-assembled into rod-like nanoparticles thanks to the hydrophobicity of the (YG)<sub>6</sub><sup>168</sup> and to the  $\pi$ - $\pi$  stacking of aromatic groups<sup>159,169,170</sup>.

### 1.4.2.3. ELP for Drug Depot

Drug deposition is also an attractive application for ELPs due to their thermosensitivity. Indeed, the injection of an ELP with a  $T_t$  lower than body temperature will trigger its aggregation at the injection site. If therapeutic drugs are associated with this ELP, either by encapsulation or by conjugation, this will lead to a slow and continuous release of the drug contained in the depot. Good candidates for such an approach are drugs that are short-lived in serum, thus requiring their frequent administration. This is the case of glucagon-like peptide-1 (GLP-1), which is used to treat type 2 diabetes.

Chilkoti and colleagues designed several GLP-ELP fusion polypeptides using ELPs having different  $T_t$ s by alternating Glycine and Alanine as guest residue<sup>171</sup>. In addition, a proteolytic site has been genetically inserted between the GLP and ELP segments to allow the release of the hormone after its injection (Fig. 15).

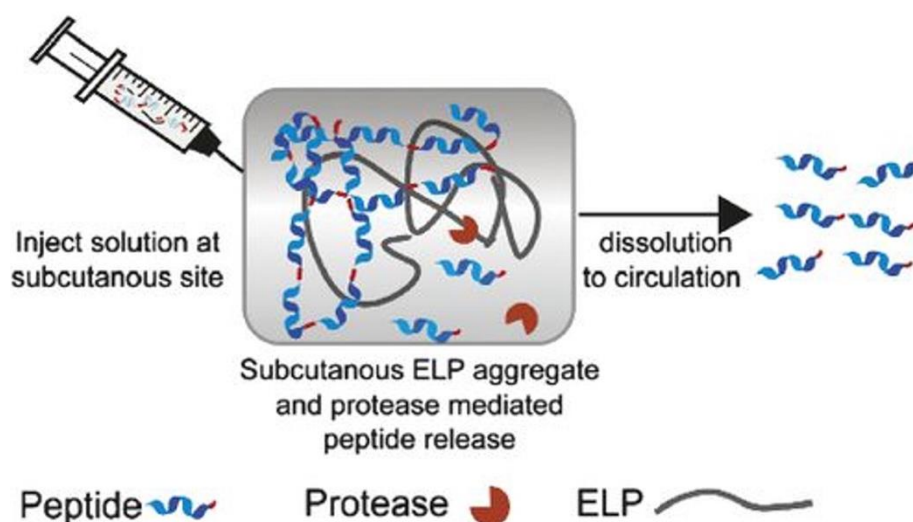


**Figure 15. Design and characterization of GLP-1 Protease-Operated Depots. Soluble fusion proteins of (peptide)<sub>n</sub>-ELP are injected and coacervate in situ in response to body temperature to form a depot. Subsequently, protease release active peptide into circulation. Adapted from Amiram and collaborators<sup>171</sup>**

After subcutaneous injection, the GLP-ELP fusion polypeptide coacervates and forms a depot, then the active peptide is gradually released into the circulation after proteolytic cleavage. Additionally, since  $T_t$  is concentration-dependent, the boundary layer of the coacervate

solubilizes upon dilution by the interstitial flow, releasing more therapeutic cargo into the circulation. This sustained-release platform, coupled with the ability of ELPs to impede renal filtration, extends the half-life of small molecules and peptides to which the ELP is fused<sup>18</sup>. The ELP depots has been reported to have longer residence time compared with soluble ELP<sup>172</sup>. A single injection of Glucagon-like peptide-1 (GLP-1) protease operated depots reduced blood sugar for a longer period than with GLP-1 alone. Interestingly, circulation time was related to ELP size, with the smallest (25 KDa) providing glucose control over 48 h, while the longest (100 KDa) provided glucose control for 120 h<sup>171</sup>.

This strategy is more difficult to implement to treat solid tumors. To allow a good diffusion of the product in the tumor, a high pressure must be applied during the injection, which leads to a high pressure of the interstitial liquid. The injected material can then spread out of the tumor before the deposit forms. To address this issue, Wenge Liu group used an <sup>131</sup>I-ELP-(GY)<sub>7</sub> compound. At low temperatures, this compound assembles into rod-shaped micelles that are less likely to dilute into the interstitial tissue than ELP monomers. After injection, the rod-shaped micelles coacervate in situ to form a hydrogel<sup>173</sup>. Interestingly, the high energy of  $\beta$ -emissions from <sup>131</sup>I further stabilizes the deposit by introducing covalent bonds into it.

The ELP-depot strategy has been successfully used to substantially increase the half-life of therapeutic molecules in a number of treatments for osteoarthritis therapy<sup>174</sup>, cancer<sup>175</sup>, diabete<sup>176</sup>, dry eyes disease<sup>177</sup>, infections illness<sup>178</sup>, and inflammation<sup>179</sup>.

#### **1.4.2.4. ELPs for hydrogels**

Due to their biocompatibility, biodegradability and coacervation property, ELPs have also been used to mimic the ECM in tissue engineering and cell therapy applications<sup>180</sup>.

Madl and Heilshorn reported ELP based hydrogels. They engineered ELP containing tyrosine residues and reacted them with 4-phenyl-1,2,4-triazoline-3,5-dione. The conjugated were then crosslinked with bicyclononyne to form hydrogels<sup>181</sup>. Then, the same group used a new strategy to engineer double crosslinked hydrogels<sup>182</sup>. As shown in Figure 16, the first step in gel formation is chemical crosslinking between the amines of the ELP and the tetrakis (hydroxymethyl)phosphonium chloride (THPC) crosslinker. The rate of crosslinking can be controlled by pH, stoichiometric ratio or reaction time.

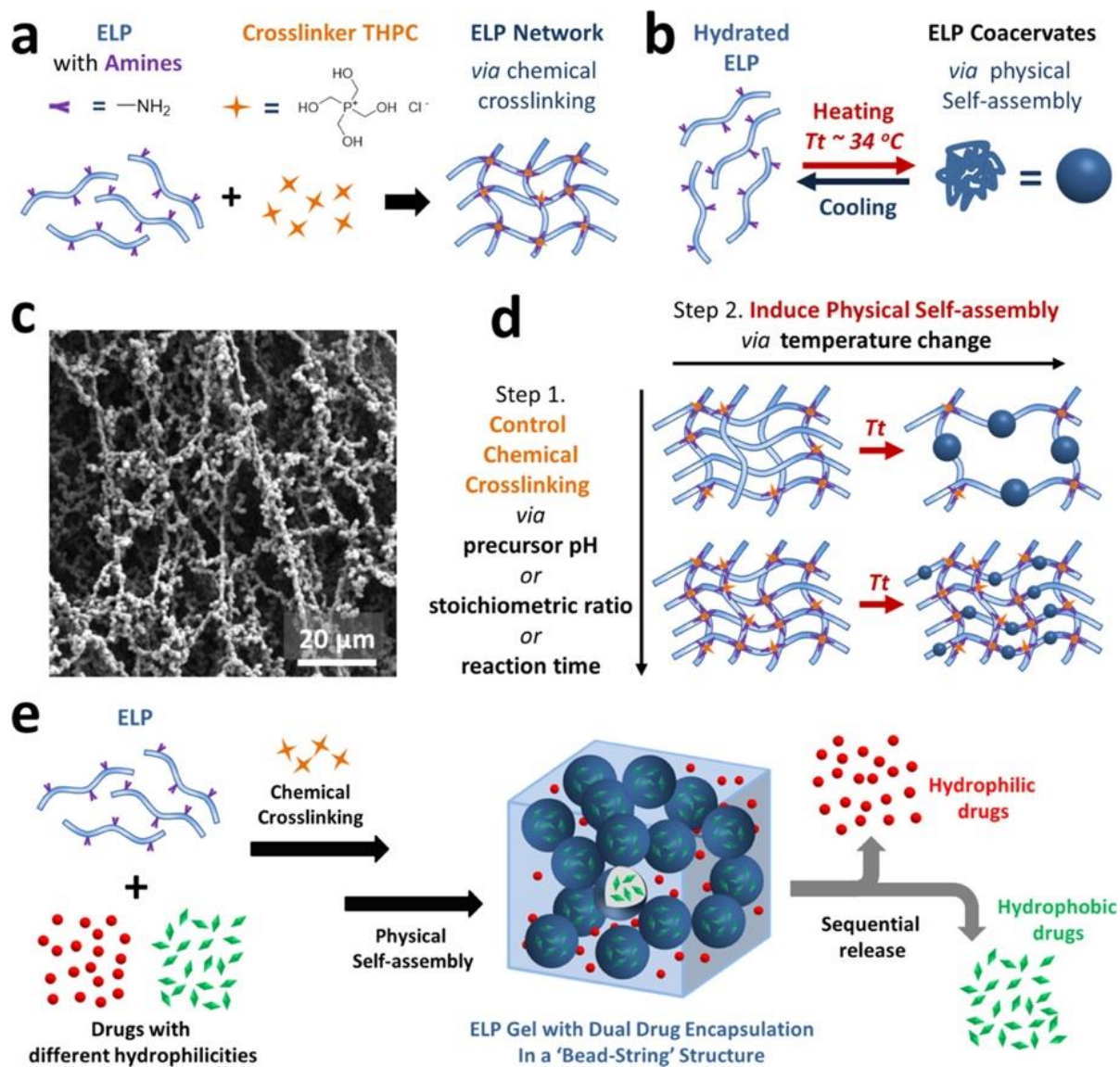


**Figure 16. Schematic of ELP hydrogel formation with controlled “bead-string” structure. (A) Covalent crosslinking of ELP network using chemical crosslinker THPC. (B) Thermally triggered physical self-assembly of ELP. (C) SEM image of “bead-string” microstructured ELP gel. (D) Proposed strategy to control hydrogel microstructure by modulating chemical crosslinking and physical self-assembly processes of ELP. (E) Simple, one-pot formation of microstructured ELP hydrogel for dual encapsulation and sequential release of hydrophilic and hydrophobic drugs. Adapted from Wang and collaborators<sup>182</sup>.**

The second step is crosslinking by physical interaction thanks to the coacervation properties of ELPs. By varying the parameters such as the pH, the molar ratio between the compounds, the reaction times, it is possible to modulate the effectiveness of the chemical crosslinking and thus

to obtain hydrogels having different rheological characteristics. These hydrogels allowed the encapsulation of hydrophobic molecules, such as coumarin-6, and hydrophilic molecules such as rhodamine B isothiocyanate-dextran. Experiments aimed at measuring the release of these drugs have shown a more rapid release of hydrophilic molecules.

Other hydrogels obtained by in situ crosslinking of ELPs with hydroxymethylphosphines were prepared by Chilkoti's group for tissue repair applications<sup>183</sup>. They obtained hydrogels with pore sizes between 200  $\mu\text{m}$  and 20  $\mu\text{m}$ , which is the right size to allow cell colonization<sup>184,185</sup>. They also tuned the swelling content and the mechanical properties of the hydrogels by varying the ratio of hydrophobic to hydrophilic domains<sup>183</sup>. They demonstrated that these gels support the survival of human mesenchymal stem cells and murine neural progenitor cells<sup>181</sup>, and the proliferation of mouse fibroblasts<sup>183</sup>.

In other studies, cell adhesion peptides such as RGD, YIGSR, or IKVAV were added to the chemically cross-linked ELP-based hydrogel to enhance cell adhesion and thus promote angiogenesis or innervation<sup>186-188</sup>.

#### **1.4.2.5. ELPs for nucleic acid encapsulation**

The use of nucleic acids as therapeutic molecules has recently become a very promising way. The difficulty comes not from the synthesis of these nucleic acids, which is quite simple and can be easily scaled-up, but rather from their addressing to the cells and their low stability in a biological medium. To circumvent these problems, nucleic acids must be encapsulated to protect them from degradation and to improve transfection of target cells. ELPs are good candidates for forming nanoparticles that encapsulate DNA or RNA. This can be achieved with cationic ELPs which can interact electrostatically with anionic nucleic acids, and which can form micelles or nanoparticles thanks to their thermosensitivity. The nanoparticles are expected to be formed by the interaction of cations and ions, and dropwise mixing of ELP (-NH<sub>2</sub>) to a negatively charged DNA solution avoid aggregates formation<sup>189,190</sup>. More specifically, cationic ELPs for DNA condensation were firstly designed from the genetic fusion of an ELP and a positively charged domain consisting of an eight residue oligolysine peptide. Efficient plasmid DNA (GFP) transfection was demonstrated with a lower toxicity than polyethylenimine<sup>191</sup>. More recently, a recombinant ELP (VPGXG)<sub>40</sub> with X = V,M (3:1) was post-modified in two steps to introduce chemoselectively either primary or secondary amine pendant groups at each

methionine residue<sup>192</sup>. This strategy was successful to produced ELP-DNA nanoparticles (Fig. 17)

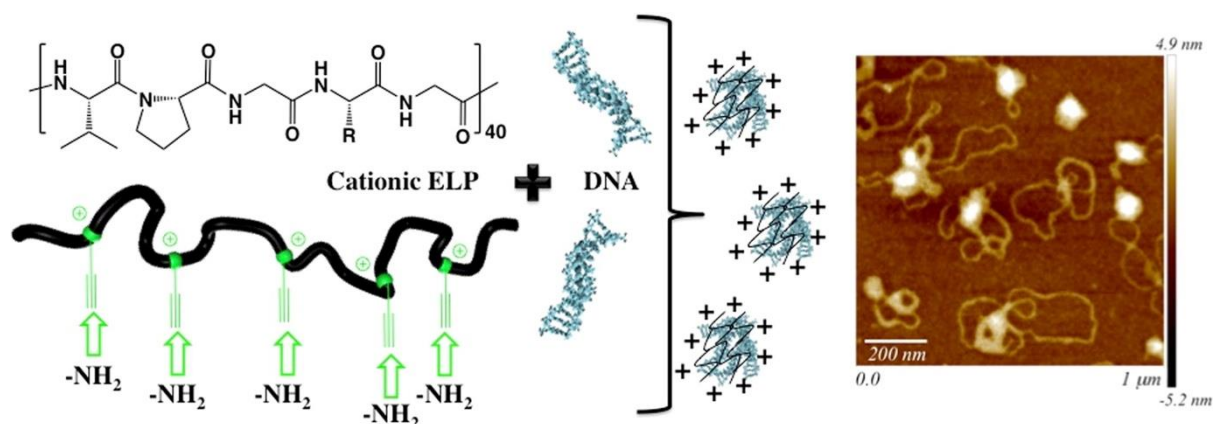


**Figure 17. Nucleic acids complexation with cationic elastin-like polypeptides. Adapted from Bravo-Anaya and collaborators<sup>192</sup>.**

Positively charged ELPs were found to be able to interact with plasmid DNA and form stable complexes for gene delivery. The plasmid/ELP(-NH<sub>2</sub>) complexes remain completely stable against dissociation in the NaCl concentration range from 0 to 0.2 M, while the stability of the complex was affected in presence of strong detergents such as SDS.

#### 1.4.2.6. ELPs conjugated with polymers, sugars and lipids

The grafting of synthetic polymers on ELP has also been evaluated. One example is the grafting of poly(2-oxazoline)s (POx) on an ELP<sup>193</sup>. This diblock was obtained by a retro Diels-Alder reaction between POx functionalized by a maleimide and the thiol of a cysteine of the ELP (Fig. 18). The ELPs used containing either one or seven cysteines, several diblocks were obtained as well as several nanoparticles of different sizes.

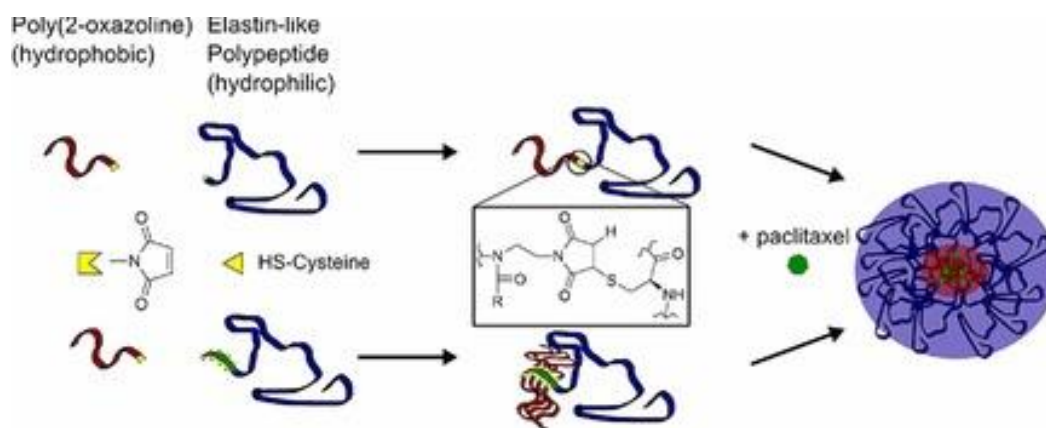


**Figure 18. Maleimide-Functionalized poly(2-oxazoline)s and their conjugation to elastin-like polypeptides. Adapted from Nawroth and collaborators<sup>193</sup>.**

It was shown that these nanoparticles could encapsulate the anti-cancer drug Paclitaxel with up to 8 wt% loading<sup>193</sup>.

Diblocks of ELP-hyaluronic acid were synthesized by Heilshorn's group via a reaction between hydrazine-modified ELP (ELP-HDY) and aldehyde-modified HA (HA-ALD) forming hydrazone bonds<sup>194,195</sup>. ELP-HDY was obtained through modifying the lysine residues of ELP, whereas HA-ALD was achieved by oxidation. The dynamic covalent crosslinking of hydrazone bond allowed the formation of ELP-HA gel at room temperature. The stiffness of the hydrogel was tuned by controlling the ratio of ALD/HYD, and the total concentration of polymers<sup>194</sup>. Furthermore, the secondary network resulting from the thermal phase transition of the ELP reinforces the hydrogel structure and decreases the erosion rate by a factor of 10 compared to a control hydrogel<sup>195</sup>. ELP-HA hydrogels modified to contain the cellular adhesive sequence-RGD are potentially interesting for the encapsulation and injection of stem cells in the context of tissue repair (Fig. 19).

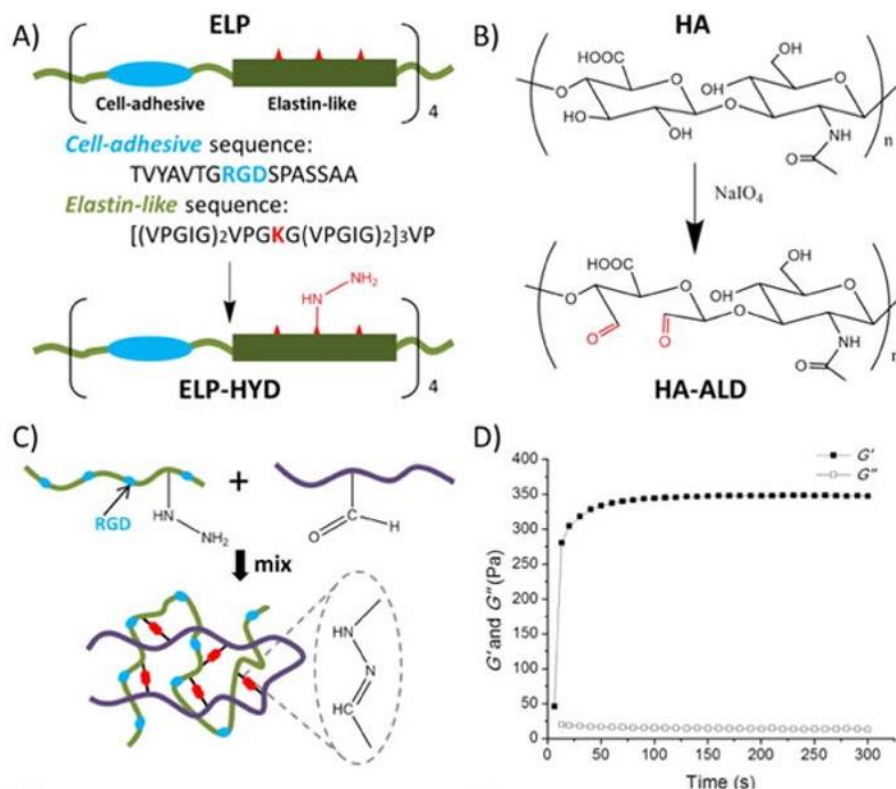


**Figure 19. Design and characterization of ELP-HA hydrogels. A) ELP-HYD. ELP (green), lysine residues (red) and cell-adhesion peptide (blue), and structural elastin-like (green) sequence. (B) Synthesis of HA-AL. (C) ELP-HA hydrogel formation. (D) Rheological characterization of ELP-HA hydrogel. Adapted from Zhu and collaborators<sup>194</sup>**

Conjugation of ELPs with lipid moieties has only been recently studied. An elegant strategy developed in Chilkoti's and Mozhdehi's groups relies on the lipidation of the ELP *in vivo* during its recombinant expression. Indeed, by fusing a specific peptide sequence at the N-terminus of ELPs, and by coexpressing the polypeptide and a yeast N-myristoyltransferase (NMT) in *E. coli* they obtained ELP-C14<sup>196</sup>. NMT catalyzes the covalent bond of activated myristoyl-CoA thioester to the N-terminal glycine of proteins containing the recognition sequence<sup>196,197</sup>. They showed that purified myristoylated ELP had a lower T<sub>cp</sub> than non-acylated ELP, and that this T<sub>cp</sub> was not concentration dependent (Fig. 20). In fact, acylated ELPs form micelles in aqueous buffer, with CMCs in the  $\mu\text{M}$  range, and the size of the micelles varies according to the size of the ELP: the larger the ELP, the smaller the micelles. Myristoylated ELP micelles successfully encapsulated doxorubicin and paclitaxel, resulting in cytotoxic effect on 4T1 and PC3-luc cells. Drug-encapsulated samples had longer plasma circulation ( $\text{IC}_{50} = 1.5 \mu\text{M}$ ) than free drug ( $\text{IC}_{50} = 0.5 \mu\text{M}$ ). They also showed that the size of the ELP had no influence on the  $\text{IC}_{50}$ .

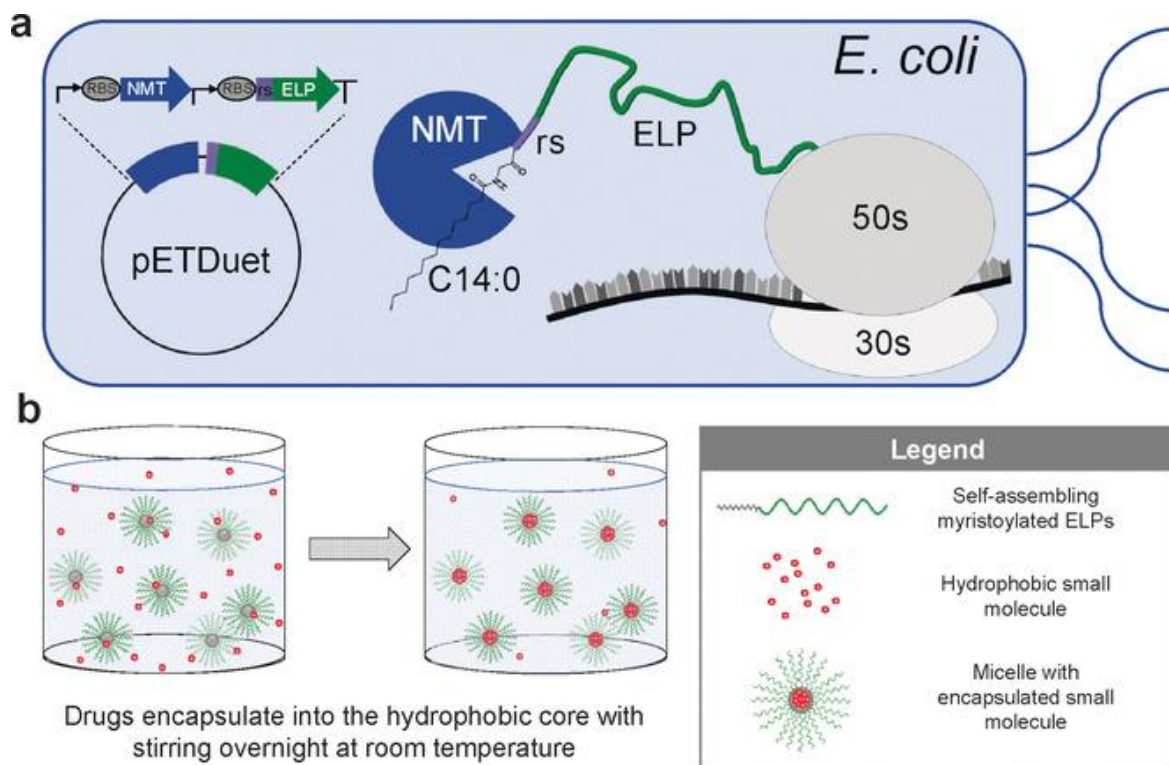


**Figure 20. Recombinant strategy used to synthesize myristoylated ELP *in vivo*.**  
Adapted from Luginbuhl and collaborators<sup>196</sup>

ELPs grafted with cholesterol have also been obtained by coupling recombinant production and *in vitro* modification<sup>198</sup>. Cholesterol modified polypeptide was purified and the characteristics of the corresponding micelles were evaluated. They then grafted the exendin-4 peptide and showed that the exendin-cholesterol conjugate self-assembles into micelles capable of activating the glucagon-like peptide-1 receptor.

This strategy of *in vivo* lipidation of ELPs is however limited because of the low yields of purified conjugates, 10-80 mg/L of culture for ELP-C14 and 5-10 mg/L for Cholesterol modified polypeptide, and by the fact that it is restricted to these lipid substrates due to the specificity of naturally available enzymes.

Other strategies are also possible, such as the grafting of lipid chains onto the side chains of ELP. This has been done with oleic acid and it has been shown that these brush-like lipoproteins can self-assemble into polymersomes<sup>199</sup>. However, these materials are highly hydrophobic due to the number of lipid molecules grafted by ELP, and therefore difficult to handle in biological media.

## 1.5. Conclusion

This chapter shows that ELPs are promising candidates as drug carriers or as hydrogel components. They can be precisely engineered by recombinant techniques, they are heat sensitive and can self-assemble, and they are biocompatible. They have also been shown to encapsulate drugs and form hydrogels after they are chemically cross-linked. However, materials based on ELP alone often do not exhibit optimal characteristics. Thus, ELP-based micelles tend to aggregate in biological media and their ability to encapsulate hydrophobic drugs is limited. As for ELP-based gels, they must often be designed by adding synthetic polymers, and they are obtained by using poorly biocompatible chemical crosslinking agents. Therefore, the current trend is rather to modify ELPs to improve their properties. This can be achieved by chemically modifying them with groups of interest, by combining them with other biologically active peptides or polypeptides, or by conjugating them to other biomolecules such as nucleic acids, sugars, or lipids.

My PhD project fits in this context. I was interested in the chemical conjugation of hydrophobic natural molecules, such as polyisoprene from natural rubber or fatty acids, on different ELPs. One of the objectives was to better understand the effect of hydrophobic chain grafting on the self-assembly of conjugated ELPs, and to obtain nanoparticles capable of effectively encapsulating and releasing hydrophobic molecules. Another objective has been to use acylated ELPs to create physical hydrogels that do not require a chemical crosslinking step. The different steps of the project are detailed in the following chapters.

## References

- 1 Y. H. Yun, B. K. Lee and K. Park, *J. Control. Release*, 2015, **219**, 2–7.
- 2 K. Strebhardt and A. Ullrich, *Nat. Rev. Cancer*, 2008, **8**, 473–480.
- 3 A. S. Hoffman, *J. Control. Release*, 2008, **132**, 153–163.
- 4 K. Park, *J. Control. Release*, 2014, **190**, 3–8.
- 5 Y. Zhang, H. F. Chan and K. W. Leong, *Adv. Drug Deliv. Rev.*, 2013, **65**, 104–120.
- 6 I. Ekladios, Y. L. Colson and M. W. Grinstaff, *Nat. Rev. Drug Discov.*, 2019, **18**, 273–294.
- 7 E. A. Simone, T. D. Dziubla and V. R. Muzykantov, *Expert Opin. Drug Deliv.*, 2008, **5**, 1283–1300.
- 8 J. W. Hickey, J. L. Santos, J. M. Williford and H. Q. Mao, *J. Control. Release*, 2015, **219**, 536–547.
- 9 J. D. Lambris, D. Ricklin and V. M. Holers, in *Advances in Experimental Medicine and Biology*, 2013, vol. 735, pp. 1–8.
- 10 D. Jao, Y. Xue, J. Medina and X. Hu, *Materials*, 2017, **10**, 1–24.
- 11 A. L. Boyle, in *Peptide Applications in Biomedicine, Biotechnology and Bioengineering*, Woodhead Publishing, 2018, pp. 51–86.
- 12 R. Song, M. Murphy, C. Li, K. Ting, C. Soo and Z. Zheng, *Drug Des. Dev. Ther.*, 2018, **12**, 3117–3145.
- 13 K. Wals and H. Ovaa, *Front. Chem.*, 2014, **2**, 1–12.
- 14 P. S. Huang, S. E. Boyken and D. Baker, *Nature*, 2016, **537**, 320–327.
- 15 N. C. Abascal and L. Regan, *Open Biol.*, 2018, **8**, 1–8.
- 16 S. Hollingshead, C. Y. Lin and J. C. Liu, *Macromol. Biosci.*, 2017, **17**, 1–57.

- 17 H. Sun, Q. Luo, C. Hou and J. Liu, *Nano Today*, 2017, **14**, 16–41.
- 18 A. Varanko, S. Saha and A. Chilkoti, *Adv. Drug Deliv. Rev.*, 2020, **156**, 133–187.
- 19 H. Gelderblom, J. Verweij, K. Nooter and A. Sparreboom, *Eur. J. Cancer*, 2001, **37**, 1590–1598.
- 20 B. Du, M. Yu and J. Zheng, *Nat. Rev. Mater.*, 2018, **3**, 358–374.
- 21 A. S. Zahr, C. A. Davis and M. V. Pishko, *Langmuir*, 2006, **22**, 8178–8185.
- 22 F. Salahpour Anarjan, *Nano-Struct.*, 2019, **19**, 1–7.
- 23 M. F. Attia, N. Anton, J. Wallyn, Z. Omran and T. F. Vandamme, *J. Pharm. Pharmacol.*, 2019, **71**, 1185–1198.
- 24 S. Barua and S. Mitragotri, *Nano Today*, 2014, **9**, 223–243.
- 25 J. K. Tee, L. X. Yip, E. S. Tan, S. Santitewagun, A. Prasath, P. C. Ke, H. K. Ho and D. T. Leong, *Chem. Soc. Rev.*, 2019, **48**, 5381–5407.
- 26 L. C. Nelemans and L. Gurevich, *Mater.*, 2020, **13**, 1–21.
- 27 R. Zhang, X. Qi, F. Kong, P. Chen and G. Pan, *Drug deliv.*, 2019, **26**, 328–342.
- 28 L. Rajendran, H. J. Knölker and K. Simons, *Nat. Rev. Drug Discov.*, 2010, **9**, 2942.
- 29 G. H. Son, B. J. Lee and C. W. Cho, *J. Pharm. Investig.*, 2017, **47**, 287–296.
- 30 K. Jastrzebska, K. Kucharczyk, A. Florczak, E. Dondajewska, A. Mackiewicz and H. Dams-Kozłowska, *Rep. Pract. Oncol. Radiother.*, 2015, **20**, 87–98.
- 31 V. Pandey, T. Haider, P. Jain, P. N. Gupta and V. Soni, *J. Drug Deliv. Sci. Technol.*, 2020, **55**, 101294.
- 32 T. Yucel, M. L. Lovett and D. L. Kaplan, *J. Control. Release*, 2014, **190**, 381–397.
- 33 F. Mottaghitalab, M. Farokhi, M. A. Shokrgozar, F. Atyabi and H. Hosseinkhani, *J. Control. Release*, 2015, **206**, 161–176.

- 34 A. S. Lammel, X. Hu, S. H. Park, D. L. Kaplan and T. R. Scheibel, *Biomaterials*, 2010, **31**, 4583–4591.
- 35 X. Wang, T. Yucel, Q. Lu, X. Hu and D. L. Kaplan, *Biomaterials*, 2010, **31**, 1025–1035.
- 36 P. Shi and J. C. H. Goh, *Powder Technol.*, 2012, **215–216**, 85–90.
- 37 A. R. Murphy and D. L. Kaplan, *J. Mater. Chem.*, 2009, **19**, 6443–6450.
- 38 K. Numata and D. L. Kaplan, *Adv. Drug Deliv. Rev.*, 2010, **62**, 1497–1508.
- 39 Z. Megeed, J. Cappello and H. Ghandehari, *Adv. Drug Deliv. Rev.*, 2002, **54**, 1075–1091.
- 40 J. L. Frandsenab and H. Ghandehari, *Chem. Soc. Rev.*, 2012, **41**, 2696–2706.
- 41 K. Numata, B. Subramanian, H. A. Currie and D. L. Kaplan, *Biomaterials*, 2009, **30**, 5775–5784.
- 42 R. Yang, M. Hou, Y. Gao, S. Lu, L. Zhang, Z. Xu, C. M. Li, Y. Kang and P. Xue, *Theranostics*, 2019, **9**, 6314–6333.
- 43 B. Mao, C. Liu, W. Zheng, X. Li, R. Ge, H. Shen, X. Guo, Q. Lian, X. Shen and C. Li, *Biomaterials*, 2018, **161**, 306–320.
- 44 K. Numata and D. L. Kaplan, in *Advanced Wound Repair Therapies*, Woodhead Publishing, 2011, vol. 20, pp. 524–551.
- 45 X. Zhi, Y. Wang, P. Li, J. Yuan and J. Shen, *RSC Adv.*, 2015, **5**, 82334–82341.
- 46 Y. Li, X. Zhi, J. Lin, X. You and J. Yuan, *Mater. Sci. Eng. C*, 2017, **73**, 189–197.
- 47 J. M. Saul, M. D. Ellenburg, R. C. de Guzman and M. Van Dyke, *J. Biomed. Mater. Res. A*, 2011, **98 A**, 544–553.
- 48 M. L. Peralta Ramos, J. A. González, L. Fabian, C. J. Pérez and M. E. Villanueva, *Mater. Sci. Eng. C*, 2017, **78**, 619–626.

- 49 M. E. Villanueva, M. L. Cuestas, C. J. Pérez, V. Campo Dall'Orto and G. J. Copello, *J. Colloid Interface Sci.*, 2019, **536**, 372–380.
- 50 Q. Li, L. Zhu, R. Liu, D. Huang, X. Jin, N. Che, Z. Li, X. Qu, H. Kang and Y. Huang, *J. Mater. Chem.*, 2012, **22**, 19964–19973.
- 51 S. Han, T. R. Ham, S. Haque, J. L. Sparks and J. M. Saul, *Acta Biomater.*, 2015, **23**, 201–213.
- 52 Y. Cao, Y. Yao, Y. Li, X. Yang, Z. Cao and G. Yang, *J. Colloid Interface Sci.*, 2019, **544**, 121–129.
- 53 Z. Yu, M. Yu, Z. Zhang, G. Hong and Q. Xiong, *Nanoscale Res. Lett.*, 2014, **9**, 1–7.
- 54 P. L. Lam, S. H. L. Kok, R. Gambari, H. Y. L. T. W. Kok, K. L. Choi, C. S. Wong, D. K. P. Hau, W. Y. Wong, K. H. Lam, Z. X. Bian, K. K. H. Lee and C. H. Chui, *Green Chem.*, 2015, **17**, 1640–1646.
- 55 J. Li and P. Yao, *Langmuir*, 2009, **25**, 6385–6391.
- 56 Y. J. Hu, Y. Liu, T. Q. Sun, A. M. Bai, J. Q. Lü and Z. B. Pi, *Int. J. Biol. Macromol.*, 2006, **39**, 280–285.
- 57 R. Tantra, J. Tompkins and P. Quincey, *Colloids Surf. B*, 2010, **75**, 275–281.
- 58 S. Curry, H. Mandelkow, P. Brick and N. Franks, *Nat. Struct. Biol.*, 1998, **5**, 827–835.
- 59 P. Yousefpour, J. R. McDaniel, V. Prasad, L. Ahn, X. Li, R. Subrahmanyam, I. Weitzhandler, S. Suter and A. Chilkoti, *Nano lett.*, 2018, **18**, 7784–7793.
- 60 D. Sleep, J. Cameron and L. R. Evans, *Biochim. Biophys. Acta Gen. Subj.*, 2013, 1830, 5526–5534.
- 61 E. N. Hoogenboezem and C. L. Duvall, *Adv. Drug Deliv. Rev.*, 2018, **130**, 73–89.
- 62 D. C. Carter, X. M. He, S. H. Munson, P. D. Twigg, K. M. Gernert, M. B. Broom and T. Y. Miller, *Science*, 1989, **244**, 1195–1198.
- 63 K. Gelse, E. Pöschl and T. Aigner, *Adv. Drug Deliv. Rev.*, 2003, **55**, 1531–1546.

- 64 S. Ricard-Blum, *Cold Spring Harb. Perspect. Biol.*, 2011, **3**, 1–19.
- 65 V. Chak, D. Kumar and S. Visht, *Int. J. Pharm. Teach. Pract.*, 2013, **4**, 811–820.
- 66 M. Violeta GHICA, M. Georgiana ALBU, L. Popa, M. Leca, L. Brăzdaru, C. Cotruț and V. Trandafir, *Rev. Roum. Chim.*, 2009, **54**, 1103–1110.
- 67 T. Luo and K. L. Kiick, *Eur. Polym. J.*, 2013, **49**, 2998–3009.
- 68 T. Luo and K. L. Kiick, *Bioconjugate Chem.*, 2017, **28**, 816–827.
- 69 F. W. Kotch and R. T. Raines, *Proc. Natl. Acad. Sci. U.S.A.*, 2006, **103**, 3028–3033.
- 70 M. A. Cejas, W. A. Kinney, C. Chen, G. C. Leo, B. A. Tounge, J. G. Vinter, P. P. Joshi and B. E. Maryanoff, *J. Am. Chem. Soc.*, 2007, **129**, 2202–2203.
- 71 M. A. Cejas, W. A. Kinney, C. Chen, J. G. Vinter, H. R. Almond, K. M. Balss, C. A. Maryanoff, U. Schmidt, M. Breslav, A. Mahan, E. Lacy, B. E. Maryanoff and M. R. Ghadiri, *Proc. Natl. Acad. Sci. U.S.A.*, 2008, **105**, 8513–8518.
- 72 Y. C. Yu, T. Pakalns, Y. Dori, J. B. Mccarthy, M. Tirrell and G. B. Fields, *Meth. Enzymol.*, 1997, **289**, 571–587.
- 73 Y. C. Yu, V. Roontga, V. A. Daragan, K. H. Mayo, M. Tirrell and G. B. Fields, *Biochemistry*, 1999, **38**, 1659–1668.
- 74 B. Vrhovski, S. Jensen and A. S. Weiss, *Coacervation characteristics of recombinant human tropoelastin*, 1997, vol. 250.
- 75 Z. Zhang, O. Ortiz, R. Goyal and J. Kohn, in *Principles of Tissue Engineering: Fourth Edition*, Academic Press, 2014, vol. 18, pp. 441–473.
- 76 L. Quintanilla-Sierra, C. García-Arévalo and J. C. Rodriguez-Cabello, *Mater. Today Bio.*, 2019, **2**, 1–17.
- 77 S. M. Mithieux and A. S. Weiss, *Adv. Protein Chem.*, 2005, **70**, 437–461.
- 78 D. W. Urry, *J. Protein Chem.*, 1988, **7**, 81–114.

- 79 A. M. J. Coenen, K. V. Bernaerts, J. A. W. Harings, S. Jockenhoevel and S. Ghazanfari, *Acta Biomater.*, 2018, **79**, 60–82.
- 80 L. Debelle and A. M. Tamburro, *Int. J. Biochem. Cell Biol.*, 1991, **31**, 261–272.
- 81 A. Hinek and M. Rabinovitch, *J Cell Biol*, 1994, **126**, 563–574.
- 82 B. Vrhovski and A. S. Weiss, *Eur. J. Biochem*, 1998, **258**, 1–18.
- 83 P. Brown-Augsburger, C. Tisdale, T. Broekelmann, C. Sloan and R. P. Mecham, *J. Biol. Chem*, 1995, **270**, 17778–17783.
- 84 L. Debelle and A. J. E. Alix, *Biochimie*, 1999, **81**, 981–994.
- 85 S. Roberts, M. Dzuricky and A. Chilkoti, *FEBS Lett.*, 2015, **589**, 2477–2486.
- 86 W. F. Daamen, J. H. Veerkamp, J. C. M. van Hest and T. H. van Kuppevelt, *Biomaterials*, 2007, **28**, 4378–4398.
- 87 D. W. Urry, T. Hugel, M. Seitz, H. E. Gaub, L. Sheiba, J. Dea, J. Xu and T. Parker, *Philos. Trans. R. Soc. B Biol. Sci.*, 2002, **357**, 169–184.
- 88 V. Samouillan, C. André, J. Dandurand and C. Lacabanne, *Biomacromolecules*, 2004, **5**, 958–964.
- 89 D. W. Urry, *Faraday Discuss. Chem. Soc.*, 1976, **61**, 205–212.
- 90 D. W. Urry, M. M. Long, B. A. Cox, T. Ohnishi, L. W. Mitchell and M. Jacobs, *Biochim. Biophys. Acta*, 1974, **371**, 597–602.
- 91 D. W. Urry, T. Ohnishi, M. M. Long and L. W. Mitche, *Int. J. Peptide Protein Res.*, 1975, **7**, 367–378.
- 92 A. K. Varanko, J. C. Su and A. Chilkoti, *Annu. Rev. Biomed. Eng.*, 2020, **22**, 343–369.
- 93 D. Kurzbach, W. Hassouneh, J. R. McDaniel, E. A. Jaumann, A. Chilkoti and D. Hinderberger, *J. Am. Chem. Soc.*, 2013, **135**, 11299–11308.
- 94 K. Widder, S. R. MacEwan, E. Garanger, V. Núñez, S. Lecommandoux, A. Chilkoti and D. Hinderberger, *Soft Matter*, 2017, **13**, 1816–1822.

- 95 B. Zhao, N. K. Li, Y. G. Yingling and C. K. Hall, *Biomacromolecules*, 2016, **17**, 111–118.
- 96 N. K. Li, F. G. Quiroz, C. K. Hall, A. Chilkoti and Y. G. Yingling, *Biomacromolecules*, 2014, **15**, 3522–3530.
- 97 J. C. Rodríguez-Cabello, S. Prieto, J. Reguera, F. J. Arias and A. Ribeiro, *J. Biomater. Sci. Polym. Ed.*, 2007, **18**, 269–286.
- 98 M. Manno, A. Emanuele, V. Martorana, P. L. San Biagio, D. Bulone, M. B. Palma-Vittorelli, D. T. Mcpherson, J. Xu, T. M. Parker and D. W. Urry, *Biopolymers*, 2001, **59**, 51–64.
- 99 D. W. Urry, *J. Phys. Chem. B*, 1997, **101**, 11007–11028.
- 100 J. C. Rodríguez-Cabello, J. Reguera, S. Prieto and M. Alonso, in *Smart Polymers*, 2007, pp. 177–209.
- 101 J. C. Rodríguez-Cabello, I. G. de Torre, S. Acosta, S. Salinas and M. Herrero, in *Self-assembling Biomaterials*, Woodhead Publishing, 2018, pp. 49–78.
- 102 R. Herrero-Vanrell, A. C. Rincón, M. Alonso, V. Rebotó, I. T. Molina-Martinez and J. C. Rodríguez-Cabello, *J. Control. Release*, 2005, **102**, 113–122.
- 103 D. W. Urry and M. M. Long, *CRC Crit. Rev. Biochem.*, 1976, **4**, 1–45.
- 104 L. D. Muiznieks, A. S. Weiss and F. W. Keeley, in *Biochemistry and Cell Biology*, National Research Council of Canada, 2010, vol. 88, pp. 239–250.
- 105 S. Rauscher, S. Baud, M. Miao, F. W. W. Keeley and R. Pomès, *Structure*, 2006, **14**, 1667–1676.
- 106 D. W. Urry, *Methods Enzymol.*, 1982, **82**, 673–716.
- 107 D. W. Urry, D. K. Chang, H. Zhang and K. U. Prasad, *Biochem. Biophys. Res. Commun.*, 1988, **153**, 832–839.
- 108 D. W. Urry, *Angew. Chem. Int. Ed. Engl.*, 1993, **32**, 819–841.

- 109 D. W. Urry, *Chem. Phys. Lett.*, 2004, **399**, 177–183.
- 110 A. Ribeiro, F. J. Arias, J. Reguera, M. Alonso and J. C. Rodríguez-Cabello, *Biophys. J.*, 2009, **97**, 312–320.
- 111 J. R. McDaniel, D. C. Radford and A. Chilkoti, *Biomacromolecules*, 2013, **14**, 2866–2872.
- 112 D. E. Meyer and A. Chilkoti, *Biomacromolecules*, 2004, **5**, 846–851.
- 113 T. Yamaoka, T. Tamura, Y. Seto, T. Tada, S. Kunugi and D. A. Tirrell, *Biomacromolecules*, 2003, **4**, 1680–1685.
- 114 R. Petitdemange, E. Garanger, L. Bataille, W. Dieryck, K. Bathany, B. Garbay, T. J. Deming and S. Lecommandoux, *Biomacromolecules*, 2017, **18**, 544–550.
- 115 W. Huang, A. Rollett and D. L. Kaplan, *Expert Opin. Drug Deliv.*, 2015, **12**, 779–791.
- 116 D. T. McPherson, C. Morrow, S. Daniel Minehan, J. W. U, E. Hunter and D. W. Urry, *Biotechnol. Prog.*, 1992, **8**, 347–352.
- 117 A. Chilkoti, M. R. Dreher and D. E. Meyer, *Adv. Drug Deliv. Rev.*, 2002, **54**, 1093–1111.
- 118 J. R. McDaniel, J. A. MacKay, F. G. Quiroz and A. Chilkoti, *Biomacromolecules*, 2010, **11**, 944–952.
- 119 M. Amiram, F. G. Quiroz, D. J. Callahan and A. Chilkoti, *Nat. Mater.*, 2011, **10**, 141–148.
- 120 S. R. MacEwan, W. Hassouneh and A. Chilkoti, *J. Vis. Exp.*, 2014, **88**, 1–8.
- 121 D. T. Mcpherson, J. Xu and D. W. Urry, *Protein Expr. Purif.*, 1996, **7**, 51–57.
- 122 R. Schipperus, G. Eggink and F. A. de Wolf, *Biotechnol. Prog.*, 2012, **28**, 242–247.
- 123 R. Schipperus, R. L. M. Teeuwen, M. W. T. Werten, G. Eggink and F. A. de Wolf, *Appl. Microbiol. Biotechnol.*, 2009, **85**, 293–301.

- 124 R. E. Sallach, V. P. Conticello and E. L. Chaikof, *Biotechnol. Prog.*, 2009, **25**, 1810–1818.
- 125 R. W. Herzog, N. K. Singh, D. W. Urry and H. Daniell, *Appl. Microbiol Biotechnol.*, 1997, **47**, 368–372.
- 126 A. J. Conley, J. J. Joensuu, A. M. Jevnikar, R. Menassa and J. E. Brandle, *Biotechnol. Bioeng.*, 2009, **103**, 562–573.
- 127 A. Kaldis, A. Ahmad, A. Reid, B. Mcgarvey, J. Brandle, S. Ma, A. Jevnikar, S. E. Kohalmi and R. Menassa, *Plant Biotechnol. J.*, 2013, **11**, 535–545.
- 128 M. Daskalova, H. Taskov, E. Dimitrova and S. Baydanoff, *Autoimmunity*, 1997, **25**, 233–241.
- 129 B. H. Gu, J. C. Choi, Y. H. Shen, L. Z. Song, M. E. Scheurer, A. Luong, A. Rodriguez, P. Woodruff, L. Koth, D. B. Corry, F. Kheradmand and S. A. LeMaire, *J. Am. Heart Assoc.*, 2019, **8**, 1–10.
- 130 S. A. Wood, J. E. Lemons, K. U. Prasad and D. W. Urry, *J. Biomed. Mater Res.*, 1986, **20**, 315–335.
- 131 D. W. Urry, T. M. Parker, M. C. Reid and D. Channe Gowda, *J. Bioact. Compat. Polym.*, 1991, **6**, 263–282.
- 132 A. C. Rincón, I. T. Molina-Martinez, B. de Las Heras, M. Alonso, C. Bañez, J. C. Rodríguez-Cabello and R. Herrero-Vanrell, *J. Biomed. Mater. Res. A*, 2006, **78**, 343–351.
- 133 S. M. Wei, E. Katona, J. Facht, T. Fülöp, L. Robert and M. P. Jacob, *Int. Arch. Allergy Immunol.*, 1998, **115**, 33–41.
- 134 F. J. Elsas, D. C. Gowda and D. W. Urry, *J. Pediatr. Ophthalmol. Strabismus*, 1992, **29**, 284–286.
- 135 K. Changi, B. Bosnjak, C. Gonzalez-Obeso, R. Kluger, J. C. Rodríguez-Cabello, O. Hoffmann and M. M. Epstein, *J. Biomed. Mater. Res. A*, 2018, **106**, 924–934.

- 136 A. Kouhi, Z. Yao, L. Zheng, Z. Li, P. Hu, A. L. Epstein and J. A. Mackay, *Biomacromolecules*, 2019, **20**, 2942–2952.
- 137 D. E. Meyer, K. Trabbic-Carlson and A. Chilkoti, *Biotechnol. Prog.*, 2001, **17**, 720–728.
- 138 D. E. Meyer and A. Chilkoti, *Nat. Biotechnol.*, 1999, **17**, 1112–1115.
- 139 L. Bataille, W. Dieryck, A. Hocquellet, C. Cabanne, K. Bathany, S. Lecommandoux, B. Garbay and E. Garanger, *Protein Expr. Purif.*, 2015, **110**, 165–171.
- 140 T. A. T. Lee, A. Cooper, R. P. Apkarian and V. P. Conticello, *Adv. Mater.*, 2000, **12**, 1105–1110.
- 141 D. J. Callahan, W. Liu, X. Li, M. R. Dreher, W. Hassouneh, M. Kim, P. Marszalek and A. Chilkoti, *Nano Lett.*, 2012, **12**, 2165–2170.
- 142 M. R. Dreher, A. J. Simnick, K. Fischer, R. J. Smith, A. Patel, M. Schmidt and A. Chilkoti, *J. Am. Chem. Soc.*, 2008, **130**, 687–694.
- 143 G. Sun, P. Y. Hsueh, S. M. Janib, S. Hamm-Alvarez and J. Andrew MacKay, *J. Control. Release*, 2011, **155**, 218–226.
- 144 P. Y. Hsueh, M. C. Edman, G. Sun, P. Shi, S. Xu, Y. A. Lin, H. Cui, S. F. Hamm-Alvarez and J. A. Mackay, *J. Control. Release*, 2015, **208**, 2–13.
- 145 L. Martín, E. Castro, A. Ribeiro, M. Alonso and J. C. Rodríguez-Cabello, *Biomacromolecules*, 2012, **13**, 293–298.
- 146 S. R. MacEwan and A. Chilkoti, *Nano Lett.*, 2012, **12**, 3322–3328.
- 147 A. J. Simnick, C. A. Valencia, R. Liu and A. Chilkoti, *ACS Nano*, 2010, **4**, 2217–2227.
- 148 Y. Takakura and M. Hashida, *Pharm. Res.*, 1996, **13**, 820–831.
- 149 G. Tiwari, R. Tiwari, S. Bannerjee, L. Bhati, S. Pandey, P. Pandey and B. Sriwastawa, *J. Pharm. Investig.*, 2012, **2**, 2–11.

- 150 P. C. A. Rodrigues, U. Beyer, P. Schumacher, T. Roth, H. H. Fiebig, C. Unger, L. Messori, P. Orioli, D. H. Paper, R. Muè and F. Kratz, *Bioorg. Med. Chem.*, 1999, **7**, 2517–2524.
- 151 A. Nathan, S. Zalipsky and J. Kohn, *J. Bioact. Compat. Polym.*, 1994, **9**, 239–251.
- 152 M. Tamara, P. Kopeckova and J. Kopecek, *J. Control. Release.*, 1999, **59**, 133–148.
- 153 T. Minko, P. Kopeckova, V. Pozharov and J. Kopecek, *J. Control. Release.*, 1998, **54**, 223–233.
- 154 T. Minko, P. Kopecková and J. Kopecek, *Pharm. Res.*, 1999, **16**, 986–996.
- 155 V. Omelyanenko, P. K. C. Gentry and J. Kopecek, *Int. J. Cancer.*, 1998, **75**, 600–608.
- 156 F. Kratz, R. Müller-Driver, I. Hofmann, J. Dreves and C. Unger, *J. Med. Chem.*, 2000, **43**, 1253–1256.
- 157 F. Kratz, U. Beyer, T. Roth, N. Tarasova, P. Collery, F. Lechenault, A. Cazabat, P. Schumacher, C. Unger and U. Falken, *J. Pharm. Sci.*, 1998, **87**, 338–346.
- 158 M. Shah, M. C. Edman, S. R. Janga, P. Shi, J. Dhandhukia, S. Liu, S. G. Louie, K. Rodgers, J. A. MacKay and S. F. Hamm-Alvarez, *J. Control. Release*, 2013, **171**, 269–279.
- 159 P. Shi, S. Aluri, Y. A. Lin, M. Shah, M. Edman, J. Dhandhukia, H. Cui and J. A. MacKay, *J. Control. Release*, 2013, **171**, 330–338.
- 160 A. S. Nigatu, H. Ashar, S. N. Sethuraman, R. Wardlow, D. Maples, J. Malayer and A. Ranjan, *Int. J. Hyperth.*, 2018, **34**, 201–208.
- 161 J. Andrew MacKay, M. Chen, J. R. McDaniel, W. Liu, A. J. Simnick and A. Chilkoti, *Nat. Mater.*, 2009, **8**, 993–999.
- 162 Y. Bae, N. Nishiyama, S. Fukushima, H. Koyama, M. Yasuhiro and K. Kataoka, *Bioconjugate Chem.*, 2005, **16**, 122–130.
- 163 J. R. McDaniel, J. Bhattacharyya, K. B. Vargo, W. Hassouneh, D. A. Hammer and A. Chilkoti, *Angew. Chem. Int. Ed.*, 2013, **52**, 1683–1687.

- 164 D. Y. Furgeson, M. R. Dreher and A. Chilkoti, *J. Control. Release*, 2006, **110**, 362–369.
- 165 J. R. McDaniel, S. R. MacEwan, M. Dewhurst and A. Chilkoti, *J. Control. Release*, 2012, **159**, 362–367.
- 166 J. Bhattacharyya, J. J. Bellucci, I. Weitzhandler, J. R. McDaniel, I. Spasojevic, X. Li, C. C. Lin, J. T. A. Chi and A. Chilkoti, *Nat. Commun.*, 2015, **6**, 1–12.
- 167 J. Bhattacharyya, X. R. Ren, R. A. Mook, J. Wang, I. Spasojevic, R. T. Premont, X. Li, A. Chilkoti and W. Chen, *Nanoscale*, 2017, **9**, 12709–12717.
- 168 J. Bhattacharyya, I. Weitzhandler, S. B. Ho, J. R. McDaniel, X. Li, L. Tang, J. Liu, M. Dewhurst and A. Chilkoti, *Adv. Funct. Mater.*, 2017, **27**, 1–9.
- 169 J. R. McDaniel, I. Weitzhandler, S. Prevost, K. B. Vargo, M. S. Appavou, D. A. Hammer, M. Gradzielski and A. Chilkoti, *Nano Lett.*, 2014, **14**, 6590–6598.
- 170 S. R. Aluri, P. Shi, J. A. Gustafson, W. Wang, Y. A. Lin, H. Cui, S. Liu, P. S. Conti, Z. Li, P. Hu, A. L. Epstein and J. A. Mackay, *ACS Nano*, 2014, **8**, 2064–2076.
- 171 M. Amiram, K. M. Luginbuhl, X. Li, M. N. Feinglos and A. Chilkoti, *Proc. Natl. Acad. Sci. U.S.A.*, 2013, **110**, 2792–2797.
- 172 W. Liu, J. A. MacKay, M. R. Dreher, M. Chen, J. R. McDaniel, A. J. Simnick, D. J. Callahan, M. R. Zalutsky and A. Chilkoti, *J. Control. Release*, 2010, **144**, 2–9.
- 173 J. L. Schaal, X. Li, E. Mastria, J. Bhattacharyya, M. R. Zalutsky, A. Chilkoti and W. Liu, *J. Control. Release*, 2016, **228**, 58–66.
- 174 H. Betre, W. Liu, M. R. Zalutsky, A. Chilkoti, V. B. Kraus and L. A. Setton, *J. Control. Release*, 2006, **115**, 175–182.
- 175 W. Liu, J. McDaniel, X. Li, D. Asai, F. G. Quiroz, J. Schaal, J. S. Park, M. Zalutsky and A. Chilkoti, *Cancer Res.*, 2012, **72**, 5956–5965.
- 176 K. M. Luginbuhl, J. L. Schaal, B. Umstead, E. M. Mastria, X. Li, S. Banskota, S. Arnold, M. Feinglos, D. D'Alessio and A. Chilkoti, *Nat. Biomed. Eng.*, 2017, **1**, 1–14.

- 177 W. Wang, A. Jashnani, S. R. Aluri, J. A. Gustafson, P. Y. Hsueh, F. Yarber, R. L. McKown, G. W. Laurie, S. F. Hamm-Alvarez and J. A. MacKay, *J. Control. Release*, 2015, **199**, 156–167.
- 178 S. B. Adams Jr., M. F. Shamji, D. L. Nettles, P. Hwang and L. A. Setton, *J. Biomed. Mater. Res. Part B Appl. Biomater.*, 2008, **90B**, 67–74.
- 179 M. F. Shamji, H. Betre, V. B. Kraus, J. Chen, A. Chilkoti, R. Pichika, K. Masuda and L. A. Setton, *Arthritis Rheum.*, 2007, **56**, 3650–3661.
- 180 A. T. Truong, K. Hamada, Y. Yamada, H. Guo, Y. Kikkawa, C. T. Okamoto, J. A. MacKay and M. Nomizu, *FASEB J.*, 2020, **34**, 6729–6740.
- 181 C. M. Madl and S. C. Heilshorn, *Bioconjugate Chem.*, 2017, **28**, 724–730.
- 182 H. Wang, A. Paul, D. Nguyen, A. Enejder and S. C. Heilshorn, *ACS Appl. Mater. Interfaces*, 2018, **10**, 21808–21815.
- 183 D. W. Lim, D. L. Nettles, L. A. Setton and A. Chilkoti, *Biomacromolecules*, 2008, **9**, 222–230.
- 184 I. V. Yannas, E. Lee, D. P. Orgill, E. M. Skrabut and G. F. Murphy, *Proc. Natl. Acad. Sci. USA*, 1989, **86**, 933–937.
- 185 F. J. O'Brien, B. A. Harley, I. V. Yannas and L. J. Gibson, *Biomaterials*, 2005, **26**, 433–441.
- 186 S. M. Staubli, G. Cerino, I. Gonzalez de Torre, M. Alonso, D. Oertli, F. Eckstein, K. Glatz, J. C. Rodríguez-Cabello and A. Marsano, *Biomaterials*, 2017, **135**, 30–41.
- 187 B. P. dos Santos, B. Garbay, M. Fenelon, M. Rosselin, E. Garanger, S. Lecommandoux, H. Oliveira and J. Amédée, *Acta Biomater.*, 2019, **99**, 154–167.
- 188 M. P. Sousa, I. Gonzalez de Torre, M. B. Oliveira, J. C. Rodríguez-Cabello and J. F. Mano, *Mater. Today Chem.*, 2017, **4**, 150–163.
- 189 F. Amaduzzi, F. Bomboi, A. Bonincontro, F. Bordini, S. Casciardi, L. Chronopoulou, M. Diociaiuti, F. Mura, C. Palocci and S. Sennato, *Colloids Surf. B*, 2014, **114**, 1–10.

- 190 S. Sennato, F. Bordi, C. Cametti, M. Diociaiuti and P. Malaspina, *Biochim. Biophys. Acta - Biomembr.*, 2005, **1714**, 11–24.
- 191 S. R. Macewan and A. Chilkoti, *J. Control. Release*, 2014, **190**, 314–330.
- 192 L. M. Bravo-Anaya, B. Garbay, J. L. E. Nando-Rodríguez, F. Carvajal Ramos, E. Ibarboure, K. Bathany, Y. Xia, J. Rosselgong, G. Joucla, E. Garanger and S. Lecommandoux, *J. Colloid Interface Sci.*, 2019, **557**, 777–792.
- 193 J. F. Nawroth, J. R. McDaniel, A. Chilkoti, R. Jordan and R. Luxenhofer, *Macromol. Biosci.*, 2016, **16**, 322–333.
- 194 D. Zhu, H. Wang, P. Trinh, S. C. Heilshorn and F. Yang, *Biomaterials*, 2017, **127**, 132–140.
- 195 H. Wang, D. Zhu, A. Paul, L. Cai, A. Enejder, F. Yang and S. C. Heilshorn, *Adv. Funct. Mater.*, 2017, **27**, 1–11.
- 196 K. M. Luginbuhl, D. Mozhdghi, M. Dzuricky, P. Yousefpour, F. C. Huang, N. R. Mayne, K. L. Buehne and A. Chilkoti, *Angew. Chem. Int. Ed.*, 2017, **56**, 13979–13984.
- 197 T. A. Farazi, G. Waksman and J. I. Gordon, *Biochemistry*, 2001, **40**, 6335–6343.
- 198 D. Mozhdghi, K. M. Luginbuhl, M. Dzuricky, S. A. Costa, S. Xiong, F. C. Huang, M. M. Lewis, S. R. Zelenetz, C. D. Colby and A. Chilkoti, *J. Am. Chem. Soc.*, 2019, **141**, 945–951.
- 199 V. Ibrahimova, H. Zhao, E. Ibarboure, E. Garanger and S. Lecommandoux, *Angew. Chem. Int. Ed.*, 2021, **60**, 1–21.

## Chapter 2. Coupling of natural rubber and Elastin-like polypeptide

### 2.1. Introduction

Polypeptides are of great interest for biomedical applications such as drug delivery and tissue engineering because they are biodegradable and biocompatible<sup>1,2</sup>. Hybrid block copolymers containing a polypeptide block and a non-polypeptide block are of interest since they can combine the intrinsic properties of polypeptide and the physico-chemical properties of the second block which could bring solubility, elasticity, strength, etc. Of particular interest, polypeptide-block-polyisoprene copolymers can mimic the natural rubber (NR), which is composed of 1,4-cis polyisoprene (PI) and a small number of proteins that are believed to play an important role in the physical properties of NR<sup>3-5</sup>. In addition, PI is enzymatically degradable<sup>6</sup> and biocompatible.

Polypeptide-block-PI copolymers can be obtained by ring opening polymerization of the N-carboxyanhydride of the selected amino acid using the PI as a macroinitiator. This approach was successfully used to synthesize poly( $\gamma$ -benzyl-glutamate)<sup>7,8</sup>, poly(L-lysine)<sup>9</sup>, and poly( $\epsilon$ -tert-butyloxycarbonyl-L-lysine)<sup>8</sup> onto polyisoprene. However, a limitation of this approach is that the polypeptide blocks were always based on a single amino acid, which is obviously not representative of the complex protein structures. In addition, the molar-mass dispersity of the polypeptide block is not negligible unlike natural proteins.

Our goal was to synthesize a diblock polymer combining PI with a recombinantly produced elastin-like polypeptide (ELP). ELPs are synthetic polypeptides bio-inspired from the hydrophobic region of tropoelastin<sup>10</sup>. They consist of multiple repeats of Val-Pro-Gly-Xaa-Gly pentapeptides, where the guest residue (Xaa) can be any natural amino acid except proline. ELPs are characterized by their thermosensitivity, being soluble in water below a transition temperature (Tt), which corresponds to the cloud point temperature, and becoming insoluble when heated above this Tt<sup>11,12</sup>. The Tt depends on the chain length, on the nature of the guest residue Xaa (e.g., polar, charged, hydrophobic), on the polypeptide concentration, and on the

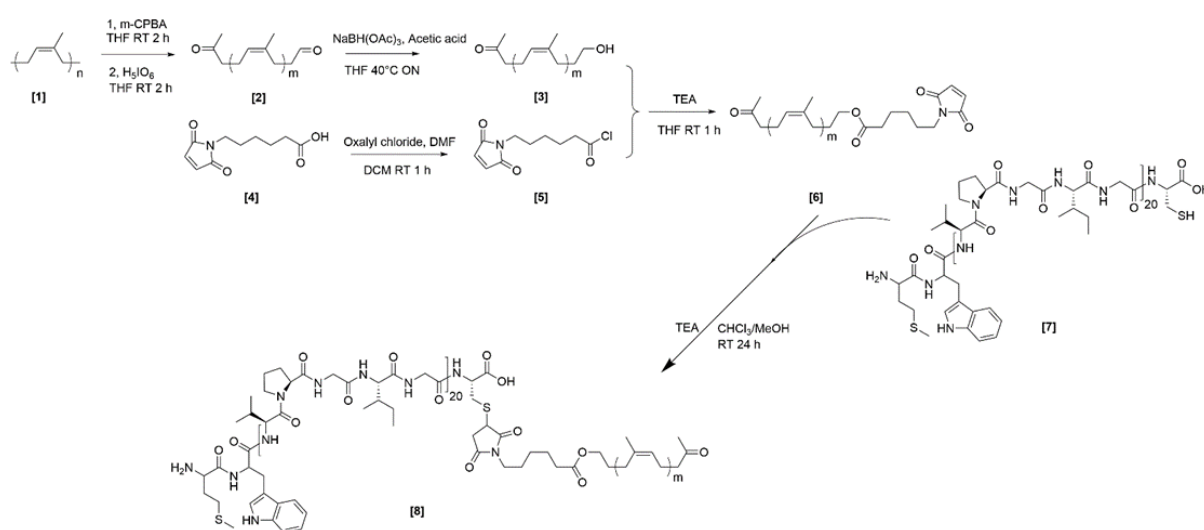
presence of salts<sup>13</sup>. Recombinantly produced ELPs are often preferred, because they have controlled sequence and can have high molecular mass contrarily to those chemically synthesized<sup>14</sup>.

To solve solubility issues between the hydrophobic PI and the hydrophilic ELP blocks we used a PI block of relatively low molar mass, i.e., below 10 000 g.mol<sup>-1</sup>. On the other hand, we selected from our library a rather hydrophobic ELP block based on the Grand Average of Hydropathy (GRAVY) index, which is calculated as the sum of hydropathy values of all the amino acids, divided by the number of residues in the sequence<sup>15</sup>. Negative GRAVY value indicates that the protein is non-polar, and positive value indicates that the protein is polar. We synthesized ELPs containing isoleucine (I) at the guest position of every VPGXG units<sup>16,17</sup>. The sequence of these ELPs is MW(VPGIG)<sub>n</sub>C, with n = 20, 40 and 60. Their molar masses vary from 8.9 to 25.9 kg.mol<sup>-1</sup>, and their GRAVY index is 1.26. Their T<sub>t</sub> values were between 12 and 19°C for a concentration of 50 μM. Among these ELPs, we selected the shortest one, MW(VPGIG)<sub>20</sub>C, referred as I20, because (i) it can be produced in higher yields than the larger ones, (ii) it has a lower tendency to aggregation than the 40 and 60 pentamers, (iii) the size of the I20 (8.9 kg.mol<sup>-1</sup>) is closer to that of the PI used, and therefore the final diblock is expected to have a rather balanced hydrophobic/hydrophilic mass ratio of approximately 0.7. In addition, the I20 block has one cysteine residue at the C-terminal position that will be conveniently used for the coupling reaction with one PI block.

## **2.2. Results and discussion**

### **2.2.1. Synthesis and purification of I20-*b*-PI**

Our goal was to graft a low MW PI block (5 to 10 kg.mol<sup>-1</sup> range) to the N-terminal cysteine of the I20 ELP to obtain an amphiphilic diblock copolymer structure. The different steps of the synthesis process are depicted in the Scheme 1.



**Scheme 1. Synthesis of I20-*b*-PI.** Five main steps were used. **1:** epoxidation and controlled hydrolysis of natural rubber to obtain keto/aldehyde PI (PIEG); **2:** reduction of the aldehyde ends of PIEG to obtain keto/hydroxyl PI (PIOH); **3:** conversion of maleimido-hexanoic acid (MalOH) to an acid chloride form (MalCl); **4:** grafting of the Maleimide group on the PIOH to obtain –polyisoprene-maleimide (PIMAL); **5:** Michael addition reaction between the maleimide group from PIMAL and the N-terminal cysteine residue of the ELP I20.

### 2.2.1.1. Synthesis, purification and characterization of ELP I20

The synthesis, purification and characterization of the recombinant ELP I20 was reported in a previous work<sup>16</sup>. Briefly, production of the recombinant protein was performed by *E. coli* cells, and purification from the cell lysate was done using the ITC protocol<sup>18</sup>. We optimized the previously used ITC procedure, by lowering the temperature of the hot-spin step from 30°C to 25°C, and by solubilizing the corresponding hot-spin pellets in deionized water instead of salt-containing solutions. These changes led to a large increase in the yield of purified I20 from  $32.7 \pm 13.5$  mg/L culture<sup>16</sup> to  $243 \pm 48$  mg/L culture ( $n = 4$ ). The size of the purified ELP was verified by SDS-PAGE analysis (Fig. 1).

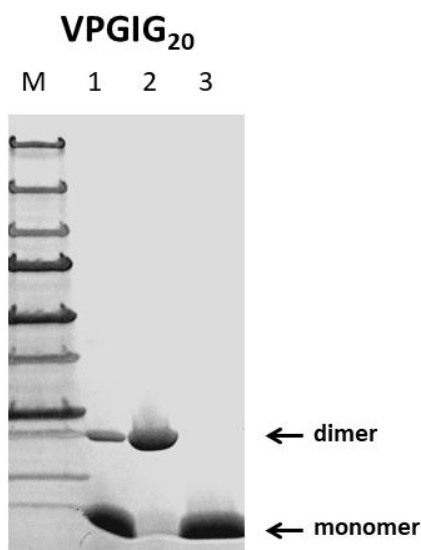


**Figure 1: SDS-PAGE analysis of purified ELP-I20.** 12  $\mu\text{g}$  of purified ELP I20 were analyzed in each lane. 1) sample after three ITC cycles of purification. 2) same sample after incubation at room temperature for 30 min with 2%  $\text{H}_2\text{O}_2$ . 3) purified I20 sample reduced by incubation with 50 mM dithiothreitol. M) Protein standards. Electrophoresis was performed with 4-20% gels. The loading buffer did not contain reducing agents.

This experiment shows that purified I20 was found under two forms, monomeric and dimeric (lane 1). The detection of homodimers is explained by the presence of one cysteine at the N-terminal position of the ELP. The oxidation of this cysteine allows the formation of intermolecular disulfide bridges (see lane 2 Fig. 1), links that can be destroyed thanks to a reducing agent such as dithiothreitol (lane 3).

### 2.2.1.2. Synthesis of polyisoprene-maleimide (PIMAL)

The polyisoprene originally found in natural rubber (NR) is of high molar mass ( $> 500 \text{ kg}\cdot\text{mol}^{-1}$ ), and to reduce it we used a protocol that has been set-up at LCPO before my arrival<sup>8,19</sup>. It consists in the partial epoxidation of NR by m-CPBA followed by cleavage with periodic acid of the formed epoxy units. The quantity of m-CPBA (mw) to add to the reaction medium for a targeted epoxidation rate was calculated as follows:

$$mW = \frac{tx \times mR \times Mm - CPBA}{P \times Miso}$$

where: tx is the targeted rate of epoxidation (%), mR is the mass of rubber (g), Mm-CPBA is the molar mass of m-CPBA (g/mol), P is the purity of m-CPBA (wt %) and Miso is the molar mass of isoprene (g/mol).

NR was first dissolved into THF, which led to an increase in the solution viscosity. Viscosity further increased when the epoxidation reaction took place, and we thus adapted the stir speed to maintain the reaction medium homogenous. After addition of the periodic acid, viscosity decreased indicating that the long chain polymers were converted into shorter chains. The final purified product heterotelechelic keto/aldehyde PI (PIEG) was characterized by  $^1\text{H}$  NMR (Fig. 2) and size exclusion chromatography (SEC, Fig. 3).

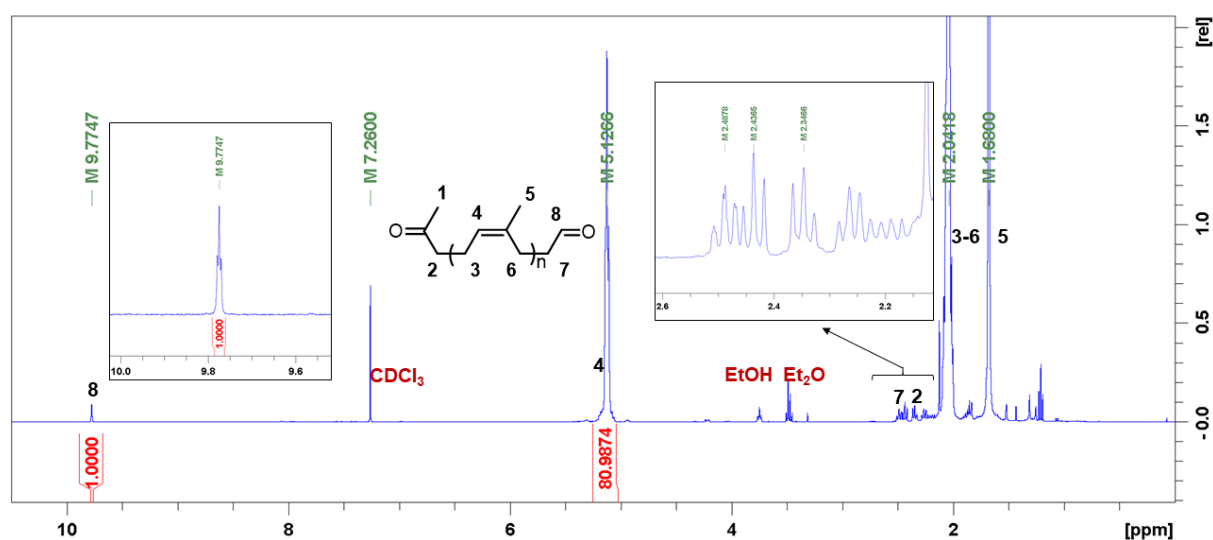


**Figure 2: NMR spectrum of purified heterotelechelic keto/aldehyde PI (PIEG). 15 mg of purified PIEG were dissolved into 500  $\mu\text{L}$  of  $\text{CDCl}_3$  and analyzed with a Bruker AVANCE III HD 400 MHz Spectrometer. Insets: zoomed regions 9.8-10 ppm (left) and 2.2-2.8 ppm (right).**

The  $^1\text{H}$  NMR spectrum confirmed the presence of a peak at 9.77 ppm corresponding to the hydrogen of the aldehyde function, and another one at 2.48 ppm corresponding to the “-CH<sub>2</sub>” group in  $\alpha$  position of the aldehyde’s carbonyl. Thanks to NMR, the number-average molar mass ( $\overline{M}_n$ ) was calculated to be around 5500  $\text{g mol}^{-1}$ .

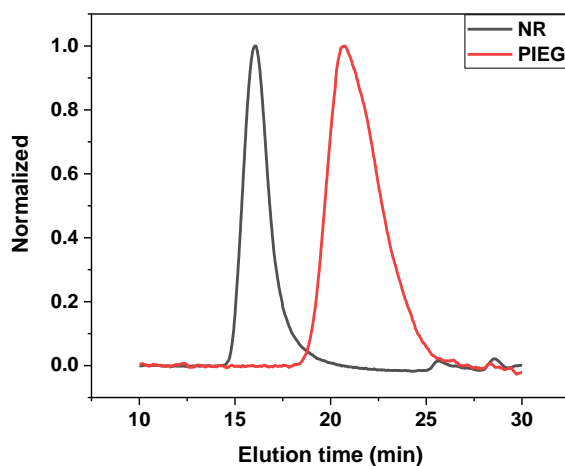


**Figure 3. SEC analysis of purified PIEG. 10 mg of purified PIEG or NR were dissolved in 2 mL THF, the solution was passed through 0.45  $\mu\text{m}$  PTFE filter, and was analyzed by SEC. The result obtained with PIEG (red line) was compared to that of the initial NR (black line).**

The SEC trace of PIEG completely shifted to higher retention time when compared to the original NR one. Using PS standards calibration, the ( $\overline{M}_n$ ) of PIEG was evaluated to be 6900  $\text{g}\cdot\text{mol}^{-1}$  and its dispersity ( $D$ ) was 1.6.

Thereafter, the aldehyde end group of PIEG was selectively reduced into a hydroxyl group using  $\text{NaBH}(\text{OAc})_3$ . Heterotelechelic keto/hydroxyl PI (PI-OH) was obtained in good yield (80%) and its structure was confirmed by  $^1\text{H}$  NMR spectrometry (Fig. 4). Indeed, the peak corresponding to the aldehyde proton of PIEG at 9.77 ppm disappeared totally, and a peak at 3.63 ppm was observed, corresponding to the “-CH<sub>2</sub>” group in  $\alpha$  position of the hydroxyl function.

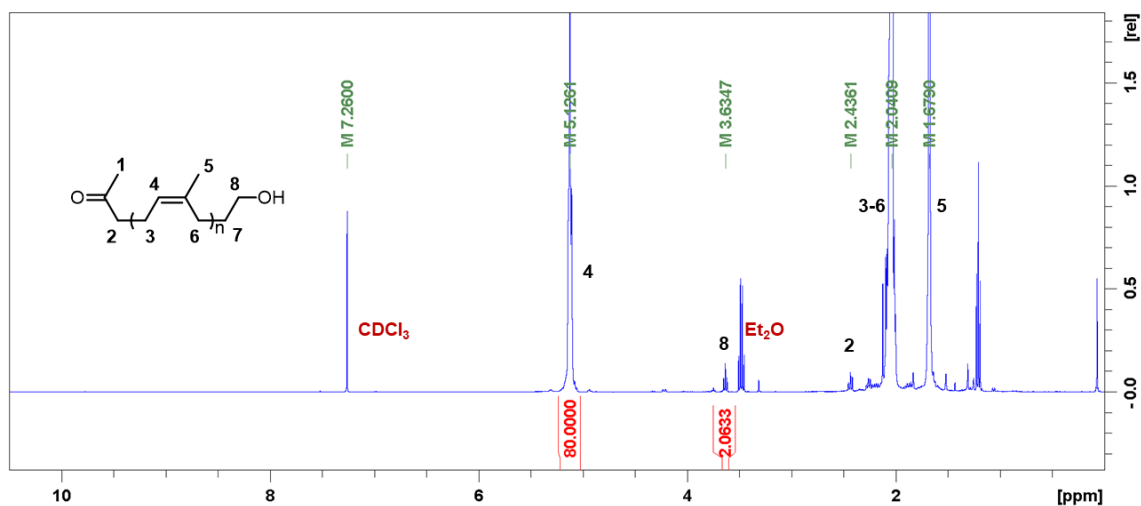


**Figure 4.** NMR spectrum of purified heterotelechelic keto/hydroxyl PI (PIOH). 15 mg of purified PIOH were dissolved into 500  $\mu\text{L}$  of  $\text{CDCl}_3$  and analyzed with a Bruker AVANCE III HD 400 MHz Spectrometer.

In parallel, we synthesized Maleimidohexanoic chloride by reacting maleimidohexanoic acid with oxalyl chloride. The purified product of the reaction was a brownish/orange powder (Fig. 5).



**Figure 5.** Visual aspect of purified Maleimidohexanoic chloride.

The  $^1\text{H}$  NMR spectrum of the purified product shows that protons from the “ $-\text{CH}_2$ ” groups in  $\alpha$  position of the carboxylic acid shifted from 2.30 ppm to 2.80 ppm, and that the broad peak around 1.61 ppm splits into two distinct peaks at 1.72 ( $-\text{CH}_2\text{CH}_2(\text{CO})\text{Cl}$ ) and 1.60 ppm ( $-\text{CH}_2\text{CH}_2\text{N}=\text{}$ ), confirming the identity of Maleimidohexanoic chloride (Fig. 6).

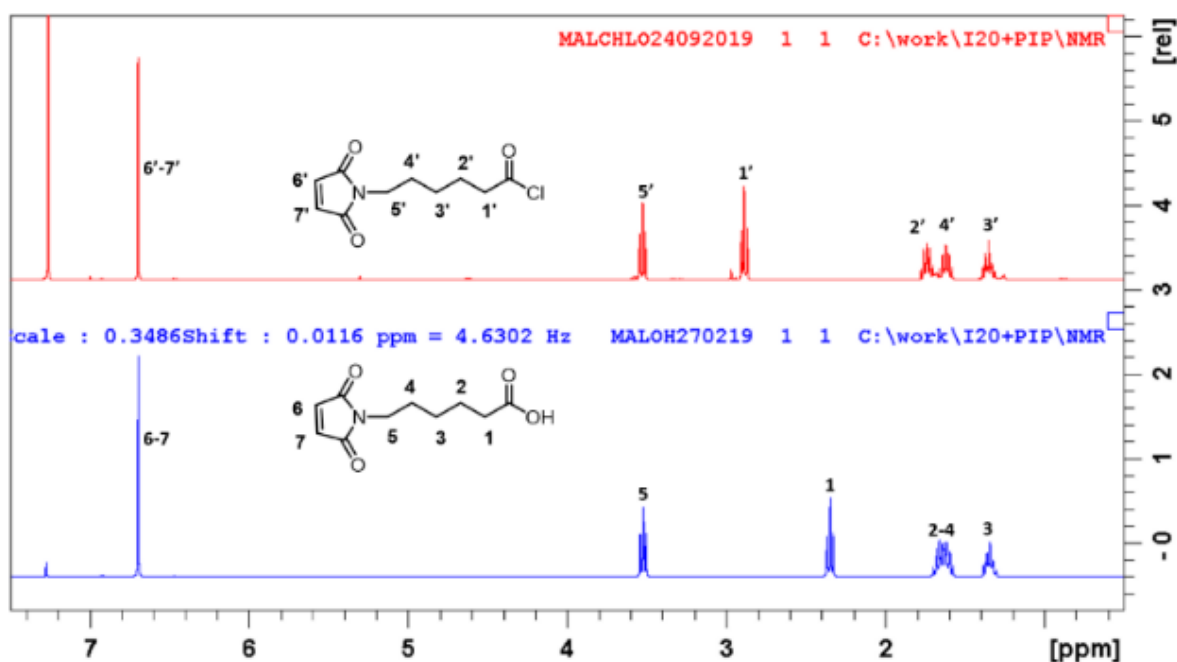


**Figure 6.** NMR spectrum of maleimido hexanoic chloride. Maleimido hexanoic acyl chloride was dissolved in 500  $\mu$ L anhydrous  $\text{CDCl}_3$ , then analyzed with a Bruker AVANCE III HD 400 MHz Spectrometer (Top spectrum in red). In parallel, 30 mg of maleimido hexanoic acid was analyzed under the same conditions (Bottom spectrum in blue).

Consecutive reaction of PI-OH with maleimide acyl chloride to obtain PI bearing a maleimido group as a chain end was successfully performed with a final yield of 90%. The N-polyisoprene-maleimide (PIMAL) structure was then characterized. <sup>1</sup>H NMR spectrum (Fig. 7) showed that the signal of the “-CH<sub>2</sub>” group in  $\alpha$  position of the hydroxyl, was totally shifted from 3.63 ppm (PIOH) to 4.03 ppm confirming the formation of the ester function. In addition, protons from the double bond of the maleimide group were visible at 6.67 ppm.

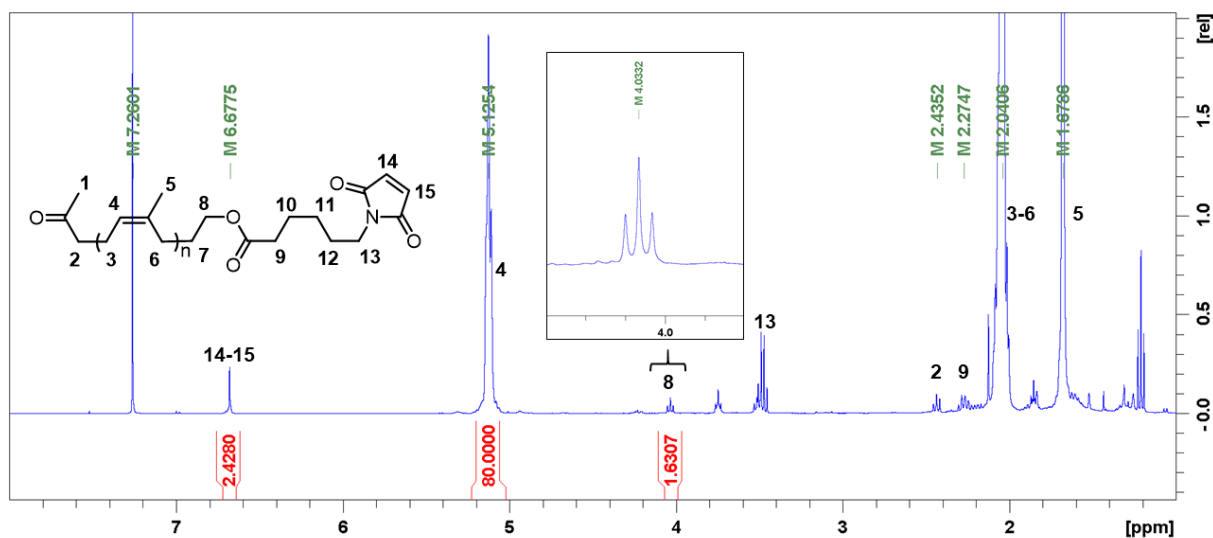


**Figure 7.** NMR analyses of purified N-polyisoprene-maleimide (PIMAL). NMR spectrum of PIMAL in CDCl<sub>3</sub>. 30 mg of dried PIMAL was dissolved into 1 mL CDCl<sub>3</sub>, then 500  $\mu$ L solution was analyzed by Bruker AVANCE III HD 400 MHz Spectrometer. Inset: zoomed region 3.8-4.6 ppm

Purified PIMAL was also analyzed with a Fourier Transform Infrared Spectrometer (FT-IR, Fig 8).

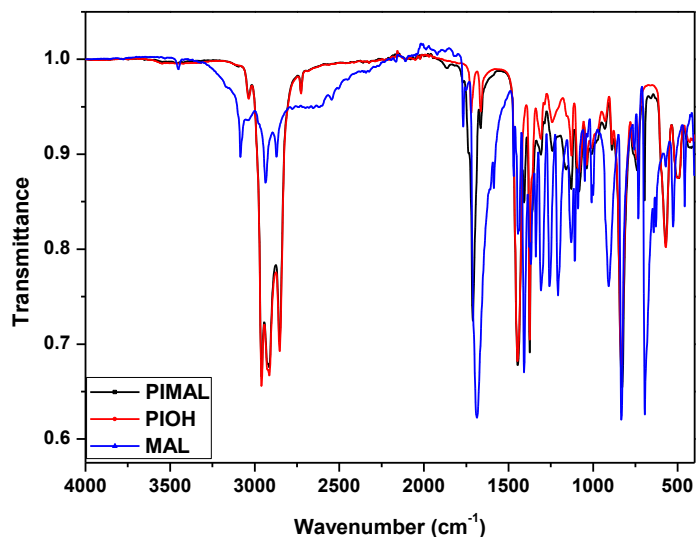


**Figure 8.** Comparison of infrared spectra of purified PIMAL, PIOH and Maleimide chloride. Purified PIMAL was analyzed with a Fourier Transform Infrared Spectrometer (FT-IR). PIMAL (black trace), PIOH (red trace), and Maleimide chloride (blue trace).

The purified PIMAL spectrum shows the presence of the stretching vibrations of -C-H from the PI backbone, and the bending vibration of -C-H of the cis double bond from the maleimide, confirming the grafting of the maleimide function at the end of the PI chains.

### 2.2.1.3. Screening for a solvent capable of solubilizing both I20 and PIMAL

After the preparation of the two blocks, the challenge was to find a solvent, or a mixture of solvents capable to solubilize both the hydrophobic PIMAL and the hydrophilic ELP.

PIMAL solubility was assessed by simple visual inspection of polymer solutions prepared in various solvents at a concentration of 50 mg/mL. The solution was agitated for several hours at room temperature.

The solubility of the polypeptide I20 at a concentration of 16 mg/mL was evaluated in different solvents. After 48 h at RT under agitation, the solution was pipetted out, filtered through 0.4  $\mu\text{m}$  nylon filter and the solvent evaporated. The dried residues were analyzed by gel electrophoresis to evaluate the protein content. A typical result is shown in Fig. 9. If there had been good solubility, the I20 polypeptide would have been present in fraction B, and absent from fraction A, which was not the case here.

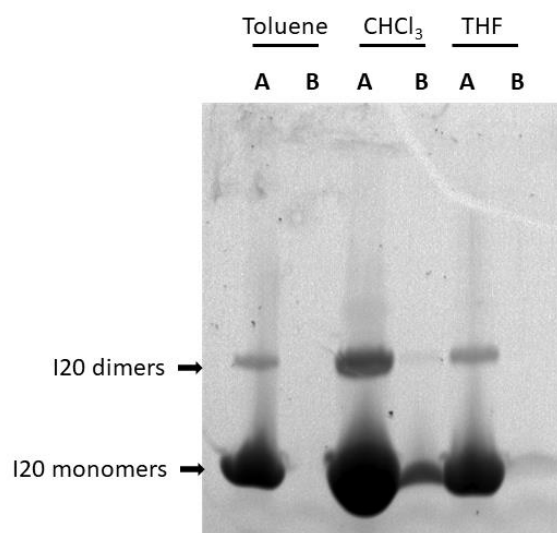


**Figure 9: Solubilization assays of I20 monitored by SDS-PAGE analysis. Non-solubilized (lanes A) and solubilized samples (lanes B) were analyzed by SDS-PAGE electrophoresis. Gels were stained with InstantBlue™. The loading buffer did not contain reducing agents.**

The results of the solubilization tests are summarized in table 1

**Table1. Solubilization assays**

	<b>PIMAL Solubilization</b>	<b>I20 Solubilization</b>
<b>Toluene</b>	<b>No</b>	<b>No</b>
<b>Chloroform</b>	<b>Yes</b>	<b>Traces (&lt; 10%)</b>
<b>Dichloromethane</b>	<b>Yes</b>	<b>No</b>
<b>Tetrahydrofurane</b>	<b>Yes</b>	<b>No</b>
<b>Cyclohexane</b>	<b>No</b>	<b>No</b>
<b>Methanol</b>	<b>No</b>	<b>No</b>

As expected from previous data from our laboratory, PIMAL was soluble in pure chloroform, dichloromethane and tetrahydrofurane. Unfortunately, ELP I20 was not soluble in these organic solvents, albeit at a low level (~10% of total polypeptide) in pure chloroform.

To go further, we looked for mixtures of solvents that were used to extract natural proteolipids from animal or plant tissues. Indeed, in mammals several proteolipids are particularly enriched in the myelin sheath of the central nervous system<sup>20,21</sup>. In the early fifties, researchers tried to purify these proteins from brains or spinal cords, and they found that mixtures of chloroform/methanol were the most efficient<sup>22</sup>. Indeed, they were able to purify the major myelin proteolipid protein which is a hydrophobic protein (GRAVY index = 0.55) containing four transmembrane segments and at least six palmitate groups covalently linked<sup>21</sup>.

We therefore tested different chloroform/methanol mixtures (1:1, 2:1 and 4:1, v/v) for solubilizing PIMAL and I20. Surprisingly, neither of them was directly solubilized by these mixtures. Therefore, PIMAL was first dissolved in pure chloroform, and then methanol was added drop by drop to reach the targeted ratio of 4:1. As for I20, it was solubilized directly in a mixture chloroform/methanol 1:1, and then chloroform was added to increase the ratio to higher values. Results are shown in Figure 10.

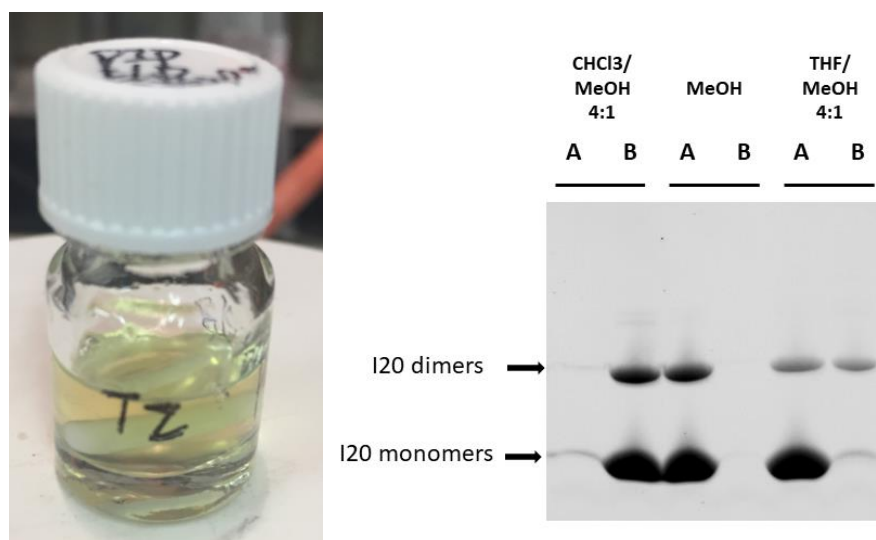


**Figure 10. Solubilization of PIMAL (right) and I20 (left) by chloroform/methanol mixtures. Total solubilization was assessed by visual inspection (right). Non-solubilized (lanes A) and solubilized samples (lanes B) were analyzed by SDS-PAGE electrophoresis. Gels were stained with InstantBlue™. The loading buffer did not contain reducing agents.**

These experiments demonstrated that a chloroform/methanol ratio of 4:1 was satisfactory for both molecules. The SDS-PAGE experiment shows that in the presence of this mixture of solvent, the majority of I20 was present in fraction B (> 95 % as estimated by densitometric analyzes of SDS-PAGE).

#### 2.2.1.4. Synthesis of I20-*b*-PI

Before the coupling reaction, the ELP I20 was reduced by a treatment with TCEP to cleave the intermolecular disulfide bridges that were formed between monomers, and therefore to generate free thiols. Because TCEP can't react with maleimide/sulfide, it will not decrease the conversion rate which could have been the case with other reducing agents such as dithiothreitol or  $\beta$ -mercaptoethanol. After this treatment, only trace amounts of dimers remained in the sample (Lane 2, Fig. 11).

The coupling of ELP I20 with the PI block was performed via a Michael addition involving the maleimide group end-grafted onto the PI and the thiol function of the C-terminal cysteine of the ELP (Scheme 1). After 20 hours of reaction, the chloroform/methanol solvent was evaporated, and the dried pellet was suspended in SDS-PAGE loading buffer that do not contains reducing agents. The progress of the coupling reaction was monitored by SDS-PAGE

analysis, because we hypothesized that the I20-*b*-PI copolymer has a lower electrophoretic mobility than that of I20. Figure 11 shows a typical result obtained for a reaction performed for 20 hours at room temperature with 50 mg of PIMAL and 16 mg of ELP I20 (molar ratio 5:1).

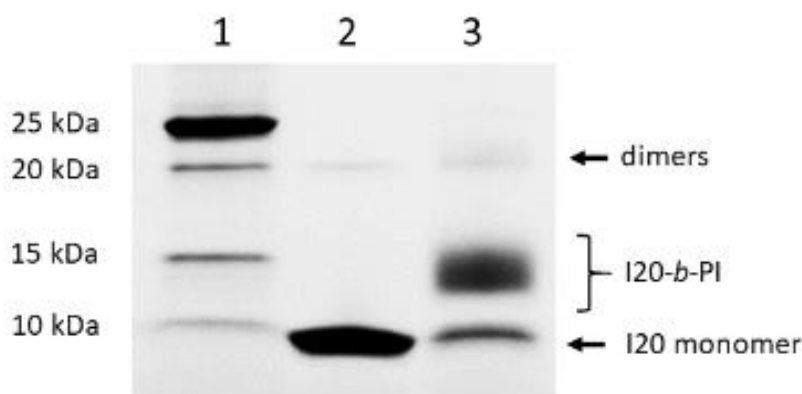


**Figure 11. SDS-PAGE analyses of the polypeptide I20 and of the copolymer I20-*b*-PI. Analyses of the reaction product. 1) Molecular mass standard. 2) I20 ELP reduced by TCEP treatment. 3) products obtained after 20 hours of reaction at room temperature.**

After the coupling reaction, we clearly see a decrease in the intensity of the band corresponding to the I20 monomer, and the appearance of a new band, the relative mobility of which, between 13 and 15 kg.mol<sup>-1</sup> by comparison with the protein standards, being between those of the I20 monomer (8.9 kg.mol<sup>-1</sup>) and dimer (17.8 kg.mol<sup>-1</sup>). We hypothesized that this new band corresponded to I20-*b*-PI. The fact that this band was slightly smearing can be explained by the dispersity of the PI block, so was the diblock. This apparent molecular mass is close to the 15 kg.mol<sup>-1</sup> expected after the coupling of the ~6 kg.mol<sup>-1</sup> PIMAL and the 8.9 kg.mol<sup>-1</sup> I20. Nevertheless, we would have expected that the diblock had a higher molar mass, close to 16 kg.mol<sup>-1</sup>, after the grafting of the ~7 kg.mol<sup>-1</sup> PIMAL on the 8.9 kg.mol<sup>-1</sup> I20 monomer. However, it has already been reported that the apparent mobility of hydrophobic proteins in SDS-PAGE, such as membrane proteins, differs from the theoretical one<sup>23</sup>. Indeed, the acylated human myelin proteolipid has a theoretical MW of 31.6 kg.mol<sup>-1</sup>, but an apparent MW of 25 kg.mol<sup>-1</sup> after SDS-PAGE analysis<sup>24</sup>.

Figure 11 also shows that not all the I20 reacted during the incubation period, because some ELP monomers and dimers were still detected on the gel (lane 3). Densitometric analyzes of the gel showed that the intensity of the I20-*b*-PI band represents around 60% of the total

intensity measured in the corresponding lane. We therefore sought for improvements. We varied the amount of TEA from 1.25 to 6.25%, the PIMAL/I20 molar ratios from 4:1 to 10:1, and the reaction time (Fig. 12) but these optimization trials only marginally improved the yield of I20-*b*-PI, which levelled off around 65-70%.

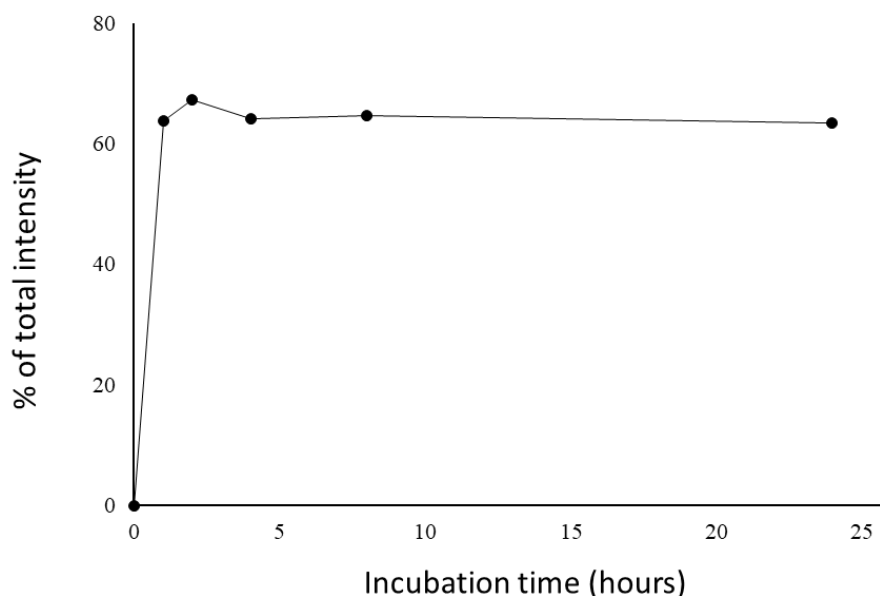


**Figure 12. Time-course study of I20-*b*-PI formation. Reaction time varied between 1 and 24 h. From each sample, 50  $\mu$ L was analyzed by SDS-PAGE. Densitometric analysis of the gel by Image Lab software allowed the quantification of each polypeptide band (I20 monomer, I20 dimer, and I20-*b*-PI). The total intensity/lane was set to 100%, and the calculated % for I20-*b*-PI was plotted.**

We therefore sought to develop a purification method to selectively enrich the I20-*b*-PI fraction.

#### **2.2.1.5. Purification of PI-*b*-I20**

At this step, our goal was to eliminate both the excess of PIMAL, and the monomers and dimers of free ELP I20 that did not react. This was achieved by several steps. After the reaction, the chloroform/methanol solvent was eliminated by evaporation, and the dried residues were recovered. We first sought to eliminate the unreacted PIMAL. To achieve this goal, the dried residues were washed three times for 3 hours with THF. The efficacy of these successive washing steps was first evaluated by visual inspection of the THF fractions, PIMAL being yellowish when solubilized in THF. We checked that the solution from the third wash was

uncolored. Then, the THF extracts were analyzed by proton NMR. These analyses confirmed that no significant traces of PIMAL were detected in the third wash (Figure 13).

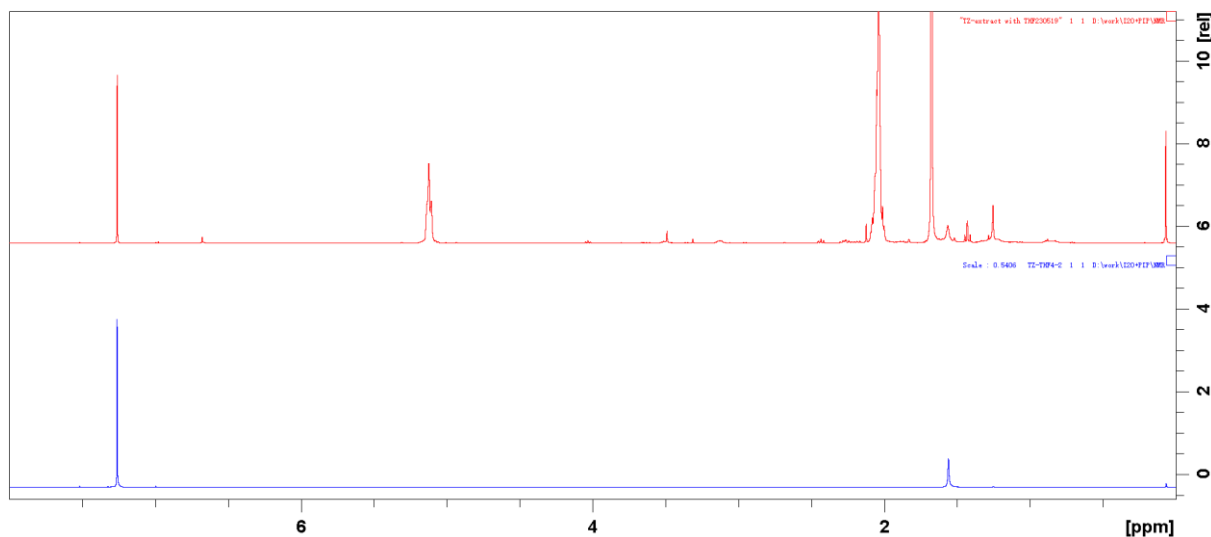


**Figure 13. Evaluation of the elimination of the unreacted PIMAL from the reaction product. After the coupling reaction, the dried product was washed three times with THF to eliminate the excess of unreacted PI. The washing fractions were collected, dried, and dissolved in deuterated THF for proton NMR analysis to determine their PIMAL content. Top: First THF wash. Bottom: Third THF wash.**

In parallel, the protein content of the THF extracts was analyzed by SDS-PAGE (Fig. 14).

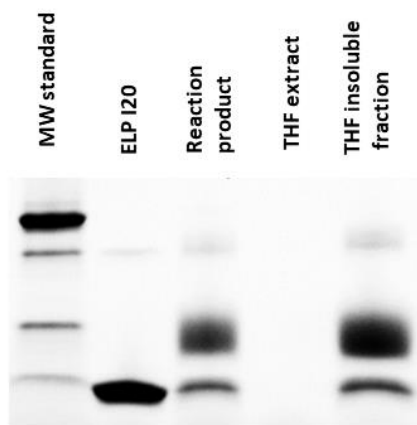


**Figure 14. SDS-PAGE analysis after reaction and extracted with THF. Pure I20 and a sample of the non-purified reaction product were analyzed as controls.**

This experiment demonstrates that neither the I20-*b*-PI, nor free I20, were solubilized during the THF extraction.

The next step was to eliminate the ELP I20 that did not react with PIMAL. Our first attempts were made by incubating the THF-insoluble fraction with cold water, as we hypothesized that the un-reacted I20 (monomers and dimers) would be solubilized in the cold-water fraction, because their Tts were around 20°C<sup>16,17</sup>, and that the I20-*b*-PI diblock would not be solubilized because of its increased hydrophobicity. However, our results showed that this step was not as efficient as expected (Fig. 15).

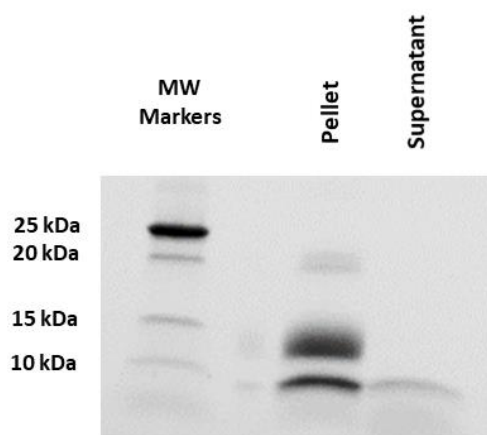


**Figure 15. Evaluation of the elimination of the unreacted I20 from the reaction product by cold-water.**

Cold-water treatment allowed only partial extraction of the free I20 monomers, roughly 50% of the sample content. In addition, none of the I20 dimers were extracted using this protocol. It thus appeared that after the reaction and the different successive steps of washing and drying of the samples, a fraction of the I20 was not water-soluble at a temperature below its Tt. This could be the consequence of the THF washes and drying steps that could have removed the water molecules closely linked to the polypeptide, and therefore preventing its further solubilization in water. A similar phenomenon has been reported for leucine-containing ELPs<sup>25</sup>. We therefore sought for other solvents, or mixtures of solvents, to remove ELP from the reaction mixture. We tested different HFIP/water and Ethanol/water mixtures and found that a solution of 70% of cold ethanol gave slightly better results than those obtained with the other mixtures (Fig. 16).

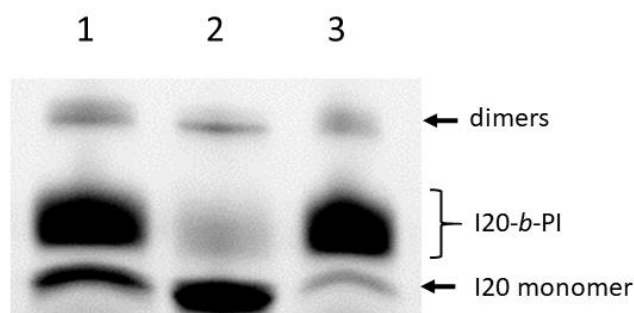


**Figure 16. Follow-up of the purification process. 1) reaction products after the THF extraction to eliminate the excess of unreacted PIMAL. 2) content of the supernatant from the ethanol wash at 4°C. 3) material that was not solubilized by cold ethanol.**

Densitometry analysis of this gel showed that the cold-ethanol fraction contains mostly I20 monomer, and only trace amounts of I20-*b*-PI (lane 2, Fig. 16). Finally, the purified fraction contained 89 % of I20-*b*-PI, and 11 % of I20 monomers and dimers (Lane 3, Fig.16). Despite our efforts to improve the purification process, this was the best result we could obtain. Finally, we evaluated the solubility of the I20-*b*-PI in different organic solvents (Table 2).

**Table 2. Solubilization of I20-PI by different solvents.**

Solvent	Respective % of I20- <i>b</i> -PI in the soluble (supernatant) and insoluble (pellet) fractions	
	Supernatant	Pellet
<b>Chloroform/methanol 4 :1</b>	<b>100%</b>	<b>0%</b>
<b>Dichloromethane</b>	<b>68%</b>	<b>32%</b>
<b>dimethylsulfoxide</b>	<b>0%</b>	<b>100%</b>
<b>dimethylformamide</b>	<b>91%</b>	<b>9%</b>
<b>Toluene</b>	<b>12%</b>	<b>88%</b>
<b>Cyclohexane</b>	<b>14%</b>	<b>86%</b>
<b>Diethyl ether</b>	<b>8%</b>	<b>92%</b>
<b>Ethyl acetate</b>	<b>10%</b>	<b>90%</b>
<b>Acetonitrile</b>	<b>11%</b>	<b>89%</b>
<b>DMF/THF 1 :4</b>	<b>95%</b>	<b>5%</b>

Beside the chloroform/methanol 4:1 mixture, the copolymer was soluble in DMF, in DMF/THF 1:4 mixture, and to a lower extent in DCM.

## 2.2.2. Characterization of I20-*b*-PI

### 2.2.2.1. Size exclusion chromatography

Purified I20-*b*-PI was first analyzed by size exclusion chromatography in DMF (Fig. 17).

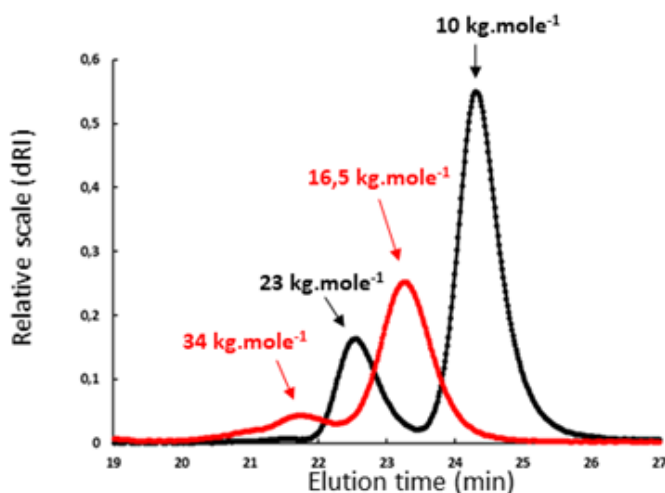


**Figure 17.** SEC traces of I20 and I20-*b*-PI using a RI detector. I20-*b*-PI (red line) and I20 (black line) were dissolved in DMF at a concentration of 5 mg/mL, and then filtrated through 0.45  $\mu\text{m}$  PTFE filters. 40  $\mu\text{L}$  of solution was injected into the column at 40°C.

The chromatogram obtained with the non-reduced I20 sample showed two peaks. The larger one representing 75% of the sample corresponds to the I20 monomers, and the smaller one corresponds to the I20 dimers. Their molar mass calculated by comparison with polystyrene standards were respectively 10 and 23  $\text{kg}\cdot\text{mol}^{-1}$ . The SEC trace for the purified I20-*b*-PI revealed one main peak with a retention time intermediate between those of the I20 monomers and dimers, and a calculated molar mass of 16.5  $\text{kg}\cdot\text{mol}^{-1}$  ( $D = 1.1$ ). A small shoulder can be noticed at low retention times corresponding most probably to some I20-*b*-PI dimers (34  $\text{kg}\cdot\text{mol}^{-1}$ ). It should be noted that the proportion of these dimers were lower after SDS-PAGE analysis (see lanes 3 Fig. 11 and Fig. 16), strongly suggesting that they are formed by non-covalent intermolecular bonds, such as hydrophobic inter-chain interactions mediated by the PI moiety.

### 2.2.2.2. Infrared spectroscopy

The IR spectra of I20, PIMAL and I20-*b*-PI were recorded and compared (Figure 18).

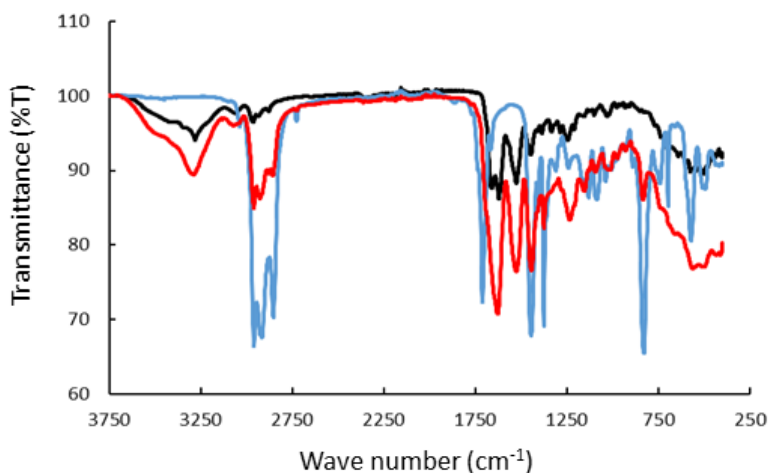


**Figure 18. Infrared spectra of ELP I20, PIMAL and I20-*b*-PI. 1 mg of dried I20, PIMAL and purified I20-*b*-PI were analyzed at room temperature by infrared with a Bruker VERTEX 70. The corresponding traces of I20 (black), PIMAL (blue) and I20-*b*-PI (red) were superimposed for comparison**

After the coupling reaction, stretching vibration of  $\text{-CH}_3$  ( $2960\text{ cm}^{-1}$ ) and  $\text{-CH}_2\text{-}$  ( $2914\text{ cm}^{-1}$ ,  $2853\text{ cm}^{-1}$ ) of PI were detected in the I20-*b*-PI compound. In addition, the reaction between the thiol function of I20 and the double bond of PIMAL led to a shift of the stretching vibration of ketone to  $1628\text{ cm}^{-1}$ , and to the disappearance of the bending vibration of  $\text{-C-H}$  cis double bond from maleimide. Altogether, these results strongly suggest that the reaction took place between the thiol function of the I20 cysteine and the double bond of the maleimide.

### 2.2.2.3. NMR analyses

To confirm the covalent linkage between the I20 and PIMAL blocks, we performed  $^1\text{H}\text{-}^{13}\text{C}$  heteronuclear single quantum correlation (HSQC) of the I20-*b*-PI copolymer. The analysis is shown in Figure 19.

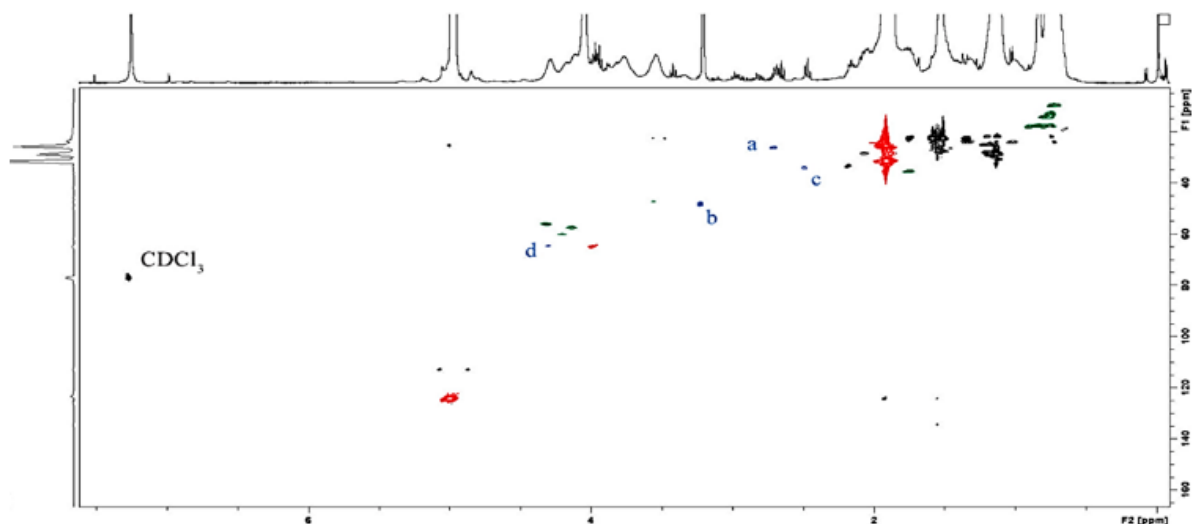


**Figure 19. 2D HSQC NMR spectra of I20-*b*-PI showing the correlation between the two blocks in CDCl<sub>3</sub>.**

Cross-peaks corresponding to the I20 part (green) and to the PIMAL part (red) are indicated. First, it must be noticed the total disappearance of the signal corresponding to the protons of the double bond from maleimide that was present in the PIMAL compound (peaks 14-15, Fig. 7) showing a quantitative conversion. In addition, the reaction between the thiol function of I20 and the double bond of PIMAL led to the appearance of new peaks corresponding to the pyrrolidine-2,4-dione moiety. The cross-peaks in blue at (a)  $\delta$  2.71/26.6 ppm, (b)  $\delta$  3.24/49.6 ppm, (c)  $\delta$  2.49/34.1 ppm, (d) 4.31/65.0 ppm were assigned to the link between the maleimide of PIMAL and the cysteine of I20.

#### 2.2.2.4. Circular dichroism analyses

Circular dichroism (CD) is a technique used for rapid determination of the 2D structure of proteins. It is based on the unequal absorption of left-handed and right-handed circularly polarized light when it passes through a solution containing the protein. Indeed, numerous studies have shown that the thermosensitivity of ELPs is the consequence of conformational changes between the soluble and aggregated state<sup>26-28</sup>. Usually, the secondary structure of soluble ELPs is a mix of random-coiled and  $\beta$ -sheets conformation, whereas the aggregated forms (above Tt) display a more ordered structure with predominant type-2  $\beta$ -turns<sup>27</sup>.

To investigate the secondary structure of I20 and I20-*b*-PI, we run CD analyses at 15°C (below the Tt of ELP I20) and 30°C (above Tt). Spectra were then analyzed using the BeStSel software<sup>29,30</sup>. Results are shown in Figure 20.

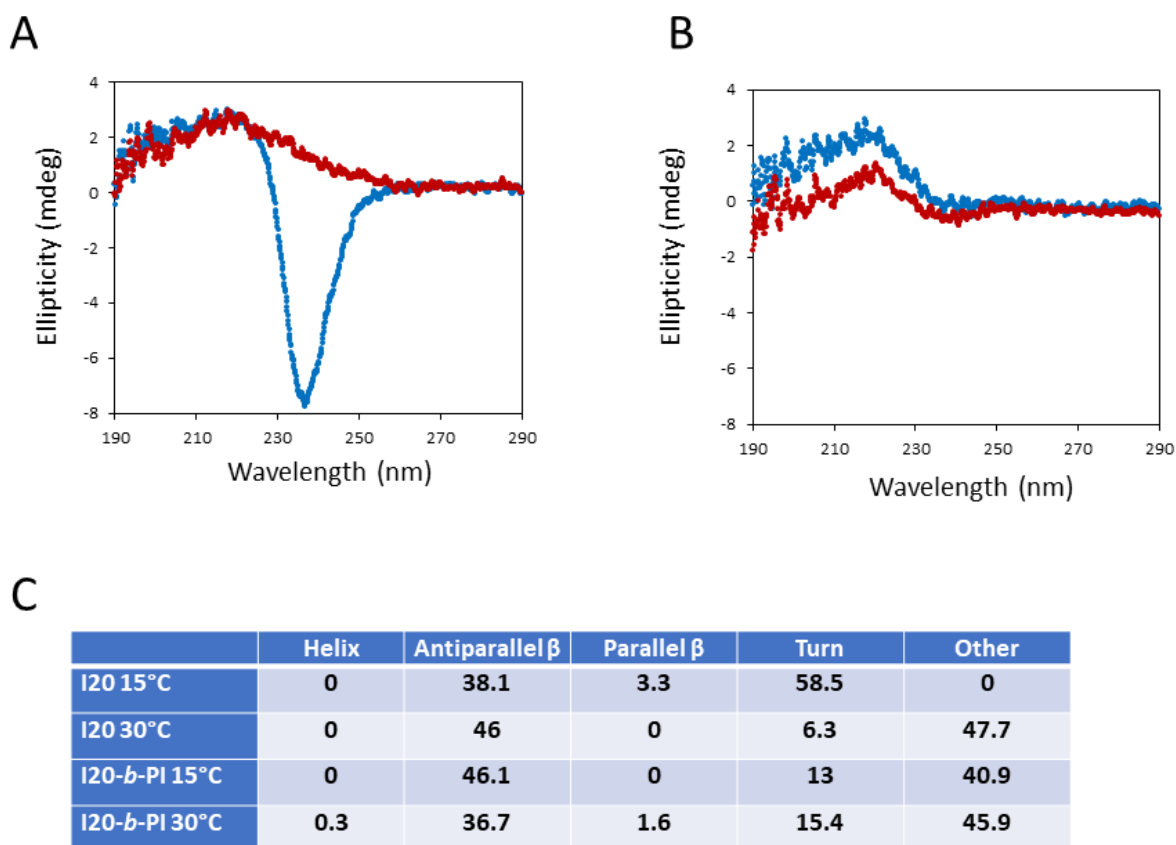


**Figure 20: Circular dichroism spectra of 10  $\mu$ M solutions of A: I20, B: I20-*b*-PI. The spectra were recorded at 15°C (blue) and 30°C (red). C: structure prediction by BESTSEL application.**

The spectrum obtained for the ELP I20 at low temperature is somewhat unusual for an ELP. Indeed, for most ELPs studied so far, the CD spectra at low temperature (below  $T_t$ ) are characterized by a large negative peak around 190-200 nm, which is characteristic of random-coiled structures. This is not the case for I20. We observed a major negative peak around 235 nm, and the spectra analysis showed that the main secondary structures are antiparallel  $\beta$  strands (38%) and  $\beta$  turns (58.5 %). This strongly suggests that this small hydrophobic ELP adopts a specific structure at low temperature. Interestingly, we previously observed that these ELPs containing isoleucine, (VPGIG)<sub>20-60</sub>, display a very specific behavior when stored for long period at 4°C: they tend to aggregate and precipitate irreversibly. This behavior has never been observed for any other ELP series made in our laboratory. Interestingly, a similar behavior has also been reported for ELPs containing leucine as the guest amino acid. It was demonstrated that these hydrophobic ELPs tend to form aggregates that were resistant to disassembly at low

temperature<sup>25</sup>. Unfortunately, CD measurements were not made with these leucine-containing ELPs to elucidate their secondary structure.

Apart from this unusual structuration of I20 at low temperature, when the solution was heated at 30°C, a deep reshuffle of the structure took place that was characterized by the disappearance of the negative peak around 235 nm. The spectrum analysis revealed an important decrease in the proportion of  $\beta$  turns (from 58.5 to 6.3 %). This structural change is consistent with previous studies showing that the thermosensitivity of ELPs is governed by drastic changes in secondary structures, leading to aggregation at temperature above their Tts<sup>31</sup>.

Different results were obtained for I20-*b*-PI. At low temperature, we did not observe a large negative peak around 235 nm. In addition, no significant changes were observed upon heating, only a small decrease in ellipticity in the 190-230 nm region. Indeed, whatever the temperature of the solution, the prediction for secondary structures was around 40% of antiparallel  $\beta$  sheets and 15% of  $\beta$  turns. Finally, the spectra obtained for I20-*b*-PI were highly similar to that of I20 at 30°C. From these results, we can conclude that the grafting of one molecule of PI at the C-terminal end of I20 led to a conformational change, and that the corresponding secondary structure is similar to that adopted when the unmodified ELP is incubated at a temperature above its Tt.

### **2.2.3. Self-assembly of I20-*b*-PI in aqueous solvent**

#### **2.2.3.1. Determination of the critical aggregation concentration (CAC)**

We chose the nanoprecipitation technique to obtain I20-*b*-PI nanoparticles. Briefly, purified diblocks were solubilized in DMF/THF solution at a concentration of 2 mg/mL, and then water was added drop by drop to form the nanoparticles. After extensive dialysis to remove the organic solvent, the resistance of the nanoparticles to dilution was tested by serial dilution. The critical aggregation concentration (CAC) of the copolymer was measured by a fluorometric method using pyrene as the fluorophore<sup>32-34</sup>. Results are shown in Figure 21.

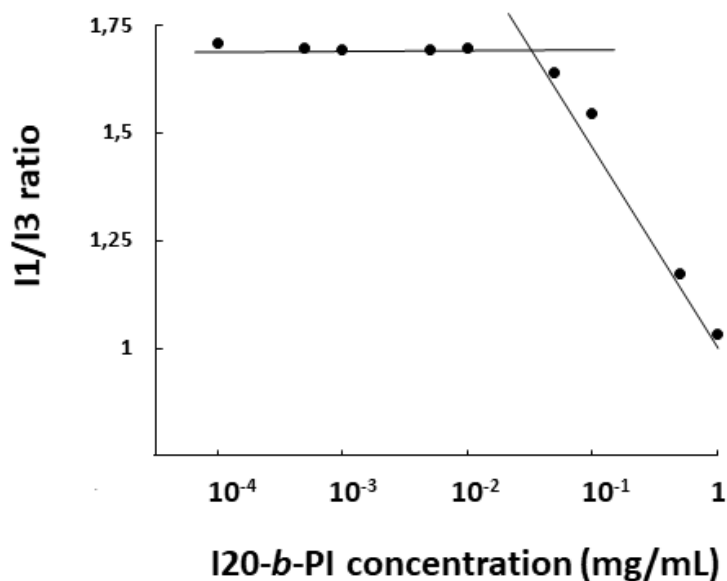


**Figure 21. CAC measurement of I20-*b*-PI. CAC was calculated by measuring the ratio of the fluorescence intensities of pyrene (10 $\mu$ M) measured at 373 nm (I1) and 385 nm (I3). This ratio was plotted against the I20-*b*-PI concentration to calculate the CAC.**

The CAC value was calculated to be 50  $\mu$ g/mL, which corresponds to a molar concentration of 3.5  $\mu$ M. This low CAC value can be explained by the presence of the very hydrophobic PI moiety in the copolymer, in agreement with previous studies which showed that both the sizes of the hydrophobic block, and the hydrophilic/hydrophobic ratio influence the CAC value<sup>35,36</sup>. According to previous studies using block polymers mPEG-*b*-p(HPMA-Bz) with different size of PEG and ratio of hydrophilic/hydrophobic, both the size of the hydrophobic block and the hydrophilic/hydrophobic ratio determine the CAC value<sup>35</sup>. In addition, the CAC value measured for I20-*b*-PI is in the same range (3-5  $\mu$ M) as that measured for ELP-C14 diblocks<sup>36</sup>.

### **2.2.3.2. Characterization of the nanoparticles by dynamic light scattering (DLS)**

The hydrodynamic radius of the particles obtained after nanoprecipitation was measured by DLS at 10°C, below the Tt of I20. A typical result is shown Figure 22.

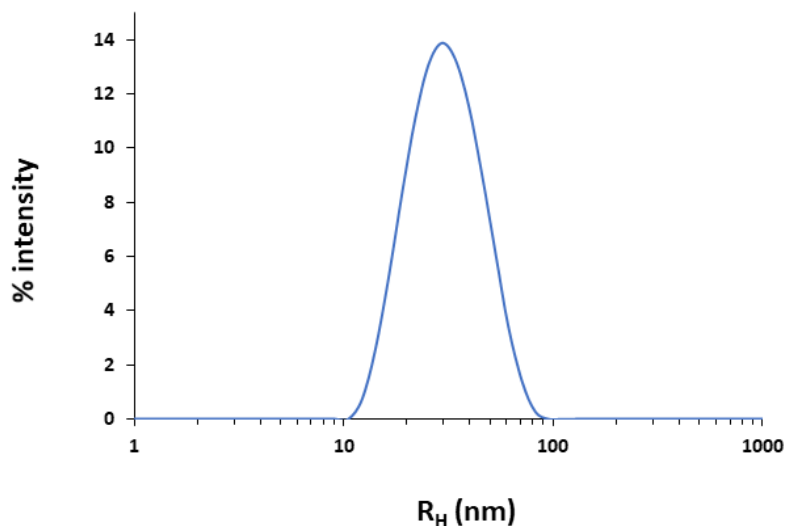


**Figure 22.** DLS analysis of particles obtained by nanoprecipitation of I20-*b*-PI. Diblock concentration was 0.27 mg/mL.

Independent experiments were performed with four different batches of I20-*b*-PI. The mean  $R_H$  of the particles was  $39 \pm 5$  nm, and the PDI was  $0.132 \pm 0.011$ . Owing to the size of the nanoparticles, we raised the hypothesis that they could correspond to micelles, with the highly hydrophobic PI block inside the structure and the ELP moiety exposed at the surface toward the aqueous solvent.

Thereafter, we studied the stability of the nanoparticles. This was first evaluated by incubating them for up to 46 days at 4°C (Table 2).

	Initial	7 days	25 days	28 days	46 days
DCR	1621	1658	1806	1771	1815
PDI	0.130	0.256	0.242	0.240	0.250

**Table 2.** Stability of the I20-*b*-PI upon storage at 4°C. Nanoprecipitated I20-*b*-PI sample was stored for 46 days at 4°C. Measurement were made at 25°C. Scattered intensity (derived count rate, DCR) and polydispersity (PDI) were recorded.

We observed a slight increase in the PDI value during the first week, from 0.13 to 0.24, but then this index did not change substantially. Concerning the scattered intensity (DCR), we measured a modest increase (+ 12%) during the period studied. Altogether, these data suggest

that no significant aggregation took place, and therefore that the nanoparticles are stable in water when stored at low temperature.

Next, we studied the behavior of the nanoparticles upon heating. Indeed, the ELP moiety of the diblock has a  $T_t$  around  $19^\circ\text{C}$ <sup>16,17</sup>, and we wanted to see if heating the nanoparticles will trigger their aggregation. The DCR and PDI remained constants during the temperature ramp indicating that no significant aggregation took place (Fig. 23).

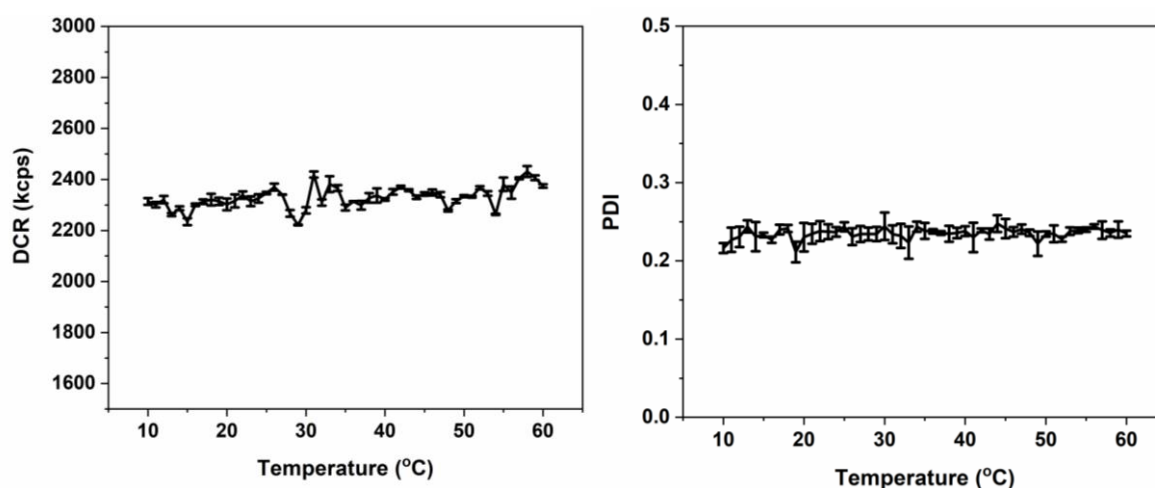


**Figure 23. Stability of the I20-*b*-PI nanoparticles upon heating. A water solution containing I20-*b*-PI nanoparticles was analyzed by DLS. Scattered intensity (derived count rate, DCR) and polydispersity (PDI) of the sample were plotted as a function of temperature upon heating. Results are mean values  $\pm$  SD (n=3)**

These results strongly suggest that the intrinsic thermosensitivity of I20 did not have a significant influence on the I20-*b*-PI nanoparticles formation and stability. Indeed, this is consistent with the data obtained by CD. We previously showed (paragraph 2.2.4.4) that the secondary structure of I20-*b*-PI is similar when the sample is incubated at a temperature below or above the  $T_t$  of ELP I20. Therefore, a change in the nanoparticle size due to a structural rearrangement of the ELP moiety was not expected.

To understand the stability of the nanoparticles in water, we measured their surface charge. Zeta value was measured to be around  $-33$  mV (Fig. 24).

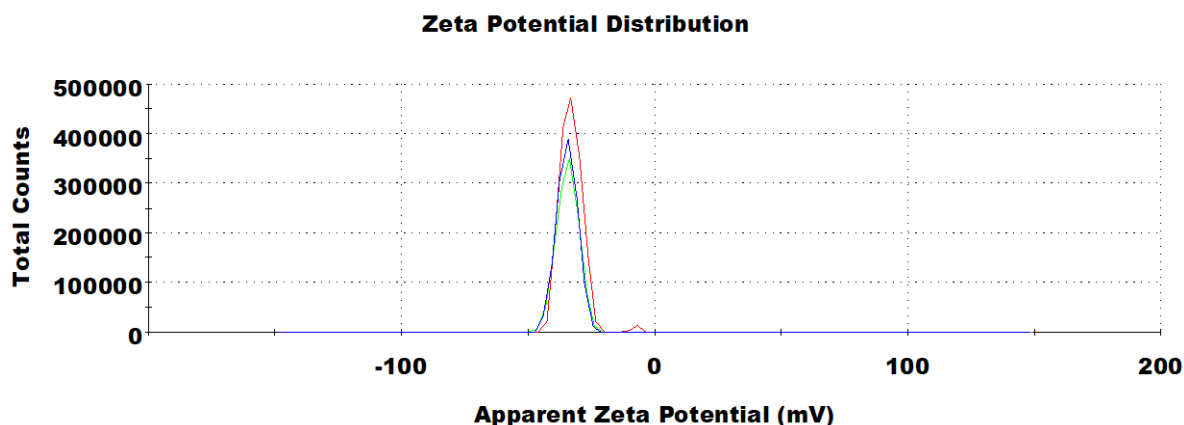


**Figure 24. Zeta measurement of I20-*b*-PI nanoparticles. Zeta measurement was done with a Nano ZS instrument (Malvern U.K.) using the signal processing M3-PALS technique. Zeta potential range was > +/- 500 mV, and maximum sample concentration was 40% w/v. Data were analyzed with the Zetasizer software. The figure shows the results obtained after three measurements of the same sample.**

This negative value explains why the nanoparticles are quite stable when stored in water. However, the presence of negative charges at the surface of the nanoparticles is not straightforward. Indeed, I20 which is exposed at the surface of the nanoparticles, does not contain any negatively-charged amino acid in its sequence such as aspartic, glutamic acid or histidine. The only charge might come from the N-terminal amine, and therefore would be expected to be a positive one. However, the average pKa of the N-terminal amine of proteins is generally in the 7–8 range<sup>37</sup>, and therefore this group should not be significantly charged in water solution. An explanation for the negative Zeta value of hydrophobic materials has already been made. Indeed, it has been previously demonstrated that when a hydrophobic material is placed in water, the OH<sup>-</sup> ions which are present in solution bind to the interface of the material, and therefore this layer of negatively charged ions provides a negative charge on the particle surface<sup>38</sup>.

Finally, we evaluated the stability of the nanoparticles in PBS buffer, which is more biologically relevant than pure water. Results of the DLS measurement are shown in Figure 25.

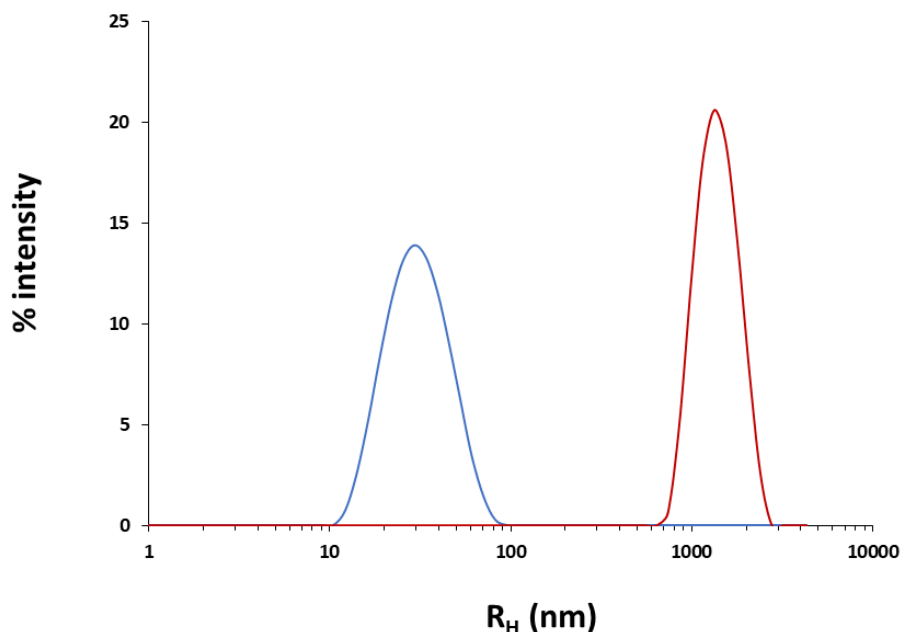


**Figure 25. DLS analysis of particles obtained by nanoprecipitation of I20-*b*-PI. Sample in water (blue trace) and same sample in PBS (red trace). Diblock concentration was 0.27 mg/mL**

PBS addition to the solution containing the nanoparticles immediately triggered their aggregation in particles of about 1.2  $\mu\text{m}$  in radius. As shown previously, the I20-*b*-PI nanoparticles are negatively charged in water, owing to the presence of an  $\text{OH}^-$  layer at their surface. When salts are added, this negative layer of hydroxide ions is screened, and the hydrophobic nanoparticles start to aggregate. Of course, we will have to take this phenomenon into account if we want to find a biomedical application for our nanoparticles.

### **2.2.3.3. Morphology of I20-*b*-PI nanoparticles**

The morphology of the I20-*b*-PI nanoparticles was also observed by TEM (Fig. 26) and AFM (Fig. 27).

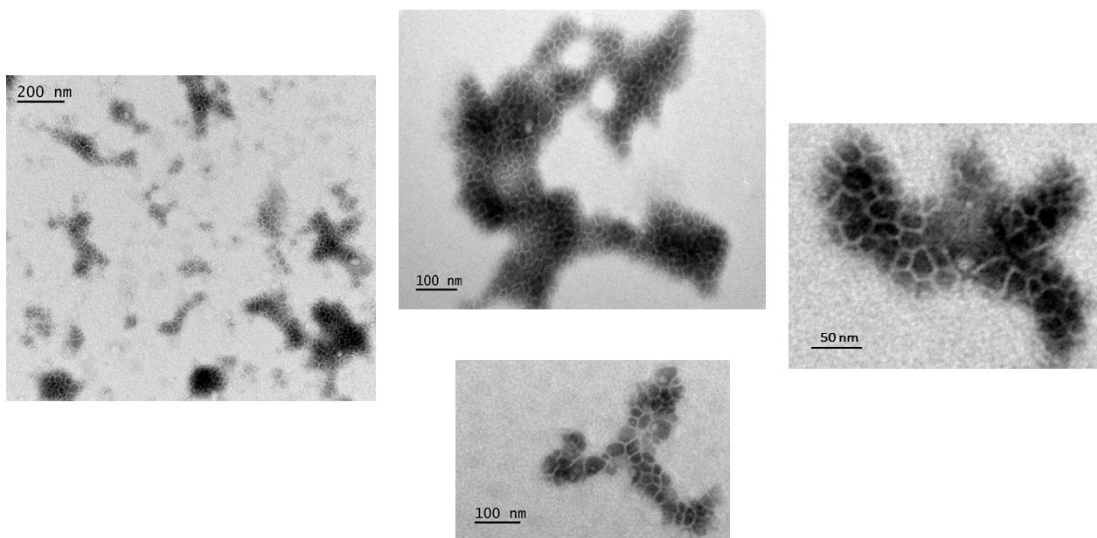


**Figure 26. TEM images of I20-*b*-PI nanoparticles at different magnification.**

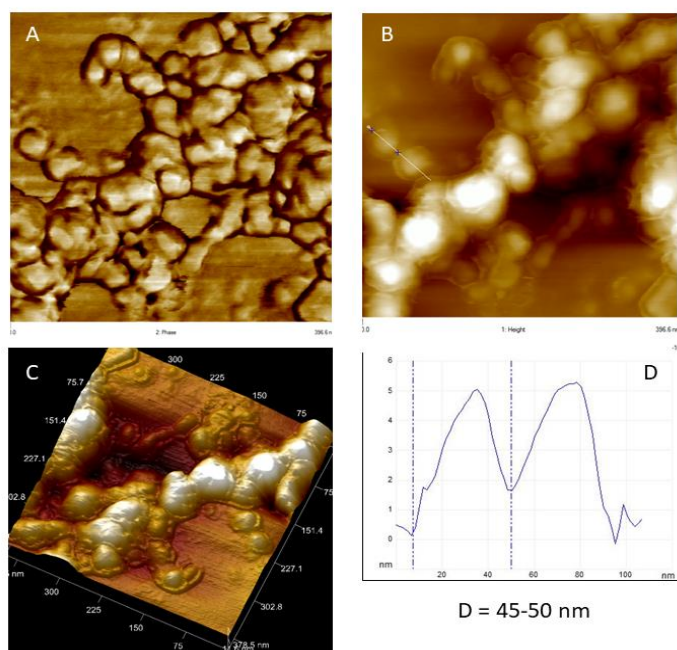


**Figure 27. AFM images of I20-*b*-PI nanoparticles. Phase contrast (A) and Height contrast (B) AFM images of I20-PI nanoparticles; (C) 3-D projection of particles combining height and phase channels; (D) selection profile of the AFM image along the white line in panel B. The high length to height ratio of the particles is in agreement with a micelle-like morphology that has collapsed during the drying step**

Particles ranging between 30 and 50 nm in radius can be seen with the two techniques, a range of size similar to that measured by DLS. The particles were aggregated as a consequence of the dehydration process during sample preparation. TEM images show particles constituted by a black core, most probably made of the PI block which is more stained by osmium because of its reactivity with the double bonds, surrounded by a clearer ring made of the ELP block that has a low electron density.

#### 2.2.3.4. Encapsulation and release of the hydrophobic dye Nile red

The capacity of the nanoparticles to encapsulate the lipophilic stain Nile red was also evaluated. I20-*b*-PI nanoparticles in water were incubated for 24 h with a Nile red solution, and then fluorescence of the sample was measured (Fig. 28).

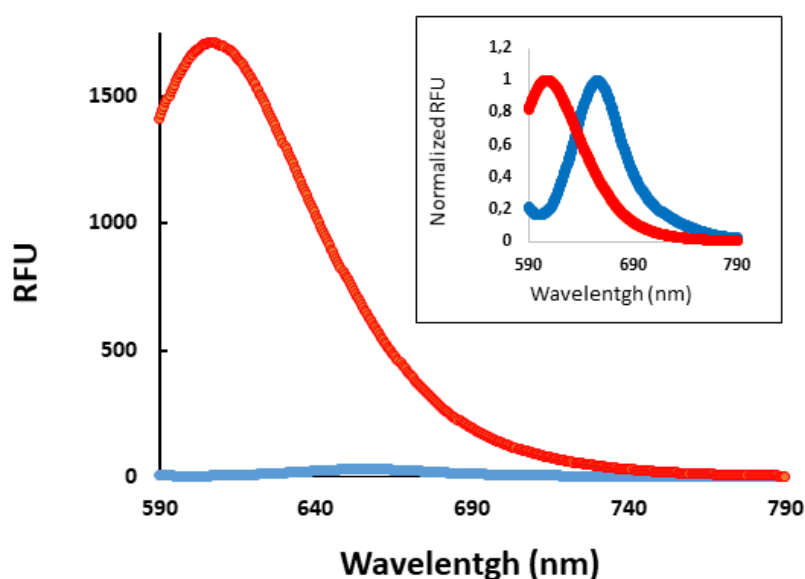


**Figure 28. Encapsulation of the lipophilic stain Nile red. Fluorescence of a Nile red solution in water (blue), and with I20-*b*-PI nanoparticles (red). Relative data to the maximal value of each sample are shown in the inset.**

When incubated in water, Nile red was barely fluorescent, with 32 relative fluorescence units (RFU) at its maximal wavelength emission of 654 nm. After incubation with I20-*b*-PI nanoparticles, the fluorescence intensity increased dramatically to 1710 RFU. In addition, the maximal wavelength emission shifted from 654 nm to 607 nm in the presence of the nanoparticles (inset Fig. 28) demonstrating that the dye was in a hydrophobic environment<sup>39</sup>. This experiment shows that the I20-*b*-PI nanoparticles can efficiently load a hydrophobic molecule.

Nile red release was studied by placing the loaded nanoparticles into a dialysis device, and by measuring the fluorescence at 607 nm at different times (Fig. 29).

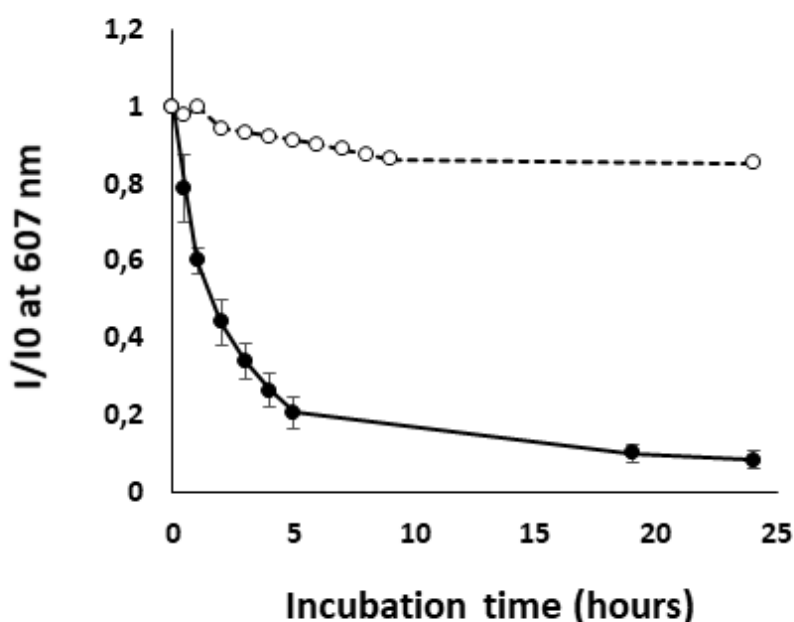


**Figure 29.** Nile red release from I20-*b*-PI nanoparticles. 1 mL of Nile red-loaded particles (0.27 mg/mL) were placed in a dialysis device and incubated in 1 L of water at 20°C. The emission of fluorescence at 607 nm was measured at different time points. Data are mean of three independent experiments  $\pm$  SD (●). As a control the fluorescence of a suspension of Nile red-loaded particles at same concentration (0.27 mg/mL) was monitored during 24h (○).

We measured a 40% decrease in the fluorescence intensity during the first hour, and then a slower decrease. After 5 h and 24 h of dialysis, the fluorescence intensities of the samples were

respectively 20% and 8% of the initial value. To control that this decrease in fluorescence was not due either to bleaching of Nile red nor to nanoparticles dissociation during the experiment, we also incubated a suspension of Nile red loaded I20-*b*-PI nanoparticles for 24 h without dialysis. We showed that under this condition the decrease in fluorescence was low, with more than 91% of the initial fluorescence intensity remaining after 5 h of incubation, and still 85% of the initial fluorescence intensity after 24 h. Altogether, these data show that a hydrophobic drug-model can be efficiently released from the I20-*b*-PI nanoparticles.

#### **2.2.4. Conclusion**

In this work, we successfully coupled poly(1,4-*cis*-isoprene) obtained from natural rubber, and an elastin-like polypeptide produced by recombinant expression in bacterial cells. After its synthesis, this bio-based diblock was characterized by different physico-chemical techniques such as SEC, NMR and IR. The secondary structure of this “proteolipid” was determined by CD. The self-assembly of this I20-*b*-PI polymer was triggered by nanoprecipitation in water and we obtained nanoparticles, which were most probably micelles, of 30–45 nm of  $R_H$ . The corresponding CAC was low (50  $\mu\text{g/mL}$ ) and the nanoparticles were stable when stored in water at low temperature. We also demonstrate that they can encapsulate and release a hydrophobic dye.

Concerning the potential biomedical applications of this material, we cannot obviously use it for drug delivery by injection into the blood stream. In this case, the nanoparticles will rapidly aggregate because of the salt concentration of human serum (around 150 mM NaCl), and they will be therefore be rapidly eliminated from the body. In addition, the injection into veins of aggregated particles can trigger a strong unwanted immunological response against the injected material<sup>40</sup>.

However, aggregation can be a benefit for other applications such as drug depot. In a previous study<sup>41</sup>, “aggregated ELPs” were injected into rat joint, and the results were compared with injection of “soluble ELPs”. The biodistribution was analyzed through following the radiolabel <sup>14</sup>C ELP. Data showed that aggregated ELPs have a joint half-life that is over 25-fold longer compared to soluble, non-aggregating ELPs. Moreover, the aggregating ELP did not appear to accumulate in the peripheral organs thereby diminishing the possibility of side-effects.

We can therefore foresee to use our material to obtain hydrophobic drug depot after injection into human tissues. After encapsulation of a hydrophobic drug into the I20-*b*-PI particles, and

injection into the human body, the saline concentration of serum will trigger their rapid aggregation at the subcutaneous or intramuscular injection site. This will lead to the formation of a drug depot which will gradually release the encapsulate drug, which could be an anticancer drug, a hydrophobic antibiotic or even an antigen for immunization purpose<sup>42-46</sup>.

Another application would be to use this rubber-based material in tissue repair strategies. Indeed, such material could be used to replace specific rubbery tissues such as intervertebral discs<sup>47</sup>.

This chapter demonstrated that the I20-*b*-PI biomaterial, although being of interest for some biomedical applications, is somewhat restricted in use owing to its high hydrophobicity and its tendency to aggregate when placed in a solution containing physiological salt concentrations. To circumvent this problem, we thought to use a more hydrophilic ELP block, but it appeared impossible to find a solvent that would allow the simultaneous solubilization of the hydrophilic ELP and the very hydrophobic PI to achieve the coupling reaction. Indeed, attempts were previously made in our laboratory by Jérémie Grange to couple PI molecule with BSA, which is a hydrophilic protein<sup>48</sup>. Emulsions were formed during the coupling reaction between the PI solubilized in toluene and BSA solubilized in phosphate buffer. However, although some kind of visual changes occurred into the reaction vial, it has not been possible to determine if the reaction had taken place.

In our quest to obtain nanoparticles capable of encapsulating hydrophobic drugs, and which do not aggregate in saline buffers, we have chosen to construct diblock proteolipids made up of rather hydrophilic ELPs and short lipids such as fatty acids. This is the subject of the next chapter.

## 2.3. Experimental procedures

### 2.3.1. Production and purification of ELP I20

Production and purification of ELP I20 was performed as already described<sup>16</sup>. Briefly, the clone R151, which is an *Escherichia coli* BLR strain ( $F^- ompT hsdS_B(r_B^- m_B^-) gal lac ile dcm \Delta(srl-recA)::TnI0(tet^R)(DE3)$ ) containing a pET44a vector with the I20 DNA coding sequence, was cultured overnight at 37°C in a rotary shaker at 200 rpm in 50 mL of lysogeny broth (LB) medium (1% bacto tryptone, 1% yeast extract, 0.5% NaCl) supplemented with 100 µg/mL ampicillin. This seed culture was then inoculated into 0.95 L of LB medium supplemented with glucose (1g/L) and ampicillin (100 µg/mL), and cells were cultivated at 37°C and 200 rpm. When the OD<sub>600nm</sub> reached a value close to 0.8, isopropyl β-D-thiogalactopyranoside (IPTG) was added to a final concentration of 0.5 mM, and the temperature of the incubator was decreased to 25 °C. After 12 h, the culture was harvested by centrifugation at 6 000 g and 4 °C for 15 min, and the cell pellet was suspended with 10 mL/g wet weight in phosphate buffer saline (PBS) buffer (137mM Sodium Chloride, 10mM phosphate, 2.7mM Potassium Chloride; pH is 7.4). Cells were then lyzed by sonication on ice, to avoid heating of the solution that would lead to precipitation of the ELP if the T°>Tt. Thereafter the insoluble debris were removed by centrifugation at 10 000 g and 4 °C for 30 min. The cleared lysate was subjected to three successive cycles of Inverse Transition Cycling (ITC)<sup>18</sup>. Briefly, ELP was precipitated at 30 °C and centrifuged at 10 000 g and 25 °C for 30 min (“warm spin”). The ELP-containing pellets were dissolved in cold water and the insoluble proteins were eliminated by centrifugation for 15 min at 10 000 g and 4 °C (“cold spin”). The protein content of the purified ELP I20 solutions was measured by spectrophotometry at 280 nm with a NanoDrop 1000 (ThermoScientific). The parameters used to determine the ELP I20 concentration were as follows: molecular mass of 8.9 kDa, and molar coefficient extinction of 5500. These parameters were obtained with the application ProtParam (<https://web.expasy.org/protparam/>) using the theoretical amino acid sequence of the polypeptide. Finally, the purified I20 was dialyzed against ultrapure water at 4 °C (Spectra Por7, MWCO1000, Spectrum Laboratories), and then lyophilized.

Follow-up of the purification steps was performed by SDS-PAGE analyses. Polypeptide-containing samples were mixed with the loading buffer (LB2X, 65.8mM Tris-HCl, pH 6.8, 26.3% (w/v) glycerol, 2.1% SDS, 0.01% bromophenol blue) and loaded onto 4–20% gradient

acrylamide gels (BioRad). Electrophoreses were performed in TGS buffer (25 mM Tris, 192 mM glycine, 0.1% SDS, pH 8.6). After migration, protein bands were revealed by the stain-free method using a Gel Doc apparatus (Biorad). Gels were also subsequently stained with InstantBlue® Coomassie protein stain. Densitometric analyses were performed with the Image Lab software (BioRad).

### **2.3.2. Synthesis of maleimide end-functionalized PI**

#### **2.3.2.1. Synthesis of heterotelechelic keto/aldehyde PI (PIEG)**

This reaction was performed as already described<sup>8,19</sup>. Briefly, 10 g of natural rubber (NR) were cut into small pieces and dissolved overnight at RT in 500 mL of THF in round-bottom flask under stirring. In parallel, 550 mg (3.2 mmol) of mCPBA were dissolved in 50 mL of THF, and then added dropwise into the NR solution to epoxidize the PI. After 2 h, a solution of 1.5 g of periodic acid (2 eq. relative to mCPBA, 6.5 mmol) in 50 mL of THF was added dropwise to the epoxidized NR solution. The reaction was carried out for 2 hours, and then 2 g of Na<sub>2</sub>CO<sub>3</sub> were added and stirred for 15 min to neutralize acids. The reaction mixture was filtered on glass filter with Celite®, concentrated using a rotary evaporator, and precipitated into a large excess of cold ethanol containing KOH (5.9 mM). The precipitated polymer was then solubilized in 50 mL of diethyl ether and filtered again on Celite®. The purified product was dried overnight at 40 °C under dynamic vacuum. This heterotelechelic keto/aldehyde PI was named PIEG and was obtained as yellowish and transparent viscous liquid. Yield: 70%, M<sub>n</sub> = 5 500 g mol<sup>-1</sup>, *D* = 1.57. <sup>1</sup>H NMR (400 MHz, CDCl<sub>3</sub>) δ (ppm): 9.77 (t, <sup>1</sup>H, -CH<sub>2</sub>CHO), 5.12 (t (broad), 80H, -CH<sub>2</sub>CH=), 2.48 (t, 2H, -CH<sub>2</sub>CHO), 2.43 (t, 2H, -CH<sub>2</sub>COCH<sub>3</sub>), 2.34 (t, 2H, -CH<sub>2</sub>CH<sub>2</sub>CHO), 2.04 (m (broad), 316H, -CH<sub>2</sub>CH= and -CH<sub>2</sub>C(CH<sub>3</sub>)=), 1.68 (s (broad), 240H, -(CH<sub>3</sub>)C=CH-). <sup>1</sup>H NMR spectrum and size exclusion chromatogram are shown in supplementary Fig. S1 and S2.

#### **2.3.2.2. Synthesis of heterotelechelic keto/hydroxyl PI (PI-OH)**

This reaction was performed under argon atmosphere as already described<sup>3</sup>. Briefly, 6 g of purified PIEG 5500 g mol<sup>-1</sup> (equivalent to 1.2 mmol of aldehyde groups) were dissolved in 25 mL of dry THF. Then, 1.02 g (4.8 mmol, 4 eq) of NaBH(OAc)<sub>3</sub> and 76 μL (1.2 mmol, 1 eq) of acetic acid were added to the reaction. The mixture was stirred at 40 °C overnight. The product

was then precipitated twice with large excess of cold methanol, solubilized in 50 mL of Et<sub>2</sub>O, filtered on a glass filter with Celite® and dried overnight at 40 °C under dynamic vacuum. Yield: 80%,  $M_n = 5500 \text{ g.mol}^{-1}$ ,  $\bar{D} = 1.56$ . <sup>1</sup>H NMR (CDCl<sub>3</sub>) δ (ppm): 5.12 (t (broad), 80H, -CH<sub>2</sub>CH=), 3.63 (t, 2H, -CH<sub>2</sub>OH), 2.43 (t, 2H, -CH<sub>2</sub>(CO)CH<sub>3</sub>), 2.04 (m (broad), 316H, -CH<sub>2</sub>CH= and -CH<sub>2</sub>C(CH<sub>3</sub>)=), 1.68 (s (broad), 240H, -(CH<sub>3</sub>)C=CH-). <sup>1</sup>H NMR spectrum is shown in Fig. S3.

### 2.3.2.3. Synthesis of Maleimidohexanoic Chloride

This reaction was performed under argon atmosphere. 2.75 g (12 mmol) of maleimidohexanoic acid were solubilized in 15 mL of dry dichloromethane (DCM). 2.25 mL (26 mmol, ~2 eq) of oxalyl chloride, and 150 μL of N,N-dimethylformamide (DMF) were added to the solution, and incubated for 1 hour at room temperature. Then, oxalyl chloride and DCM in excess were removed under dynamic vacuum by an overnight incubation at room temperature. Yield: 100%. <sup>1</sup>H NMR (Fig. S4) (CDCl<sub>3</sub>) δ (ppm): 6.69 (s, 2H, -CH=CH-), 3.52 (m, 2H, -CH<sub>2</sub>N=), 2.88 (m, 2H, -CH<sub>2</sub>(CO)Cl), 1.73 (m, 2H, -CH<sub>2</sub>CH<sub>2</sub>(CO)Cl), 1.62 (m, 2H, -CH<sub>2</sub>CH<sub>2</sub>N=), 1.34 (m, 2H, -CH<sub>2</sub>CH<sub>2</sub>CH<sub>2</sub>(CO)Cl).

### 2.3.2.4. Synthesis of N-polyisoprene-maleimide (PIMAL)

This reaction was performed under argon atmosphere. A mixture of 2 mL of dry TEA (14 mmol, 40 eq) and 8 mL of anhydrous THF containing 1 g of Maleimidohexanoic Chloride (4.3 mmol, 10 eq) was slowly added to a solution of 8 mL of dry THF containing 2 g of PIOH (containing 0.36 mmol of OH group). The reaction was done for 4 h at 25 °C. The product of the reaction was separated by two successive precipitations into a large excess of cold methanol, then dissolved in Et<sub>2</sub>O, filtered on a glass filter with Celite®, concentrated using a rotary evaporator, and dried overnight at room temperature under dynamic vacuum. Yield: 90%,  $M_n = 5500 \text{ g.mol}^{-1}$ ,  $\bar{D} = 1.64$ . <sup>1</sup>H NMR (CDCl<sub>3</sub>) δ (ppm): 6.67 (s, 2H, -CH=CH-), 5.12 (t (broad), 80H, -CH<sub>2</sub>CH=), 4.00 (t, 2H, -CH<sub>2</sub>OCO-), 3.5 (t, 2H, -CH<sub>2</sub>N), 2.43 (t, 2H, -CH<sub>2</sub>COCH<sub>3</sub>), 2.27 (t, 2H, -CH<sub>2</sub>(CO)O-), 2.04 (m (broad), 316H, -CH<sub>2</sub>CH= and -CH<sub>2</sub>C(CH<sub>3</sub>)=), 1.68 (s (broad), 240H, -(CH<sub>3</sub>)C=CH-). IR-FT: stretching vibration of =C-H (3036 cm<sup>-1</sup>), -CH<sub>3</sub> (2960 cm<sup>-1</sup>), -CH<sub>2</sub>- (2914 cm<sup>-1</sup>, 2853 cm<sup>-1</sup>), -CO- (1720 cm<sup>-1</sup> which was overlapped with CO of maleimide), C=C (1665 cm<sup>-1</sup>), -C-H deformation from-CH<sub>2</sub> (1446 cm<sup>-1</sup>) and -CH<sub>3</sub> (1375 cm<sup>-1</sup>), =C-H wagging at 828 cm<sup>-1</sup> and -CH<sub>2</sub> rocking at 740 cm<sup>-1</sup> from PI backbone. The stretching vibration of CO

(1711  $\text{cm}^{-1}$ ), wagging of =CH (833  $\text{cm}^{-1}$  which is overlapped with =C-H wagging of PI) and deformation vibration of -C-H of cis  $\text{R}_1\text{CH}=\text{CHR}_2$  (696  $\text{cm}^{-1}$ ) from maleimide.  $^1\text{H}$  NMR spectrum is shown in Fig. S5, and IR spectrum in Fig. S6.

### 2.3.3. Synthesis and purification of the I20-*block*-PI copolymer (I20-*b*-PI)

2 mL of an aqueous solution of ELP I20 (8 mg/mL, 1.8  $\mu\text{mol}$ ) were incubated for 3 h at 4  $^\circ\text{C}$  with 100  $\mu\text{L}$  of tris(2-carboxyethyl) phosphine hydrochloride (TCEP) 1 M to reduce the intermolecular disulfide bridges. The reduced I20 was recovered by an ITC cycle, dried under dynamic vacuum for 1 h, and then dissolved in 450  $\mu\text{L}$  of a 2:1 (v/v) mixture of chloroform and methanol. After this solubilization step, 300  $\mu\text{L}$  of chloroform were added to the glass vial to increase the chloroform/methanol ratio to 4:1 (v/v), and the solution was further incubated under magnetic stirring for 1 h at room temperature. In parallel, 50 mg (9 mmol) of PIMAL 5500  $\text{g mol}^{-1}$  were solubilized in 800  $\mu\text{L}$  of chloroform. After 1 h of incubation, 200  $\mu\text{L}$  of methanol were added to obtain a final chloroform-methanol ratio of 4:1 (v/v). Finally, the two solutions containing the solubilized ELP and PIMAL were mixed, and 100  $\mu\text{L}$  of TEA (0.46 M) was added. The reaction mixture containing 1.8  $\mu\text{mol}$  of ELP and 9  $\mu\text{mol}$  of PIMAL was stirred at room temperature for 24 h. A sample of 50  $\mu\text{L}$  was then pipetted out, dried, and solubilized in SDS-PAGE loading buffer (BioRad) for analysis. After the reaction, the chloroform-methanol mixture was evaporated, and the dry residues were washed three times for 3 h under magnetic stirring with THF to eliminate the unreacted PIMAL. The supernatants were analyzed by NMR to check their content in PIMAL. To extract the unreacted I20, dried residues were then incubated with 1 mL of 70% ethanol for 24 h at 4  $^\circ\text{C}$  under magnetic agitation, centrifuged at 10.000 g for 30 min at 4  $^\circ\text{C}$ , and the supernatant containing the I20 was eliminated. The pellet enriched in I20-*b*-PI was kept for further analyses. All these purification steps were monitored by SDS-PAGE analyses.

### 2.3.4. Self-assembly of I20-*block*-PI copolymer in aqueous solution

5 mg of I20-*b*-PI were dissolved in 1 mL of a 1:4 (v/v) mixture of DMF/THF and filtered through 0.45  $\mu\text{m}$  pore size PTFE membrane. The block copolymer was nanoprecipitated by adding 1.5 mL of milliQ water in 200  $\mu\text{L}$  of I20-*b*-PI solution under stirring at room temperature using a syringe pump R-99 E (RAZELTM) at a flow rate of 100  $\mu\text{L}/\text{min}$ . The final

polymer concentration was 0.27 mg/mL. The organic solvent was removed from the particle dispersion by two successive dialysis steps of 24 h against 2 L of deionized water.

### **2.3.5. Methods**

#### **Size exclusion chromatography (SEC)**

The molar masses of polymers were determined by SEC using an Ultimate 3000 system from ThermoScientific equipped with a diode array detector. The system was also equipped with a multi-angle light scattering detector and a differential refractive index detector from Wyatt technology. Polymers were separated on two Shodex Asahipack gel columns GF310 and GF510 (300 x 7.5 mm) (exclusion limits from 500 g.mol<sup>-1</sup> to 300 000 g.mol<sup>-1</sup>) using DMF and lithium bromide (1 g/L) at 50°C as eluent at a flow rate of 0.5 mL/min. The dn/dc value for I20-*b*-PI was determined as 0.13 using the differential refractive index detector of the SEC. An Easyvial kit of polystyrene from Agilent was used as standards (Mn from 162 to 364 000 g.mol<sup>-1</sup>) to calibrate the column.

#### **Fourier transform infrared spectroscopy (FT-IR)**

Spectra of the polymer powders were acquired between 4000 and 400 cm<sup>-1</sup> in attenuated total reflectance (ATR) mode with a Bruker Vertex 70 instrument equipped with a GladiATR diamond.

#### **Nuclear magnetic resonance (NMR)**

<sup>1</sup>H, DOSY, HSQC and HMBC NMR spectra were recorded in CDCl<sub>3</sub> at 298 K on a Bruker Avance NEO spectrometer operating at 400.3 MHz. All DOSY (Diffusion Ordered Spectroscopy) measurements were performed with a 5 mm Bruker multinuclear z-gradient direct cryoprobe-head capable of producing gradients in the z direction with strength 53.5 G cm<sup>-1</sup>. Each sample was dissolved in 0.4 mL of CDCl<sub>3</sub> for internal lock and spinning was used to minimize convection effects. The DOSY spectra were acquired with the ledbpgp2s pulse program from Bruker topspin software. The duration of the pulse gradients and the diffusion time were adjusted to obtain full attenuation of the signals at 95% of maximum gradient strength. The values were 5.0 ms for the duration of the gradient pulses and 300 ms for the

diffusion time. The gradients strength was linearly incremented in 16 steps from 5% to 95% of the maximum gradient strength. A delay of 5 s between echoes was used. The data were processed using 8192 points in the F2 dimension and 128 points in the F1 dimension with the Bruker topspin software. Field gradient calibration was accomplished at 25 °C using the self-diffusion coefficient of H<sub>2</sub>O + D<sub>2</sub>O at  $19.0 \times 10^{-10} \text{ m}^2 \text{ s}^{-1}$ .

### **Circular dichroism (CD)**

CD spectra were recorded on a Jasco J-1500 equipped with a Peltier temperature control accessory (JASCO, Hachioji, Japan). Each spectrum was obtained by averaging two scans collected at 50 nm.min<sup>-1</sup>. The CD spectrum of pure water solution was subtracted from the average scan for each sample.

### **Determination of the critical aggregation concentration (CAC)**

The CAC of the copolymer in aqueous solution was determined as previously described<sup>32-34</sup>. Briefly, solutions of I20-*b*-PI in deionized water with concentrations varying from 10<sup>-6</sup> mg/mL to 2.10<sup>-1</sup> mg/mL were prepared. Then, 1 μL of pyrene solution at 1 mg/mL in THF was added into 500 μL of particle dispersion prepared at various concentrations and incubated under stirring at 300 rpm for 10 h at room temperature. The dispersions were characterized by fluorescence spectroscopy using a Jasco FP 8500 spectrofluorometer. The excitation wavelength was set at 319 nm, and the fluorescence emission of pyrene was recorded between 360 and 400 nm. The intensities of the first (I1) and third (I3) vibrionic band of pyrene were determined at 373 nm and 385 nm respectively. The I1/I3 ratio was plotted as function of the polymer concentration. The CAC was determined from the onset of the decrease in I1/I3.

### **Dynamic light scattering (DLS)**

DLS analyses of the suspension of PI-*b*-ELP nanoparticles were performed at 25 °C by using a Nano ZS instrument (Malvern U.K.) working at a 90° angle detection. The hydrodynamic radius (R<sub>H</sub>) and the polydispersity index (PDI) were calculated from autocorrelation functions using the cumulant method. The derived count rate (DCR) was defined as the mean scattered intensity normalized by the attenuation factor. The zeta potential was measured with the same apparatus using the M3-PALS technique.

## **Transmission electron microscopy (TEM)**

20  $\mu\text{L}$  of the polymer dispersion at 0.27 mg/mL were deposited onto lacey carbon grids, and then water was evaporated at room temperature. The grid was incubated with vapor of osmium tetroxide ( $\text{OsO}_4$ , 4% in aqueous solution) for 12 h at room temperature. TEM analyses were performed at 80 kV acceleration voltage with a Hitachi H7650 microscope equipped with an Orius camera (Gatan, Paris, France). Pictures were acquired with the digital micrograph software.

## **Atomic force microscopy (AFM)**

Adsorbed structures at the solid/solution interface were examined using a NanoScope IIIa Multimode atomic force microscope (Digital Instruments, CA) in Contact Mode, equipped with a standard fluid cell. Standard cantilevers were used with sharpened  $\text{Si}_3\text{N}_4$  tips. These were irradiated with ultraviolet light for 30 min prior to use. The solution was held in a Plexiglas fluid cell, sealed by a silicone O-ring and resting on a muscovite mica substrate. The cell and the cantilever were cleaned by sonication for 30 min in deionized water at 40 °C and then dried using filtered nitrogen prior to use. The mica substrate was cleaved using adhesive tape and immediately used, to avoid contamination by ambient dust particles or volatile molecules. The cell was completely filled with about 0.5 mL of the nanoparticle solution at a concentration of 0.27 mg/mL. Before imaging the surfaces, the polymer was allowed to adsorb onto mica during at least 12 h.

## **Nile Red encapsulation and release**

Encapsulation of Nile red was as follows: 2  $\mu\text{L}$  of Nile red at 1 mg/mL in DMSO were added in 600  $\mu\text{L}$  of a solution of I20-*b*-PI nanoparticles at 0.27 mg/mL. The solution was incubated under stirring for 24 h at room temperature. The fluorescence emission spectrum of the Nile red-loaded particles was recorded between 587 and 800 nm ( $\lambda_{\text{ex}} = 570$  nm) with a Jasco FP 8500 spectrofluorometer, and compared to the spectrum obtained with a solution of Nile red in water. Nile red release was studied by placing loaded nanoparticles (600  $\mu\text{L}$  at 0.27 mg/mL) into a dialysis device Spectra-Por® Float-A-Lyzer® G2 (3.5-5 kDa MWCO). The device was then placed in 1 L of water, and incubated at room temperature in the dark under magnetic stirring. After excitation at 570 nm the fluorescence of the dialyzed sample was measured

between 587 nm and 800 nm. The experiment was performed in triplicate and the data was presented as mean  $\pm$  SD.

### 2.3.6. Materials

Natural rubber (NR) PB235 was kindly provided by UMR iATE in Thailand. 3-chloroperoxybenzoic acid (mCPBA) (70-75%, Acros), periodic acid ( $H_5IO_6$ ) ( $\geq 99\%$ , Aldrich), acetic acid (99%, Aldrich), sodium triacetoxyborohydride ( $NaBH(OAc)_3$ ) (97%, Aldrich),  $Na_2CO_3$  ( $>99.5\%$ , Sigma-Aldrich), KOH (85%), 6-maleimidohexanoic acid ( $>90\%$ , Sigma-Aldrich), oxalyl chloride ( $\geq 99\%$ , Sigma-Aldrich), Tris(2-carboxyethyl)phosphine hydrochloride (TCEP.HCl) (Sigma-Aldrich), NaCl (Sigma-Aldrich), DMSO (Sigma-Aldrich), PBS 10X (Eurobio), Pyrene (98%, Alfa Aesar), Osmium tetroxide (Delta microscopy), and Nile Red (Carl Roth) were used without further purification. Celite® was purchased from Sigma-Aldrich. Tetrahydrofuran (THF), dimethylformamide (DMF), and dichloromethane (DCM) were purified using the PureSolv MD7 system from INERT. Triethylamine (TEA) (99% Acros organics) was dried using  $CaH_2$  and distilled prior to use. Chloroform (VWR chemicals), methanol, ethanol and diethyl ether (reagent grade, Aldrich) were used as received. Laemmli Sample Buffer, Tris/glycine/SDS buffer (TGS buffer), Precision Plus Protein™ Unstained Standards, and 4–20% Mini-PROTEAN™ TGX Stain-Free™ polyacrylamide gels were purchased from BioRad. InstantBlue® Coomassie protein stain was from Sigma-Aldrich. Ultrapure water (18  $M\Omega \cdot cm$ ) was obtained by passing in-house deionized water through a Millipore Milli-Q Biocel A10 purification unit. Bacto Tryptone (Sigma), Yeast extract (Sigma), Ampicillin (Sigma) and isopropyl  $\beta$ -D-thiogalactopyranoside (IPTG, VWR chemicals) were used for cell culture.

## 2.4. References

- 1 M. Morell and J. Puiggali, *Polymers (Basel)*, 2013, **5**, 188–224.
- 2 T. Deming, H.-A. Klok and H. Schlaad, in *Advances in Polymer Science*, eds. H.-A. Klok and H. Schlaad, Springer-Verlag, Berlin/Heidelberg, 2006, **202**, 1–18.
- 3 J. Yunyongwattanakorn, Y. Tanaka, S. Kawahara, W. Klinklai and J. Sakdapipanich, *Rubber Chemistry and Technology*, 2003, **76**, 1228–1240.
- 4 S. Amnuayporn Sri, J. Sakdapipanich, S. Toki, B. S. Hsiao, N. Ichikawa and Y. Tanaka, in *Rubber Chemistry and Technology*, Rubber Division of the American Chemical Society, 2008, **81**, 753–766.
- 5 Y. Tanaka, *Progress in Polymer Science*, 1989, **14**, 339–371.
- 6 S. Sato, Y. Honda, M. Kuwahara and T. Watanabe, *Biomacromolecules*, 2003, **4**, 321–329.
- 7 R. Yoda, Y. Hirokawa and T. Hayashi, *European Polymer Journal*, 1994, **30**, 1397–1401.
- 8 A. v. Radchenko, J. Grange, A. Vax, F. Jean-Baptiste-Dit-Dominique, R. Matmour, S. Grelier and F. Peruch, *Polymer Chemistry*, 2019, **10**, 2456–2468.
- 9 J. Rodríguez-Hernández, J. Babin, B. Zappone and S. Lecommandoux, *Biomacromolecules*, 2005, **6**, 2213–2220.
- 10 D. W. Urry, T. L. Trapane and K. U. Prasad, *Biopolymers*, 1985, **24**, 2345–2356.
- 11 D. W. Urry, *Progress in Biophysics and Molecular Biology*, 1992, **57**, 23–57.
- 12 B. Li, D. O. Alonso and V. Daggett, *J Mol Biol*, 2001, **305**, 581–92.
- 13 D. E. Meyer and A. Chilkoti, *Biomacromolecules*, 2004, **5**, 846–851.
- 14 E. Garanger and S. Lecommandoux, *Angewandte Chemie International Edition*, 2012, **51**, 3060–3062.

- 15 J. Kyte and R. F. Doolittle, *Journal of Molecular Biology*, 1982, **157**, 105–132.
- 16 L. Bataille, W. Dieryck, A. Hocquellet, C. Cabanne, K. Bathany, S. Lecommandoux, B. Garbay and E. Garanger, *Protein Expression and Purification*, 2016, **121**, 81-87.
- 17 L. Bataille, W. Dieryck, A. Hocquellet, C. Cabanne, K. Bathany, S. Lecommandoux, B. Garbay and E. Garanger, *Protein Expression and Purification*, 2015, **110**, 165–171.
- 18 D. E. Meyer and a Chilkoti, *Nat Biotechnol*, 1999, **17**, 1112–1115.
- 19 S. Gillier-Ritoit, D. Reyx, I. Campistron, A. Laguerre and R. Pal Singh, *Journal of Applied Polymer Science*, 2003, **87**, 42–46.
- 20 J. Folch-Pi and P. J. Stoffyn, *Ann N Y Acad Sci*, 1972, **195**, 86–107.
- 21 M. B. Lees, *Neurochemical Research*, 1998, **23**, 261–271.
- 22 M. B. Folch, J., and Lees, *J. Biol. Chem.*, 1951, **191**, 807–817.
- 23 A. Rath, M. Glibowicka, V. G. Nadeau, G. Chen and C. M. Deber, *Proc Natl Acad Sci U S A*, 2009, **106**, 1760–1765.
- 24 O. A. Bizzozero, F. Dominguez, J. M. Pasquini and E. F. Soto, *Journal of Neurochemistry*, 1985, **45**, 1228–1231.
- 25 M. S. Bahniuk, A. K. Alshememry, S. v. Elgersma and L. D. Unsworth, *Journal of Nanobiotechnology*, 2018, **16**, 15.
- 26 T. Yamaoka, T. Tamura, Y. Seto, T. Tada, S. Kunugi and D. A. Tirrell, *Biomacromolecules*, 2003, **4**, 1680–1685.
- 27 S. M. Janib, M. F. Pastuszka, S. Aluri, Z. Folchman-Wagner, P. Y. Hsueh, P. Shi, Y. A. Lin, H. Cui and J. A. Mackay, *Polymer Chemistry*, 2014, **5**, 1614–1625.
- 28 F. G. Quiroz and A. Chilkoti, *Nature Materials*, 2015, **14**, 1164–1171.
- 29 A. Micsonai, F. Wien, L. Kernya, Y.-H. Lee, Y. Goto, M. Réfrégiers and J. Kardos, *Proceedings of the National Academy of Sciences*, 2015, **112**, E3095–E3103.

- 30 A. Micsonai, F. Wien, É. Bulyáki, J. Kun, É. Moussong, Y. H. Lee, Y. Goto, M. Réfrégiers and J. Kardos, *Nucleic Acids Research*, 2018, **46**, W315–W322.
- 31 K. N. Greenland, M. F. C. A. Carvajal, J. M. Preston, S. Ekblad, W. L. Dean, J. Y. Chiang, R. L. Koder and R. J. Wittebort, *Journal of Physical Chemistry B*, 2018, **122**, 2725–2736.
- 32 J. Aguiar, P. Carpena, J. A. Molina-Bolívar and C. Carnero Ruiz, *Journal of Colloid and Interface Science*, 2003, **258**, 116–122.
- 33 A. Mohr, P. Talbiersky, H. G. Korth, R. Sustmann, R. Boese, D. Bläser and H. Rehage, *Journal of Physical Chemistry B*, 2007, **111**, 12985–12992.
- 34 L. Piñeiro, M. Novo and W. Al-Soufi, *Advances in Colloid and Interface Science*, 2015, **215**, 1–12.
- 35 M. Bagheri, J. Bresseleers, A. Varela-Moreira, O. Sandre, S. A. Meeuwissen, R. M. Schiffelers, J. M. Metselaar, C. F. van Nostrum, J. C. M. van Hest and W. E. Hennink, *Langmuir*, 2018, **34**, 15495–15506.
- 36 K. M. Luginbuhl, D. Mozhdzhi, M. Dzuricky, P. Yousefpour, F. C. Huang, N. R. Mayne, K. L. Buehne and A. Chilkoti, *Angewandte Chemie - International Edition*, 2017, **56**, 13979–13984.
- 37 G. R. Grimsley, J. M. Scholtz and C. N. Pace, *Protein Science*, 2009, **18**, 247–251.
- 38 C. S. Tian and Y. R. Shen, *Proc Natl Acad Sci U S A*, 2009, **106**, 15148–15153.
- 39 R. Plenderleith, T. Swift and S. Rimmer, *RSC Advances*, 2014, **4**, 50932–50937.
- 40 E. M. Moussa, J. P. Panchal, B. S. Moorthy, J. S. Blum, M. K. Joubert, L. O. Narhi and E. M. Topp, *J Pharm Sci*, 2016, **105**, 417–430.
- 41 K. D. Allen, S. B. Adams and L. A. Setton, *Tissue Eng Part B Rev*, 2010, **16**, 81–92.
- 42 H. Betre, W. Liu, M. R. Zalutsky, A. Chilkoti, V. B. Kraus and L. A. Setton, *Journal of Controlled Release*, 2006, **115**, 175–182.

- 43 W. Wang, A. Jashnani, S. R. Aluri, J. A. Gustafson, P. Y. Hsueh, F. Yarber, R. L. McKown, G. W. Laurie, S. F. Hamm-Alvarez and J. A. MacKay, *Journal of Controlled Release*, 2015, **199**, 156–167.
- 44 C. A. Gilroy, S. Roberts and A. Chilkoti, *Journal of Controlled Release*, 2018, **277**, 154–164.
- 45 C. A. Gilroy, M. E. Capozzi, A. K. Varanko, J. Tong, D. A. D’Alessio, J. E. Campbell and A. Chilkoti, *Sci Adv*, 2020, **6**, eaaz9890.
- 46 D. Asai, T. Fukuda, K. Morokuma, D. Funamoto, Y. Yamaguchi, T. Mori, Y. Katayama, K. Shibayama and H. Nakashima, *Macromolecular Bioscience*, 2019, **19**, 1900167.
- 47 R. D. Bowles and L. A. Setton, *Biomaterials*, 2017, **129**, 54–67.
- 48 theses.fr – Jérémie Grange, Functionalization of polyisoprene: toward the mimic of natural rubber, **2018**, <https://www.theses.fr/2018BORD0004>.

# Chapter 3. Lipid-Elastin like peptide hybrid polymer self-assembly

## 3.1. Introduction

The development of new biomaterials for biomedical applications is a rapidly growing area of research. For most of them, the targeted use will be drug delivery, tissue-engineering and regenerative medicine. Polypeptide-based materials are good candidates for these applications because they are biosourced, biocompatible, biodegradable, and if carefully designed non-toxic and weakly immunogenic<sup>1</sup>. Among them, recombinant polypeptides are interesting for biomedical applications because they can be produced at an industrial level using GMP standards, contrarily to the polypeptides extracted from biological tissues which can be contaminated by virus or prions.

Elastin-like polypeptides (ELPs) are a class of polypeptides derived from the hydrophobic domain of mammalian elastin<sup>2</sup>. Usually, they are made of repetitions of the pentapeptide sequence Val-Pro-Gly-X-Gly, where X can be any natural amino acid but proline. An interesting feature of these ELPs is that they are thermosensitive, being soluble in aqueous buffers below their transition temperature (Tt), and aggregating into polymer-rich particles when heated above this Tt<sup>3,4</sup>. The Tt depends on the chain length, on the nature of the guest residue Xaa (e.g. polar, charged, hydrophobic), on the polypeptide concentration, and on the presence of salts in the solution<sup>5,6</sup>. Recombinantly produced ELP are preferred over the chemically synthesized ones, because they have controlled sequence and can be of higher molecular masses<sup>7,8</sup>. Regarding their interesting biological and physico-chemical properties, ELPs were used in recent years to develop new hydrogels and innovative drug delivery systems<sup>8</sup>.

Two different strategies have been developed for drug delivery using ELPs. In the first one, the drug is covalently linked to the polypeptides, either by fusion at the gene level for therapeutic peptide or proteins or by conjugation of the therapeutic molecules on purified

ELPs. However, some hydrophobic drugs cannot be conjugated, or lose their activity after conjugation. In this case, a second strategy can be used where ELPs are engineered to self-assemble into nanoparticles, such as micelles or polymersomes, which can sequester hydrophobic molecules in their apolar compartments. Of particular interest, amphiphilic block polypeptides obtained by association of two ELP blocks having different Tts can be genetically synthesized. These polypeptide structures showed self-assembly properties (micelles, vesicles) when incubated in aqueous buffer at a temperature between the Tt of each corresponding block, the hydrophobic block forming the core of the micelles, whereas the hydrophilic block forms the corona<sup>9</sup>. It was later shown that the length of the two blocks and the hydrophilic/hydrophobic mass ratio influence the size of the micelles<sup>10,11</sup>. However, it has been also demonstrated that these ELP diblocks formed rather loose micelles, with a relatively high level of hydration of the hydrophobic core, thereby preventing the formation of well segregated micelles<sup>12-14</sup>. Consequently, the encapsulation of hydrophobic drugs is quite inefficient through this approach<sup>15</sup>. Furthermore, micelles obtained from amphiphilic ELPs are generally not very stable at low polypeptide concentrations, with in particular the possibility of micelle disassembly when diluted in biological fluids after injection.

To drastically increase the stability of ELP-based micelles, the grafting of lipid moieties like cholesterol, myristic acid (C14:0), oleic acid (C18:1) or fatty acid (FA) analogues to the ELP blocks was evaluated. Two different strategies were developed in the past. In the first one, recombinantly expressed ELPs were purified and chemically modified on specific amino acids selected as guest residues of the ELP sequence. By doing so, cholesterol can be grafted on lysine residues<sup>16</sup> and oleic acid on methionine residues<sup>17</sup>. In both cases, the grafting of lipid chains to the ELP backbone yielded brush-like lipoproteins that can self-assemble into micelles with ELP-cholesterol, or polymersomes with ELP-C18:1. However, these materials are highly hydrophobic owing to the number of lipid molecules grafted per ELP, and therefore difficult to handle in biological media. More recently, a short synthetic lipid (*O*-octadecylhydroxylamine) was also successfully grafted to the N-terminal serine of an ELP via a pH-responsive oxime bond<sup>18</sup>.

A second elegant strategy developed in Chilkoti's and Mozhdehi's group relies on the lipidation of the ELP *in vivo* during its recombinant expression. Indeed, by fusing a specific peptide sequence at the N-terminus of ELPs, and by coexpressing the polypeptide and a yeast N-myristoyltransferase (NMT) in *Escherichia coli* they obtained ELP-C14<sup>15</sup>. This material self-

assembled into micelles that were used to deliver hydrophobic drugs to mammalian cells. The *in vivo* synthetic chemistry was then declined to produce ELP-C14 that contains a  $\beta$ -sheet-forming peptide<sup>19</sup>, or to acylate an analogue of myristic acid<sup>20</sup>. In a slightly different approach, an ELP containing a sterol binding site at its C-terminal domain was recombinantly expressed and purified, and then cholesterol was grafted *in vitro* to obtain ELP-cholesterol<sup>21</sup>. Finally, these approaches were successfully combined to produce a C14-ELP-cholesterol lipopolyptide. Although interesting, these approaches have some limitations. Concerning the *in vivo* acylation, the main inconvenient came from the low yields of purified lipopolyptide: for ELP-cholesterol the quantity purified was in the range of 5-10 mg/L culture<sup>21</sup>, and about 40 mg/L culture for C14-ELP<sup>15</sup>. These yields are at least one order of magnitude lower than those usually obtained for unmodified ELPs. Another limitation comes from the small repertoire of natural lipids that can be grafted to ELPs using this strategy. Also, for fatty acids, the approach is restricted to C14 or analogs of comparable length because of the specificity of the NMT enzyme. Longer fatty acids such as palmitate, stearate or oleate cannot be used, nor can unsaturated fatty acids.

In this work, we report the synthesis of 15 ELP-FAs with variation in the length and saturation of the FA moiety as well as the length of the ELP block. The carboxyl group of FA was condensed with the primary amine of the N-terminal methionine of the ELPs. Acylated ELPs were characterized, and their self-assembly in a biologically relevant buffer was studied to elucidate the respective roles of FA structure and ELP length on micelle properties. The possibility to encapsulate and release hydrophobic molecules was also evaluated.

## 3.2. Results and discussion

### 3.2.1. Synthesis and purification of ELP-FAs

Our goal was to obtain a library of 15 ELP-FAs, differing by the length of the ELP block and the nature of the FA. The amino acid sequences of the ELP are MW[(VPGVG)(VPGMG)(VPGVG)<sub>2</sub>]<sub>5,10,20</sub>, and therefore they differ by their number of pentapeptide repetitions, from 20 to 80. For sake of clarity, they will be referred respectively as M20, M40 and M80. We selected different FAs among those abundant in membranes phospholipids<sup>22</sup>. Myristic (C14:0), palmitic (C16:0) and stearic acids (C18:0) were considered to assess the influence of the hydrophobic block length on the self-assembly properties, while oleic (C18:1) and linoleic (C18:2) acids are expected to provide insight into the effect of the unsaturation degree. Main physico-chemical characteristics of the FAs used in this study are shown in Table 1.

**Table 1. Physico-chemical characteristics of the fatty acids used in the study.**

Fatty acid	Common Name	MW (Da)	Log P	Melting Point (°C)
C14:0	Myristic acid	228.37	6.11	53.9
C16:0	Palmitic acid	256.42	7.17	61.8
C18:0	Stearic acid	284.5	8.23	68.8
C18:1	Oleic acid	282.5	7.73	13.4
C18:2	Linoleic acid	280.4	7.05	-8.5

ELPs were designed in such a way that a single primary amine is present in the whole polypeptide sequence, namely at the N-terminal methionine (Fig. 1).

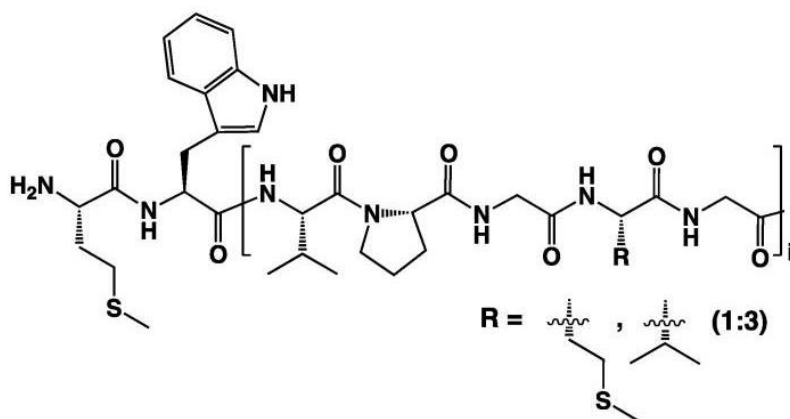


**Figure 1. Chemical structure of the ELP M-series. The guest amino acid is either a methionine or a valine, with a molar ratio 1:3. The number of pentapeptide repetition(i) is 20, 40 and 80.**

Then, the condensation of the carboxylic group of FA with this amine group is a simple way to afford ELP-FA conjugates. The condensation reaction was performed by using *O*-(1*H*-6-chlorobenzotriazole-1-yl)-1,1,3,3-tetramethyluronium hexafluorophosphate (HCTU) as activating agent, in presence of *N,N*-diisopropylethylamine (DIPEA). HCTU is a nontoxic, nonirritating and noncorrosive activating reagent that is typically used for solid-phase peptide syntheses in DMF<sup>23,24</sup>, and DIPEA is a sterically hindered organic base commonly used in amide coupling reactions between an activated carboxylic acid and a nucleophilic amine<sup>24</sup>. The condensing reactions were performed overnight at room temperature (Fig 2).

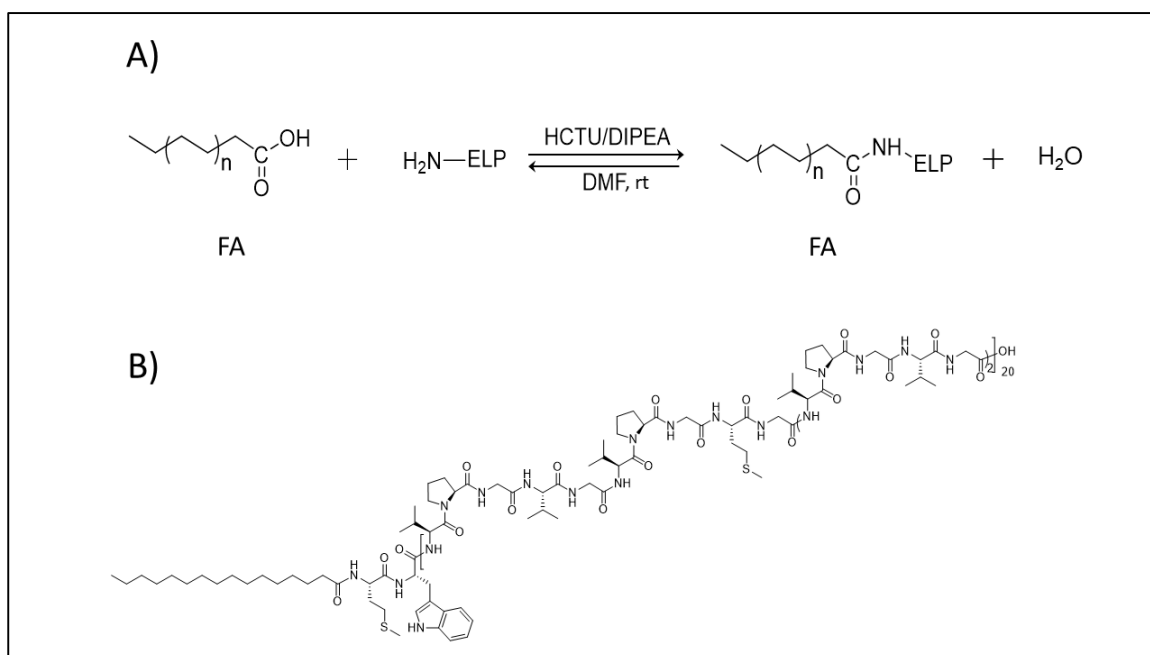


**Figure 2. A) Condensation reaction between FA and ELP. B) Example of ELP-FA structure, here the M20-C16.**

The reaction product ELP-FA was successively precipitated first by diethyl ether, and then by acetone, before being washed three times with diethyl ether to eliminate traces of HCTU, DIPEA and unreacted FAs. After drying, the product was suspended in cold water, centrifuged at 2 500 g to eliminate insoluble material, and the supernatant was dialyzed against milliQ water, and then lyophilized.

The physico-chemical characteristics (MW, ELP/FA mass ratio) of the 15 diblocks and of the three ELPs are summarized in Table 2.

**Table 2. Targeted ELP-FAs.**

	C14		C16		C18		C18:1		C18:2	
	MW	ELP/FA								
M20	8 687	38.1 :1	8 925	33.9 :1	8 953	30.5 :1	8 951	30.8 :1	8 949	31.0 :1
M40	17 035	74.7 :1	17 274	66.5 :1	17 301	59.9 :1	17 300	60.4 :1	17 298	60.8 :1
M80	33 735	148.0 :1	33 974	131.8 :1	34 002	118.8 :1	34 000	119.6 :1	33 998	120.5 :1

*Theoretical MW in g.mole<sup>-1</sup>. Data for ELP were obtained from ProtParam<sup>25</sup>. ELP/FA: mass ratio*

### 3.2.2. Characterization of ELP-FAs

#### 3.2.2.1. Reversed-Phase-High Performance Liquid Chromatography (RP-HPLC)

To analyze the purified ELP-FA conjugates we chose the RP-HPLC technique because it can separate compounds based on their hydrophobic character. The stationary phase was C18, and the mobile phase a gradient of a mixture of water/methanol. Detection was done at 230 nm to detect the peptide amide bonds. First, we checked that the acylation of the ELP did not lead to a significant change in the UV absorption at this wavelength (Fig. 3).

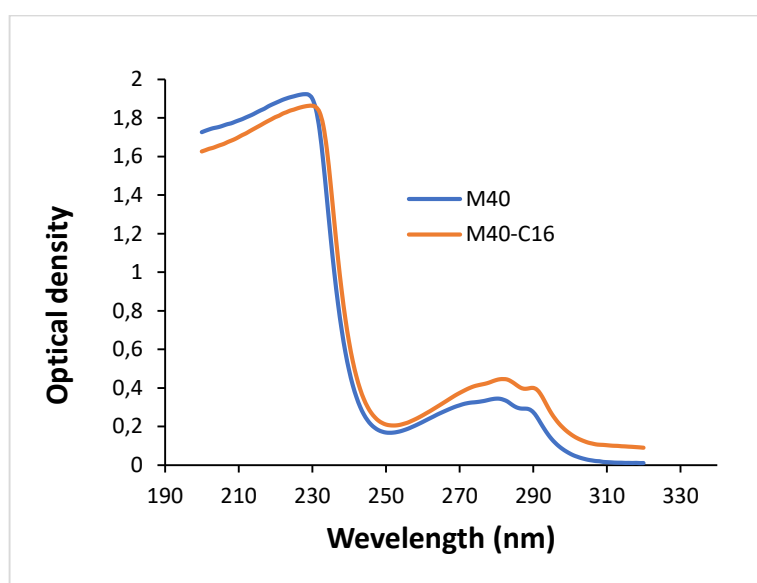


**Figure 3. UV spectra of M40 and M40-C16. Each sample was dissolved in water at a concentration of 1 mg/mL. M40 (blue line) and M40-C16 (orange line).**

Interestingly, we can observe a slight difference between the two spectra around 280 nm, which corresponds to the maximal absorption of the tryptophan residue present at the N-terminal end of the ELP. Considering that fatty acylation occurred at this N-terminal end, close to the tryptophan residue, this might have changed the hydrophobic environment and therefore its absorption characteristics<sup>26</sup>. Nevertheless, this experiment showed that the absorption at 230 nm was similar for both samples, indicating that quantitative data could be gathered after integration of the peaks obtained at this wavelength after RP-HPLC separation.

Fig. 4 shows the chromatograms obtained for the free ELP (M20, M40 and M80) and for their five Mx-FA conjugates.

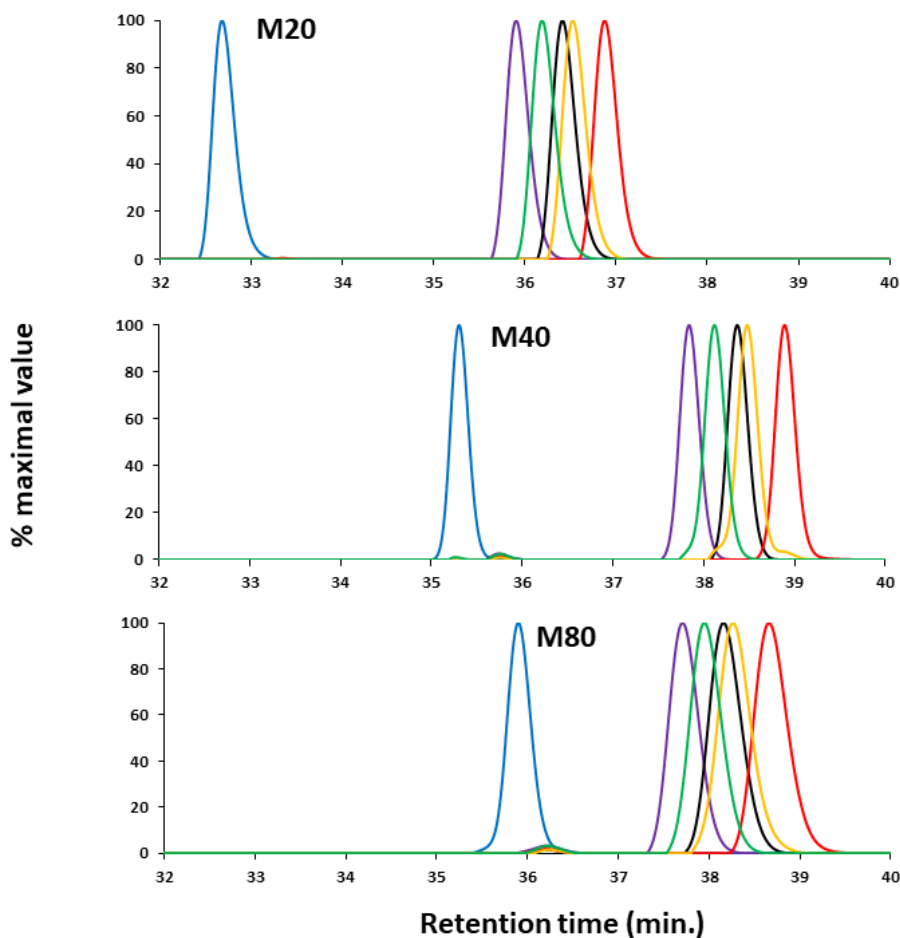


**Figure 4.** RP-HPLC traces of ELPs and of ELP-FAs. ELP-FAs were injected at 70  $\mu\text{M}$  in water. The eluent was a gradient of a water/methanol mixture. The absorbance at 230 nm was normalized to the maximal value. Unmodified ELP (blue lines), ELP-C14 (purple lines), ELP-C16 (black lines), ELP-C18 (red lines), ELP-C18:1 (orange lines) and ELP-C18:2 (green lines).

These RP-HPLC chromatograms were analyzed and the retention times and conversion rates are summarized in Table 3. As expected, the retention time of the of M-FAs were significantly increased when compared to the unmodified ELPs. In addition, it can be seen that the purification step was efficient, as judged by the absence of significant amounts of unmodified ELPs (purity > 96%, Table 3).

**Table 3. RP-HPLC analysis of ELP-FAs**

		ELP	ELP-C14	ELP-C16	ELP-C18	ELP-C18:1	ELP-C18:2
M20	Retention time	32.7	35.9	36.4	36.9	36.5	36.2
	Purity (%)		99	99	99	99	99
M40	Retention time	35.3	37.8	38.4	38.9	38.5	38.1
	Purity (%)		96	99	98	98	96
M80	Retention time	35.9	37.7	38.2	38.7	38.3	38.0
	Purity (%)		96	97	97	98	96

*Retention times in min.*

*The percentage of purity was calculated by dividing the area of the peak corresponding to the ELP-FA by the area of all the peaks detected on the same chromatogram.*

Retention times vary inversely with the ELP chain length: + 4.2 min between M20 and M20-C18; + 3.8 min between M40 and M40-C18; +2.6 min between M80 and M80-C18. Thus, the impact of the acylation in terms of hydrophobic/hydrophilic ratios on the retention times was more pronounced for the shorter ELP M20 than for the larger M80. Retention times also increased systematically as the chain length increased from 14 to 18 carbons, with the longest retention times always measured with ELP-C18 conjugates. However, the presence of unsaturation in the C18 chain reduced the elution times due to a difference in hydrophobicity<sup>27</sup>.

### 3.2.2.2. Mass-spectrometry analyses

To further confirm the identity of the conjugated, they were analyzed by mass-spectrometry. First, we tried the MALDI-MS technique. An example of the spectra obtained with M20 and some M20-FAs is shown in Fig. 5.

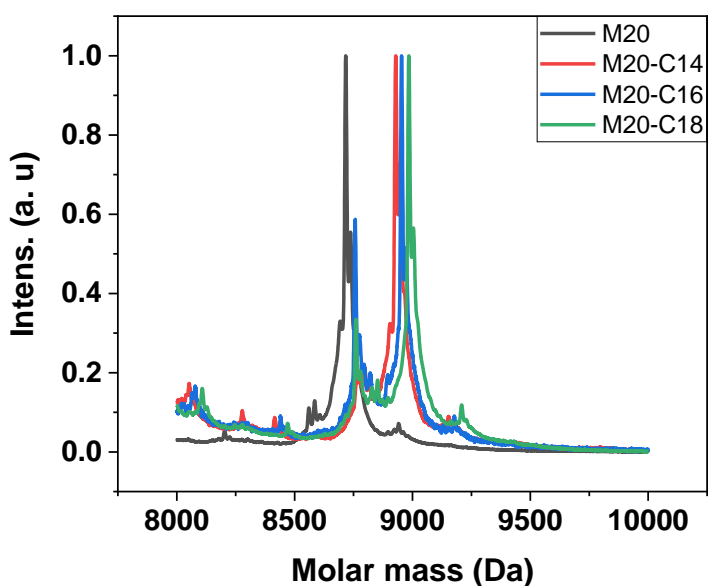
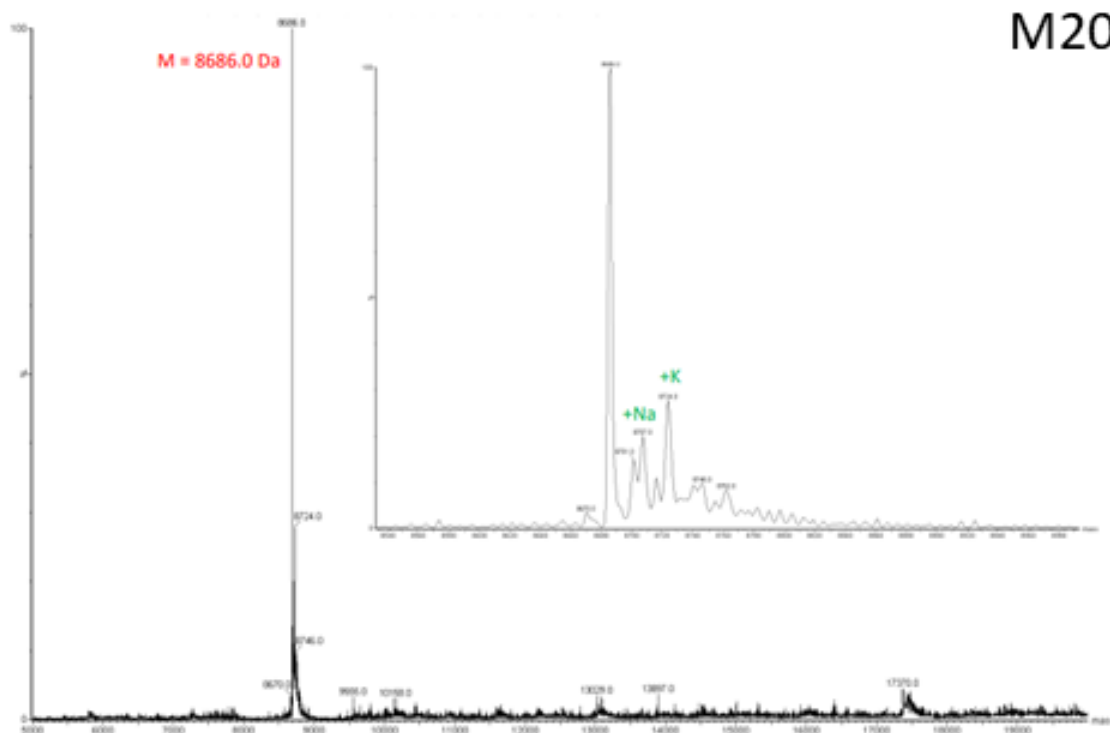


**Figure 5. MALDI-MS spectra of M20 and M20-FA.**

We obtained a single peak for the M20 ELP, but two peaks for the M20-FAs analyzed: one around 9000 Da corresponding to the acylated form, and one with a molar mass slightly higher than that of the unmodified ELP. This second peak around 8,800 Da is of weaker intensity than that around 9,000 Da, but clearly visible in the samples M20-C16 (blue trace) and M20-C18 (green trace). Two hypotheses can be put forward to explain the presence of this species. The first is that the coupling reaction between the FA and the ELP was not efficient, and therefore some ELP M20 remained in the purified sample. This hypothesis is very unlikely because the same samples were previously analyzed by RP-HPLC, and the quantity of free ELP was negligible (see paragraph 3.2.2.1). The second hypothesis is that the analysis by MALDI-MS leads to the degradation of part of the sample. This technique is in fact based on the ionization of a matrix containing the sample thanks to laser irradiation<sup>28</sup>. In some cases, the laser energy may be too high and damage the molecule to be analyzed. Lowering the laser intensity can alleviate this problem, but the polypeptides might not be ionized enough to fly into the mass spectrometer.

To circumvent this problem, we used electrospray ionization (ESI), which is known to preserve better sample integrity<sup>28</sup>. Fig. 6 shows the result obtained for M20 and M20-C18. For each sample, only one major peak was obtained thus confirming their purity, as well as the absence of degradation during the analysis. The results for the other Mx-FAs are shown in Fig. S1 and summarized in Table 4.



M20

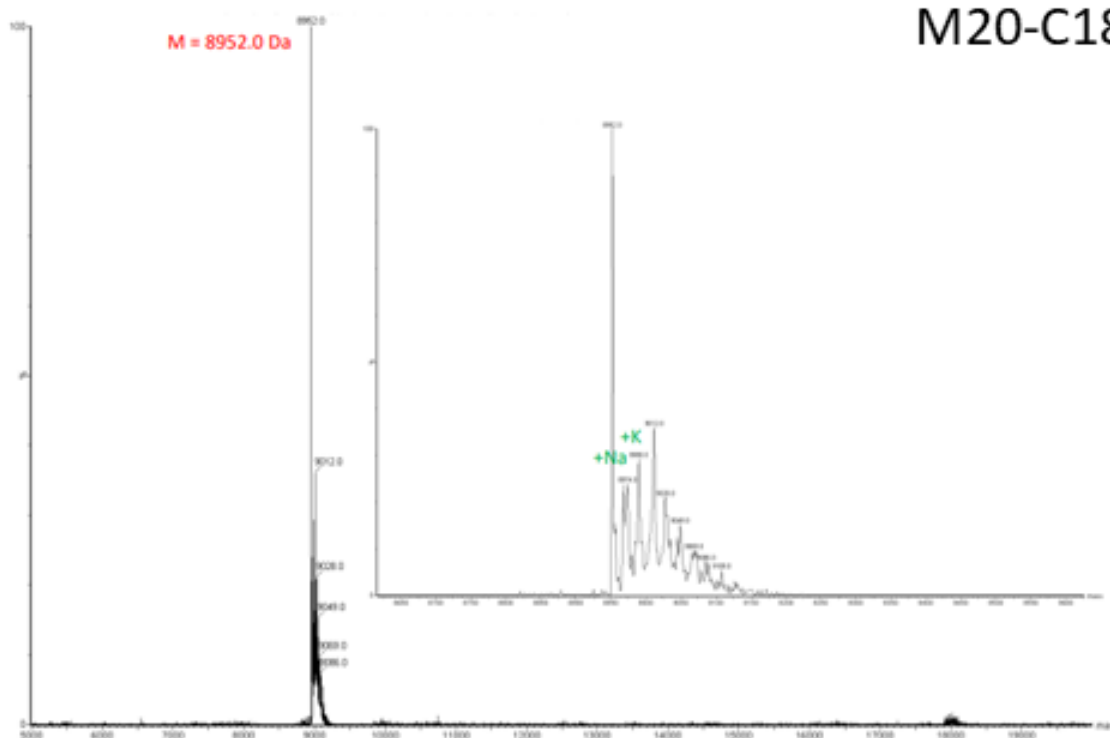


**Table 4. Molecular weight of Mx and Mx-FAs samples measured by ESI-MS**

ELP and ELP-FA	Theoretical MW (Da)	Expérimental MW (Da)
M20	8 687	8 686
M20-C14	8 897	8 896
M20-C16	8 925	8 924
M20-C18	8 953	8 952
M20-C18:1	8 951	8 950
M20-C18:2	8 949	8 948
M40	17 035	17 037
M40-C14	17 246	17 246
M40-C16	17 274	17 274
M40-C18	17 302	17 302
M40-C18:1	17 300	17 300
M40-C18:2	17 298	17 298
M80	33 736	33 739
M80-C14	33 946	33 946
M80-C16	33 974	33 973
M80-C18	34 002	34 002
M80-C18:1	34 000	34 000
M80-C18:2	33 998	33 998

The experimental mass values were in very good agreement with the theoretical ones, with shifts of 210, 238, 266, 264, and 262 Da after acylation of the ELPs by C14, C16, C18, C18:1 and C18:2, respectively.

### 3.2.2.3. Circular-dichroism analyses

We have previously shown that grafting a PI molecule to the C-terminus of ELP I20 results in a dramatic change in the secondary structure of the diblock compared to that of the ELP I20 (see 2.2.2.4). We therefore investigated if the secondary structure of ELPs was affected by the acylation with FAs. The secondary structure of M40, M80, M40-C16 and M80-C16 were analyzed by CD in water at 10°C, that is, below the Tt of M40 and M80, and also at 50°C, *i.e* above Tt (Fig. 7). The spectra were then analyzed and the secondary structure determined using the BeStSel software<sup>29,30</sup> (Table 5).

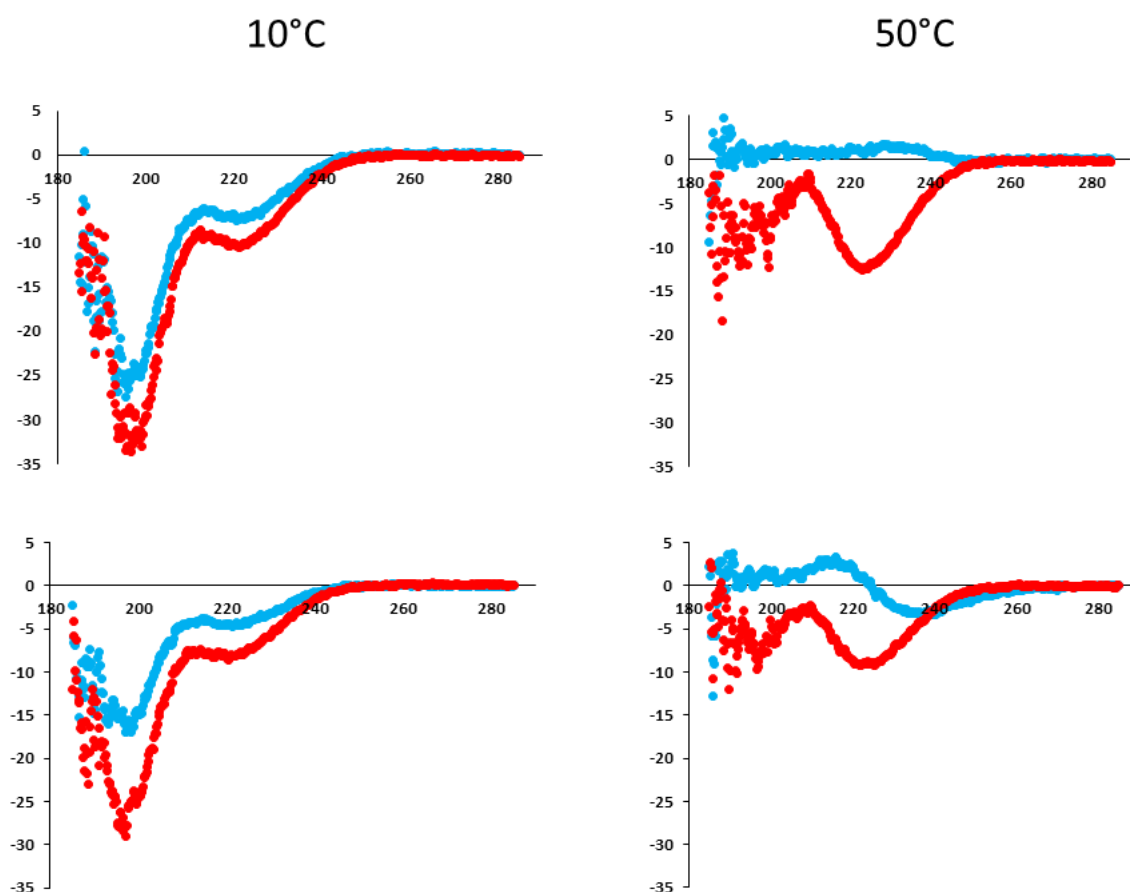


**Figure 8: Circular dichroism spectra of 10  $\mu$ M solutions of M40, M80, M40-C16 and M80-C16 in water. The spectra were recorded at 10°C (left side) and 50°C (right side). Blue traces correspond to non-modified ELPs, red traces correspond to ELP-FAs.**

The spectra obtained for M40 and M80 at 10°C were similar to those previously reported for ELPs below their Tts, with a large negative peak around 190-200 nm, which is characteristic of random-coiled structures and a smaller negative peak around 220 nm<sup>11,31,32</sup>. For these two ELPs, the prediction of secondary structures indicates a majority of antiparallel  $\beta$ -sheets (50-70%), and a smaller proportion of  $\alpha$ -helix (12-17%). When heated above Tt, there is a dramatic change in the secondary structure of the polypeptides with the disappearance of the two negative peaks at 190-200 nm and 220 nm. Such a change can be ascribed to the disappearance of  $\alpha$ -helix, and a moderate diminution of antiparallel  $\beta$ -sheets (-20% of total structures). In addition, the BeStSel software predicts the apparition of  $\beta$ -turns in the structure, which is more important in M80 (60.5 %) than in M40 (7.8 %), probably because of the larger size of the polypeptide.

**Table 5. CD spectra analysis with BeStSel software for secondary structure predictions.**

	Helix	Antiparallel $\beta$	Parallel $\beta$	Turn	Other
M40 10°C	17.4	71.6	0	0	10.9
M40 50°C	0	56.2	0	7.8	36
M40-C16 10°C	23.1	76.9	0	0	0
M40-C16 50°C	25.6	30.6	0	16.3	27.5
M80 10°C	11.8	52.7	0	1.7	33.8
M80 50°C	0	28.8	0	60.5	10.7
M80-C16 10°C	20.9	71	0	0	8.1
M80-C16 50°C	21.6	27.4	0	15.9	36.2

The CD spectra recorded at low temperature for M40-C16 and M80-C16 conjugates are very similar to those recorded for unmodified ELPs, suggesting that ELP acylation did not lead to a profound reshuffle of the secondary structure of the polypeptides. A similar result was previously obtained for myristoylated ELPs, with no change in the secondary structure at low temperature compared to non-myristoylated ELPs<sup>19</sup>. For M40-C16 and M80-C16, around 71-77% of the secondary structure was antiparallel  $\beta$ -sheets, and 21-23%  $\alpha$ -helix. After heating at 50°C, the spectra dramatically changed of secondary structure with a large decrease in antiparallel  $\beta$ -sheets (around – 45% of total structures) concomitant with the apparition of  $\beta$ -turns. The observed changes in secondary structure after heating of ELP-FAs are therefore similar to those observed for unmodified ELPs, confirming that the ELP conformation is globally not altered by acylation. The only difference is that  $\alpha$ -helix disappeared from the ELP structure upon heating, whereas they are conserved (21-26%) in ELP-FAs.

The main conclusion is that the secondary structure of ELP-FAs varies with temperature. Thus, acylation of M-series ELP by long chain fatty acids does not totally alter the thermosensitive nature of the polypeptide, although a minor change does occur as evidenced by the % helix which remained constant during heating, whereas it drastically decreased in the non-acylated ELPs. This contrasts sharply with what was observed for polyisoprene-ELP copolymers, which adopted the same structure whatever the temperature (see section 2.2.2.4).

#### 3.2.2.4. Turbidimetry analyses for determination of cloud point

We next performed turbidimetry experiments at different temperatures (T-scans) to measure the Tts of the 3 ELPs (Fig. 9) and the cloud point temperature (Tcps) of the 15 ELP-FAs (Fig.

10 and Fig. S2). Indeed, we think that the term  $T_{cp}$  was more appropriate for ELP-FAs than  $T_t$  because it corresponds to the temperature of aggregation of the preformed ELP-FAs micelles and not to the temperature triggering micelles formation.

These experiments were performed in PBS buffer because it is similar to human body fluids in terms of ion concentration, osmolarity, and pH. The absorbance of ELP-FAs solutions at 350 nm was monitored when the temperature was ramped up and then down at a rate of 1 °C/min.

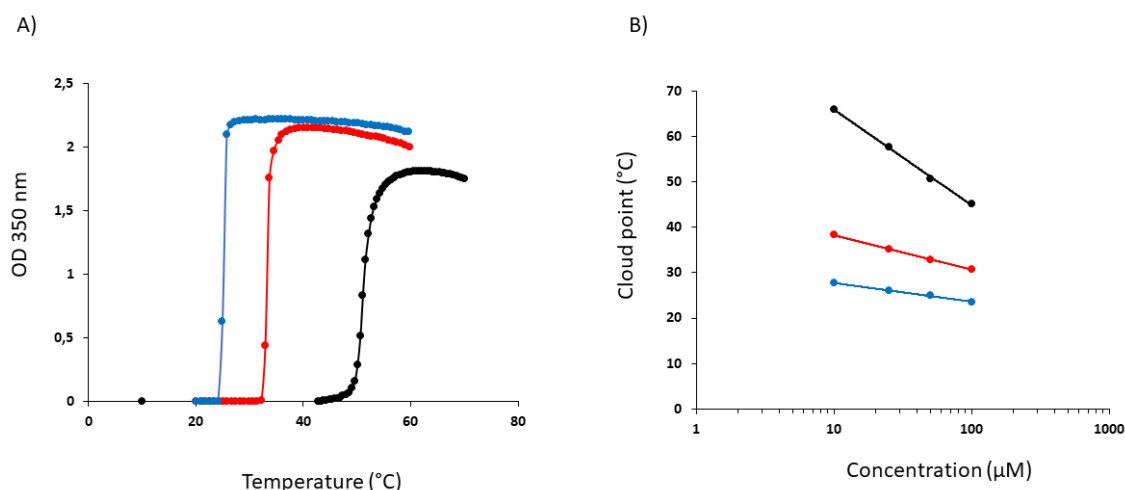


**Figure 9. T-scan analyses of the ELPs M20, M40 and M80 by. A) Solutions of 50  $\mu$ M of M20 (black line), M40 (red line) and M80 (blue line) in PBS B). The cloud point values obtained for different ELP concentrations were plotted versus the Log concentration.**

These results are consistent with those previously obtained in our laboratory<sup>33–35</sup> and in the literature<sup>5</sup>. The  $T_t$  of the ELPs of the M-series is inversely correlated to their chain length (Fig. 9A), and the concentration effect on the cloud point value decreases when the ELP size increase (Fig. 9B).

Results obtained with M40-FAs are shown in Fig. 10, and the other graphs are shown in Fig. S2. The  $T_t$  values determined at four different concentrations for each product are shown in table 6. In addition, the reversibility of the coacervation was verified for the 15 products, and an example is shown for M40-C18:2 in Fig. 11.

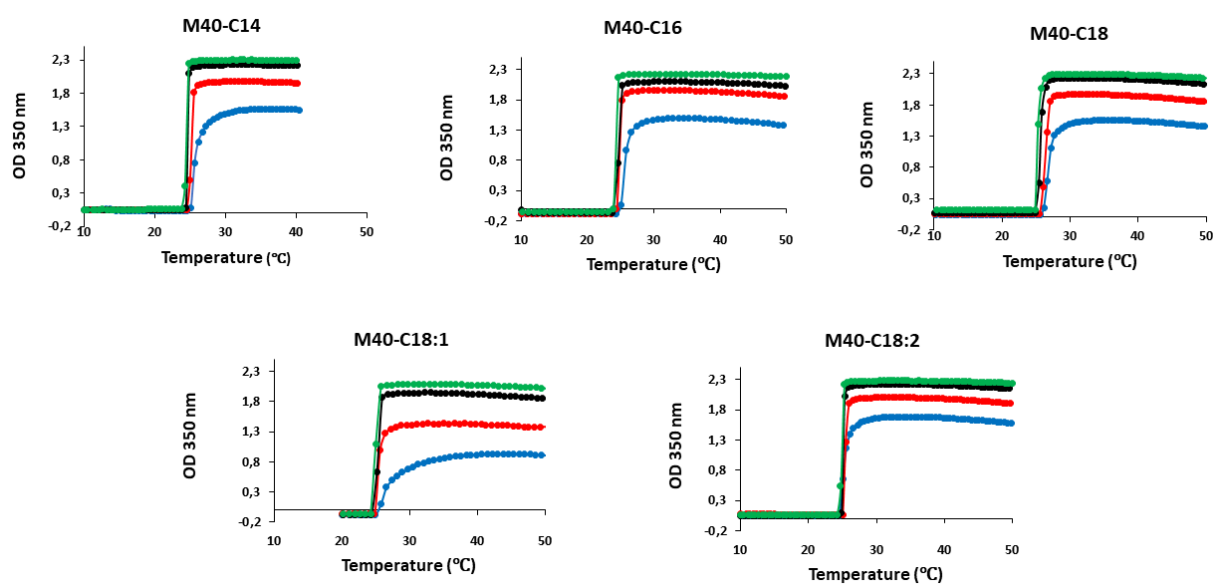


**Figure 10.** Turbidimetry measurements of M20-FA conjugates prepared at different concentrations in PBS during temperature ramps as function of the temperature. Sample concentrations were 100  $\mu\text{M}$  (green), 50  $\mu\text{M}$  (black), 25  $\mu\text{M}$  (red) and 10  $\mu\text{M}$  (blue).

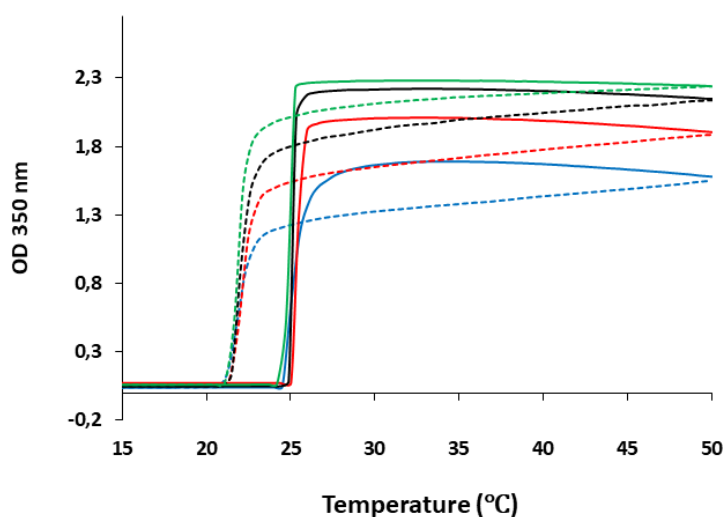


**Figure 11.** T-scans of M40-C18:2 in PBS. Concentration of the sample was 10  $\mu\text{M}$  (blue lines), 25  $\mu\text{M}$  (red line), 50  $\mu\text{M}$  (black line) and 100  $\mu\text{M}$  (green line). Solid lines for the heating ramp, dotted lines for the cooling ramp.

**Table 6. T<sub>cp</sub> values in °C of ELP-FAs at different concentrations in PBS.**

	concentrations	C14	C16	C18	C18:1	C18:2
<b>M20</b>	100 $\mu$ M	33.2	34.4	36.8	34.2	34.8
	50 $\mu$ M	33.9	34.5	37.5	34.9	34.8
	25 $\mu$ M	34	35.2	38.1	35	35.2
	10 $\mu$ M	34.6	35.8	38.8	33.5	36.1
<b>M40</b>	100 $\mu$ M	24.2	23.9	24.8	24.2	24.7
	50 $\mu$ M	24.4	24.6	25.4	25.1	24.9
	25 $\mu$ M	24.9	24.4	26	24.8	25
	10 $\mu$ M	25.1	25	27.7	26.5	24.5
<b>M80</b>	100 $\mu$ M	20	20.4	20.3	19.7	20.5
	50 $\mu$ M	20.1	20.2	20.4	19.9	20.6
	25 $\mu$ M	20.8	20.7	21.1	20.3	20.8
	10 $\mu$ M	20.9	21.1	21.2	20.4	20.9

The T<sub>cp</sub> values measured for ELP-FAs were lower than the T<sub>t</sub> values of the corresponding ELPs. At a concentration of 50  $\mu$ M, T<sub>t</sub> was around 33°C for M40, and T<sub>cps</sub> were around 25°C for all the M40-FAs studied (Fig. 10). Such a decrease after acylation was also observed for the other ELPs (Table 6).

This was expected because it has been demonstrated that an increase in the ELP hydrophobicity results in a decrease in the T<sub>t</sub> value<sup>15</sup>. We were however surprised by the fact that, for the same ELP and concentration, the highest T<sub>cp</sub> was measured for the conjugate containing stearic acid. Indeed, being the most hydrophobic compound, we expected the corresponding T<sub>cps</sub> to be the lowest.

The aggregation of ELP-FAs was fully reversible, the optical density (OD) at 350 nm retrieving its initial value upon cooling (Fig. 11 and Fig. S2). Here again, for a given ELP the transition temperature observed during cooling was almost identical whatever the FA, with a constant temperature hysteresis of about 3.5°C.

Thus, the consequence of acylation is important, but the nature of the FA is less so. On the contrary, the intrinsic hydrophobicity of the ELP moiety is the key parameter driving the phase separation. Indeed, for a given FA, the T<sub>cps</sub> measured for the M80-FAs were respectively 5°C and 13°C lower than those measured for the M40-FAs and M20-FAs. Therefore, if a specific

Tcp is targeted, the size or hydrophobicity of the ELP should be considered before the type of FA.

Another observation is that acylation of ELPs reduces the inverse dependence of Tcp on concentration. When Tcp is plotted versus ELP-FAs concentration on a semi-log scale, the slopes are flatter than that obtained for non-acylated ELPs (Fig. 12).

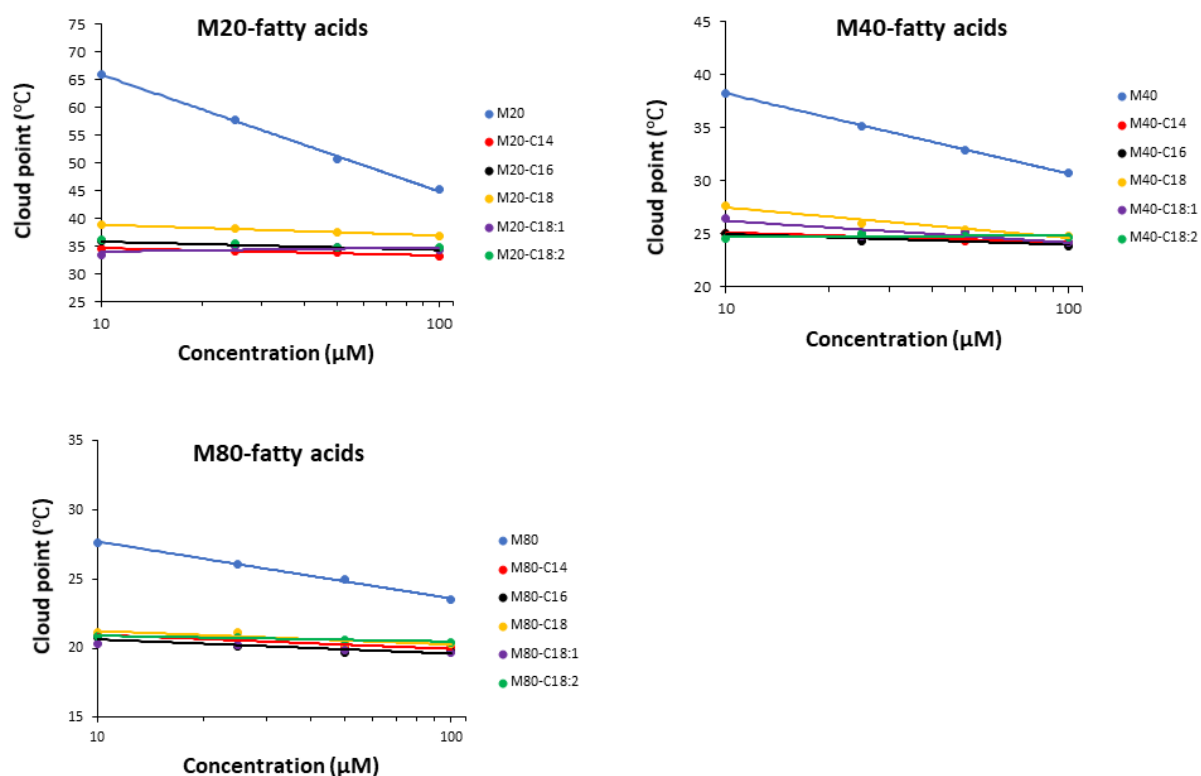


**Figure 12. Concentration dependence of the cloud point temperatures of ELPs and ELP-FAs. ELP (blue), ELP-C14 (red), ELP-C16 (black), ELP-C18 (orange), ELP-C18:1 (purple) and ELP-C18:2 (green).**

Such an effect, already reported for ELP90A,120--C14<sup>15</sup>, has some consequences on the ELP self-assembly<sup>36</sup>. Chilkoti's group previously showed that conjugation of small hydrophobic molecules with  $\text{Log}P > 1.5$  to a hydrophilic ELP resulted in enhanced self-assembly properties, and that Tcps values were almost independent on the conjugate concentration. They raised the hypothesis that the aggregation was controlled by the local ELP concentration within the nanoparticles and not by the total conjugate concentration in solution<sup>37</sup>.

### 3.2.3. Solution self-assembly of ELP-FAs

#### 3.2.3.1. Determination of the critical aggregation concentration

Results obtained by turbidimetry analyses strongly suggested that ELP-FAs could self-assemble. Owing to their composition, made of a water-soluble polypeptide with a fatty-acid tail, we hypothesized that they can form micelles in aqueous solution as was previously showed for other ELP-lipids<sup>15,38</sup>.

The critical micelle concentration (CMC) value, which is characteristic of each micelle-forming compound, was first determined using pyrene as a fluorescent hydrophobic probe<sup>39–41</sup>. CMC measurements were performed in PBS to give some insight about the self-assembly properties of the conjugates in biological fluids. All experiments were performed at 15°C to avoid the desolvation of the ELP moiety.

Fig. 13 shows the variation of the I1/I3 ratio obtained for M80-C16, where I1 and I3 correspond to the intensity of the first and third vibronic peaks of pyrene<sup>42,43</sup>.

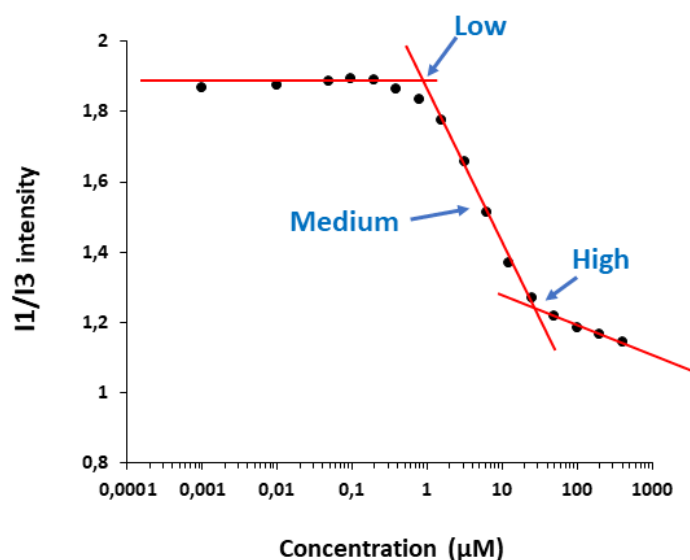


**Figure 13.** Variation of the I1/I3 ratio for M80-C16 as function of the ELP-FAs concentrations in PBS at 15°C. Three self-assembly regimes are depicted as low, medium and high CMC.

The sigmoidal aspect of the I1/I3 plot is typical of surfactants or amphiphilic block

copolymers<sup>39</sup>. Below the CMC the pyrene 1:3 ratio value corresponds to a polar environment. As the surfactant concentration increases, the 1:3 ratio decreases indicating that the pyrene is in a more hydrophobic environment. Thereafter, the ratio stabilized to a constant value because of the incorporation of the probe into the hydrophobic region of the micelles. For the determination method of the CMC value, some authors used the point labelled as “high” in Fig. 13, which corresponds to the interception of the second and third linear part of the plot<sup>44,45</sup>. This point corresponds to a surfactant concentration for which all the monomers are self-assembled. On the contrary, some consider the CMC as the interception of the first and second part of the plot, the so-called “low” CMC, which corresponds to the formation of pre-micellar aggregates. This latter is thought to be more appropriate for surfactants with low CMC, below 1 mM<sup>46</sup>. In some instance, the CMC value was determined as the middle point between “Low” and “High” (labelled medium in Fig. 13).

We measured the three CMC values for the 15 ELP-FAs studied (Fig S3 and Table 7). “Low” CMC values varied between 0.7 and 2  $\mu$ M, and “high” CMC values between 11 and 49  $\mu$ M. These values are rather low when compared to molecular surfactants for which CMC are typically in the mM range<sup>47</sup>, but similar to those previously measured for myristoylated ELP. The “Low” CMC values for C14-ELP<sub>90A,120</sub>, C14-ELP<sub>90A,80</sub>, C14-ELP<sub>90A,40</sub>, and C14-ELP<sub>100V,40</sub> were respectively 5.1, 3.2, 3.4 and 5.3  $\mu$ M<sup>15</sup>. Therefore, ELP-FAs are rather hydrophobic compounds.

**Table 7 High (H), medium (M) and low (L) CMC values in PBS at 15°C for the 15 ELP-FAs studied. CMC values are given in  $\mu$ M.**

	C14			C16			C18			C18:1			C18:2		
	L	M	H	L	M	H	L	M	H	L	M	H	L	M	H
<b>M20</b>	<b>1.9</b>	<b>8.2</b>	<b>36</b>	<b>1.1</b>	<b>6.2</b>	<b>36</b>	<b>0.9</b>	<b>4.0</b>	<b>18</b>	<b>1.5</b>	<b>7.9</b>	<b>42</b>	<b>2.0</b>	<b>9.8</b>	<b>49</b>
<b>M40</b>	<b>1.9</b>	<b>7.7</b>	<b>31</b>	<b>1.3</b>	<b>6.0</b>	<b>29</b>	<b>0.7</b>	<b>3.7</b>	<b>19</b>	<b>1.3</b>	<b>6.9</b>	<b>36</b>	<b>1.6</b>	<b>7.6</b>	<b>36</b>
<b>M80</b>	<b>1.6</b>	<b>7.0</b>	<b>32</b>	<b>0.9</b>	<b>4.8</b>	<b>26</b>	<b>0.8</b>	<b>2.9</b>	<b>11</b>	<b>1.3</b>	<b>5.5</b>	<b>24</b>	<b>1.3</b>	<b>6.3</b>	<b>30</b>

To get insights into the effect of the ELP size and/or of the fatty acid nature, we graphically represented the low and high CMC values of the 15 compounds (Fig. 14).

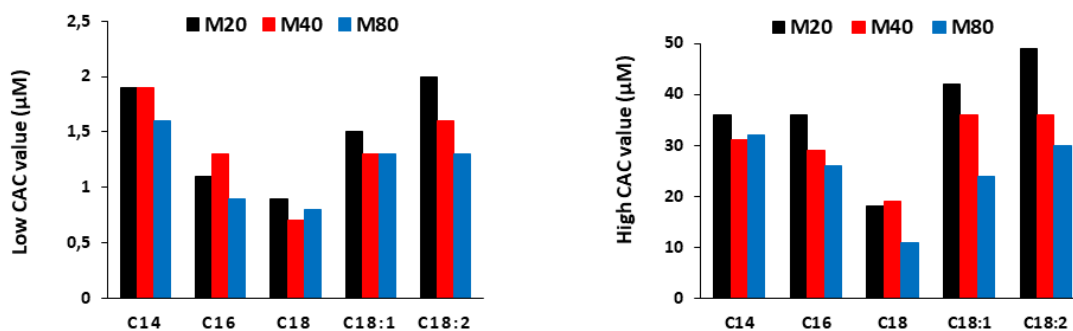


**Figure 14. CMC values for M20-FAs (black), M40-FAs (red) and M80-FAs (blue).**

Although not identical, the graphs obtained with the two CMC values showed similar trends. When the length of the saturated fatty acid chain increased, the CMC values decreased. The lowest values were always measured with C18 whatever the size of the ELP moiety. The presence of unsaturation in the C18 chain led to an increase in the CMC value, this increase being somewhat proportional to the level of unsaturation (see C18.1 vs. C18.2).

A general trend can also be observed for the ELP moiety. In most cases, the lowest CMC value for a given FA was obtained for ELP M80, and the highest for ELP M20. However, the differences in CMC values between two ELPs acylated by the same FA were much lower than those between a given ELP acylated by different FAs. Thus, the main driving force for the self-assembly of ELP-FAs at 15°C, *i.e.*, below the  $T_{cp}$ , clearly comes from the hydrophobicity of the FAs. Finally, the “low” CMC values measured for the 15 ELP-FAs were below 3 µM, that is, below the 10 µM concentration used to determine the  $T_{cp}$  by turbidimetry. This confirms that the  $T_{cp}$  determined during turbidity experiments corresponds to the aggregation of premicellar ELP-FA structures already formed at low temperatures.

### 3.2.3.2. Determination of the size of the self-assembled material by DLS

The size of the self-assembled ELP-FA particles was determined by DLS. First, we measured the size at low temperature (15°C) in PBS, below the  $T_{cp}$ . We chose a concentration of 5 mg/mL which corresponds to molar concentrations of 560  $\mu\text{M}$ , 290  $\mu\text{M}$  and 147  $\mu\text{M}$  for M20-FAs, M40-FAs and M80-FAs, respectively. The concentration of 5 mg/mL, which is much higher than the ‘high’ CMC values (Table 7), was required to have enough scattering intensity to perform DLS measurements in good conditions. A typical result obtained for M80-C16 in PBS at 15°C is shown in Fig. 15.

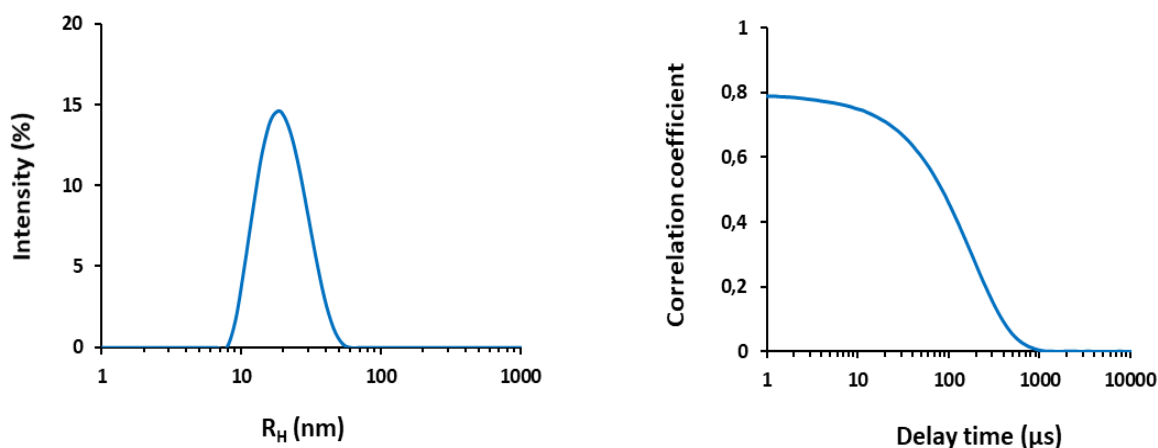


**Figure 15. DLS analysis M80-C16. A solution of M80-C16 at 5 mg/mL in PBS (147  $\mu\text{M}$ ) was analyzed at 15°C.**

At temperature below  $T_{cp}$ , M80-C16 formed nanoparticles with a hydrodynamic radius ( $R_H$ ) of about 21 nm, a typical size for micelle structures. The PDI value of 0.116 suggested that no significant amounts of large aggregates were present in the solution. Similar experiments were performed for the 15 conjugates, and the corresponding  $R_H$  and PDI values are shown in Table 8.

**Table 8.  $R_H$  (nm) and PDI values of ELP-FAs in PBS measured by DLS at 15°C**

		ELP-C14	ELP-C16	ELP-C18	ELP-C18:1	ELP-C18:2
M20-fatty acid	$R_H$	9	9	11	10	9
	PDI	0.029	0.030	0.022	0.054	0.018
M40-fatty acid	$R_H$	14	16	18	15	16
	PDI	0.104	0.188	0.056	0.134	0.172
M80-fatty acid	$R_H$	18	21	23	19	18
	PDI	0.074	0.116	0.075	0.080	0.046

A graphical representation is shown in Figure. 16.

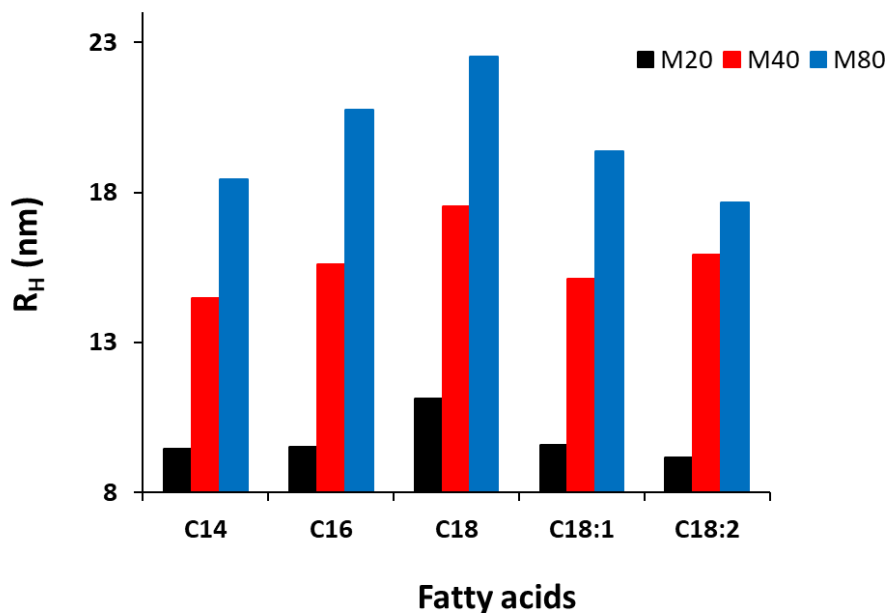


**Figure 16.  $R_H$  values (% intensity) of the 15 ELP-FAs measured at 15°C (5 mg/mL in PBS).**

For the 15 ELP-FAs studied, only one homogeneous population of objects was detected in PBS at 15°C, as confirmed by the PDI values ranging between 0.02 and 0.19. These nanoparticles varied in size according to the nature of the FAs and the size of the ELPs.

Regarding FAs, the size of the particles increased proportionally to the length of the carbon chain. The increases in  $R_H$  between the ELP-C14 and ELP-C18 were +17%, +21% and +22% for respectively M20, M40 and M80. On the contrary, when unsaturation is introduced into the stearic chain, the  $R_H$  decreased. This can be explained by the fact that double bonds introduce a bending of the acyl-chain, and therefore that the overall length is decreased (Fig. 17).

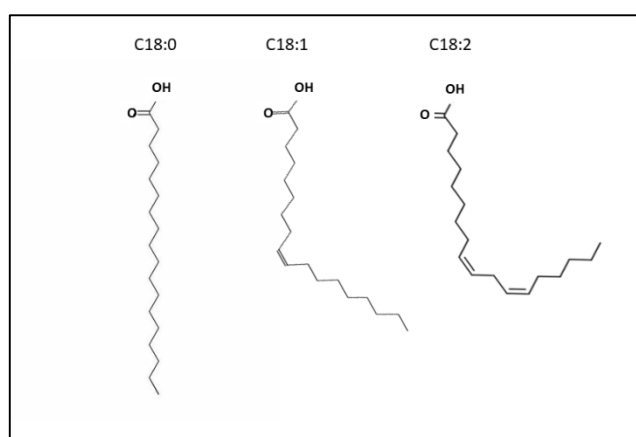


**Figure 17. Schematic representation of stearic, oleic and linoleic fatty acids.**

Our results also show that the size of the nanoparticles mainly depends on the molecular mass of the ELP. The  $R_H$  of M20-FA micelles are around 10 nm, in the range 14-18 nm for M40-FAs, and 18-23 nm for M80-FAs. In addition, for a given FA the micelles obtained with the M80 conjugate were always the largest, and the micelles of the M20 conjugate the smallest.

These results are different from those published for myristoylated ELPs<sup>15</sup>. Indeed, Luginbuhl and collaborators studied the effect of the length of the ELP on the morphology of the self-assembled nanoparticles. They engineered three ELP-C14 (ELP<sub>90A,120</sub>, ELP<sub>90A,80</sub> and ELP<sub>90A,40</sub>), and measured the higher CMC value for the larger ELP<sub>90A,120</sub> (5.1  $\mu$ M), whereas these values were around 3.2  $\mu$ M for the smaller ones. In our system, the lower CMC value was always measured for the larger ELP (M80) whatever the nature of the fatty acid. In addition, these authors measured by DLS smaller  $R_H$  for the ELP<sub>90A,120</sub> (22.7 nm) than for the shorter ELP<sub>90A,40</sub> (81.9 nm). They explained this difference by the fact that ELP<sub>90A,40</sub>-C14 formed rod-

like micelles whereas ELP<sub>90A,120</sub> formed spherical micelles. We did not observe this behavior with the ELP used in our study,  $R_H$  increasing with the ELP size. We cannot offer any definitive explanation for the differences observed between the two studies, however, some differences in the ELP design should be pointed out. In the work of Luginbuhl and colleagues, the N-terminal sequence of each ELP contains the NMT recognition sequence, which corresponds to the peptide Gly-Leu-Tyr-Ala-Ser-Lys-Leu-Phe Ser-Asn-Leu. This peptide is rather hydrophilic and contains one positive charge on the lysine residue at physiological pH. In addition, the overall hydrophobicity of the sequence VPGAG used to build the ELP<sub>90A</sub> series (GAVY = 0.72) is lower than that of our ELPs made of repeats of VPGVG and VPGMG (GRAVY = 1.085). Altogether, we can raise the hypothesis that the difference seen between both studies might come from the use of ELPs with different solubility, and therefore that the hydrophobic or hydrophilic nature of the polypeptide could be a determinant factor for the morphology of the ELP-FA micelles.

In conclusion, our results showed that it is possible to fine-tuned the size of ELP-FA micelles by playing either with the FA chain length and saturation, or with the size of the ELP.

We then evaluate the stability of the micelles in PBS upon storage at 4°C for several days. This experiment was performed with the M80-C16. (Fig. 18).

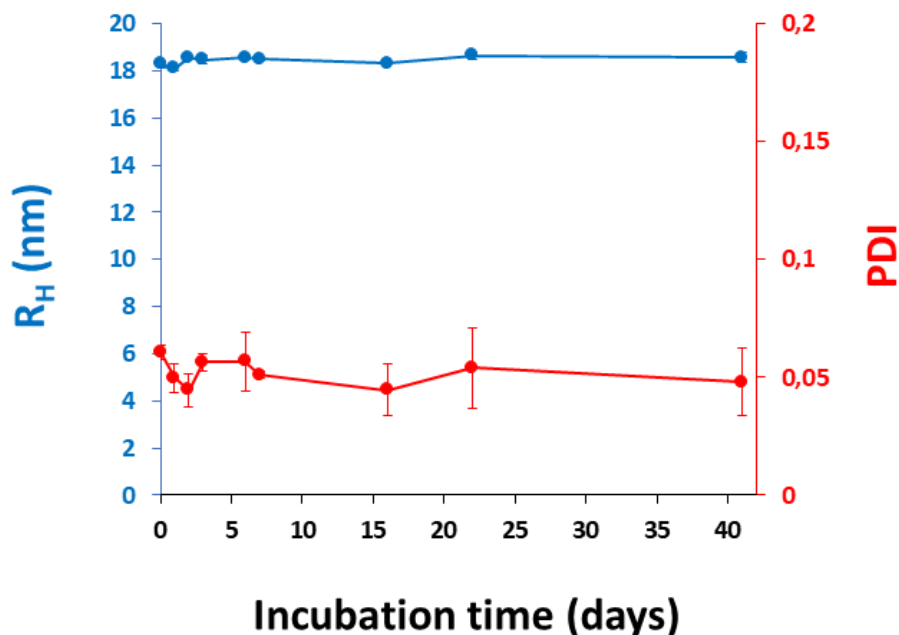


**Figure 18. Stability of M80-C16 micelles upon storage at 4°C in PBS buffer. M80-C16 was solubilized into PBS at a concentration of 5 mg/mL (147 μM). The sample was stored at 4°C, and R<sub>H</sub> (nm) and PDI were recorded at 15°C. For each value, data are mean of three measures ± SD.**

This experiment shows that the M80-C16 micelles were stable for the whole period studied, with no significant increase in R<sub>H</sub> or PDI.

To understand the stability of the nanoparticles, we measured their surface charge. We could not precisely measure the Zeta potential of the nanoparticles in PBS, due to the high salt concentration of the buffer, but we measured a Zeta value of -15.4 mV for the M80-C16 micelles in water, confirming that the crown was negatively charged in water (Fig. 19).

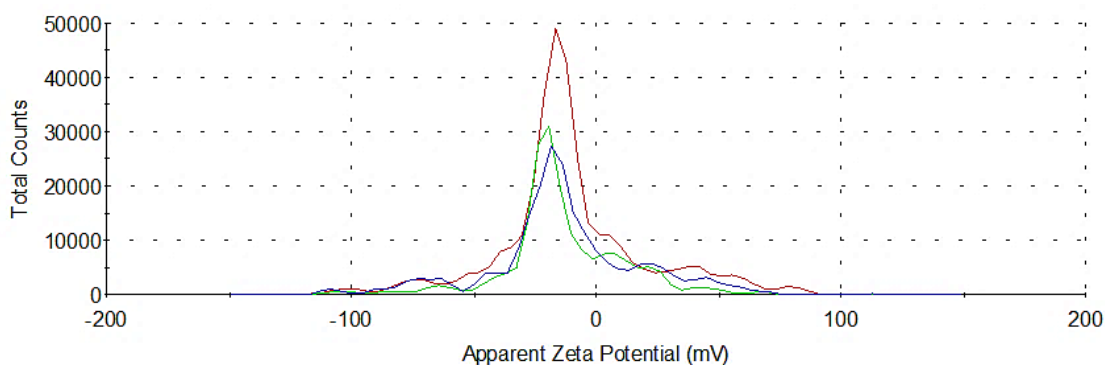


**Figure 19. Zeta measurement of M80-C16 micelles. Zeta measurement was done with a Nano ZS instrument (Malvern U.K.) using the signal processing M3-PALS technique. Zeta potential range was  $> \pm 200$  mV, and maximum sample concentration was 40% w/v. Data were analyzed with the Zetasizer software. The figure shows the results obtained after three measurements of the same sample.**

When ELP-FAs self-assembled into micelles the corona is made of the ELP. Acylation of the ELP taking place at its N-terminus, the C-terminus is therefore exposed to the solvent. The pKa of the corresponding carboxyl group being  $< 4$ <sup>48</sup>, negative charges will be present at the surface of the nanoparticles in PBS buffer (pH 7.2), and these negative charges prevents particles aggregation by electrostatic repulsion. In addition, it has been previously demonstrated that when a hydrophobic material is placed in water, the OH<sup>-</sup> ions which are present in solution bind to the interface of the material, and therefore provide a negative charge on the particle surface<sup>49</sup>.

We then studied the effect of temperature on the size of the micelles. Knowing from turbidimetry experiments that those micelles aggregate above their T<sub>cp</sub>, these DLS heating experiments were performed at concentrations of 1 mg/mL in PBS buffer. Results obtained for the M80-C16 are shown in Fig. 20, and in Fig. S4 for the other M80-FA conjugates.

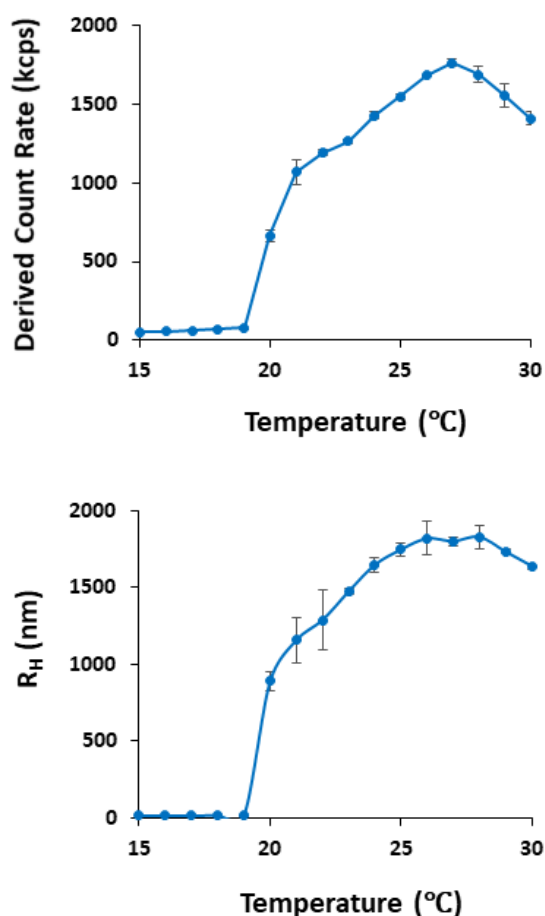


**Figure 20. DLS measurements during a temperature ramp. A solution of M80-C16 at a 1 mg/mL concentration (29  $\mu$ M) was incubated into PBS buffer, and DLS measurements were recorded between 15 and 30  $^{\circ}$ C. Scattered intensity expressed as derived count rate versus temperature. For each value, data are mean of three measures  $\pm$  SD.**

These experiments confirmed the results obtained by turbidimetry. Below the  $T_{cp}$ , we have one homogeneous population of micelles with  $R_H$  around 20 nm, which when heated above  $T_{cp}$  aggregated to form micron-sized objects. The  $T_{cp}$  measured by DLS at 20  $^{\circ}$ C is close to the one measured by turbidimetry for M80-C16 at 25  $\mu$ M (20.67  $^{\circ}$ C, see table 6). The decrease in scattered intensity observed in Fig. 20 after 27  $^{\circ}$ C might indicate that these large objects started to sediment at the bottom of the cuvette. Table 9 shows the results obtained for the other M80-FAs at  $T^{\circ} > T_{cp}$  in PBS

**Table 9. DLS analyses of M80-FAs nanoparticles at 25°C in PBS (1 mg/mL concentration)**

	<b>M80-C14</b>	<b>M80-C16</b>	<b>M80-C18</b>	<b>M80-C18:1</b>	<b>M80-C18:2</b>
<b>Rh(nm)</b>	<b>1730</b>	<b>1899</b>	<b>1684</b>	<b>1623</b>	<b>1816</b>
<b>PDI</b>	<b>0.115</b>	<b>0.111</b>	<b>0.045</b>	<b>0.123</b>	<b>0.094</b>

For all the acyl-M80 conjugates studied, we observed large micron-sized particles when the samples were incubated at 25°C, which strongly suggests the aggregation of micelles due to their ELP crowns. The fact that the PDI values are low cannot be attributed to a good polydispersity of the aggregates, but rather to the fact that DLS analyzes are not well suited to the study of micrometer-sized objects.

### **3.2.3.3. Effect of salts on self-assembly of ELP-FAs**

To have a better view of the morphology of the nanoparticles, we wished to perform TEM experiments. However, it was not possible to use samples dispersed into PBS, which composition is as follows: Na<sub>2</sub>HPO<sub>4</sub> 10 mM, KH<sub>2</sub>PO<sub>4</sub> 1.8 mM, KCl 2.7 mM and NaCl 137 mM. The salt content of this buffer being high, crystals formed during the preparation of the sample preventing the obtaining of good quality images. Consequently, we chose another buffer, Tris 10 mM pH 7.2, which does not contain significant amounts of salts. However, a prerequisite was to demonstrate that ELP-FAs formed nanoparticles when placed in Tris buffer, and that these nanoparticles were similar to that obtained in PBS.

First, we performed turbidimetry experiments (Fig. 21 and Fig. 22).

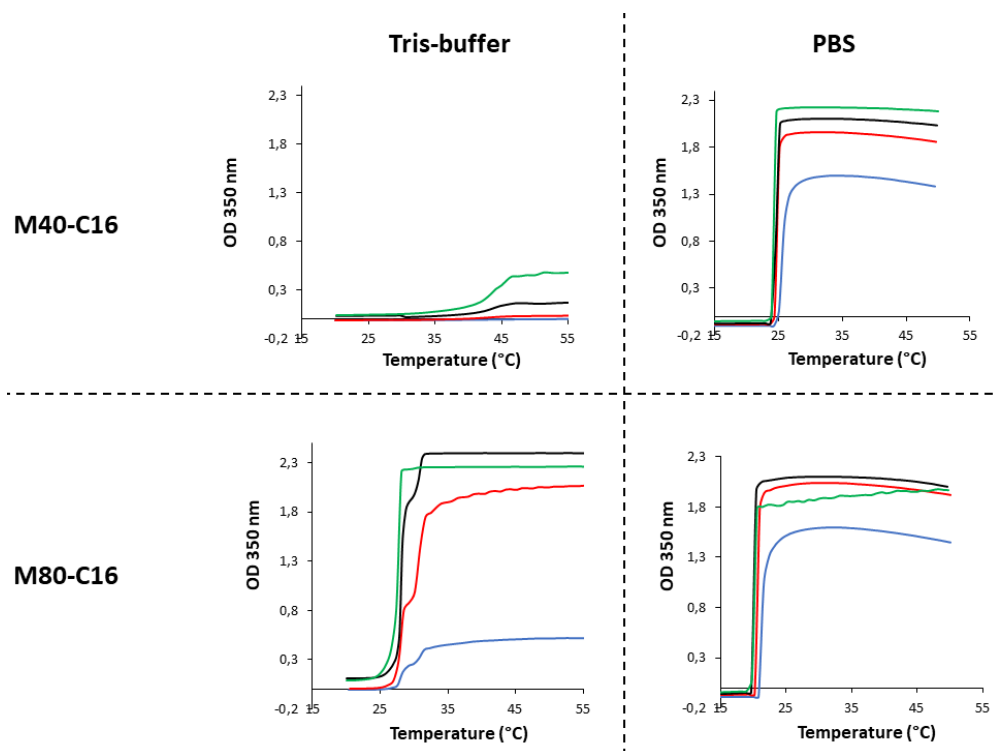


Figure 21. Turbidimetry experiments of M40-C16 and M80-C16 in Tris buffer. Concentration of the samples were 10  $\mu\text{M}$  (blue lines), 25  $\mu\text{M}$  (red line), 50  $\mu\text{M}$  (black line) and 100  $\mu\text{M}$  (green line).

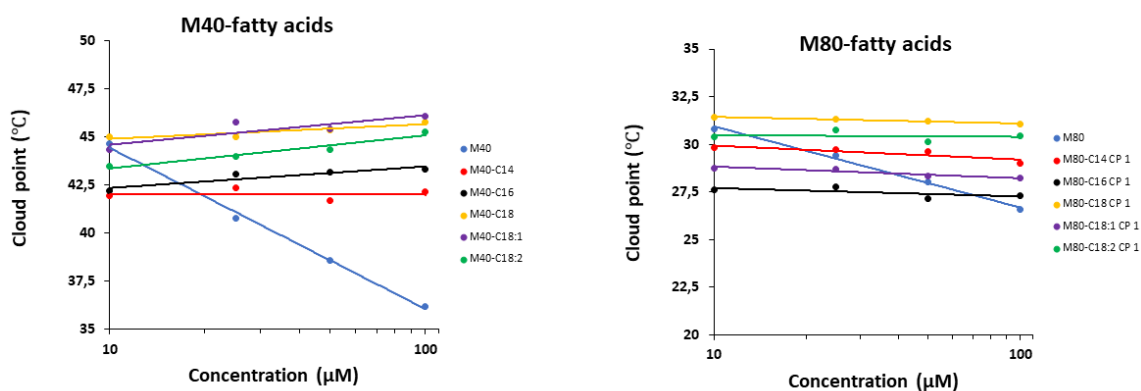


Figure 22. Concentration dependence of the cloud point temperatures of ELPs and ELP-FAs in Tris buffer. ELP (blue), ELP-C14 (red), ELP-C16 (black), ELP-C18 (orange), ELP-C18:1 (purple) and ELP-C18:2 (green).

In terms of independence of the  $T_{cp}$  value regarding the concentration of the sample, the results obtained in Tris buffer were similar to those previously obtained in PBS. However, several differences were also noticed.

First, the  $T_{cp}$  values of ELP-FAs were several degrees above those measured in PBS (compare Fig. 22 and Fig. 12). This was expected because it has been demonstrated that  $T_{cp}$  values decrease when salt concentration increases<sup>50</sup>.  $T_{cp}$  values in PBS were around 25°C for M40-FAs and 20°C for M80-FAs, whereas they are respectively in the ranges 40-45°C and 26-35°C in Tris buffer. In addition, we were not able to detect any increase in OD for the M20-FAs when temperature was increased from 20 to 60°C (Fig. S5).

Another variation comes from the difference in  $T_{cp}$  values between the non-acylated ELP and their acylated forms. In PBS,  $T_{cp}$  values were significantly lower (-5 to -15°C) for ELP-FAs than the  $T_t$ s of the ELPs (see Fig. 12). This was attributed to the increase in hydrophobicity resulting from the coupling of the fatty acid moiety. We did not observe such a  $T_{cp}$  decrease in Tris buffer, those of M40-FAs and M80-FAs being even higher than the  $T_t$ s of M40 and M80 at high concentrations. From our point of view, the difference observed with the two buffers is explained by the fact that the main driving force of monomer aggregation (ELP) or micelle aggregation (ELP-FA) comes from the ELP, and therefore any factor that will affect the  $T_t$  of ELP, such as salt concentration, will change the  $T_{cp}$  value of the corresponding ELP-FAs.

A third difference was that the maximal OD values obtained when the samples were heated above the  $T_{cp}$  were much lower in Tris buffer than in PBS. This is obvious for M40-C16, with a maximal OD of 0.5 for 100  $\mu$ M in Tris buffer, and a maximal OD of 2.2 in PBS. This strongly suggests that the transition from micelles to large aggregates  $> 1 \mu$ m observed in PBS upon heating does not take place in Tris buffer. In this case, the small increase in OD observed above  $T_{cp}$  cannot be attributed to the formation of large aggregates. This was confirmed by visual inspection of the cuvettes. After heating in PBS, the solution was highly turbid and opaque, whereas the solution remained quite transparent after heating in Tris buffer. Quite a similar phenomenon was observed for M80-C16, although the difference in the T-scans obtained between the Tris and PBS conditions was only evident at low concentration (below 25  $\mu$ M).

Another intriguing result was obtained with the M80-C16 samples. In Tris buffer, we observed a two-step transition during temperature ramps, suggesting that two different mechanisms took place (Fig. 21). We do not believe this to be an artifact as the same behavior has been observed for other M80-C14 and M80-C18:1 during heating and cooling ramps (Fig. 23).

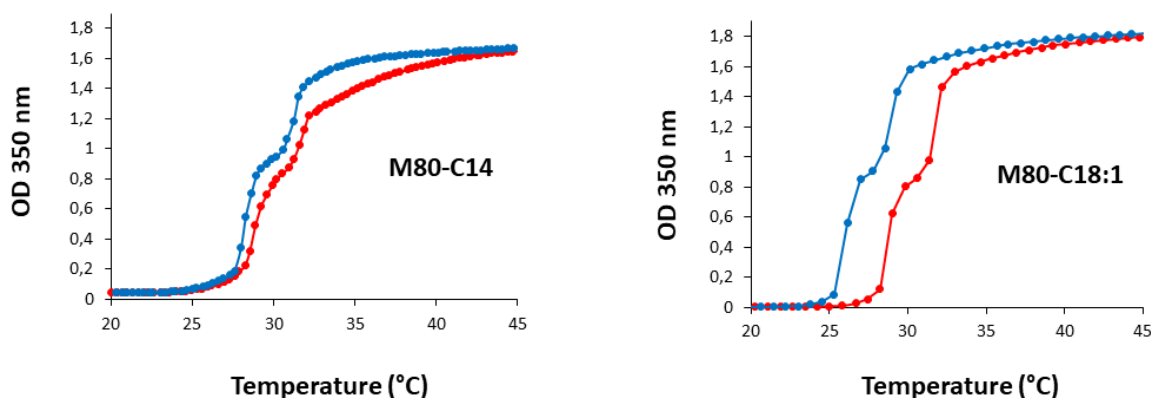


**Figure 23.** Turbidimetry experiments of M80-C16 and M80-C18:1 in Tris buffer. M80-C14 and M80-C18:1 were solubilized at a final concentration of 25  $\mu\text{M}$  in Tris 10 mM pH 7.2. Data recorded during heating (red lines) and cooling (blue lines) ramps.

So in the case of M80-FAs, two Tcps can be measured, each one corresponding to a specific transition. These values are shown in Table 10.

**Table 10.** T<sub>cp</sub> values (°C) of M80-FA conjugates at different concentrations in Tris buffer.

		M80-C14	M80-C16	M80-C18	M80-C18:1	M80-C18:2
50 $\mu\text{M}$	Tt1	29.6	27.8	31.2	28.3	30.1
	Tt2	32.2	30.6	35.3	30.7	33.3
25 $\mu\text{M}$	Tt1	29.7	27.8	31.3	28.7	30.8
	Tt2	32.3	30.1	35.5	31.1	32.8
10 $\mu\text{M}$	Tt1	29.8	27.6	31.4	28.8	30.4
	Tt2	32.9	30.8	36.2	31.1	32.4

These data show that for a given M80-FA, both Tcps were independent of concentration. To try to better understand the self-assembly of M80-FA in Tris buffer, we performed DLS measurements. At low temperature, we obtained only one population of nanoparticles the  $R_H$  of which varied between 16 and 24 nm (Table 11)

**Table 11. Comparison of  $R_H$  values for M80-FAs in PBS and Tris buffer at 15°C**

		M80-C14	M80-C16	M80-C18	M80-C18:1	M80-C18:2
Tris buffer	$R_H$ (nm)	19	21	24	20	17
	PDI	0.102	0.192	0.140	0.215	0.051
PBS	$R_H$ (nm)	18	21	23	19	18
	PDI	0.074	0.116	0.075	0.080	0.046

*Sample concentration was 5 mg/mL (147  $\mu$ M)*

This experiment shows that the sizes of M80-FA micelles were similar when measured in the two buffers at low temperature. As previously observed for PBS, the  $R_H$  measured in Tris buffer increased with increasing fatty acid chain length, and decrease with the number of unsaturation. Therefore, at low temperature, the size of the M80-FA nanoparticles is independent from the salt content of the solution. We also verified that these nanoparticles were stable when stored at 4°C in Tris buffer (Fig. S6).

Thereafter, we did DLS measurement with M80-C16 during temperature increase (Fig. 24).

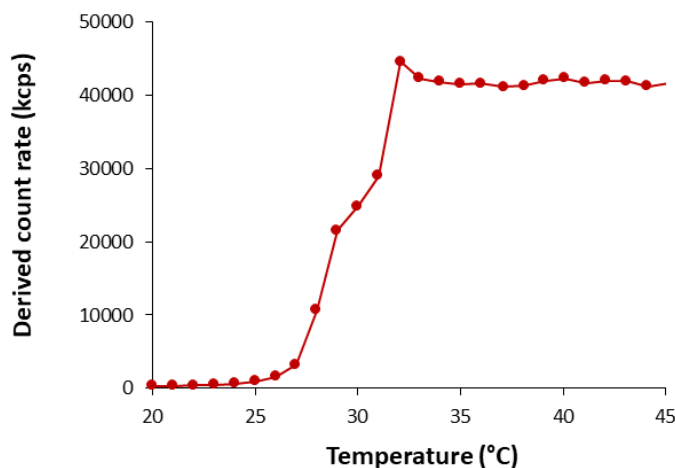


**Figure 24. DLS measurements of M80-C16 in Tris buffer during a temperature ramp. A solution of M80-C16 at a 5 mg/mL concentration (147  $\mu$ M) was incubated in Tris buffer, and DLS measurements were recorded between 20 and 45 °C. Scattered intensity expressed as derived count rate versus temperature.**

As observed for the turbidimetry experiments, we obtained a biphasic curve when the scattered intensity was plotted versus temperature.

To have better insight into the changes occurring during this double transition,  $R_H$  was measured between 25°C and 33°C (Fig. 25).

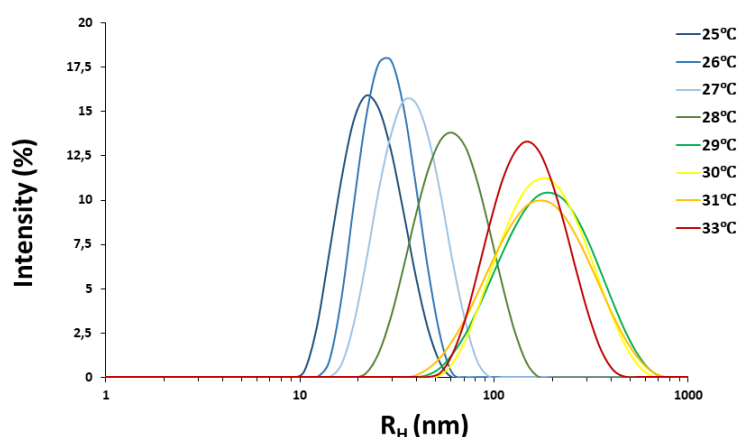


**Figure 25.  $R_H$  measurements of M80-C16 in Tris buffer between 25 and 33°C. A solution of M80-C16 at a 5 mg/mL concentration (147  $\mu$ M) was incubated in Tris buffer, and DLS measurements were recorded at different temperatures.**

We observed that the  $R_H$  value increases between 25°C and 30°C, from 20 nm to about 200 nm. Additional heating of the sample to 33°C did not significantly change this value. We can therefore hypothesize that the first increase in DCR observed in Figure 24 between 25°C and 30°C corresponded to an increase in the size of the M80-C16 nanoparticles, and that the second increase in DCR between 30°C and 33°C could be attributed to further dehydration of the hydrophobic core leading to higher density and hence increased light scattering.

Anyway, the heating of M80-C16 micelles in Tris buffer did not result in the formation of large aggregates as those formed in PBS, but triggered the apparition of particles of ~200 nm that could be either large micelles or vesicles. This assembly mechanism was reversible, micelles of  $R_H \sim 20$  nm being recovered after cooling.

In conclusion, we showed that the size of ELP-FA micelles is similar when measured at low temperature in PBS or Tris buffer. However, when the temperature is increased above  $T_{cp}$ , the micelles self-aggregate in high salt solution, whereas they form uncharacterized objects of

$R_H \sim 150-200$  nm in weakly ionic buffer. Of course, it would be very interesting to better characterize these objects in a future work.

#### 3.2.3.4. Morphology of ELP-FA micelles

The morphology of the ELP-FA micelles was observed by TEM. As previously explained, the corresponding samples were dissolved in Tris buffer, and incubated at 4°C before being deposited on the TEM grid.

We used negative staining, so the particles appeared white on a dark background (Fig. 26).

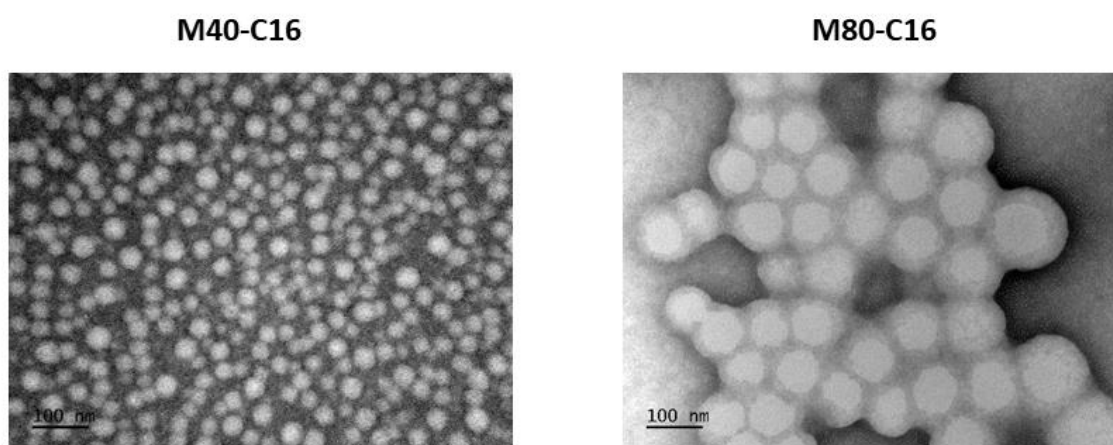


**Figure 26. TEM images of M40-C16 and M80-C16 micelles. Scale bars 100 nm.**

The images obtained for these two samples show that they are spherical micelles. The size of approximately 20 nm in radius obtained for M40-C16 was consistent with that measured by DLS ( $R_H \sim 20$  nm), whereas that measured for the M80-C16 micelles, 40-50 nm in radius, was larger than that previously measured ( $R_H \sim 20$  nm by DLS). To explain this discrepancy, we hypothesized that the  $T^\circ$  being difficult to control during the preparation of the samples for microscopy, it may have increased slightly during the drying step leading to an increase in the size of the micelles of M80-C16 as previously observed in Tris buffer (see Fig. 25).

### 3.2.4. Encapsulation and release of a hydrophobic molecule

We next evaluated the potential of ELP-FA micelles to encapsulate and release a hydrophobic molecule. Our main objective was to investigate the role of the FA chain length. We therefore focused on M80-FAs because we previously showed that they form larger nanoparticles than the M40-FAs and M20-FAs, and thus could encapsulate more hydrophobic molecules. As a model of hydrophobic molecule, we chose Nile red because it fluoresces when placed into a hydrophobic environment, which is a convenient way to measure its encapsulation.

The encapsulation efficiency was first evaluated. Briefly, M80-FAs were dissolved in PBS at a concentration of 1 mg/mL, and incubated with Nile red (2  $\mu$ M) for 24 hours at 10°C. Then, the solution was centrifuged to eliminate the unincorporated Nile red, which aggregates in aqueous solvent because of its insolubility ( $\text{Log}P$  2.8). The supernatant containing the nanoparticles was freeze-dried, and the material was resuspended in DMSO before being analyzed with a fluorimeter. The concentration of Nile red was calculated by comparing the results with a standard curve of Nile red in DMSO (Fig. S7). A negative control was performed in the absence of nanoparticles. The fluorescence data were then used to calculate the encapsulation efficiency, which is the percentage of initial Nile red quantity (127 ng) that was incorporated by 200 ng of M80-FAs micelles (Table 12).

**Table 12.** Nile red encapsulation of M80-FAs micelles

	<b>M80-C14</b>	<b>M80-C16</b>	<b>M80-C18</b>	<b>PBS control</b>
<b>Fluorescence intensity (611 nm)</b>	<b>4767</b>	<b>7277</b>	<b>10235</b>	<b>110</b>
<b>Nile red quantity (ng)</b>	<b>26</b>	<b>39.7</b>	<b>55.8</b>	<b>0.6</b>
<b>Encapsulation efficiency (%)</b>	<b>20.4</b>	<b>31.2</b>	<b>43.8</b>	<b>0.4</b>

This experiment clearly showed that the fatty acid chain length is an important factor for the encapsulation of Nile red into our micelles. From our point of view, this is not directly related to the fact that the longer the acyl chain, the more Nile red accumulate because of a more favorable hydrophobic environment. Our hypothesis is rather that the size of the micelles increased proportionally to the length of the acyl chains creating more room for the Nile red accumulation.

The encapsulation efficiency of M80-FA micelles (20-40%) was higher than that measured for the encapsulation of doxorubicin by a myristoylated ELP-C14 (3-5%)<sup>15</sup>. However, these figures cannot be directly compared because the hydrophobicity of the encapsulated molecules are quite different, the Log*P* values being respectively 2.8 and 1.3 for Nile red and doxorubicin. Therefore, owing to its higher hydrophobicity, Nile red might have a better avidity for the hydrophobic core of our M80-FAs micelles.

The next step was to measure the Nile red release from the micelles. In this case, after encapsulation of Nile red the samples were dialyzed for several hours in PBS buffer at 10°C, and fluorescence intensity of the samples were measured at different times (Fig. 27).

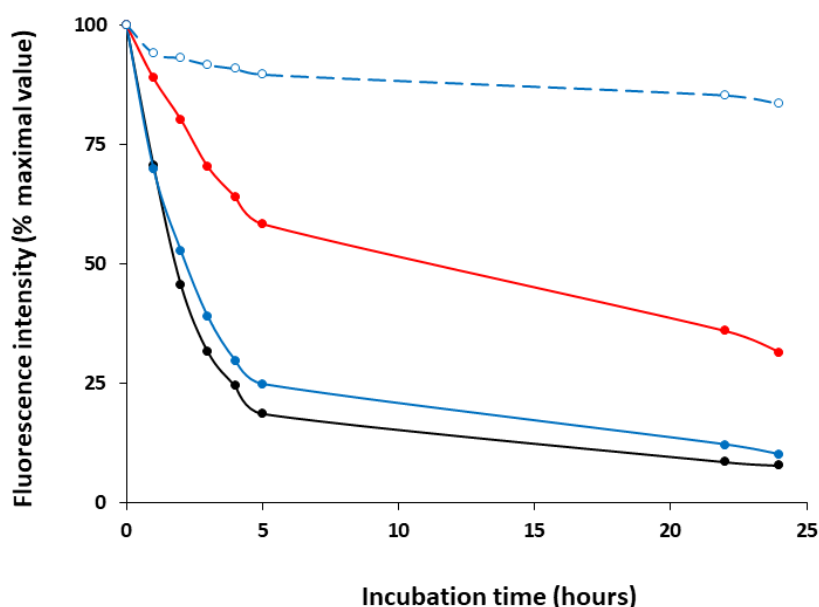


**Figure 27. Fluorescence of the encapsulated Nile red versus time.** 1 mL of Nile red-loaded micelles were placed in a dialysis device and incubated in 1 L of PBS at 10 °C. The emission of fluorescence at 610 nm was measured at different time points. Data are mean value of three measures. M80-C14 (black line), M80-C16 (blue line) and M80-C18 (red line). As a control, the fluorescence of a suspension of Nile red-loaded M80-C16 was monitored during 24 h (dashed blue line).

The kinetic of Nile red release was quite similar for M80-C14 and M80-C16, with a fast release of 70-80% of the Nile red content during the first five hours, and a slower one afterward. Around 10-15% of fluorescence was detected after 24 hours of dialysis. The situation was quite

different for M80-C18. Nile red was released at a slower pace, 60% remaining in the nanoparticles after 5 hours. After 24 hours of dialysis, 35% of fluorescence was still detected into this sample.

Finally, these experiments demonstrate that the length of the fatty acid chain is of great importance both for the loading capacity of the ELP-FA micelles, but also for the release kinetics of the hydrophobic molecule. We therefore anticipate the possibility of refining the design of the ELP-FAs to obtain micelles capable of encapsulating different amounts of hydrophobic drugs, and of releasing them more or less rapidly.

### **3.2.5. Obtention of ELP-FA micelles compatible with a medical application**

In the previous paragraphs, we obtained ELP-FAs micelles in physiological buffer (PBS) that were stable at temperature below  $T_{cp}$ . Among these materials, M80-FA micelles appeared to be the most interesting owing to their size and to their ability to encapsulate significant amounts of hydrophobic molecules. Unfortunately, we also showed that in the presence of salts, the  $T_{cps}$  of M80-FAs were in the 20°C range, therefore preventing their potential application as drug-delivery system *in vivo*. We therefore sought for a mean to increase their  $T_{cp}$  in PBS buffer, while keeping their size and encapsulation capacities. To increase the  $T_{cp}$  of the conjugates in PBS buffer, we oxidized M80 to replace thioethers groups of methionine by sulfoxide groups as this has been shown previously in our group to significantly increase the  $T_t$  value<sup>33,35</sup>.

Using the protocol developed by Petidmange and collaborators<sup>33</sup> we oxidized M80, and the characterization of the oxidized M80 ( $M^O80$ ) is shown in Fig. 28.

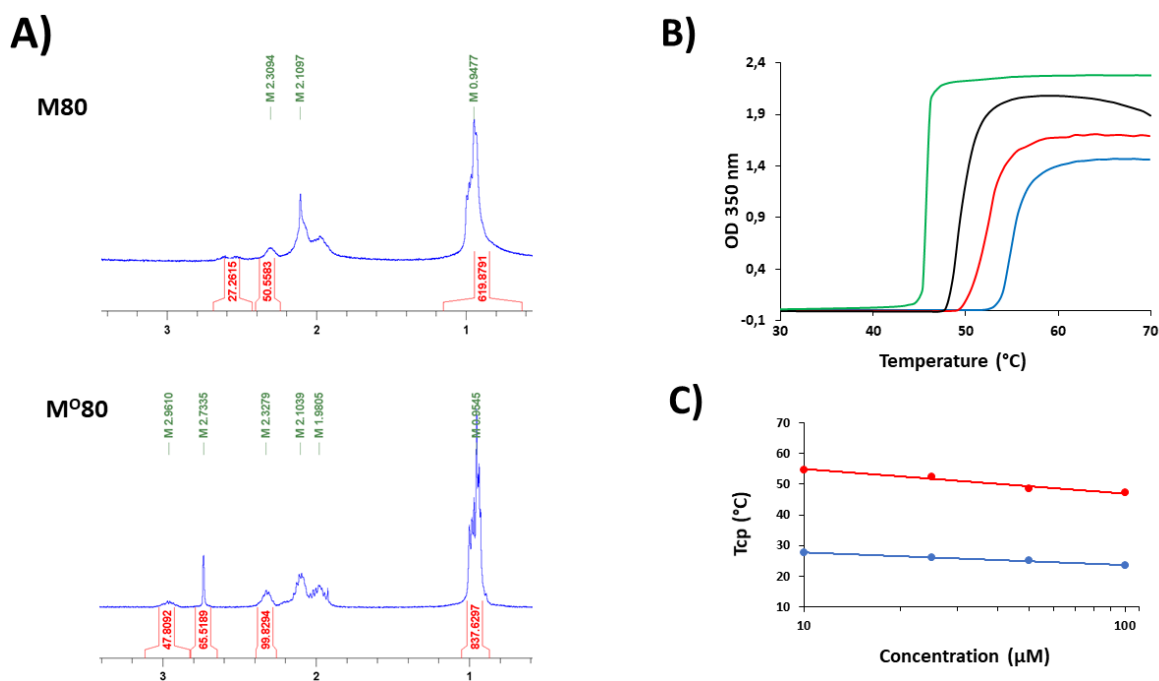


**Figure 28. Characterization of the oxidized M80. A) Comparison of the  $^1\text{H}$  NMR spectra in  $\text{D}_2\text{O}$  of M80 (Top) and  $\text{M}^{\text{O}}80$  (bottom). B) Turbidimetry experiments with different concentrations of  $\text{M}^{\text{O}}80$  in PBS buffer: 10  $\mu\text{M}$  (blue line), 25  $\mu\text{M}$  (red line), 50  $\mu\text{M}$  (black line) and 100  $\mu\text{M}$  (green line). C) Tt values plotted against M80 (blue line) and  $\text{M}^{\text{O}}80$  (red line) concentrations.**

After oxidation of M80,  $^1\text{H}$  NMR analyses showed the apparition of a characteristic peak corresponding to the sulfoxide function at 2.73 ppm<sup>33</sup>. Quantification of this peak indicate that 100% of the methionine were oxidized. Turbidimetry experiments were performed with  $\text{M}^{\text{O}}80$  in PBS, and as expected the Tts were in the range 45-55°C, twice those measured with unoxidized M80.

Next, we conjugated palmitic acid to  $\text{M}^{\text{O}}80$  using the protocol already described for the non-oxidized ELPs. The efficiency of the conjugation reaction was assessed by RP-HPLC. The retention times were 10.09 min and 13.54 min for  $\text{M}^{\text{O}}80$  and  $\text{M}^{\text{O}}80\text{-C16}$ , respectively. Quantification showed that the  $\text{M}^{\text{O}}80\text{-C16}$  conjugate was pure at 97%.

Turbidimetry experiments were performed to determine the Tcp of  $\text{M}^{\text{O}}80\text{-C16}$  in PBS.

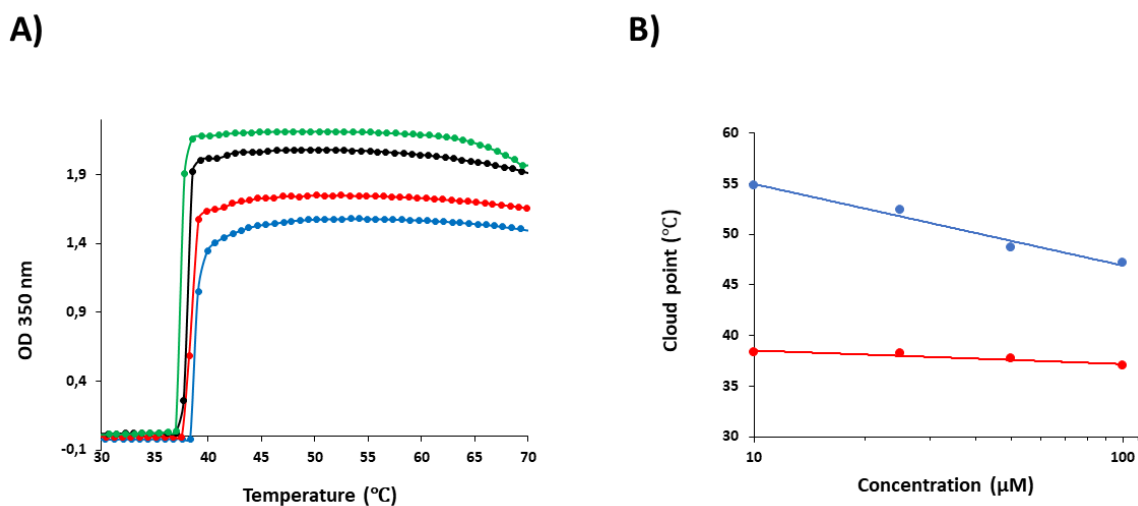


**Figure 29.** Turbidimetry experiments with different concentrations of M<sup>O</sup>80-C16 in PBS buffer. A) T-scan experiments 10 μM (blue line), 25 μM (red line), 50 μM (black line) and 100 μM (green line). B) Tcp values plotted against M<sup>O</sup>80 (blue line) and M<sup>O</sup>80-C16 (red line) concentrations.

As previously observed for the non-oxidized ELP, acylation of M<sup>O</sup>80 resulted in a decrease in the Tcps values, from 45-55°C to 37-38°C. This is an additional proof that the conjugation of C16 with M<sup>O</sup>80 was successful. We also observed that the Tcps values were almost independent on the conjugate concentration. Indeed, the Tcp was 39°C at 10 μM, and 37.5°C at 100 μM. These temperatures are significantly higher than those measured for M80-C16 (~20°C, see paragraph 3.2.2.4).

Finally, we checked the size of the M<sup>O</sup>80-C16 nanoparticles in PBS by DLS (Fig. 30).

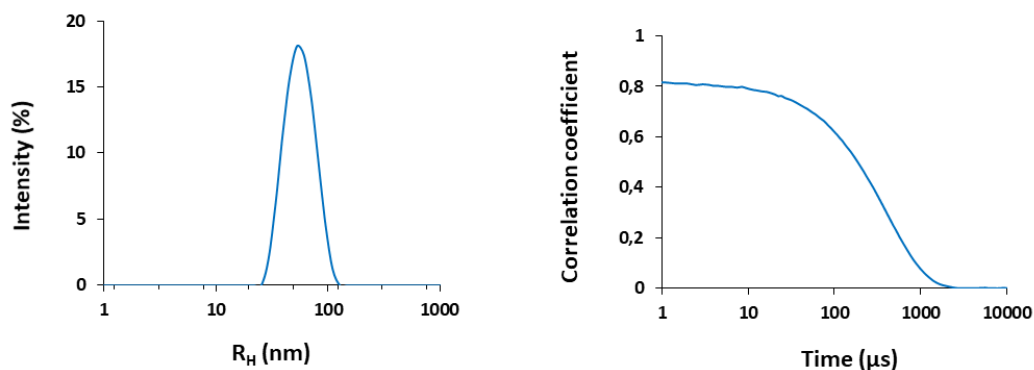


**Figure 30.** DLS analysis of M<sup>O</sup>80-C16. The compound was dissolved into PBS at a concentration of 2 mg/mL. DLS was recorded at 25°C.

As expected, M<sup>O</sup>80-C16 formed nanoparticles at  $T^{\circ} < T_{cp}$  in PBS. Their  $R_H$  was around 58 nm, and the dispersity was correct (PDI = 0.162). Their size was slightly bigger than that measured for M80-C16 under the same condition ( $R_H = 21$  nm). We think that this may be due to the fact that the corona formed by M<sup>O</sup>80 is less densely packed than that formed by M80, because of a lower overall hydrophobicity. However, other physical measures should be done to confirm this hypothesis.

In conclusion, we demonstrate that it is possible to fine-tune the  $T_{cp}$  of our ELP-FAs by a simple chemical reaction which results in the oxidation of the methionine residues present in our ELP. We obtained nanoparticles in PBS which are stable up to a temperature of 37.5°C. Of course, these  $T_{cp}$  temperatures are still quite close to the human body temperature, and therefore a  $T_{cp}$  close to 42 °C would have been better. Nevertheless, we demonstrated here that tuning the  $T_{cp}$  of ELP-FAs could be achieved by varying the hydrophilicity of the ELP moiety, either by chemical modification of the purified ELP, or by molecular engineering of the ELP to introduce some hydrophilic amino acids as guest residues.

### 3.2.6. Conclusions

In this work, we successfully conjugated five natural fatty acids onto three elastin-like polypeptides using a simple protocol that can be easily scaled up to large quantities. These biobased compounds have been characterized and their self-assembly studied. We have shown that the micelles formed are stable in PBS at a temperature below the  $T_{cp}$ , and that this  $T_{cp}$  depends mainly on the characteristics of the ELP group, which are its molecular weight and/or its hydrophobicity. The size of the micelles, with a  $R_H$  between 9 and 22 nm, can be tuned to a specific size by modifying either the ELP fragment and/or the fatty acid chain length or saturation. These micelles can encapsulate small hydrophobic molecules, and the encapsulation efficiency and drug release kinetics can also be tuned by changing the molecular design of the ELP-FAs. Finally, depending on their  $T_{cp}$ , two applications can be provided. First, when  $T_{cp}$  is above body temperature, as in the case of M<sup>O</sup>80-C16, the corresponding micelles could be evaluated for the delivery of therapeutic drugs after their injection into the plasma. Second, when the  $T_{cp}$  is below 37°C, the micelles containing the encapsulated drug will aggregate soon after their injection into a tissue and thus form a drug depot.

### 3.3. Experimental section

#### 3.3.1. Materials

Myristic acid (Fluka Chemistry, 98.0%), Palmitic acid (Riedel-de-haenTM, 98%), Stearic acid (Sigma-Aldrich, 98.5%), Oleic acid (Sigma-Aldrich, 99%), Linoleic acid (Sigma-Aldrich, 99%), O-(1H-6-Chlorobenzotriazole-1-yl)-1,1,3,3-tetramethyluronium hexafluorophosphate (HCTU, Novabiochem), Nile red (Carl Roth), Pyrene (Alfa Aesar, 98%), Samarium (III) acetate hydrate (Sigma-Aldrich, 99.9%), Sodium thiosulfate (Sigma-Aldrich, 99%), N,N-Diisopropylethylamine (DIPEA, Sigma-Aldrich, 99.5%), N,N-Dimethylformamide (DMF, VWR chemicals, 99.9%), Tetrahydrofuran (Acros organics, 99.6%), Diethyl ether (VWR international, 100%), Acetone (VWR international, 99%), Acetonitrile (VWR international, 99.95%), Methanol (VWR international, 100%), Hydrogen peroxide (Acros organics, 35 wt.% solution in water), Toluene (VWR international, 100.0%), Trifluoroacetic acid (Sigma-Aldrich, 99%), Acetic acid (Sigma-Aldrich, 99.8%), Phosphate Buffer Saline 10X, (PBS 10X, Euromedex) were used without further purification. Ultrapure water (18 MΩ cm) was obtained by passing in-house deionized water through a Millipore Milli-Q Biocel A10 purification unit. Bacto Tryptone (Sigma), Yeast extract (Sigma), Ampicillin (Sigma) and isopropyl β-D-thiogalactopyranoside (IPTG, VWR chemicals) were used for cell culture.

#### 3.3.2. Production and purification of ELPs

Production and purification of the ELP, M20, M40 and M80 was performed as already described<sup>33,34</sup>. Briefly, a single bacterial colony was cultured overnight at 37 °C in a rotary shaker at 200 rpm in 50 mL of lysogeny broth (LB) medium (1% bacto tryptone, 1% yeast extract, 0.5% NaCl) containing 100 µg/mL ampicillin. Thereafter, this seed culture was inoculated into 0.95 L of LB medium supplemented with glucose (1 g/L) and ampicillin (100 µg/mL), and cells were cultivated at 37 °C. When the OD<sub>600nm</sub> reached a value close to 0.8, isopropyl β-D-thiogalactopyranoside (IPTG) was added to a final concentration of 0.5 mM, and temperature of the incubator was decreased to 25 °C. After 12 h the culture was harvested by centrifugation at 6 000 g and 4 °C for 15 min, and the cell pellet was suspended with 10 mL/g wet weight in phosphate buffer saline (PBS) buffer. Thereafter cells were lysed by sonication, and the insoluble debris were removed by centrifugation at 10 000 g and 4 °C for

30 min. The cleared lysate was subjected to three successive cycles of Inverse Transition Cycling (ITC)<sup>51</sup>. Briefly, ELP was precipitated at 30 °C for M40 and M80, or at 40°C for M20 and then centrifuged at 10 000 g and 35 °C for 30 min (“warm spin”). The ELP-containing pellets were dissolved in cold water and the insoluble proteins were eliminated by centrifugation for 15 min at 10 000 g and 4 °C (“cold spin”). The protein content of the purified ELP solutions was measured by spectrophotometry at 280 nm with a NanoDrop 1000 (ThermoScientific). Finally, purified ELPs were dialyzed against ultrapure water at 4 °C (Spectra Por7, MWCO1000, Spectrum Laboratories), and then lyophilized.

Oxidation of M80 was performed as previously described<sup>33</sup>. The ELP was dissolved in 30% H<sub>2</sub>O<sub>2</sub> and 1% AcOH in water and stirred at 0 °C for 30 min. After quenching with a few drops of 1 M sodium thiosulfate aqueous solution, the reaction mixture was transferred to a 1 KDa MWCO dialysis tubing (Spectra/Por®) and dialyzed against DI water for 48 h with water changes twice per day. The content of the dialysis bag was then lyophilized to yield M<sup>0</sup>80 (95% yield). <sup>1</sup>H NMR (400 MHz, D<sub>2</sub>O): δ 4.4 ppm (160 H, αCH Val + αCH Pro), δ 4.17 ppm (t, 60 H, αCH Val guest residue, as reference peak), δ 3.72-3.97 ppm (br m, 478 H, 160 H δCH<sub>2</sub> Pro + 320 H αCH<sub>2</sub> Gly), δ 2.96 ppm (47 H, γCH<sub>2</sub> Met), δ 2.73 (65 H, εCH<sub>3</sub> Met), δ 1.98-2.32 (515 H = 140 H βCH Val + 42 H βCH<sub>2</sub> Met + 160 H βCH<sub>2</sub> Pro + 160 H γCH<sub>2</sub> Pro) δ 0.9-1.05 ppm (br m, 837 H, γCH<sub>3</sub> Val).

### 3.3.3. Synthesis of ELP-FAs

The first step was the activation of the carboxylic acid of the fatty acids. Myristic, palmitic, stearic, oleic and linoleic acid solutions prepared at 3 mM in anhydrous DMF were stirred for 1 h at RT. The activation of carboxylic acids was achieved by adding 7.4 mg (18 μmol) of HCTU and 4.6 μL (26 μmol) of DIPEA to the solution containing 18 μmol of FA, and performing the reaction for 15 min in the dark. The second step was the conjugation of the activated fatty acid with the primary amine of the ELP. There is only one primary amine per polypeptide, located at the N-terminal methionine. For conjugation, 1.5 μmol of activated fatty acid was reacted with 1 μmol of ELP for 12 h in the dark.

The reaction product was precipitated by 10 volumes of acetone, collected by centrifugation for 5 min at 2 500 g and 20°C, and then re-suspended in DMF. After a second precipitation step using 10 volumes of diethyl ether, the pellets were recovered by centrifugation and washed three times with 10 volumes of diethyl ether. After drying for 2 h at room temperature, the product was dissolved in cold water, centrifuged at 2 500 g for 10 min at 4°C to remove

insoluble impurities. The clear supernatant was dialyzed (1 KDa, Spectra/Por® membrane) against ultrapure water for 2 days at 4°C. The product was then lyophilized and stored at -20°C.

### 3.3.4. Methods

**Reversed-phase high performance liquid chromatography (RP-HPLC)** was performed using a Ultimate 3000 system (Thermo Scientific) instrument using a hydrophobic C18 stationary phase (ZORBAX Eclips Plus C18, 4.6 x 250 mm, 5 µm, Agilent Technologies) and a gradient of solvent A (H<sub>2</sub>O + 0.1% TFA)/solvent B (methanol + 0.1% TFA). The flow rate was 1 mL/min. 35 µL of ELP or ELP-FA samples (70 µM) were injected, and the absorbance at 230 nm was recorded with a diode array detector (Thermo Scientific). The gradient program used is shown below.

**Buffer A: Water + 0.1% TFA**  
**Buffer B: Methanol + 0.1% TFA**

Time (min)	% buffer A	% buffer B
0	100	0
3	100	0
35	0	100
45	0	100
46	100	0
55	100	0

Data obtained by RP-HPLC were used to calculate the percentage of purity of the ELP-FA conjugates. This was achieved by integrating the area below the peak of the ELP-FA, and by subtracting the area under the peak, if any, of the unmodified ELP.

**Mass spectrometry analysis (ESI-MS)** were performed on a ESI-QTOF (Q-TOF Premier, Waters, Manchester, UK). Water and acetonitrile (LC-MS grade) and formic acid (99%) were purchased from Thermo Fisher Scientific. Lyophilized compounds were resuspended in acetonitrile/0.1% aqueous formic acid (1:1 v/v) to a final concentration of around 30 µmol/L and infused into the electrospray ionization source at a flow rate of 5 µL/min. The mass spectrometer was operated in the positive mode with external calibration performed with a solution of the standard protein at a concentration of 1 µmol/L in acetonitrile/0.1% aqueous

formic acid (1:1 v/v). The ESI mass spectra showed the characteristic charge state distribution corresponding to the desired ELPs and their derivatives. Data were then processed with the maximum entropy deconvolution system MaxEnt (MaxEnt Software, Waters) to determine the MWs.

**Cloud point temperatures** ( $T_{cp}$ ) were determined by measuring the turbidity at 350 nm between 10 and 50 °C at a 1 °C·min<sup>-1</sup> scan rate. Data were collected with a Cary 100 UV–vis spectrophotometer equipped with a multicell thermoelectric temperature controller from Agilent Technologies. The  $T_{cp}$  is defined as the maximum of the first derivative of absorbance versus temperature.

**Circular dichroism** spectra were recorded on a Jasco J-1500 equipped with a Peltier temperature control accessory (JASCO, Hachioji, Japan). Each spectrum was obtained by averaging two scans collected at 50 nm min<sup>-1</sup>. The CD spectrum of pure water solution was subtracted from the average scan for each sample.

**The critical micelle concentration** (CMC) of ELP-FAs in PBS was determined as previously described<sup>40,41</sup>. Briefly, solutions of ELP-FAs in PBS with concentrations varying from 10<sup>-6</sup> mg/mL to 2.10<sup>-1</sup> mg/mL were prepared. Then, 1 μL of pyrene solution at 5mM in THF was added into 500 μL of particle dispersion prepared at various concentrations and incubated under stirring at 300 rpm for 10 h at 4°C. The dispersions were characterized by fluorescence spectroscopy using a Jasco FP 8500 spectrofluorometer. The excitation wavelength was set at 319 nm, and the fluorescence emission of pyrene was recorded between 360 and 400 nm. Bandwidths were respectively 20 nm and 5 nm for excitation and emission. The intensities of the first (I1) and third (I3) vibronic band of pyrene were determined at 373 nm and 385 nm respectively. The I1/I3 ratio was plotted as function of the polypeptide concentration.

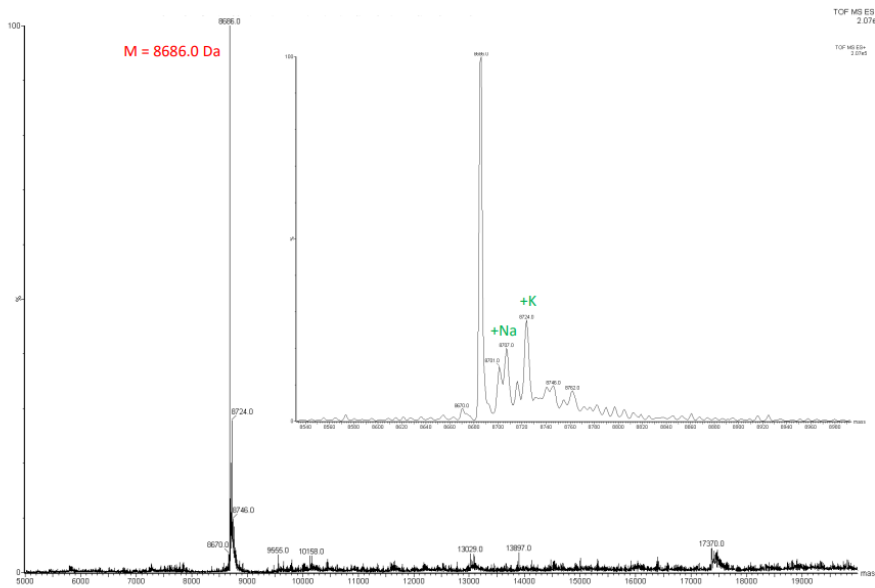
Dynamic light scattering (DLS) analysis of the of ELP-FAs micelles was performed using a Nano ZS instrument (Malvern U.K.) working at a 90° angle detection. All samples were filtrated through 0.22 μm PVDF devices (Millex, Merck Millipore) just before measurement. The hydrodynamic radius ( $R_H$ ) and the polydispersity index (PDI) were derived from the autocorrelation functions using the cumulant method. The zeta potential was measured with the same apparatus using the M3-PALS technique.

**The morphology of ELP-FA micelles** was examined by transmission electron microscopy (TEM) after negative staining of the samples. 20  $\mu\text{L}$  of a solution of ELP-fatty acid in Tris buffer at 5 mg/mL was first dropped on the carbon grid. After incubation for 5 min, the excess liquid was taken out and the grid was dried at room temperature. 20  $\mu\text{L}$  of a 2% samarium acetate solution (filtered with 0.45  $\mu\text{m}$  CA device) was deposited on the grid, incubated for 5 min at 15°C, and excess liquid was removed and the grid was air-dried. TEM analyses were performed at 80 kV acceleration voltage with a Hitachi H7650 microscope equipped with an Orius camera (Gatan, Paris, France). Pictures were acquired with the digital micrograph software.

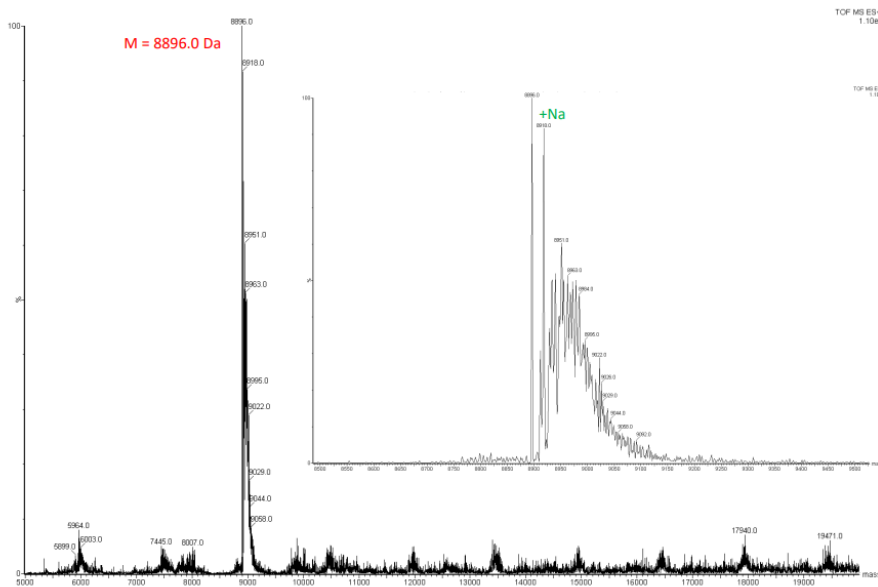
**The drug loading capability** was evaluated using the Nile red as model hydrophobic molecule. M80-FAs were dissolved in PBS at a concentration of 1 mg/mL, and incubated with Nile red (2  $\mu\text{M}$ ) for 24 hours at 4°C. Then, the solution was centrifuged at 18 500 g for 10 min at 4°C to eliminate the excess Nile Red which aggregates in aqueous solvent due to its low solubility in PBS. The supernatant containing the nanoparticles was freeze-dried, and the material was dispersed in DMSO for fluorescence analysis (Jasco FP 8500). The excitation wavelength was set at 550 nm and the fluorescence emission at 626 nm. The concentration of Nile Red was calculated from a calibration curve performed in DMSO using a 2  $\mu\text{M}$  Nile Red solution in PBS as blank. For drug release experiments, 6  $\mu\text{L}$  of a Nile Red solution in DMSO at 1 mg/mL were injected in 1.8 mL of M80-FA solutions (1 mg/mL in PBS). The solution was kept for 24 h at 10°C under stirring at 300 rpm. 600  $\mu\text{L}$  of sample was then transferred into a Spectra-Por® Float-A-Lyzer® device (molecular weight cut-off 1 kDa), and dialyzed at 10°C against 1 L of PBS. The fluorescence of the dialyzed sample was measured at different time-points with an excitation set at 550 nm and the emission at 610 nm.

### 3.4. Supplementary figures

Spectre ESI échantillon ELP M20 non modifié

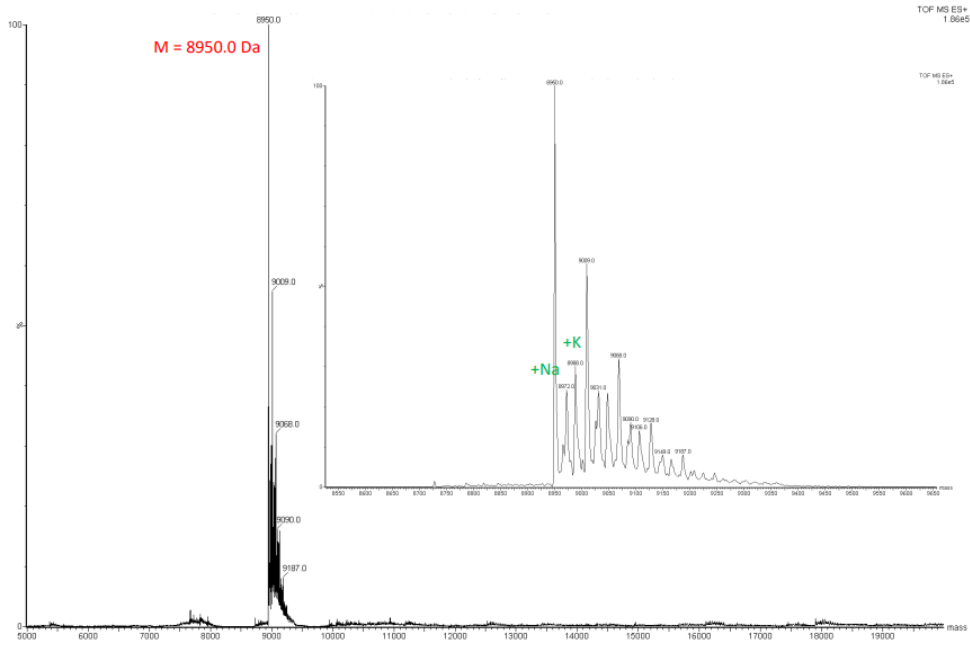


Spectre ESI échantillon ELP M20 + C14

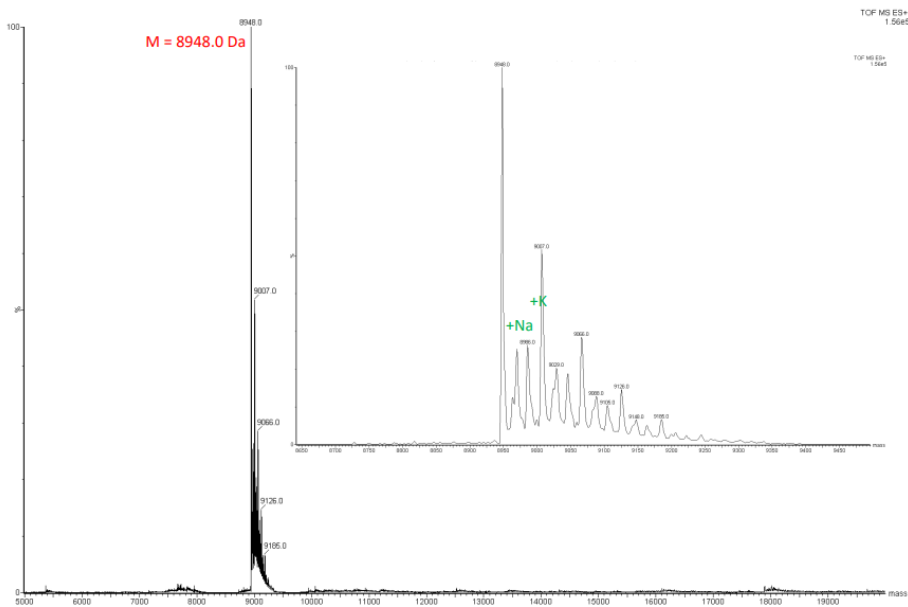




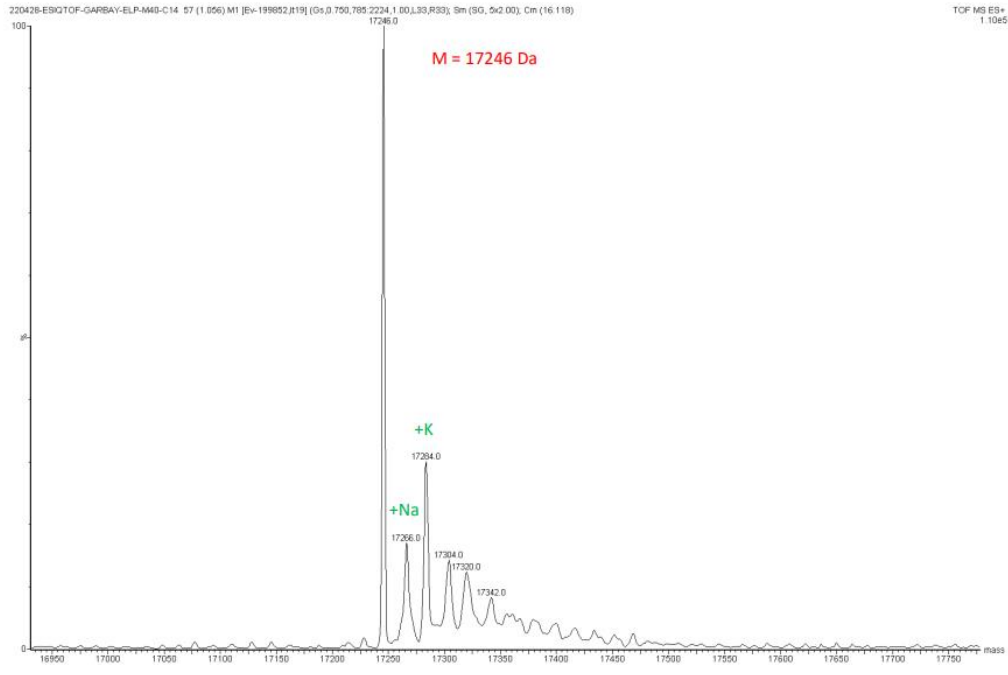
Spectre ESI échantillon ELP M20 + C18:1



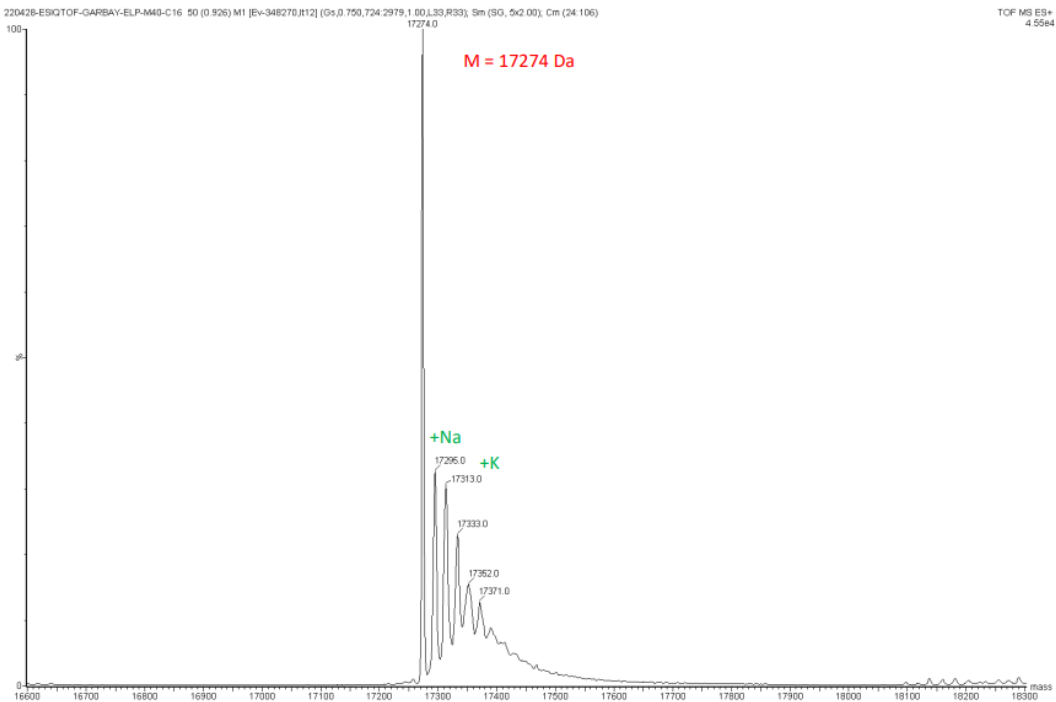
Spectre ESI échantillon ELP M20 + C18:2



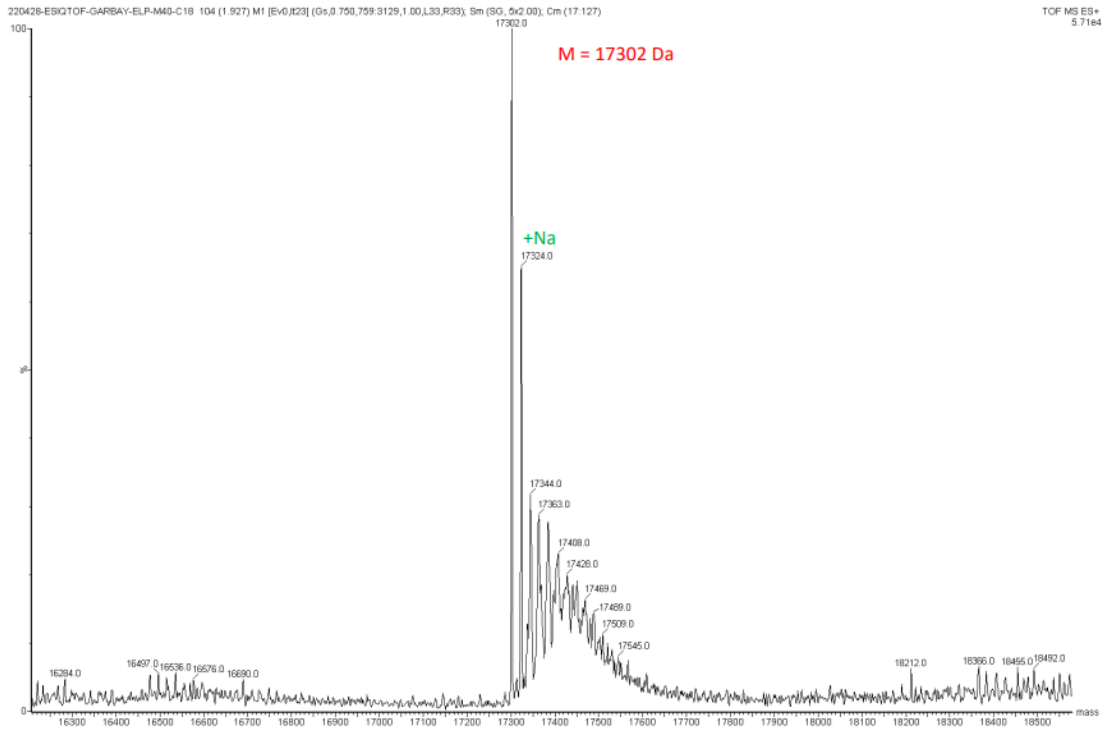
Spectre ESI échantillon ELP M40 + C14



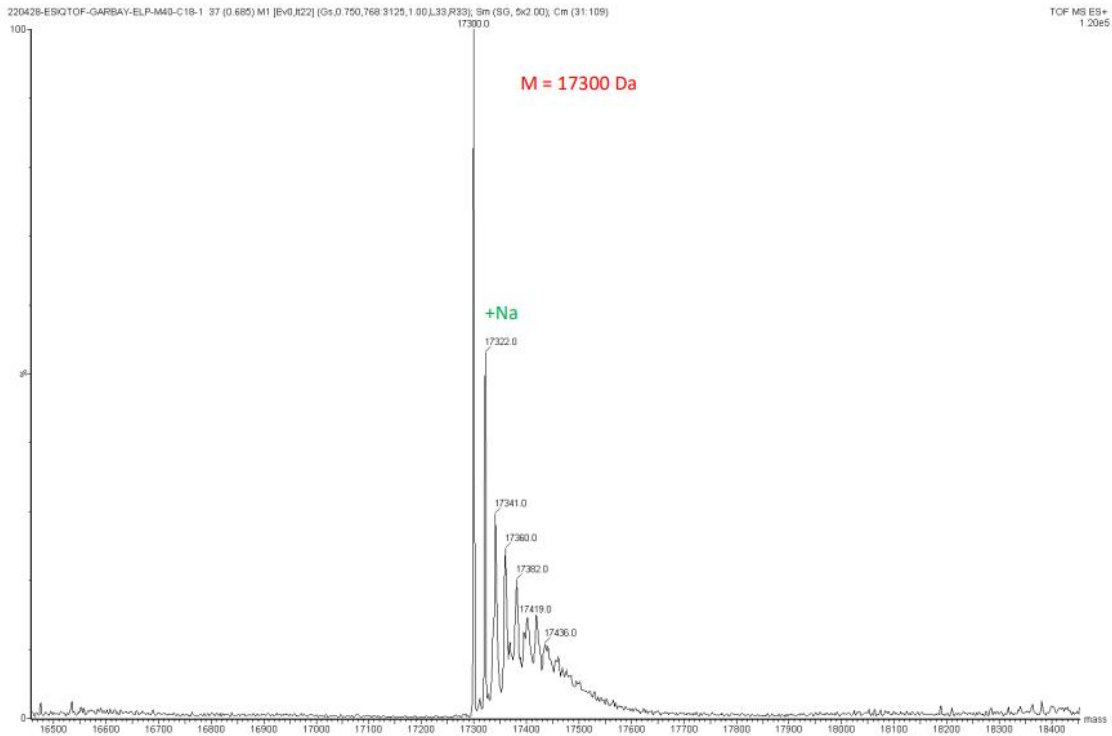
Spectre ESI échantillon ELP M40 + C16



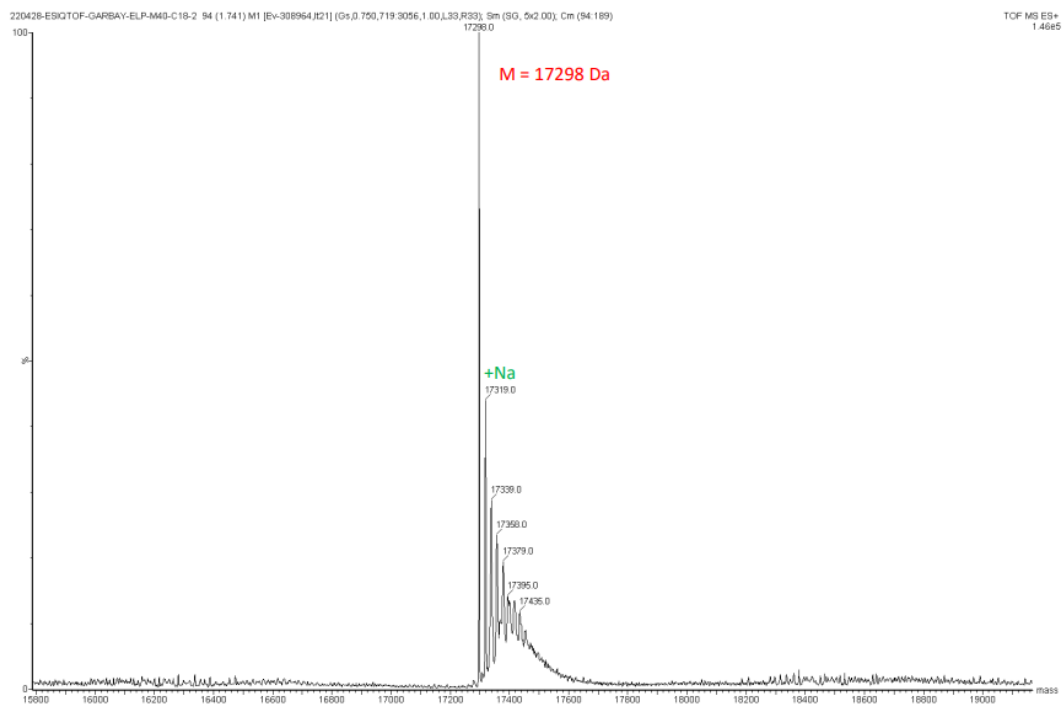
Spectre ESI échantillon ELP M40 + C18



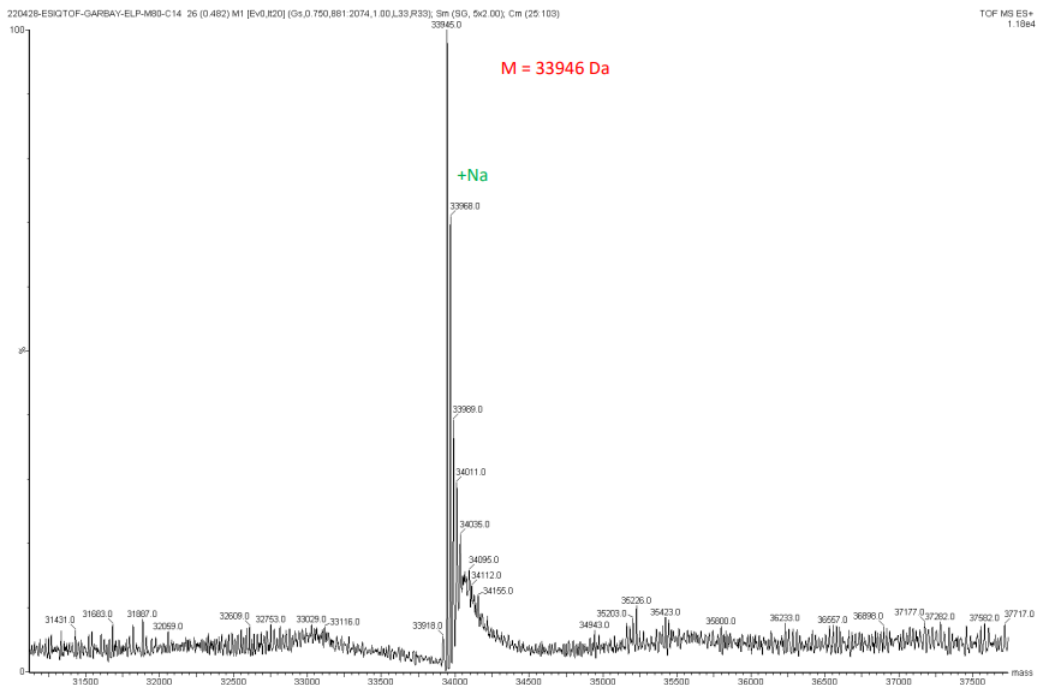
Spectre ESI échantillon ELP M40 + C18:1



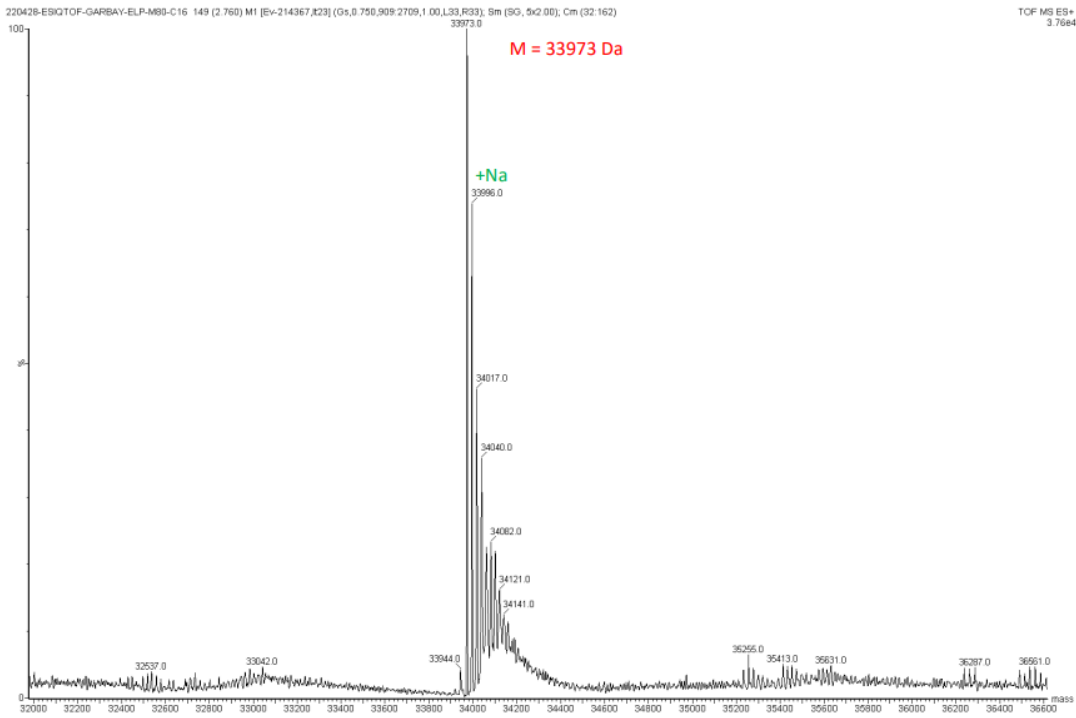
Spectre ESI échantillon ELP M40 + C18:2



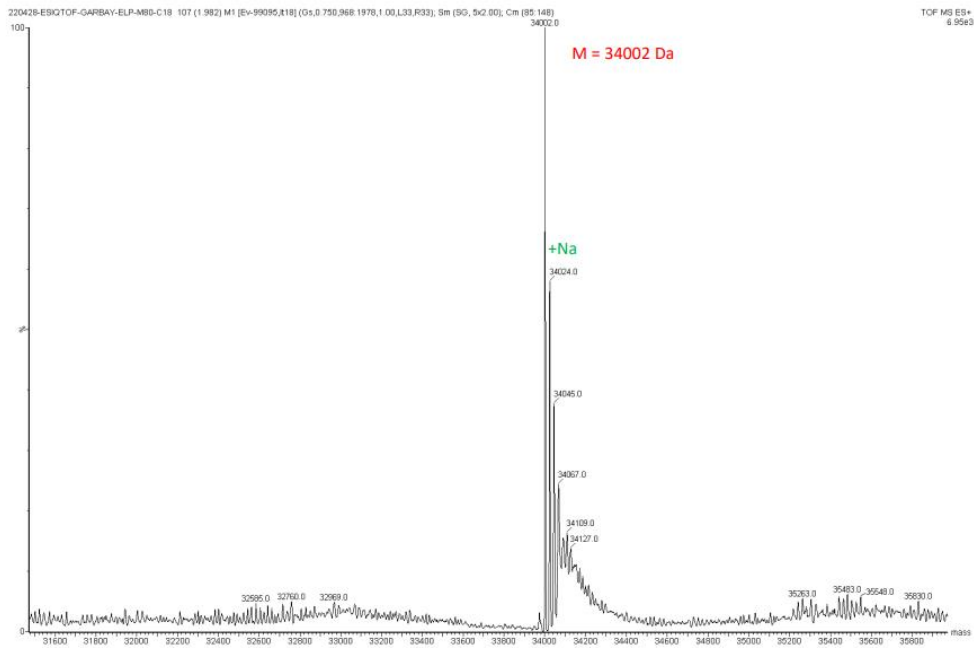
Spectre ESI échantillon ELP M80 + C14



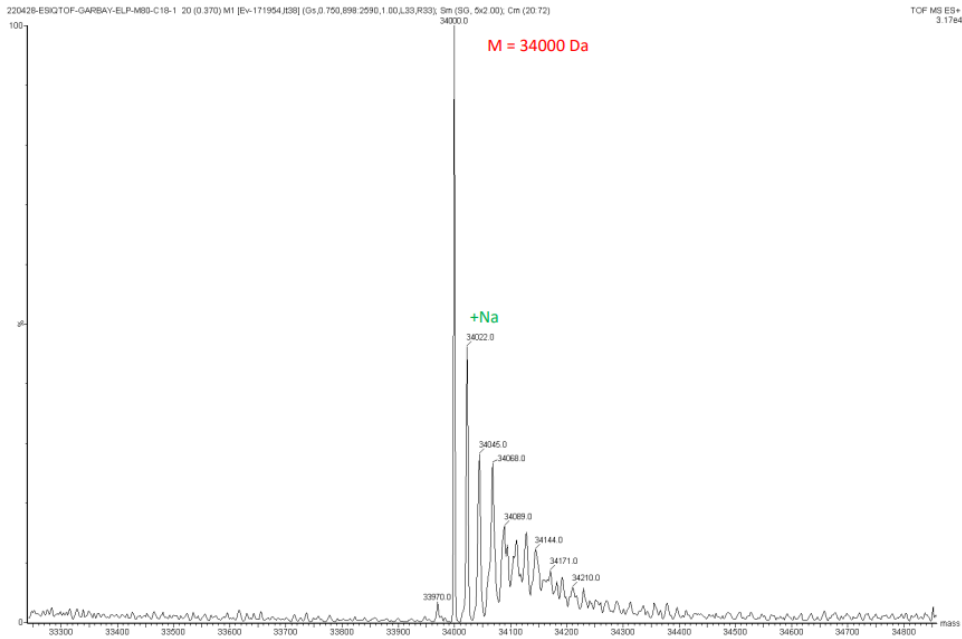
Spectre ESI échantillon ELP M80 + C16



Spectre ESI échantillon ELP M80 + C18



Spectre ESI échantillon ELP M80 + C18:1



Spectre ESI échantillon ELP M80 + C18:2

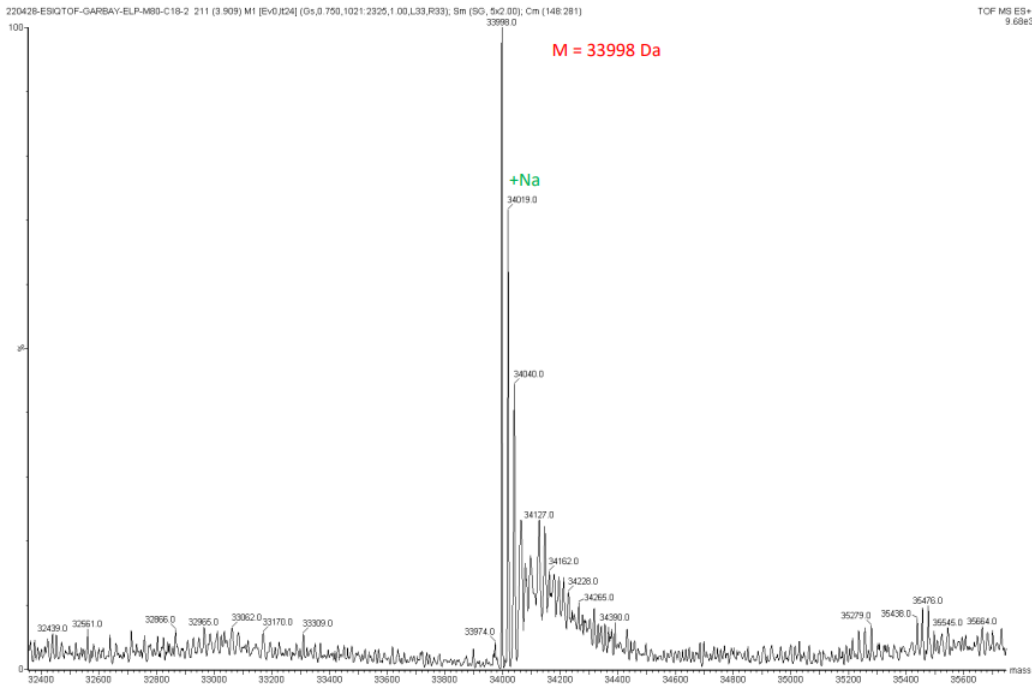
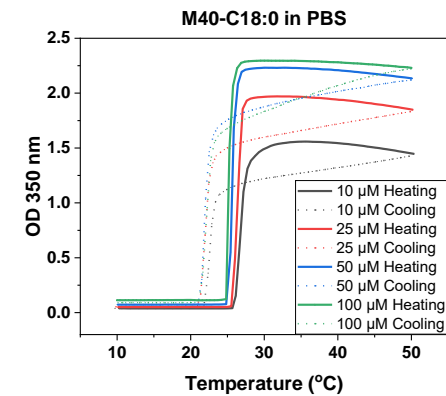
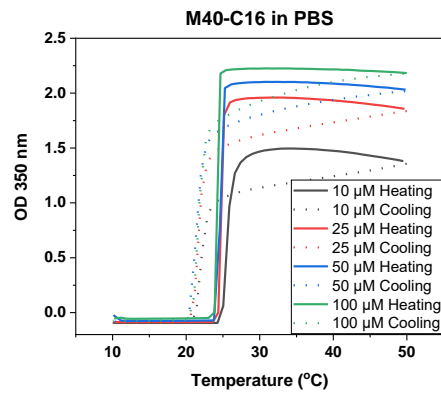
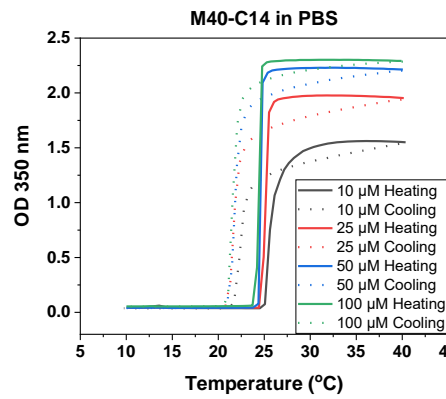
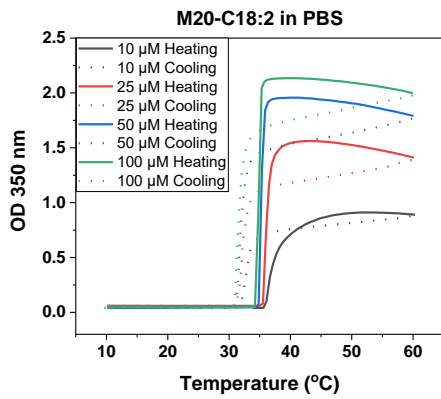
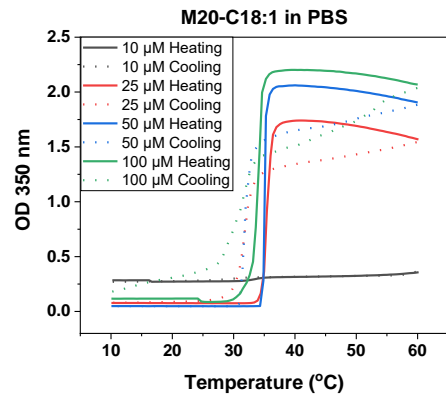
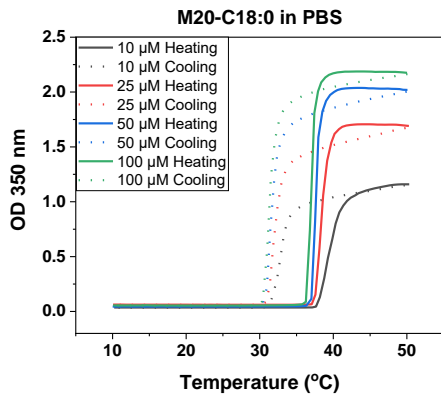
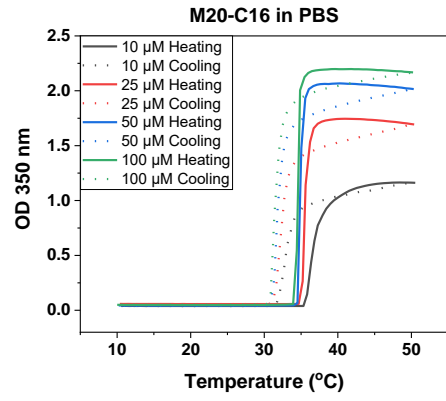
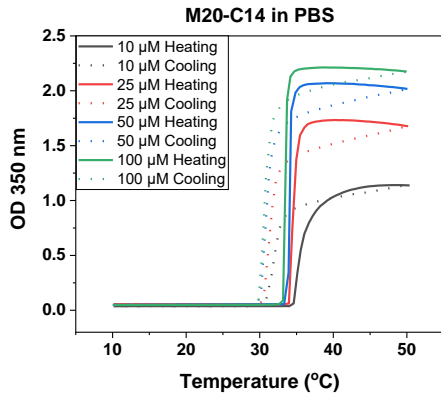
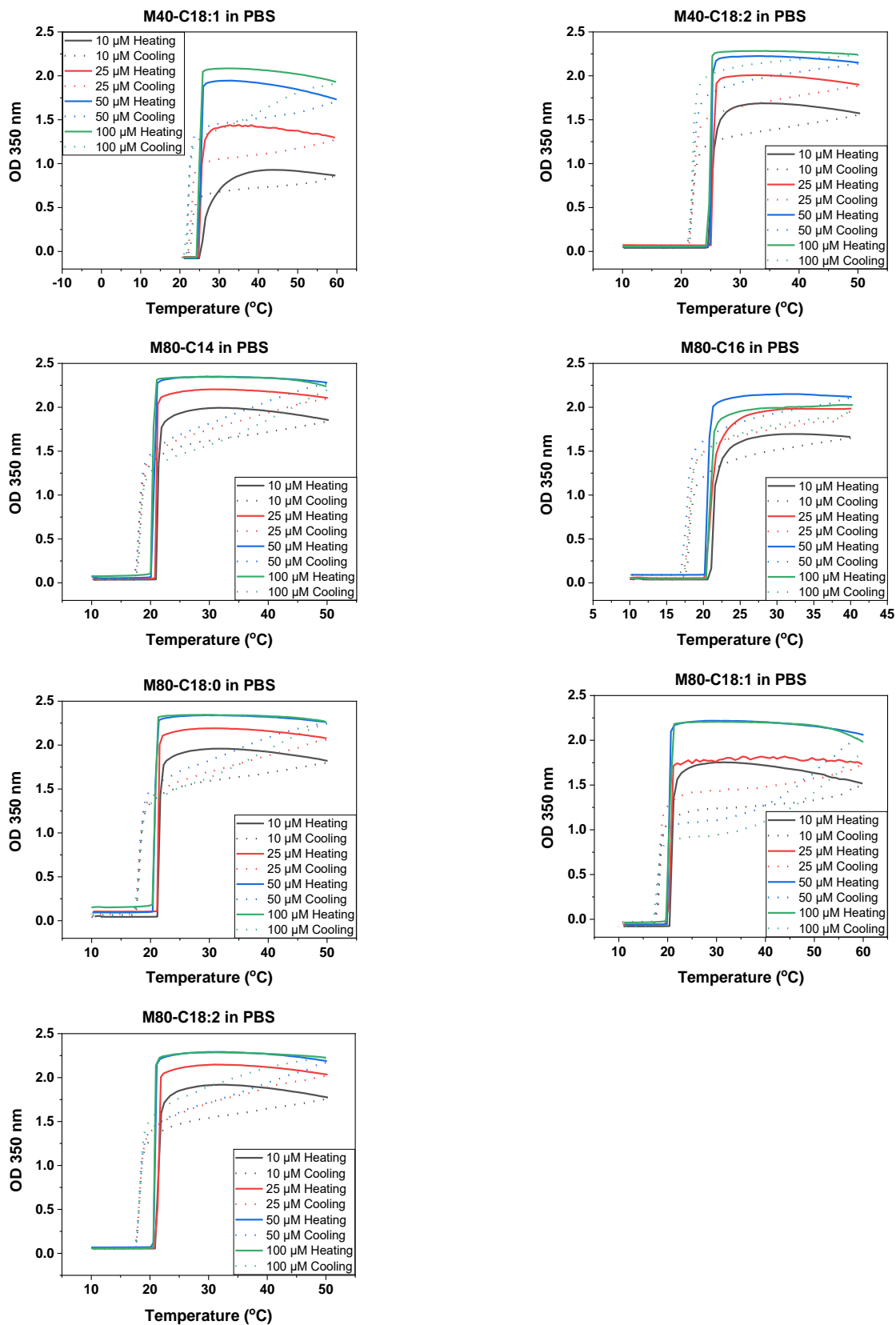
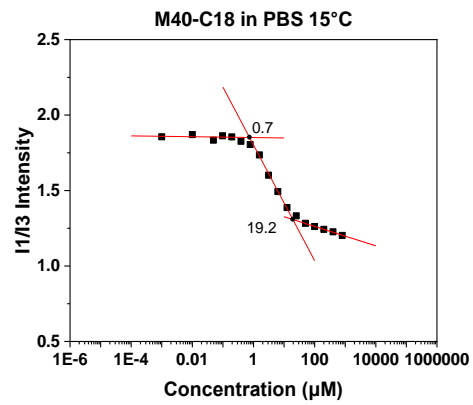
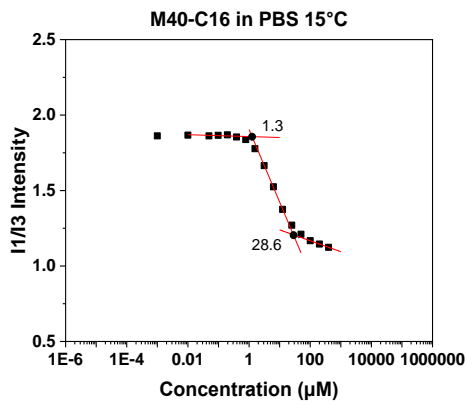
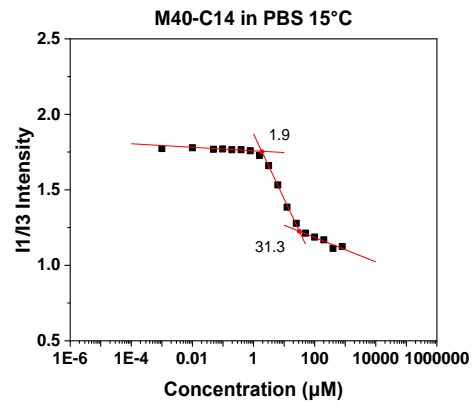
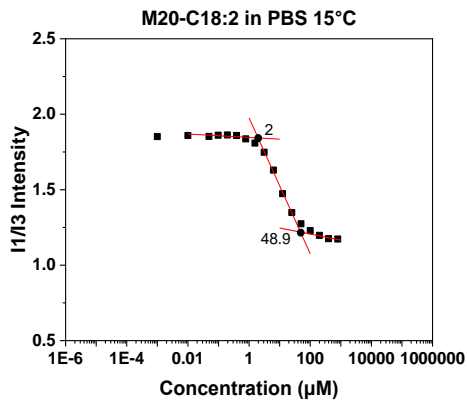
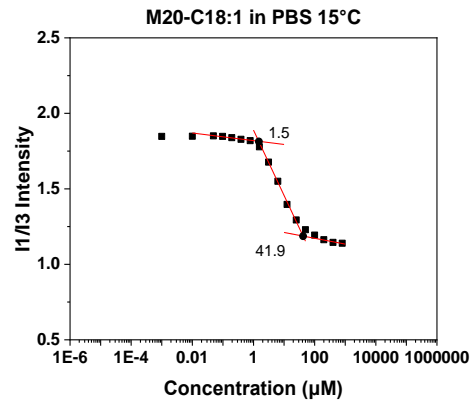
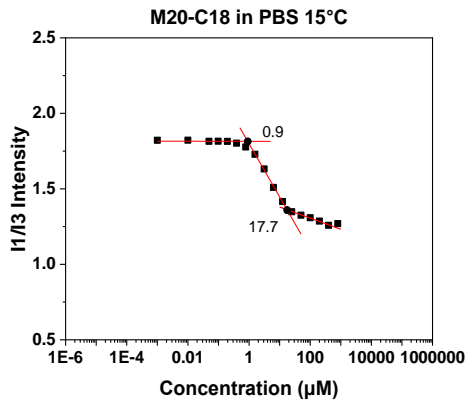
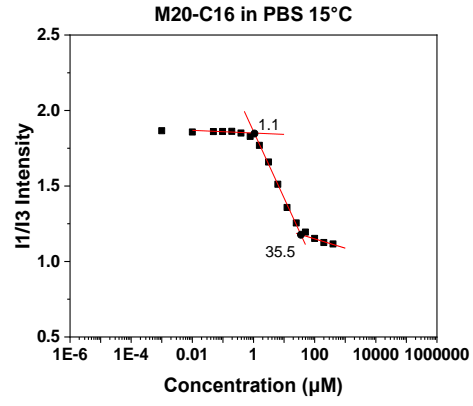
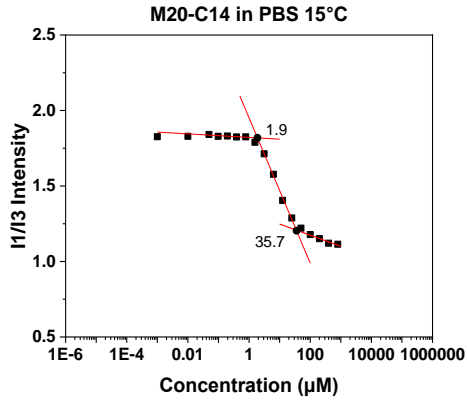


Figure S1. ESI-MS spectra of Mx-FAs





**Figure S2. Turbidimetry experiments for the 15 ELP-FAs at various concentrations in PBS buffer. Heating ramps (Plain lines) and cooling ramps (dashed lines) at 10  $\mu$ M (black), 25  $\mu$ M (red), 50  $\mu$ M (blue) and 100  $\mu$ M (green).**



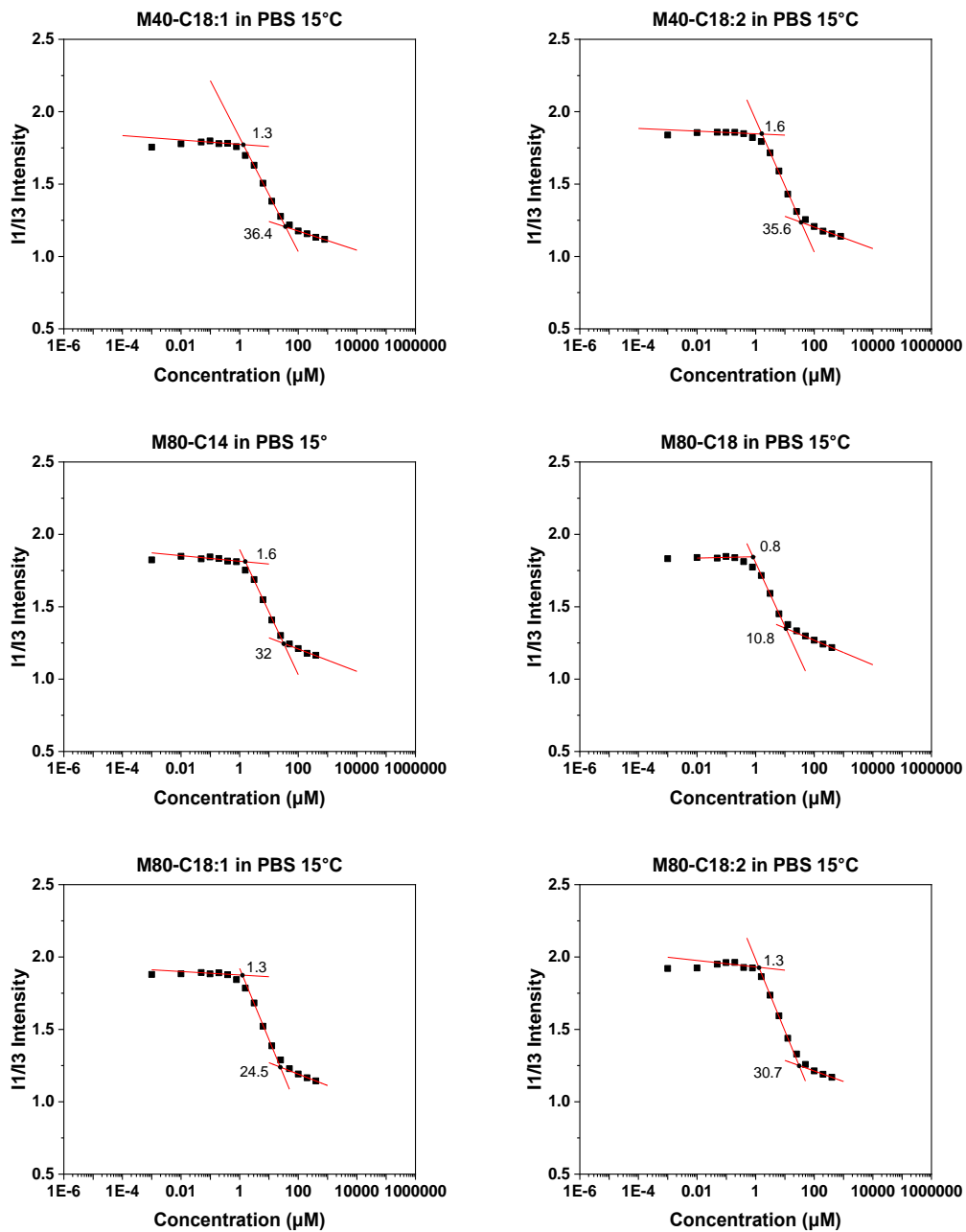


**Figure S3. CMC values of ELP-FAs in PBS at 15°C. The CMC values shown on the graphs correspond to the “low” and “high” CMC values.**

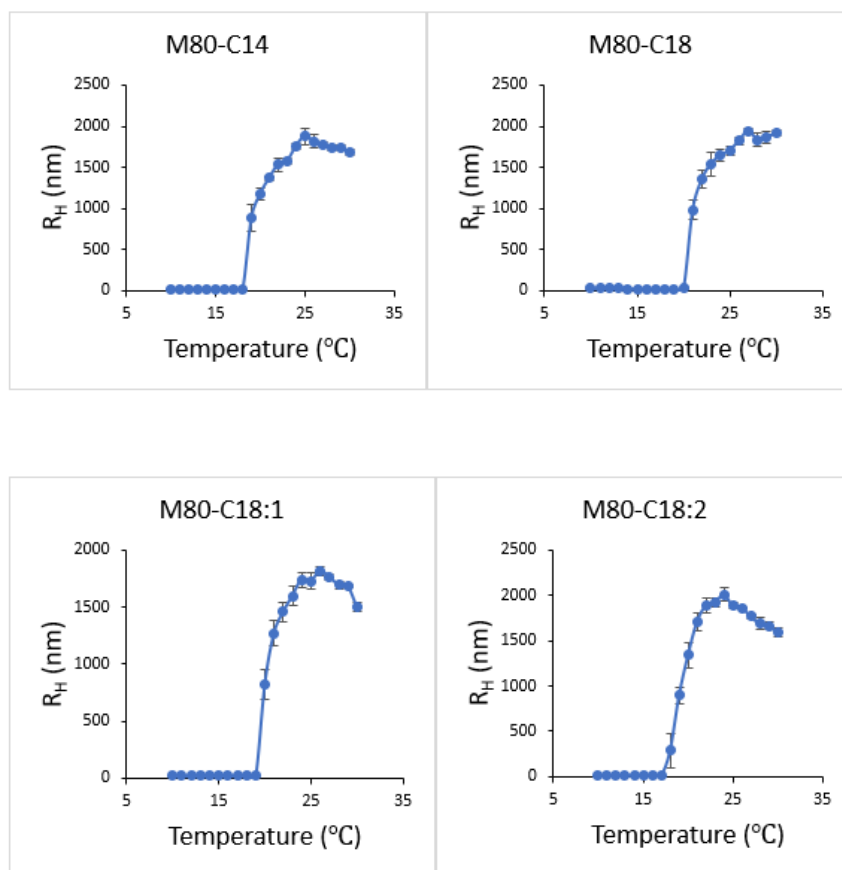


**Figure S4:  $R_H$  measurement by DLS during a temperature ramp. Solution of M80-C14, M80-C18, M80-C18:1 and M80-C18:2, each at a concentration of 1 mg/mL were incubated into PBS buffer, and DLS measurements were recorded between 10 and 30  $^{\circ}\text{C}$ . For each value, data are mean of three measures  $\pm$  SD.**

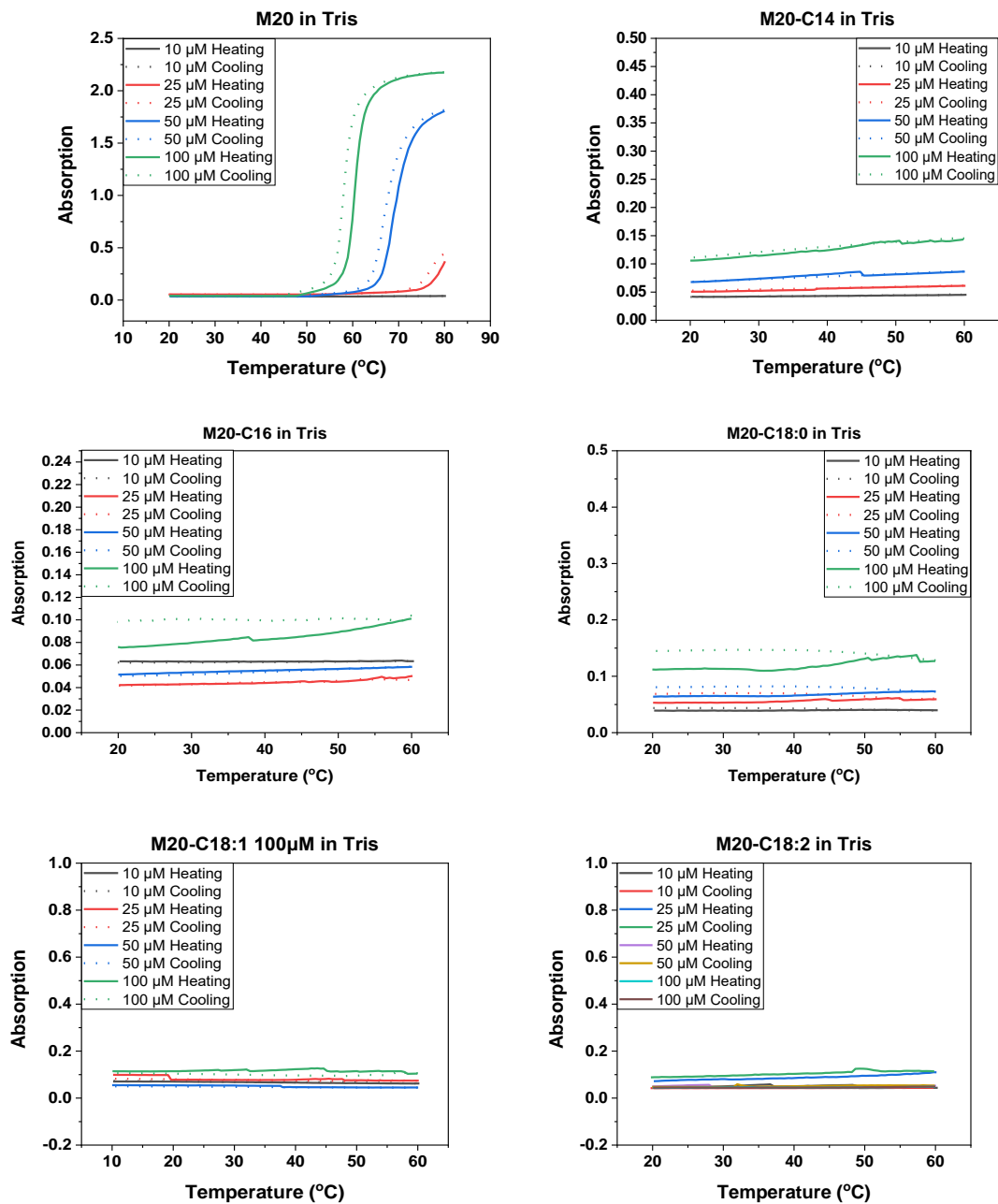
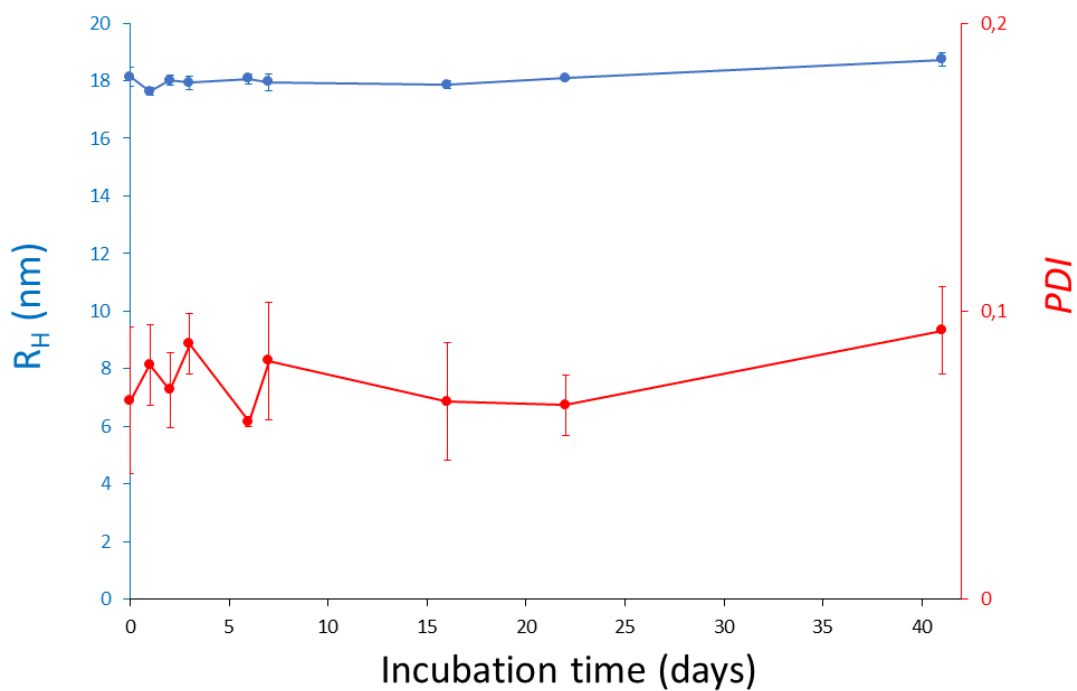
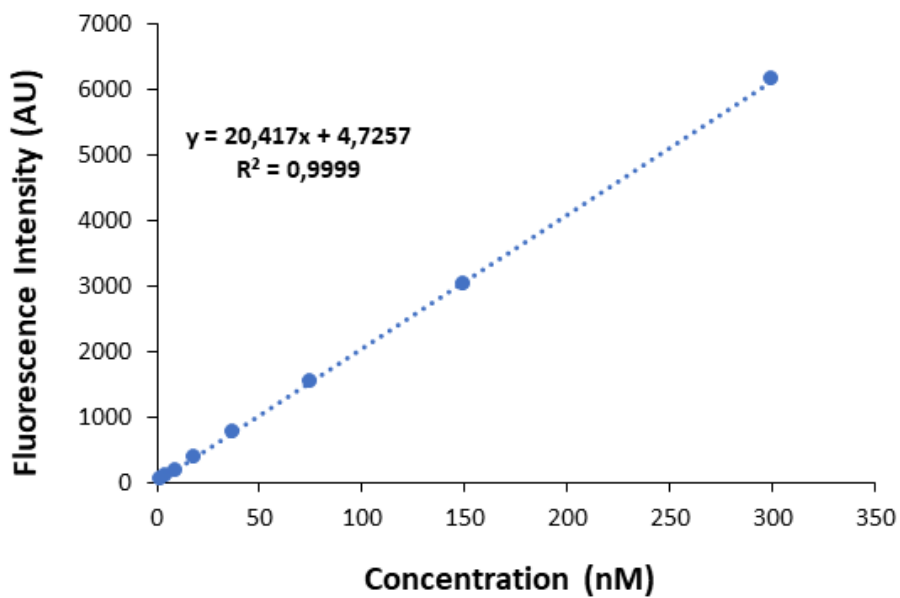


Figure S5. Turbidimetry experiments for M20 and M20-FAs in Tris buffer.



**Figure S6. Stability of M80-C16 nanoparticles (5 mg/mL) stored in Tris buffer at 4°C. For each value, data are mean of three measures ± SD.**



**Figure S7. Fluorescence intensity versus Nile red concentration.**

### 3.5. References

- 1 A. Varanko, S. Saha and A. Chilkoti, *Advanced Drug Delivery Reviews*, 2020, **156**, 133–187.
- 2 D. W. Urry, T. L. Trapane and K. U. Prasad, *Biopolymers*, 1985, **24**, 2345–2356.
- 3 D. W. Urry, *Progress in Biophysics and Molecular Biology*, 1992, **57**, 23–57.
- 4 B. Li, D. O. Alonso and V. Daggett, *J Mol Biol*, 2001, **305**, 581–92.
- 5 D. E. Meyer and A. Chilkoti, *Biomacromolecules*, 2004, **5**, 846–851.
- 6 D. W. Urry, B. Haynes and R. D. Harris, *Biochemical and Biophysical Research Communications*, 1986, **141**, 749–755.
- 7 E. Garanger and S. Lecommandoux, *Angewandte Chemie International Edition*, 2012, **51**, 3060–3062.
- 8 A. K. Varanko, J. C. Su and A. Chilkoti, *Annual Review of Biomedical Engineering*, 2020, **22**, 343–369.
- 9 E. R. Wright and V. P. Conticello, *Advanced Drug Delivery Reviews*, 2002, **54**, 1057–1073.
- 10 M. R. Dreher, A. J. Simnick, K. Fischer, R. J. Smith, A. Patel, M. Schmidt and A. Chilkoti, *J Am Chem Soc*, 2007, **130**, 687–694.
- 11 S. M. Janib, M. F. Pastuszka, S. Aluri, Z. Folchman-Wagner, P. Y. Hsueh, P. Shi, Y. A. Lin, H. Cui and J. A. Mackay, *Polymer Chemistry*, 2014, **5**, 1614–1625.
- 12 W. Hassouneh, E. B. Zhulina, A. Chilkoti and M. Rubinstein, *Macromolecules*, 2015, **48**, 4183–4195.
- 13 E. Garanger, S. R. MacEwan, O. Sandre, A. Brûlet, L. Bataille, A. Chilkoti and S. Lecommandoux, *Macromolecules*, 2015, **48**, 6617–6627.
- 14 K. Widder, S. R. MacEwan, E. Garanger, V. Núñez, S. Lecommandoux, A. Chilkoti and D. Hinderberger, *Soft Matter*, 2017, **13**, 1816–1822.

- 15 K. M. Luginbuhl, D. Mozhdghi, M. Dzuricky, P. Yousefpour, F. C. Huang, N. R. Mayne, K. L. Buehne and A. Chilkoti, *Angewandte Chemie - International Edition*, 2017, **56**, 13979–13984.
- 16 L. Poocha, F. Cipriani, M. Alonso and J. C. Rodríguez-Cabello, *ACS Omega*, 2019, **4**, 10818–10827.
- 17 V. Ibrahimova, H. Zhao, E. Ibarboure, E. Garanger and S. Lecommandoux, *Angew Chem Int Ed Engl*, 2021, **60**, 15036–15040.
- 18 D. M. Scheibel, M. S. Hossain, A. L. Smith, C. J. Lynch and D. Mozhdghi, *ACS Macro Letters*, 2020, **9**, 371–376.
- 19 D. Mozhdghi, K. M. Luginbuhl, J. R. Simon, M. Dzuricky, R. Berger, H. S. Varol, F. C. Huang, K. L. Buehne, N. R. Mayne, I. Weitzhandler, M. Bonn, S. H. Parekh and A. Chilkoti, *Nat Chem*, 2018, **10**, 496–505.
- 20 M. S. Hossain, C. Maller, Y. Dai, S. Nangia and D. Mozhdghi, *Chemical Communications*, 2020, **56**, 10281–10284.
- 21 D. Mozhdghi, K. M. Luginbuhl, M. Dzuricky, S. A. Costa, S. Xiong, F. C. Huang, M. M. Lewis, S. R. Zelenetz, C. D. Colby and A. Chilkoti, *J Am Chem Soc*, 2019, **141**, 945–951.
- 22 S. K. Abbott, P. L. Else, T. A. Atkins and A. J. Hulbert, *Biochimica et Biophysica Acta (BBA) - Biomembranes*, 2012, **1818**, 1309–1317.
- 23 C. A. Hood, G. Fuentes, H. Patel, K. Page, M. Menakuru and J. H. Park, *J Pept Sci*, 2008, **14**, 97–101.
- 24 J. R. Dunetz, J. Magano and G. A. Weisenburger, *Organic Process Research and Development*, 2016, **20**, 140–177.
- 25 E. Gasteiger, C. Hoogland, A. Gattiker, S. Duvaud, M. R. Wilkins, R. D. Appel and A. Bairoch, *The Proteomics Protocols Handbook*, 2005, **112**, 571–607.
- 26 S. W. Lin and T. P. Sakmar, *Biochemistry*, 1996, **35**, 11149–11159.

- 27 J. S. Patton, B. Stone, C. Papa, R. Abramowitz and S. H. Yalkowsky, *Journal of Lipid Research*, 1984, **25**, 189–197.
- 28 R. B. Cole, *Electrospray and MALDI Mass Spectrometry*, Wiley, 2012.
- 29 A. Micsonai, F. Wien, L. Kernya, Y.-H. Lee, Y. Goto, M. Réfrégiers and J. Kardos, *Proceedings of the National Academy of Sciences*, 2015, **112**, E3095–E3103.
- 30 A. Micsonai, F. Wien, É. Bulyáki, J. Kun, É. Moussong, Y. H. Lee, Y. Goto, M. Réfrégiers and J. Kardos, *Nucleic Acids Research*, 2018, **46**, W315–W322.
- 31 T. Yamaoka, T. Tamura, Y. Seto, T. Tada, S. Kunugi and D. A. Tirrell, *Biomacromolecules*, 2003, **4**, 1680–1685.
- 32 F. G. Quiroz and A. Chilkoti, *Nature Materials*, 2015, **14**, 1164–1171.
- 33 R. Petitdemange, E. Garanger, L. Bataille, W. Dieryck, K. Bathany, B. Garbay, T. J. Deming and S. Lecommandoux, *Biomacromolecules*, 2017, **18**, 544–550.
- 34 M. Dai, E. Georgilis, G. Goudounet, B. Garbay, J. Pille, J. C. M. van Hest, X. Schultze, E. Garanger and S. Lecommandoux, *Polymers (Basel)*, 2021, **13**, 1470.
- 35 J. R. Kramer, R. Petitdemange, L. Bataille, K. Bathany, A.-L. Wirotius, B. Garbay, T. J. Deming, E. Garanger and S. Lecommandoux, *ACS Macro Letters*, 2015, **4**, 1283–1286.
- 36 J. R. McDaniel, I. Weitzhandler, S. Prevost, K. B. Vargo, M. S. Appavou, D. A. Hammer, M. Gradzielski and A. Chilkoti, *Nano Lett*, 2014, **14**, 6590–6598.
- 37 J. R. McDaniel, J. Bhattacharyya, K. B. Vargo, W. Hassouneh, D. A. Hammer and A. Chilkoti, *Angewandte Chemie International Edition*, 2013, **52**, 1683–1687.
- 38 D. Mozhdehi, K. M. Luginbuhl, J. R. Simon, M. Dzuricky, R. Berger, H. S. Varol, F. C. Huang, K. L. Buehne, N. R. Mayne, I. Weitzhandler, M. Bonn, S. H. Parekh and A. Chilkoti, *Nature Chemistry*, 2018, **10**, 496–505.
- 39 J. Aguiar, P. Carpena, J. A. Molina-Bolívar and C. Carnero Ruiz, *Journal of Colloid and Interface Science*, 2003, **258**, 116–122.

- 40 A. Mohr, P. Talbiersky, H. G. Korth, R. Sustmann, R. Boese, D. Bläser and H. Rehage, *Journal of Physical Chemistry B*, 2007, **111**, 12985–12992.
- 41 L. Piñeiro, M. Novo and W. Al-Soufi, *Advances in Colloid and Interface Science*, 2015, **215**, 1–12.
- 42 K. Kalyanasundaram and J. K. Thomas, *J Am Chem Soc*, 2002, **99**, 2039–2044.
- 43 A. Yekta, J. Duhamel, P. Brochard, H. Adiwidjaja and M. A. Winnik, *Macromolecules*, 2002, **26**, 1829–1836.
- 44 M. Frindi, B. Michels and R. Zana, *Journal of Physical Chemistry*, 2002, **96**, 6095–6102.
- 45 O. Regev and R. Zana, *Journal of Colloid and Interface Science*, 1999, **210**, 8–17.
- 46 R. Zana, H. Lévy and K. Kwetkat, *J Colloid Interface Sci*, 1998, **197**, 370–376.
- 47 E. Fuguet, C. Ràfols, M. Rosés and E. Bosch, *Analytica Chimica Acta*, 2005, **548**, 95–100.
- 48 G. R. Grimsley, J. M. Scholtz and C. N. Pace, *Protein Science*, 2009, **18**, 247–251.
- 49 C. S. Tian and Y. R. Shen, *Proc Natl Acad Sci U S A*, 2009, **106**, 15148–15153.
- 50 Y. Cho, Y. Zhang, T. Christensen, L. B. Sagle, A. Chilkoti and P. S. Cremer, *Journal of Physical Chemistry B*, 2008, **112**, 13765–13771.
- 51 D. E. Meyer and a Chilkoti, *Nat Biotechnol*, 1999, **17**, 1112–1115.



## Chapter 4. Physical hydrogel based on C16-ELP-C16 triblock

### 4.1. Introduction

In the previous chapter, we demonstrated that it was possible to obtain micelles by simply grafting one molecule of fatty acid onto one molecule of ELP. Being involved in other projects where we sought to develop hydrogels for tissue engineering applications, we thought about means to use our micelles to form gels. Usually, ELP-based hydrogels are obtained by chemical, enzymatic, and  $\gamma$ -irradiation cross-linking<sup>1-8</sup>. The corresponding hydrogels have good rheological properties, but they often contain chemical components which are necessary for the crosslinking reaction but which are not very biocompatible. Furthermore, these hydrogels are not reversible because their integrity is maintained by covalent bonds. However, for certain therapeutic applications physical hydrogels are more suitable, in particular because of their self-healing properties. These physical hydrogels are usually made of associative polymers, also called telechelic polymers, which are BAB triblock copolymer with a hydrophilic backbone (block A) and two hydrophobic groups (blocks B). They associate in aqueous medium in so-called “flower micelles”: when the concentration increases and the micelles start to interact, the hydrophobic grafts come together to create microdomains, which leads to the formation of a 3D physical network<sup>9,10</sup>. This process is illustrated in Figure 1.

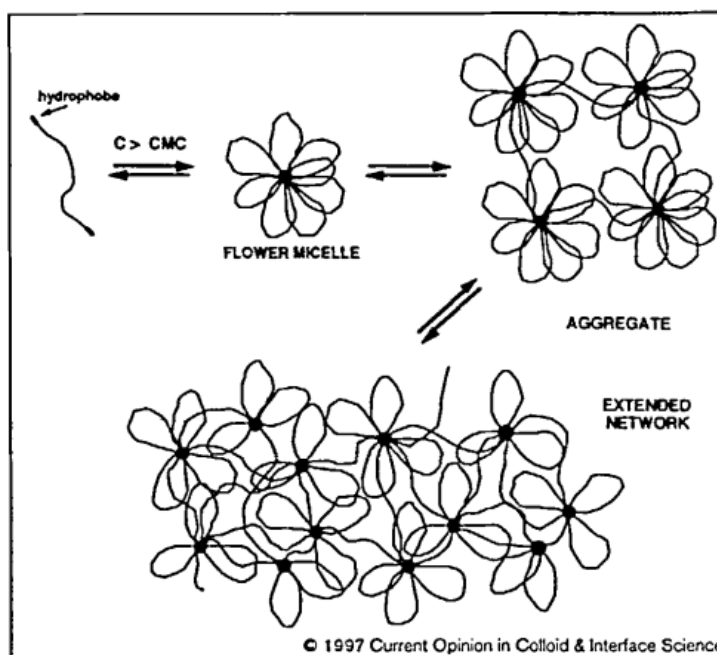


**Figure 1. Representation of the combination of BAB-type triblock copolymers according to Winnik and Yetka<sup>10</sup>.**

To the best of our knowledge, only two examples of physical hydrogels based on ELP blocks have been published. Wright and Conticello used BAB triblocks where B was a hydrophobic ELP containing isoleucine,  $[(IPAVG)_4(VPAVG)]_n$ , and A a hydrophilic bloc containing the charged residue glutamic acid  $[(VPGVG)_4(VPGEG)]_m$ <sup>11</sup>. When the aqueous solution containing the polymer was heated above 15°C, the hydrophobic blocks aggregated leading to hydrogel formation. However, the high polymer concentrations needed to achieve gel formation, above 25%, was a limit to the use of this material. More recently, our group reported the characterization of physical hydrogels obtained with an ELP-based ABC triblock<sup>12</sup>. Blocks B and C consisted of hydrophilic and hydrophobic ELPs, respectively, and block A was a hydrophobic synthetic poly(trimethylene carbonate) (PTMC). This polymer self-assembled into micelles in water, and at a temperature higher than the Tt of the ELP diblock, these micelles aggregated to form a physical hydrogel (Figure 2).

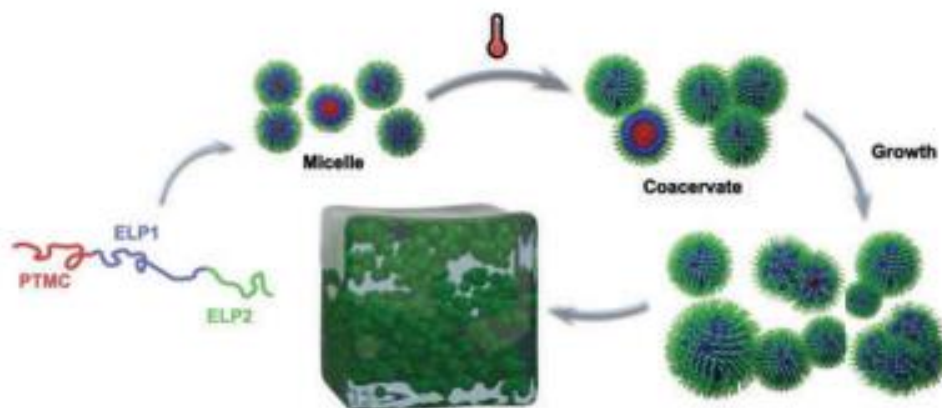


**Figure 2. Self-assembly of ABC-type triblock copolymers designed by Dai and colleagues<sup>12</sup>.**

However, this system had certain limitations. First, to obtain a stable hydrogel, the polymer concentration had to be exactly 4%. Below this concentration, the solution was viscous and at 5% syneresis was observed. Moreover, the synthesis of the ABC triblock requiring several successive chemical reactions and therefore numerous purification steps, the yield of the purified ABC triblock was low.

We therefore looked to a simpler approach, by grafting two fatty acid molecules at the extremities of an ELP backbone. We had three possibilities to achieve this goal. The first one was to start with the ELP-FAs already synthesized, and to graft an additional FA on their carboxyl-terminal ends. To this end, several strategies could be evaluated: coupling via the formation of an anhydride or coupling through a modified FA that will react more easily with the carboxylic moiety of the ELP. For instance, FA could be reacted first with a diamine to have an amine moiety that this will react with the carboxylic acid as performed during the preceding chapter. The beauty of this route is that the FAs present at both chain-end of ELP could be of different nature. The second possibility was to add a second primary amine in the ELP sequence, by inserting a lysine residue at the terminal end of ELPs of the M series. Doing this, the new ELP will possess one primary amine at each end, one corresponding to the N-terminus and the second one at its C-terminus (Lys). Once obtained, fatty acid condensation on the two primary amines could be performed using the same chemical reaction as that described in the previous chapter, allowing the synthesis of FA-ELP-FA. Finally, a third strategy was evaluated. It is based on the use of an FA-ELP which would form dimers of the FA-ELP-ELP-

FA type. For this, the ELP must contain at one of its ends a chemical group that can react with another ELP to form a covalent bond. This is the case for ELPs containing a cysteine at their C-terminal end, two monomers being able to form dimers after an oxidation step. After acylation on the primary amine of these dimers, we could obtain B-A-A-B tetra-blocks. Of course, such copolymers will be susceptible to the action of reducing agents, as will be the corresponding hydrogel. We already had in the LCPO's library the ELP M40C with a cysteine at its C-terminal end. This ELP can form dimers when oxidized by the formation of an intermolecular disulfide bridge. We therefore acylated these M40C dimers to obtain the desired compound, FA-M40C-CM40-FA.

The second and third strategies described above were used in this work.

## 4.2. Results and discussion

### 4.2.1. Construction of MxK producing clones

The easiest way to insert a Lysine codon at the C-terminal end of an ELP is to use site directed mutagenesis. Briefly, this is based on PCR amplification of a cDNA sequence using primers that are specific for the sequence of interest but contain an additional codon that will be present in the PCR products. Several kits are available on the market and we used the Takara's In-Fusion Cloning kit. To insert bases with this technology, two primers are designed to include 15-bp overlaps with each other at their 5' ends and contain the desired insertion within the overlapping region (Fig. 3). Only the 15 bases at the 5' ends of the primers are required to overlap. A PCR reaction will amplify a linear fragment corresponding to the plasmid with the two primer sequences at each end, and then a recombination reaction will reconstitute the circular plasmid with the mutation.

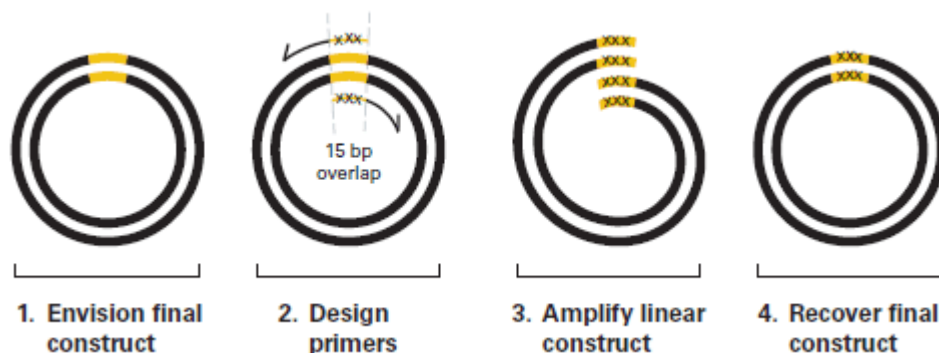


**Figure 3. Description of the four successive steps required for site directed mutagenesis.**

This technique works well with the majority of the genes, but is less reliable when used with highly repetitive sequences like those of ELPs. In this case, the primers can bind at different sites, and therefore lead to the amplification of smaller sequences than those expected. Moreover, this problem increased with the size of the DNA sequence, the number of repetitions increasing accordingly. Indeed, in our hand when starting with the M40 sequence, we obtained M20K and M40K plasmids. However, when starting with the M100 sequence, we only obtained M40K and M60K clones. Therefore, to obtain M80K we used an alternative strategy: starting with an M60K clone, we inserted the M20 sequence between the MW dipeptide of the N-terminal extremity and the M60K coding sequence by using conventional restriction digestion/ligation techniques. These approaches are summarized in Fig. 4.

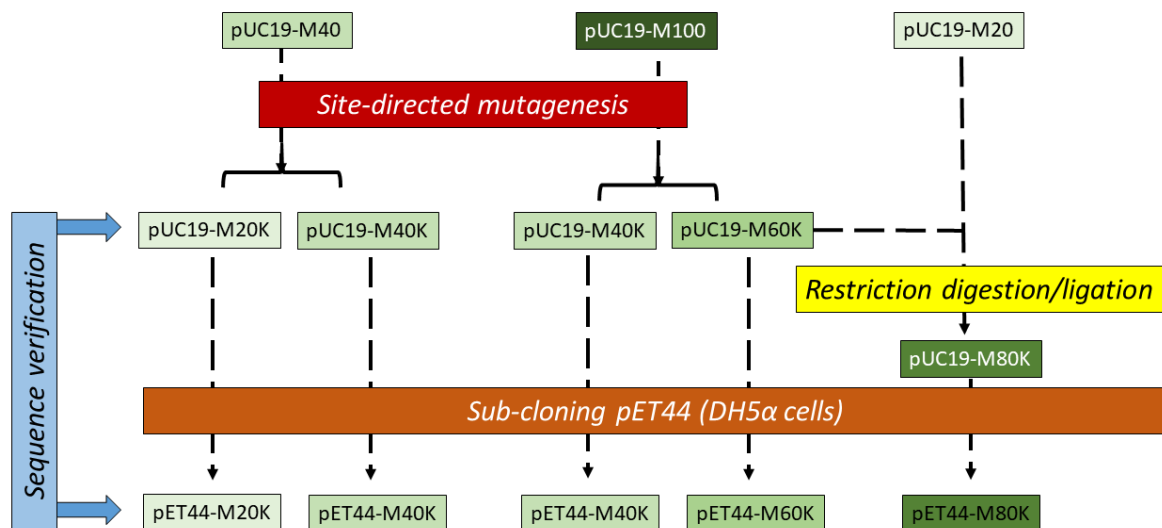


**Figure 4. Cloning strategy for obtaining M20K, M40K, M60K and M80K**

For the sake of clarity, we will not present all the results obtained during these cloning procedures, focusing only on the construction of the producer clone of M40K as an example.

An *E. coli* clone containing the pUC19-M40 plasmid has been previously obtained in our laboratory. A culture was performed, the plasmid was purified and its quality was evaluated by agarose gel electrophoresis before or after digestion by the restriction enzyme *Bam*HI that cuts the circular plasmid at one specific site (Fig. 5)

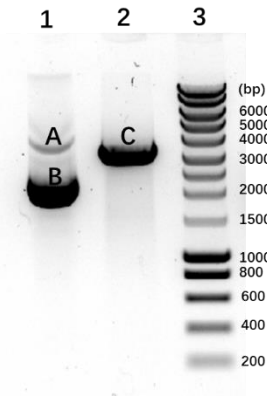


**Figure 5. Agarose gel electrophoresis of purified pUC19-M40. 1) non-digested plasmid. 2) *Bam*HI restriction product. 3) DNA ladder.**

Two bands are visible in the non-digested sample. Band A corresponds to the circular form of the plasmid, band B corresponds to the supercoiled one. As expected for good quality plasmid, the supercoiled form is the most abundant. After digestion by the restriction enzyme *Bam*HI, which cuts this plasmid once, we obtained the linear form (band C), the size of which was compatible with the theoretical size of 3301 bp.

The next step was to perform PCR amplification using primers that will introduce the triplet AAA (lysine codon) just upstream of the M40 TAA stop codon (Fig. 6).

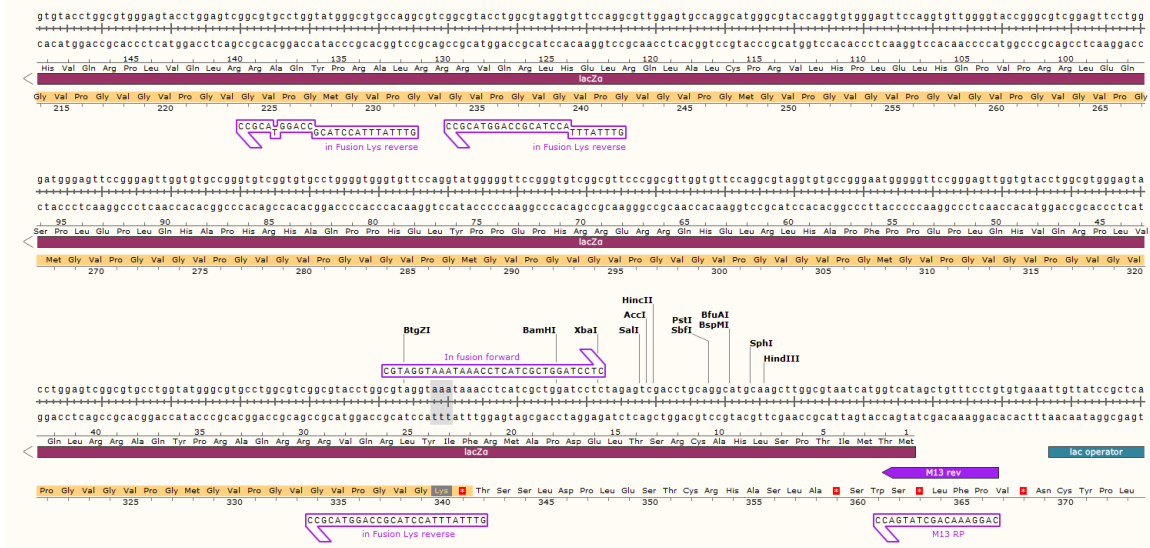


**Figure 6. Graphic representation of the M40K coding sequence (3' side) with primers used for mutagenesis. The M40K amino acid sequence is in orange. Forward and reverse primers are indicated by boxed arrows.**

The PCR products were then analyzed by agarose gel electrophoresis (Fig. 7).

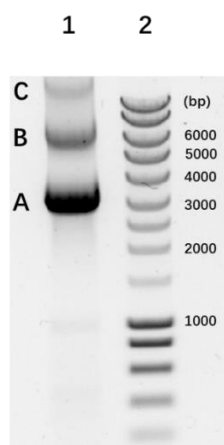


**Figure 7. Analysis of PCR products on agarose gel. Lane 1 corresponds to the PCR products. Lane 2 is the size marker.**

Three main bands are seen in lane 1. The more intense (band A) had a size between 3000 and 3300 bp. In fact, it encompasses two fragments of respectively 3000 and 3300 bp as was demonstrated in following experiments. This is due to the fact that the M40 sequence is the direct repetition of two identical M20 sequences. Therefore, one of the two primers used (reverse complimentary primer) can hybridize at the end of the M40 DNA sequence present in the plasmid, but also in the middle of this M40 DNA sequence (see Figure 4). We therefore simultaneously amplified the linear plasmids pUC19-M40K and pUC19-M20K DNA. The bands B and C, corresponding to larger double-stranded DNA are in fact dimers (B) and trimers (C) of the plasmid. Indeed, knowing that the two extremities of the PCR product are self-complimentary, two (or three) fragments can stick together and be used as matrix in the following PCR cycle. Once again, this is due to the fact that we worked with highly repeated sequences. The next step was therefore to purify band A by gel excision to eliminate bands B and C, as well as the pUC19-M40 plasmid which served as the matrix for the PCR. Indeed, this pUC19-M40 plasmid being supercoiled, it will have an advantage during the transformation of the competent cells and this might lead to a large number of M40 (not mutated) colonies. The concentration of the purified DNA (band A) was checked by spectrophotometry and its quality by gel electrophoresis (Figure 8)

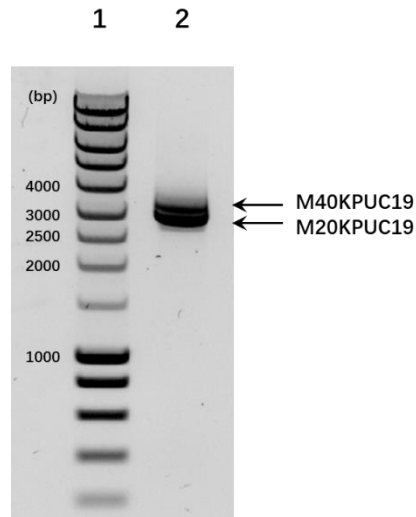


**Figure 8. M40K-pUC19 and M20K-pUC19 on gel agarose gel**

This gel clearly shows that we have succeeded in eliminating the multimeric forms of the plasmid (bands B and C Fig. 7), and that we have purified two bands corresponding to pUC19 containing the M40K and M20K sequences. Owing to their close size, it was not possible to efficiently separate these two plasmids. We therefore decided to use this mixture in the following steps, knowing that the segregation of the two types of plasmids will take place during the cloning procedure: each clone obtained after the transformation step will contain only one of the two species. The next step was to circularize the linear pUC19 plasmids generated during the PCR. This was achieved using a specific recombinase provided in the In-Fusion kit. The circular plasmids were then transformed into chemically competent *E. coli* Stellar cells, and clones which contain a pUC19 plasmid were selected on LB agar plates containing ampicillin. After overnight growth, several colonies were obtained, and they were screened by PCR using primers flanking the ELP DNA sequence. Of course, using this screening, it was not possible to discriminate the original pUC19 M40 plasmid from the pUC19 M40K plasmid, the insertion of the three bases of the lysine codon not significantly modifying the size of the amplified product. (722 and 725 bp, respectively). However, using this strategy we were able to discriminate between clones containing inserts corresponding to M40 or M20 (Fig. 8).

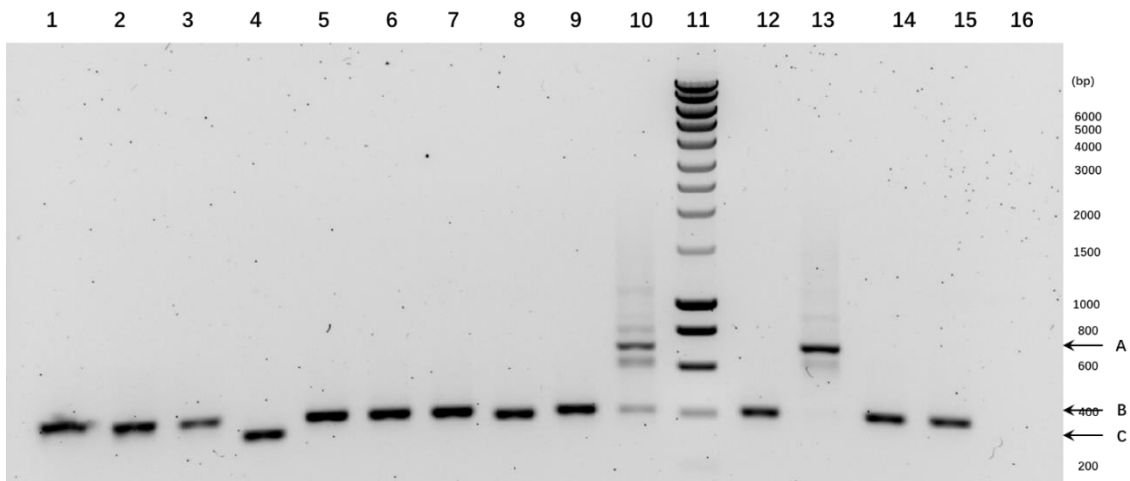


**Figure 8. Colonies screening by PCR and agarose gel electrophoresis. After transformation, bacterial clones containing the pUC19 plasmid were selected on ampicillin-agarose plates. After overnight growing at 37°C, colonies were selected and used to perform PCR amplification with pUC19 specific primers.**

Of the 14 clones screened in this experiment, 11 gave an amplicon of approximately 400 bp (arrow B), which corresponds to the size expected for the M20 and M20K sequences. One clone (No. 4, arrow C) gave a product of approximately 380 bp, corresponding to a sequence shorter than M20 and therefore a deleted form. Only two clones, # 10 and 12, gave a PCR product of approximately 700 bp (arrow A) which could correspond to the M40 or M40K sequences. The fact that some other bands are observed in the corresponding lanes is again explained by the fact that the DNA sequences of the ELP are very repeated, and that these internal repetitions can lead to artifacts during the PCR process. (hairpin formation in the single strand products or base pairing at the wrong position).

Plasmids from clones 10 and 12 were then purified, double-digested by the restriction enzymes *NdeI* and *BamHI* to release the M40(K) insert from the pUC19 backbone, and the digestion products were separated by electrophoresis (Fig. 9).

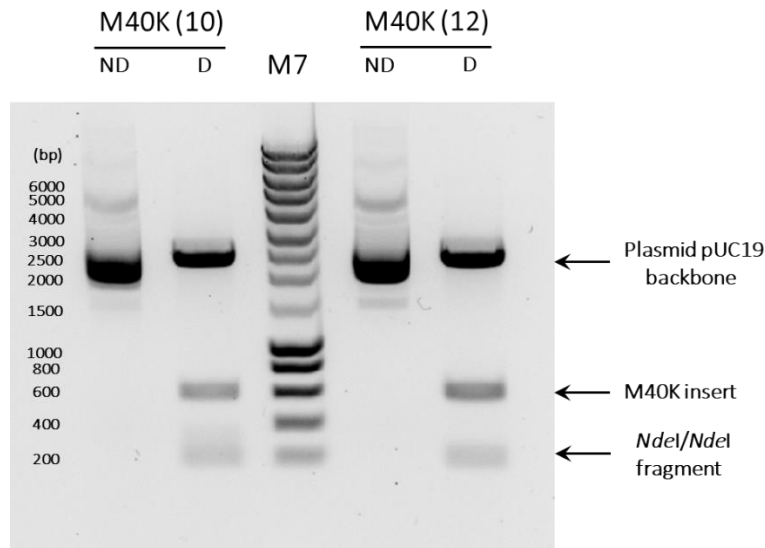


**Figure 9. Agarose gel electrophoresis of purified plasmids from clones 10 and 12. ND: non digested plasmids. D: plasmid double-digested by *NdeI* and *BamHI*.**

After digestion, we expected to see three bands: one at 2452 bp, corresponding to the pUC19 backbone, a second one at 626 bp corresponding to M40(K) insert, and a third one of 226 bp corresponding to the pUC19 fragment present between two *NdeI* sites. Our results confirmed that the plasmids from clones 10 and 12 corresponded to M40 or M40K sequences.

The next step was to sequence the corresponding plasmids to verify that the insertion of the lysine codon did take place (Fig. 10).

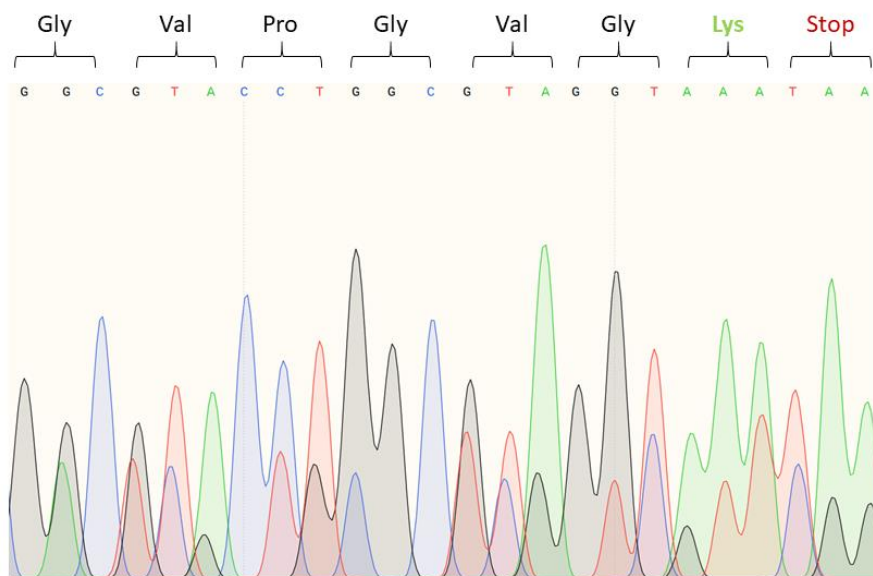


**Figure 10. Sequencing results of clone #10. Purified pUC19 plasmid from clone 10 (M40K) was sequenced. The corresponding chromatogram and the deduced nucleic and amino acid sequence were obtained using the SnapGene viewer software.**

The results showed that the directed mutagenesis worked well and that we obtained the desired pUC19-M40K plasmid.

The next step was the sub-cloning of the ELP DNA sequences into the expression vector pET44a. The 626 bp DNA fragments obtained after *NdeI/BamHI* double digestion was gel-purified. In parallel, the vector pET44 was also double digested with the same restriction enzymes, dephosphorylated to prevent self-ligation in the absence of the M40K cDNA, and gel-purified. After ligation with the ELP inserts, BLR *E. coli* competent cells were transformed by heat-shock. After overnight growth on selecting agar plates containing ampicillin, three clones were screened by PCR (Fig. 11).

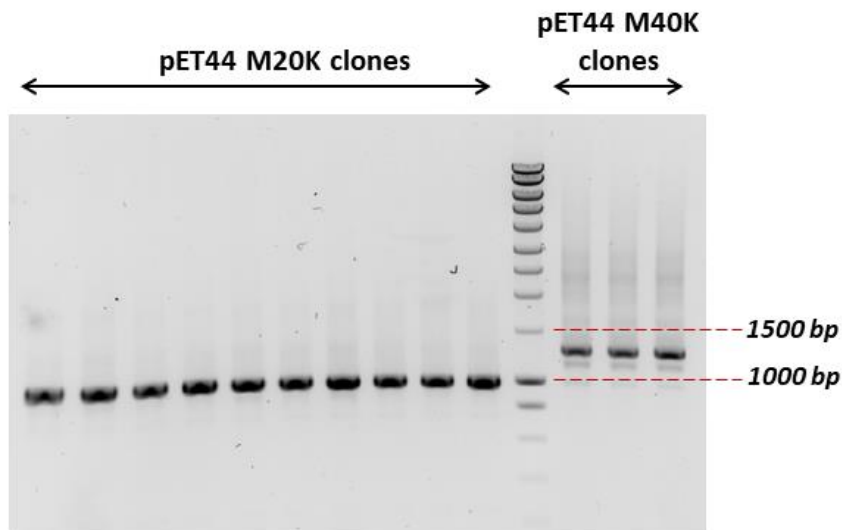


**Figure 11. PCR colony screening of pET44-M20K and PET44-M40K clones.**

The PCR products obtained from the ten M20K clones had a size compatible with the expected one (988 bp). For the M40K clones, we obtained a PCR fragment close to the expected size (1288 bp) for three of them. To confirm the identity of the plasmids, each one was purified and sequenced.

#### 4.2.2. Production and purification of MxK and MxC polypeptides

The next step consisted in the expression of the recombinant protein. Once again, we will illustrate this part with M40K.

Briefly, a preculture of selected clone #1 containing pET44-M40K was used to seed 400 mL of LB medium supplemented with 1g/L glycerol and 100 µg/mL ampicillin. When OD<sub>600nm</sub> reached a value between 0.6 and 0.8, IPTG was added to the culture at a final concentration of 0.5 mM and the incubation temperature was lowered from 37°C to 25°C. After an overnight growth, cells were recovered by centrifugation, suspended into cold water and lysed by sonication. Insoluble debris were removed by centrifugation, and the soluble protein fraction was used for purification of the M40K protein by the ITC technique. Follow-up of this production and purification process was achieved by analyzing the protein content of the different fractions by SDS-PAGE analysis (Fig. 12).

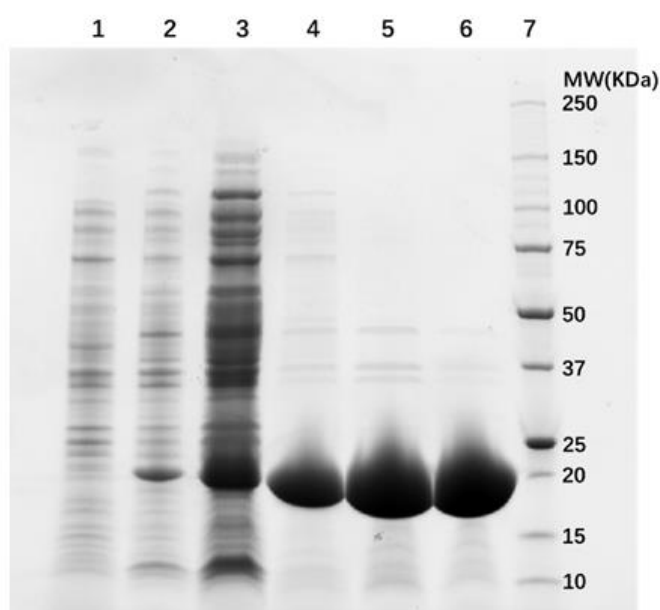


**Figure 12. SDS-PAGE analyses of the different protein fractions obtained during the production and purification process. Lane 1: non-induced cell culture. Lane 2. 12 H induction by IPTG. Lane 3: soluble protein fraction after cell lysis. Lane 4-6: protein content after the first, second and third ITC cycles. Lane 7: Protein standard (Precision Plus Polypeptide Standard). MW of the standard proteins in kDa. Normalization of the protein content between lanes 1 and 2 was achieved by using the same number of cells according to the OD measured for each sample of the culture.**

Comparison of the samples obtained before (lane 1) and after the IPTG induction (lane 2) clearly shows the accumulation of a new protein of ~ 18 kDa, close to the theoretical mass of 17.2 kDa. This protein was enriched in the soluble fraction (lane 3), and efficiently purified during the ITC cycles, although traces of some contaminant proteins remained in the purified fraction even after 3 purification cycles. However, these contaminants represent less than 2 % of the total protein content as estimated by densitometry analysis of the gel. Finally, after dialysis and lyophilization the yield of purified M40K was 150 mg/L culture, which is in the range obtained for the other ELP of the M series produced in our laboratory (60-180 mg/L culture). All the ELP produced and purified in this study were analyzed by SDS-PAGE electrophoresis (Fig. 13)

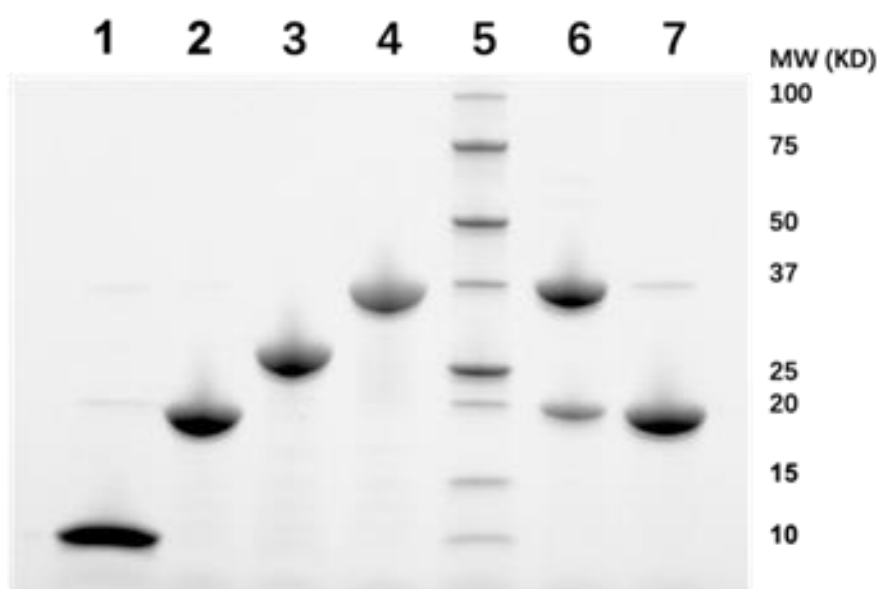


**Figure 13. SDS-PAGE analyses of the purified ELP samples (20  $\mu$ g/lane). Lane 1: M20K. Lane 2: M40K. Lane 3: M60K. Lane 4: M80K. Lane 5: Protein standard (Precision Plus Polypeptide Standard). Lane 6: M40C (unreduced). Lane 7: M40C after reduction of the disulfide bridges by  $\beta$ -mercaptoethanol. MW of the standard proteins in kDa.**

### 4.2.3. Synthesis and characterization of FA-ELP-FA

For ELP MxK, the acylation reaction was carried out directly with the purified ELP monomers which contain two primary amines, the N-terminal one and that of the lysine residue. For the MxCs which have only one primary amine at their N-terminus, we had to obtain dimers by oxidation of the C-terminal cysteine residues. To set up this reaction, we kept in mind that the oxidation must trigger the formation of disulfide bridges, but not the oxidation of the methionine residues presents in the M40C sequence. Indeed, the apparition of sulfoxides in the polypeptide will trigger drastic changes in its Tt (see paragraph 3.2.5.). To find the right balance between cysteine and methionine oxidation, we tested different conditions and the formation of dimers was evaluated by SDS-PAGE electrophoresis whereas the apparition of sulfoxides was monitored by  $^1\text{H}$  NMR. Two parameters were varied to find the best reaction condition: the molar ratio of hydrogen peroxide/ELP and the incubation time. A typical result is shown in Figure 14.

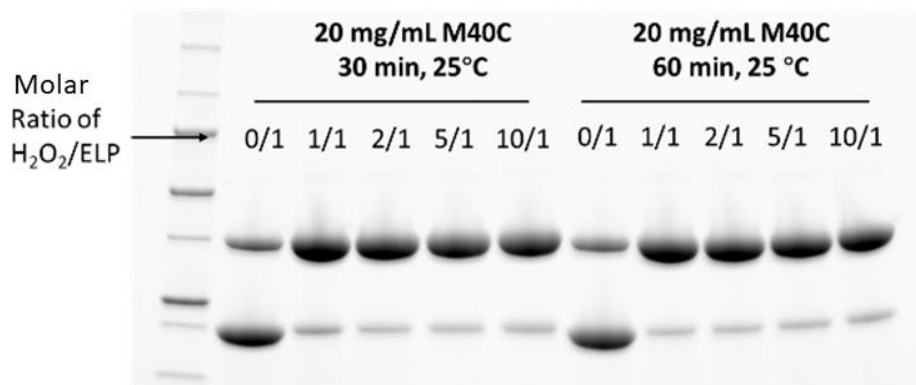


**Figure 14. SDS-PAGE analysis of M40C oxidized products. 20 mg of ELP in Tris 10 mM pH 8.8 were incubated with various amount of  $\text{H}_2\text{O}_2$  for different times. 15  $\mu\text{g}$  of each sample was analyzed per lane.**

In the absence of  $\text{H}_2\text{O}_2$ , we observe a major band corresponding to M40C monomers, and a second band of higher MW corresponding to M40C dimers. Densitometric analysis of these gels showed that dimers represent between 30 and 40% of the sample. Their presence is simply explained by the fact that during their purification by ITC, the samples were heated for several minutes at  $40^\circ\text{C}$  to trigger their aggregation, and that these heating steps are known to cause the oxidation of cysteines. When incubated with  $\text{H}_2\text{O}_2$ , the percentage of dimers in the solution

increased rapidly to reach 90-95% of the sample. It should be noted that we never obtained a sample containing 100% of dimers, even with higher concentrations of H<sub>2</sub>O<sub>2</sub> or longer incubation times. Of course, we could have tried to separate both products by size-exclusion chromatography but we thought that this will lead to a loss of product that was not worth it. For the following experiment, we decided to oxidize M40C with 0.017 % hydrogen peroxide (H<sub>2</sub>O<sub>2</sub>/ELP molar ratio 5:1) for 30 min at 25°C in Tris buffer. We next checked by <sup>1</sup>H NMR if the corresponding product did not contain sulfoxides (Fig. 15).

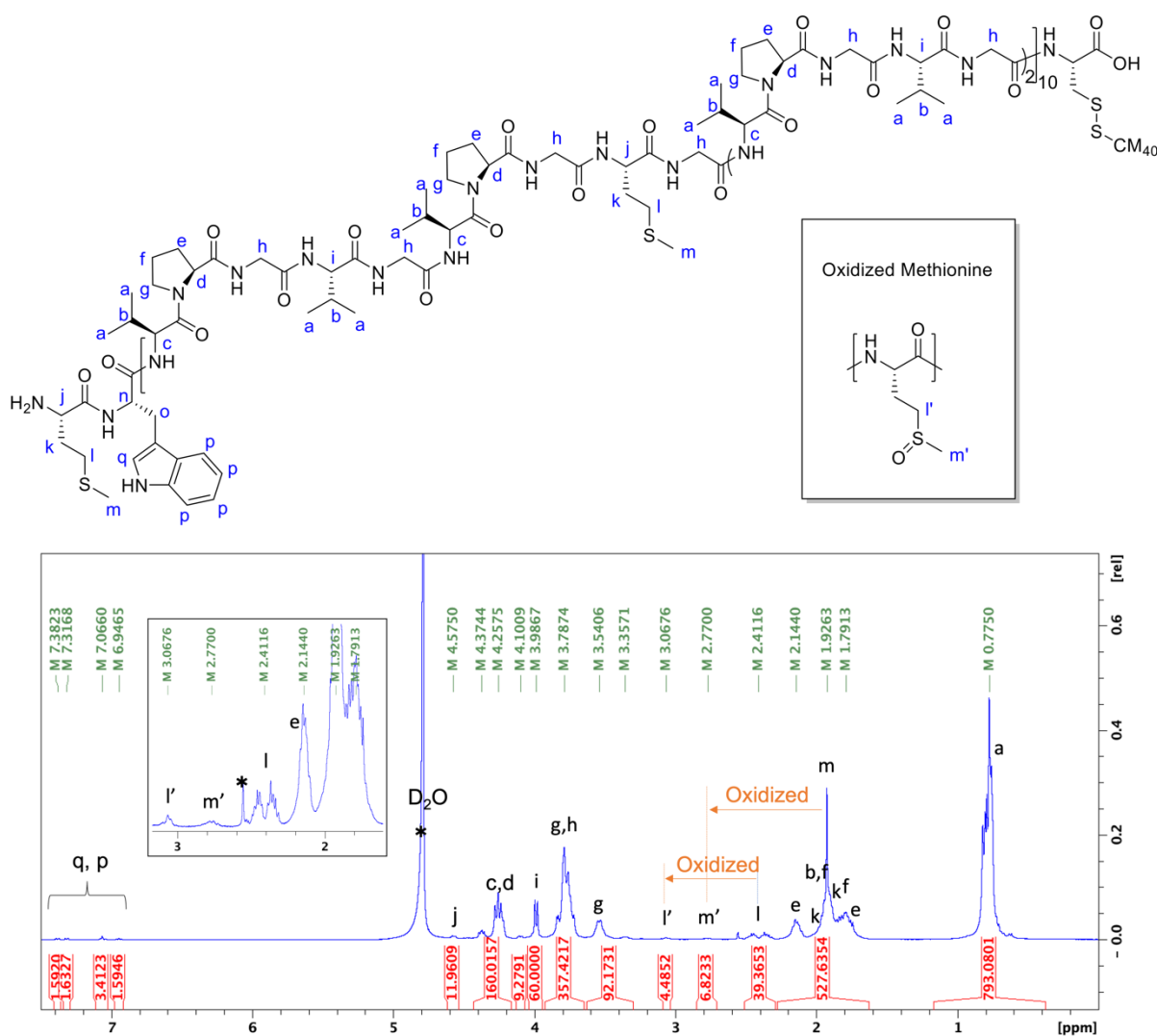


**Figure 15.** <sup>1</sup>H NMR spectrum of oxidized M40C in D<sub>2</sub>O.

When methionine residues are oxidized in sulfoxides, the NMR signals of the protons close to the sulfur atom shift to higher ppm, from 2.41 ppm for  $\gamma$ CH<sub>2</sub> Met (l) to 3.06 ppm (l'), and from 1.92 ppm for  $\epsilon$ CH<sub>3</sub> Met (m) to 2.77 ppm (m'). These shifts can be explained by the deshielding effect of the oxygen atoms. Therefore, by integrating the corresponding peaks it was possible

to measure the sulfoxide/methionine ratio in our ELP. We found that after oxidation by H<sub>2</sub>O<sub>2</sub>, this ratio was 10% indicating that the M40C dimers contained 2 sulfoxides and 20 non-oxidized methionine.

The reaction of ELP acylation was performed as already described in chapter 3.2.1, the only modification was that the molar ratio of fatty acid/ ELP was increased to 3:1 to have a fatty acid/primary amine ratio of 1.5/1. The acylated products were then analyzed by RP-HPLC. Figure 16 shows the results obtained after palmitoylation of M20K, M40K, M60K and M80K

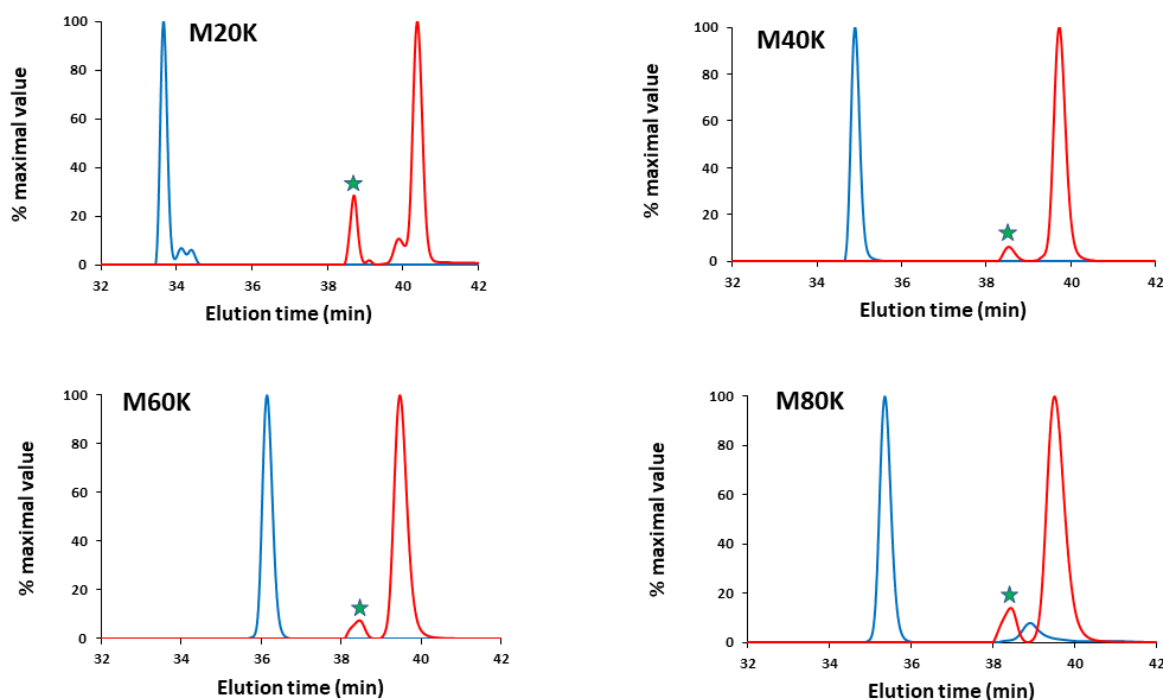


**Figure 16. RP-HPLC traces of ELPs and of FA-ELP-FAs. A solution at 70  $\mu$ M in water was analyzed for each compound. Eluent was a gradient of a water/methanol mixture. The intensity at 230 nm was normalized to maximal value. Traces for unmodified ELP (blue lines), and for palmitoylated ELP (red lines). The green stars indicate the pic corresponding to the mono-palmitoylated compounds.**

Prior to acylation, a single peak was observed except for M80K where a small peak at around 39 min was observed. We believe that this peak could correspond to small amounts of M80K dimers although none of these dimers were detected after SDS-PAGE analysis of the same sample, which strongly suggests that they are not bound by covalent bonds. After acylation by

C16, we observed the total disappearance of the peak corresponding to the free ELPs, and the presence of two peaks with higher retention times. We believe that the larger peak, with higher retention times, corresponds to the expected FA-ELP-FA compounds, while the smaller peak, indicated by a green star in Figure 16, could correspond to the FA-ELPs. The retention times and the percentage of peak 2 for each compound are shown in Table 3.

**Table 3. RP-HPLC analysis of ELP-FAs**

	Palmitoylated M20K	Palmitoylated M40K	Palmitoylated M60K	Palmitoylated M80K	Palmytoylated M40C dimers	Stearoylated M40C dimers
Peak 1 retention time (min.)	38.7	38.5	38.5	38.4	38.7	39.0
Peak 2 retention time (min.)	40.4	39.7	39.5	39.5	39.8	40.8
% peak 2	83%	95%	93%	90%	92%	88%

The retention time measured for peak 1 was around 38.5 min, whatever the ELP size In paragraph 3.2.2.1, the retention time measured for M20-C16, M40-C16 and M80-C16 were respectively 36.4, 38.4 and 38.2 min. Thus, the results obtained for M40K and M80K are compatible with the hypothesis that peak 1 is mono-palmitoylated ELP. However, the data for the acylated M20K are less conclusive because the retention time for peak 1 was 2 min higher than that measured for M20-C16. In addition, the palmitoylated M20K contains only 83% of C16-M20K-C16 whereas the conversion rates were at least 90% for the other MxK studied, suggesting that the reaction was not as efficient with the smaller ELP.

In conclusion, these experiments showed that we obtained C16-MxK-C16 in good yields, but that these samples contained small amounts of ELP acylated by one palmitate molecule. Similar analyses were performed after palmitoylation of the M40C dimers (Fig. 17).

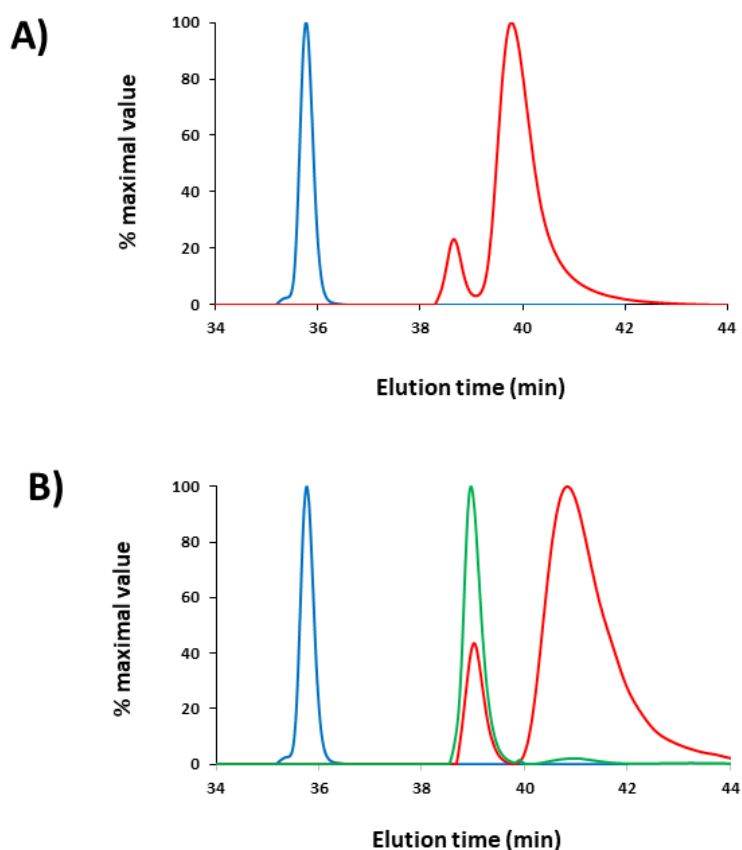


**Figure 17. RP-HPLC traces of M40C dimers before and after acylation. A) Traces for M40C dimers (blue line) and after acylation by C16 (red line). B) Traces for M40C dimers (blue line), after acylation by C18 (red line), and after incubation of the C18-M40C dimers with 50 mM dithiothreitol for 12 hours (green line).**

After palmitoylation of the M40C dimers, we observed a main peak at 39.8 min corresponding to the dimer conjugated to two palmitate molecules. This peak represented 92% of the acylated sample. Again, a small peak at 38.6 min was observed. This peak could contain either M40C dimers with a palmitate unit, or M40C monomers with one palmitate, or a mixture of the two species. We also used stearic acid to acylate the M40C dimers (Fig. 16B). The condensation reaction proceeded as evidenced by the appearance of a compound with a retention time of 40.8 min, although approximately 12% of the reaction product had eluted at 39 min. Again, this minor peak could correspond to ELP dimers with stearate or M40C-C18 monomers. To test these hypotheses, the same sample was incubated with dithiothreitol to reduce the disulfide bridges, and thus generate the C18-M40C and M40C-C18 monomers. Under this condition, the peak at 40.8 min disappeared, and a single peak at 39 min was detected confirming that it

indeed corresponded to M40C conjugated to a stearate molecule. Indeed, if it had corresponded to dimers of M40C with a single palmitate, the reduction of the disulfide bridges would have given both M40C and M40C-C18. However, we did not detect any peak corresponding to M40C after reduction. In conclusion, these results suggest that the addition of two fatty acids on the M40C dimers was effective, although approximately 10% of the M40C-FA monomers were present in the final reaction product.

#### 4.2.4. Cloud point determination of FA-ELP-FA

We first sought to measure the cloud point temperature of the FA-ELP-FA in PBS buffer. Indeed, we previously showed (Chapter 3) that ELP-FAs formed stable micelles in PBS at temperatures below their  $T_{cp}$ . Unfortunately, this was not the case for the di-acylated ELPs: when placed in PBS buffer they rapidly aggregated and precipitated, even at low temperature (4°C). This is a first indication that the structuration of the FA-ELP-FA monomers in solution and/or their self-assembly is rather different from that observed for ELP-FAs. We therefore decided to measure the  $T_{cp}$  values in 10 mM Tris buffer. Results for C16-MxK-C16 are shown in Figure 18, and those for the palmitoylated M40C dimers in Figure 19.

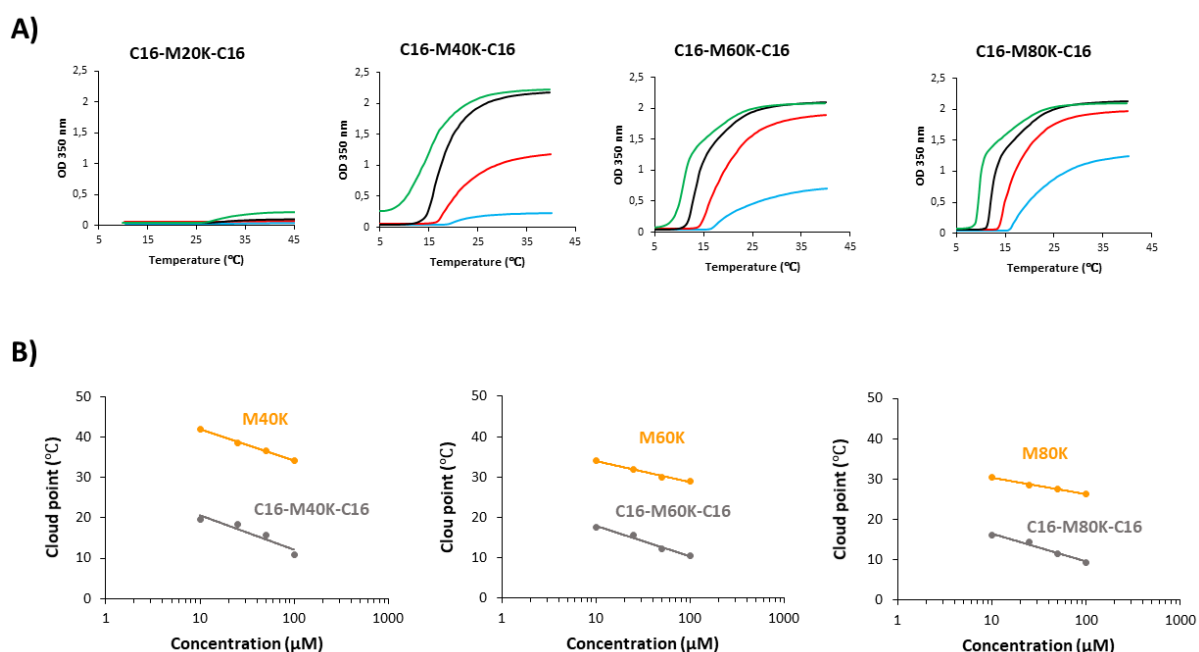


**Figure 18. Cloud point temperature of di-palmitoylated MxK in Tris buffer. A) T-scans of samples at different concentrations: 10 μM (blue lines), 25 μM (red line), 50 μM (black line) and 100 μM (green line). B) Relationship between  $T_{cp}$  and concentration.**

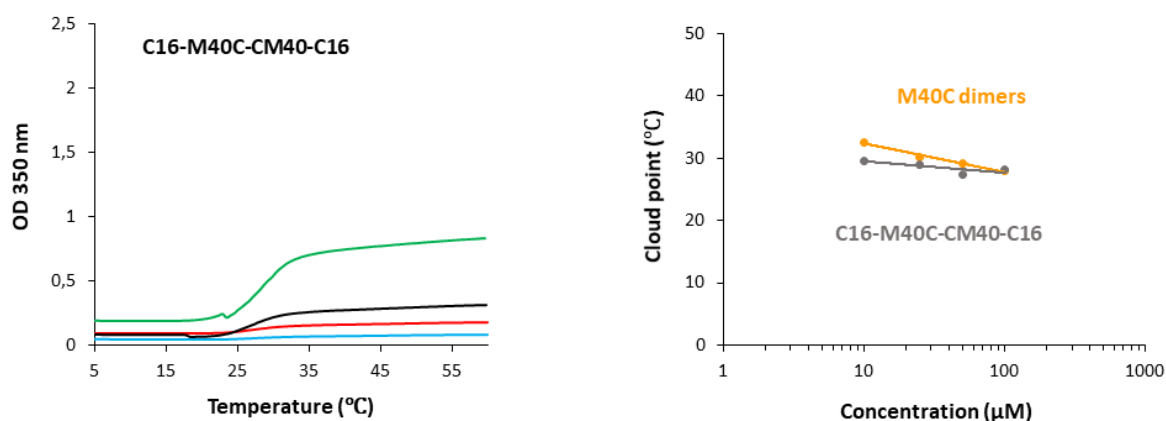


**Figure 19. Cloud point temperature of palmitoylated M40C dimers in Tris buffer. A) T-scans of samples at different concentrations: 10  $\mu\text{M}$  (blue lines), 25  $\mu\text{M}$  (red line), 50  $\mu\text{M}$  (black line) and 100  $\mu\text{M}$  (green line). B) Relationship between T<sub>cp</sub> and concentration.**

Several conclusions can be drawn from these results. First, the size of the ELP moiety is important as showed by the fact that we did not observe significant increase in turbidity when the C16-M20K-C16 sample was heated, whereas turbidity increased for larger di-palmitoylated ELPs, whatever the concentration studied. Similar conclusions were made for mono-acylated ELPs (see paragraph 3.2.3.3). Second, the addition of two fatty acids on the MxK backbone drastically decreased the T<sub>cp</sub> values when compared to those of the unmodified ELP. This was expected because acylation increased the hydrophobicity of the conjugate, and therefore diminished its solubility upon heating. However, if such a decrease in T<sub>cp</sub> values was previously observed for ELP-FAs in PBS buffer (see Paragraph 3.2.2.5), this was not observed in Tris buffer where the T<sub>cp</sub> of the ELP-FAs were higher (M40-FAs) or similar (M80-FAs) to the T<sub>t</sub> of the free ELP. This is another indication that ELP-FAs and FA-ELP-FA behave differently in aqueous buffers. Interestingly, this strong decrease in T<sub>cp</sub> was not observed for M40C dimers, the corresponding values being similar before and after palmitoylation (Fig. 19). Third, our results show that FA-ELP-FA T<sub>cp</sub> values vary with sample concentration, similar to what is observed for non-acylated ELPs, whereas ELP-FA T<sub>cp</sub> values were almost independent of concentration. In the case of ELP-FAs, the hypothesis was that the aggregation was controlled by the local high and invariant concentration of ELP in the micelles, and not by the total concentration of the compound in solution. In the case of FA-ELP-FA, which probably also form micelles at low temperature in aqueous buffers (without salts), it can be hypothesized that there are additional interactions between these micelles, independent of those triggering

the coacervation of ELPs, and that these interactions increase with FA-ELP-FA concentrations. Finally, an intriguing fact is the differences observed between palmitoylated M80K and M40C dimers. These two ELPs species contained exactly the same number of repeats, and their sizes are nearly identical: M40C dimers contained only three additional amino acids compared to M80K, one cysteine, one tryptophan and one methionine (see Figure 20).

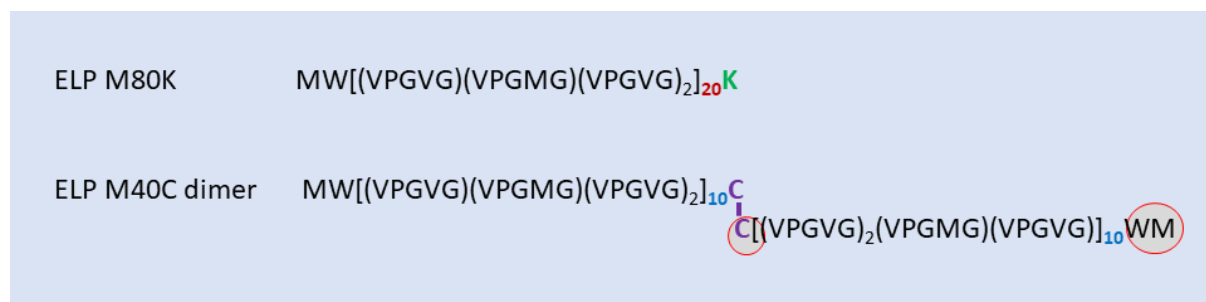


**Figure 20. Schematic representation of the M80K and M40C dimer amino acid sequences. Amino acids specific for each sequence are in green (M80K) and purple (M40C dimer). The additional amino acids of the M40C dimer are indicated by circles.**

Despite these negligible different in terms of MW, they behaved quite differently after acylation by two palmitate units. The  $T_{cp}$  of acylated M80K decreased by 15 to 20°C compared to that of M80K, and upon heating the  $OD_{350nm}$  reached a value of about 2 for concentrations above 25  $\mu$ M. On the contrary, the  $T_{cp}$  values measured for the acylated M40C dimers were similar to those of the non-acylated compound, and the  $OD_{350nm}$  values reached upon heating were well below 1, even at a concentration of 100  $\mu$ M. These results strongly suggested that these two palmitoylated compounds have different intrinsic physical properties although having very similar chemical composition.

#### 4.2.5. Characterization of FA-ELP-FA by DLS

Our hypothesis was that FA-ELP-FA forms “flower like” micelles in aqueous buffer at a temperature below their  $T_{cp}$ . We therefore measured the  $R_H$  of these acylated ELPs in Tris buffer at a concentration of 1mg/mL (Fig. 21).

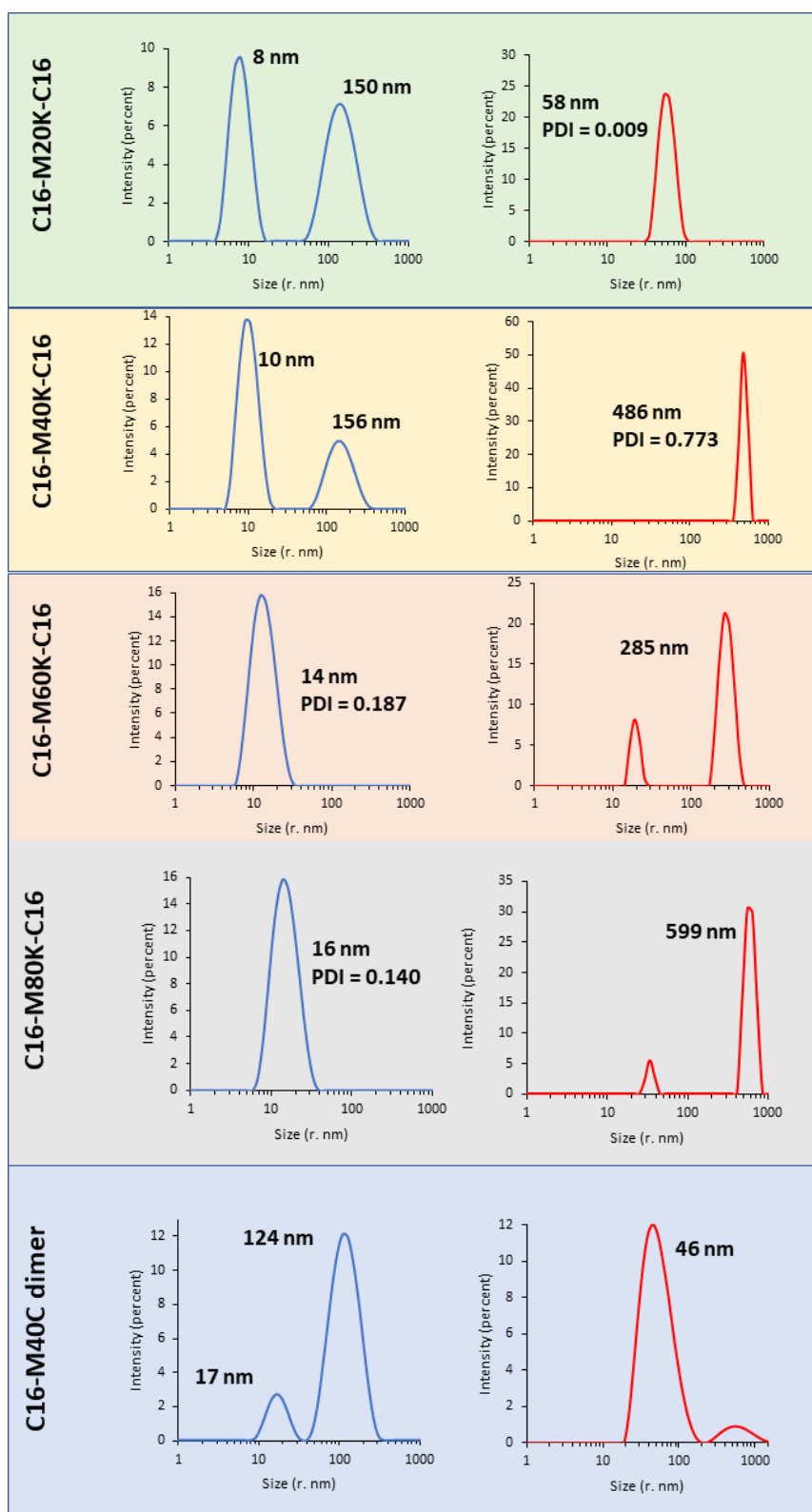


**Figure 21. DLS analysis of the palmitoylated compounds. Samples were at a concentration of 1 mg/mL in 10 mM Tris buffer. Measurements were made at 4°C (blue traces) and 40°C (red traces). Results obtained by intensity are shown. PDI values are shown for samples where only one population was detected.**

At low temperature, we detected in each sample a population of a few nanometers which increases with the ELP block length, from 8 nm for M20K to ~16-17 nm for M80K and M40C dimers. This result is similar to what we previously observed for ELP-FAs (see chapter 3, paragraph 3.2.3.2). However, in the case of di-palmitoylated MxK, the sizes of the micelles were significantly lower than those of their mono-palmitoylated counterparts (Table 4).

**Table 4: comparison of RH values (% intensity) for mono- and di-palmitoylated ELPs**

ELP backbone	Mono palmitoylated	Di-palmitoylated
M20	10 nm	8 nm*
M40	16 nm	14 nm
M80	21 nm	16 nm

*\*This value corresponds to the population of smaller size in the % intensity graph*

To explain the difference in  $R_H$ , the following hypothesis can be put forward: with a molecule of C16, the ELP is exposed at the surface of the micelle and it can unfold freely in the aqueous medium. On the other hand, when a palmitate molecule is grafted to each end of the ELP, the two fatty acids are anchored in the micelle, and the ELP segment therefore cannot unfold as freely in the aqueous medium. This is illustrated in Figure 22.

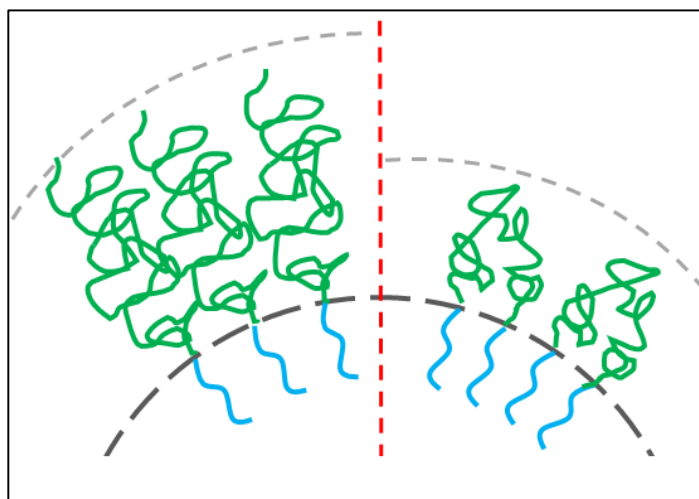


**Figure 22. Schematic representation of the possible organization of ELP-FAs and FA-ELP-FA into micelles. Blue for fatty acid moieties, green for ELP moieties. Dark grey line illustrates the curvature of the micelle core; light grey illustrates the curvature of the micelle corona. Left of the red dashed line: ELP-FAs, and right from the same line FA-ELP-FA.**

Another population of ~120-150nm was also present in the palmitoylated M20K, M40K and M40C dimers, most probably corresponding to aggregates.

When heating above  $T_{cp}$ , different types of behavior were observed. With the small ELP M20K block, we obtained a monodisperse population (PDI= 0.009) of particles with an  $R_H$  of 58 nm, which is seven times the value measured at 4°C. We have not further investigated the nature of these nanoparticles. For larger ELP blocks, increasing temperature led to the formation of 300–500 nm aggregates. However, some discrepancy was observed between the samples: while the di-palmitoylated M40K was fully aggregated, some smaller particles were still present in the di-palmitoylated M60K and M80K samples. In the case of palmitoylated M40C, even though we observed a small peak at ~500 nm, the majority of the population corresponded to nanoparticles of 46 nm of  $R_H$ .

Overall, these results are consistent with those previously obtained by turbidimetry. After heating, we observed by DLS the formation of aggregates for the di-palmitoylated M40K, M60K and M80K, which explains why the  $OD_{350nm}$  measured by turbidimetry reaches high values (>2). On the contrary, heating of palmitoylated M20K and palmitoylated M40C dimers results in the formation of small nanoparticles of 58 and 46 nm, respectively, which explains why the  $OD_{350nm}$  values measured by turbidimetry were below 1.

#### **4.2.6. Hydrogel formation and characterization**

As explained in the introduction, our goal was to obtain physical hydrogels. We therefore performed a quick screening study. We dissolved our compounds into water at a concentration of 5% (w/vol) by incubating under stirring at 10 °C (below  $T_{cp}$ ). Gel formation occurred after 12 to 24 h of stirring. Using this simple protocol, we obtained hydrogels for di-palmitoylated M80K and M40C dimers. For the other samples, we increased the concentration to 10%, and we obtained some gel with the di-palmitoylated M60K compounds (Fig. 23).

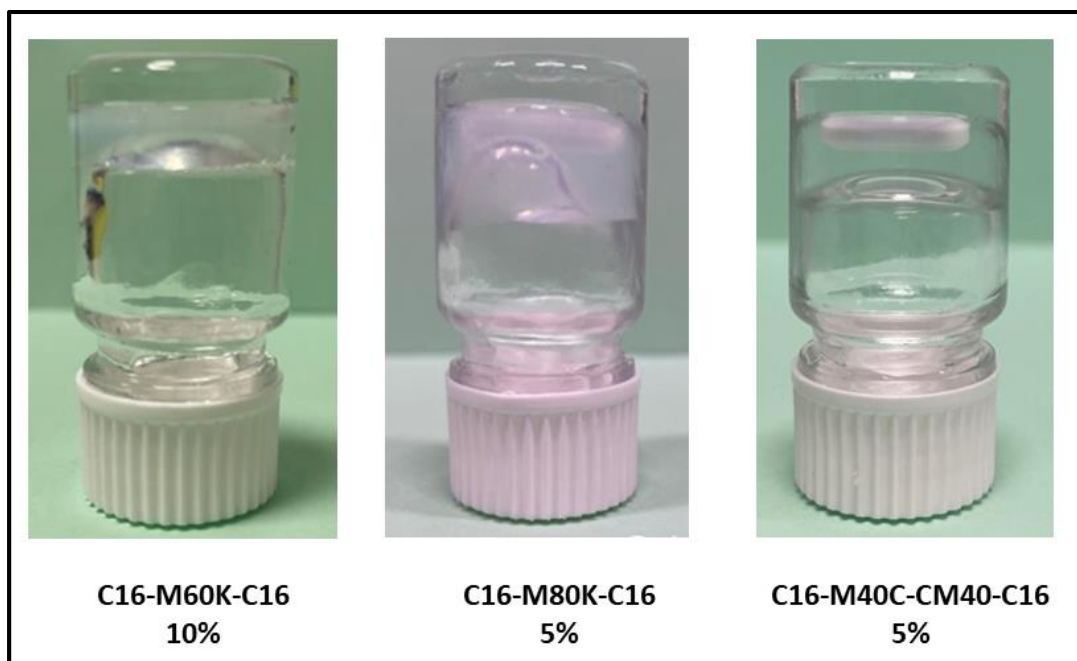


**Figure 23. Pictures of hydrogels**

The fact that we did not obtain hydrogels with short ELP blocks M20 and M40 can be explained. If we consider that the formation of the hydrogel requires physical interactions between the micelles, and that these interactions occurs when an acylated chain leaves its micelle to go and plug into a neighboring micelle, then the size of the ELP on which the fatty acid is grafted is decisive. The longer the ELP, the easier it will be to connect distant micelles. Of course, the micelle concentration is of major importance, and we could probably form gels with the short ELP blocks, but that would require increasing the concentrations. However, this is a problem for future applications since the cost of recombinant proteins is high. It is therefore not reasonable to work with higher concentrations of ELP, knowing that the production of 10 mL of 10% hydrogel would require between 6 and 10 Liters of culture.

This preliminary test also showed that it was possible to obtain hydrogels with 10% C16-M60K-C16. However, the problem was that the gel was not homogeneous, with a whiteish gel phase and a transparent liquid phase, strongly suggesting that the hydrogel underwent syneresis. This can be observed when the interaction force between the micelles is strong enough to push some of the water out of the gel. This phenomenon occurs generally when the equilibrium solvent/macromolecules are not fulfilled, disturbing the network<sup>13</sup>.

Finally, hydrogels were obtained with 5% palmitoylated M80K, and 5% palmitoylated M40C dimers. In the latter case, the gels were perfectly transparent.

Next, we measured the rheological parameters of the gels obtained with 5% of C16-M80K-C16 (Fig. 24).

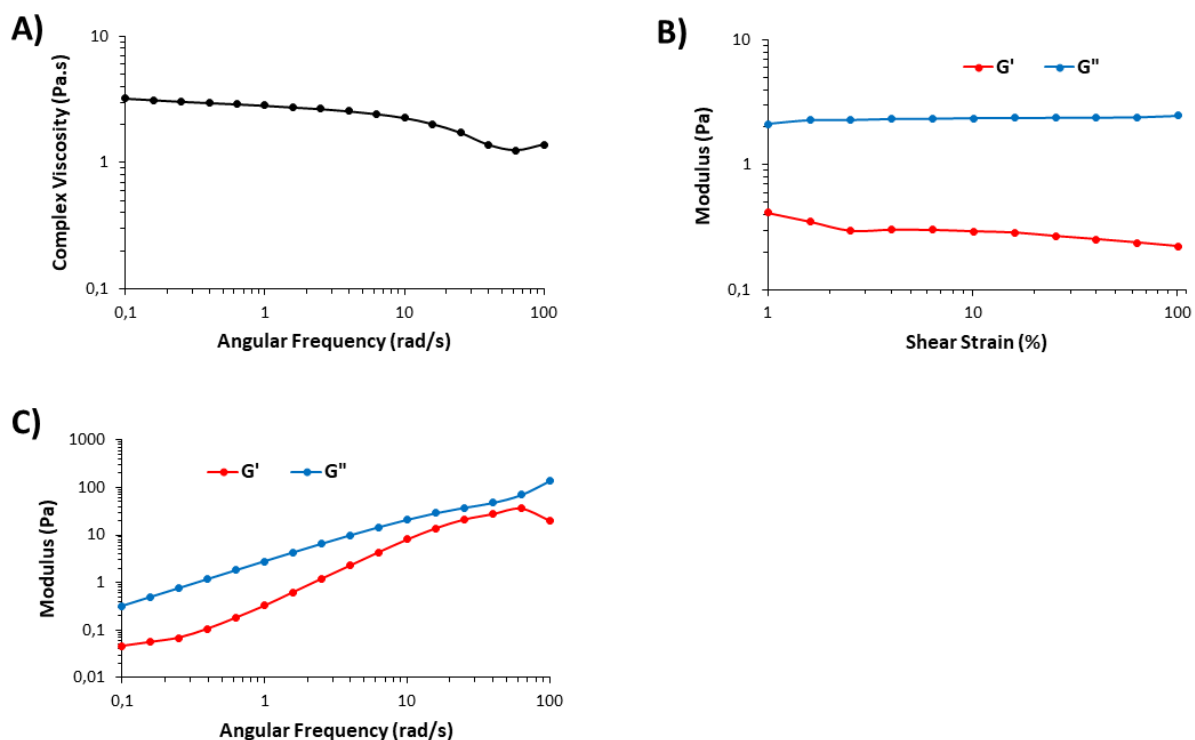


**Figure 24. Rheological parameters of C16-M80K-C16 gel at 4°C. A). Complex viscosity versus angular frequency. B) Storage modulus ( $G'$ ) and loss modulus ( $G''$ ) versus shear strain at 1 rad/s. C) Storage modulus ( $G'$ ) and loss modulus ( $G''$ ) versus frequency.**

The linear domain of the gel phase was first analyzed at 1 rad/s (Fig. 24B). The data showed that we did not obtain a gel at low temperature, but rather a material that behave like a viscoelastic liquid. Then sweep frequency was performed (Fig. 24C), and results confirmed the viscoelastic behavior of the material, with a terminal zone at low frequency, with  $G''$  varying as  $\omega$  and  $G'$  as  $\omega^2$ . A crossing point between  $G'$  and  $G''$  was almost reached at  $\omega > 50$  rad/s.

We also measured the rheological properties of the material at different temperatures to evaluate the effect of the thermosensitivity character of the ELP. (Fig. 25).

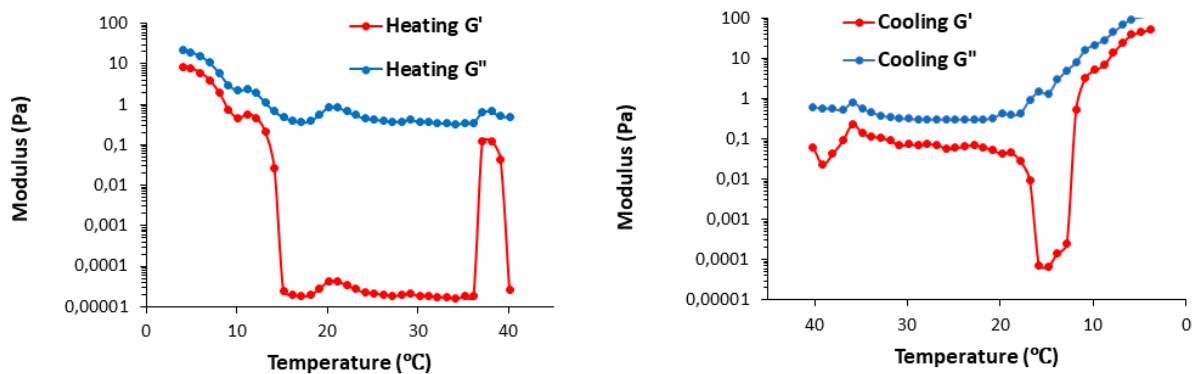


**Figure 25. Evolution of gel properties with temperature. Storage moduli ( $G'$ ) and loss moduli ( $G''$ ) of the aqueous solution of C16-M80K-C16 in water in response to temperature changes. Left: heating ramp. Right, cooling ramp. The polymer concentration was 5%. Angular frequency of set at 10 rad/s. Data below 0.01 Pa are indicated on the graph but they are below what the rheology device used can accurately measure**

Between 4 and 15°C, the  $G''$  value slightly decreased from 21 Pa to 1 Pa, and then remained constant for higher temperatures. The  $G'$  values also slightly decreased up to 12°C, and then dropped below 0.1 Pa. Data recorded at higher temperatures are not reliable. Similar results were obtained when the sample was cooled between 40 and 4°C showing, that the phenomenon was reversible. Interestingly, the values measured at 4°C after the cooling step, which were respectively 52 Pa and 94 Pa for  $G'$  and  $G''$ , were slightly higher than those measured at 4°C before the heating and cooling cycles. This could suggest that the successive heating and cooling steps could promote the formation of a slightly higher number of connections inside the material.

To evaluate the influence of the disulfide bridges on the rheological properties of the gel, we then studied the C16-M40C-CM40-C16 (Fig. 26).

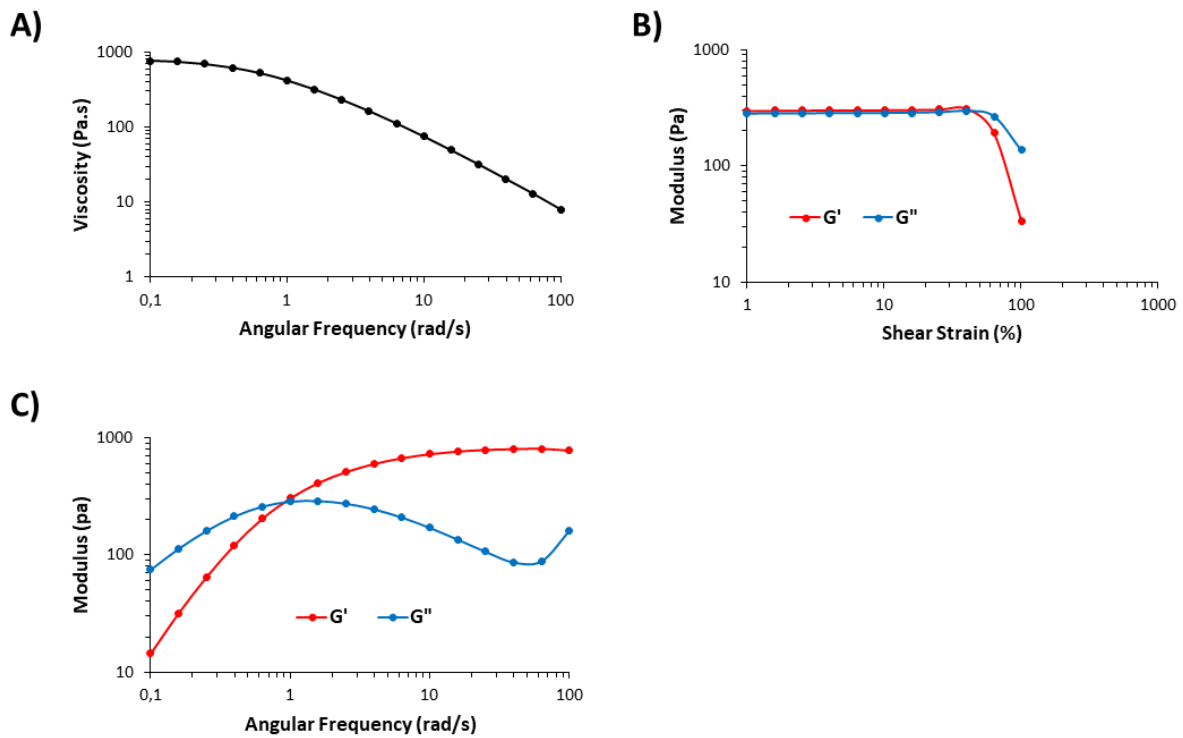


**Figure 26. Rheological parameters of C16-M40C-CM40-C16 gel at 4°C. A) Complex viscosity versus angular frequency. B) Storage modulus ( $G'$ ) and loss modulus ( $G''$ ) versus shear strain at 1 rad/s. C) Storage modulus ( $G'$ ) and loss modulus ( $G''$ ) versus frequency.**

Here, we clearly see an elastic behavior at frequencies higher than 1 rad/s, and a terminal flow area at low frequency. This is typical signature of transient network obtained by reversible connections between flower-like micelles<sup>14,15</sup>. The cross point between  $G''$  and  $G'$  in such transient network has been ascribed to the relaxation time of a hydrophobic end cap in a micelle. In our case, the cross point corresponds to a relaxation time of 1 s. This relaxation time is slightly higher than that found in the literature for telechelic associative polymers with C16 end blocks, which varies between 0.1 and 0.3 s for gel concentration between 2% and 4%<sup>16,17</sup>. Interestingly, we measured  $G'$  values  $\sim 700$  Pa at frequencies equal or higher than 10 rad/s, which is in the range previously obtained for crosslinked hydrogels of ELP (100-1000 Pa)<sup>1,8,18-21</sup>.

We next investigated the behavior of this physical hydrogel as a function of the temperature (Fig. 27).

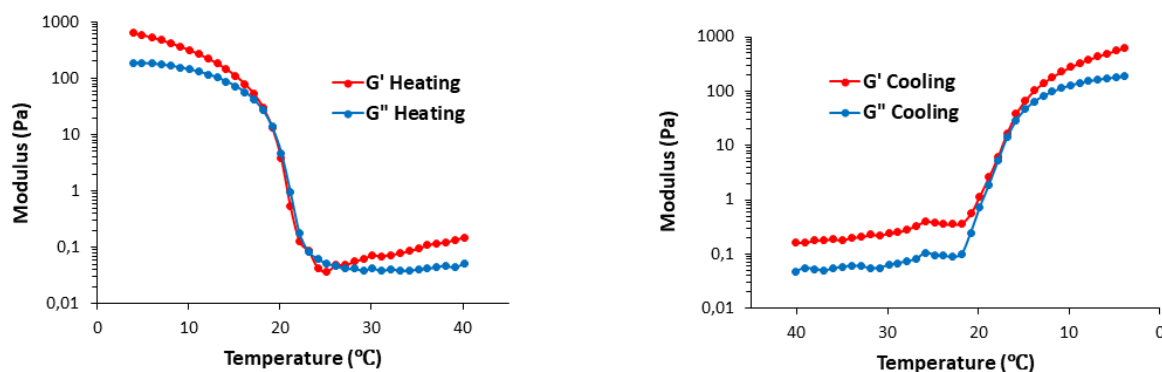


**Figure 27. Evolution of gel properties with temperature. Storage moduli ( $G'$ ) and loss moduli ( $G''$ ) of the aqueous solution of palmitoylated M40C dimers in water in response to temperature changes. Left: heating ramp. Right, cooling ramp. The polymer concentration was 5%. Angular frequency of set at 10 rad/s.**

At low temperature, we measured values for  $G'$  and  $G''$  of respectively 630 and 190 Pa. Upon heating, both modules decreased gradually until 18°C, and then dropped to values below 1 Pa indicating a disruption of the gel. When cooling the sample, we observed a similar trend: low values below 1 Pa for both moduli between 40 and 22°C, then a sharp increase until the temperature reached 16°C. At this temperature, the  $G'$  value became higher than that of  $G''$  indicating gel formation. Finally, at 4°C the values of  $G'$  and  $G''$  were respectively 615 and 180 Pa, almost identical to those measured initially before the heating and cooling cycles showing that the formation of the gel and its disassembly were perfectly reversible. This may indicate that the network structure is at thermodynamic equilibrium.

The dissociation of the gel observed at temperature higher than 18-20°C can be explained by the fact that the ELP block undergoes a transition towards a more hydrophobic character. The flower-like micellar structure is then lost due to the aggregation of ELPs in the corona, and the pre-existing connections between the different micelles are then broken (Fig. 28).

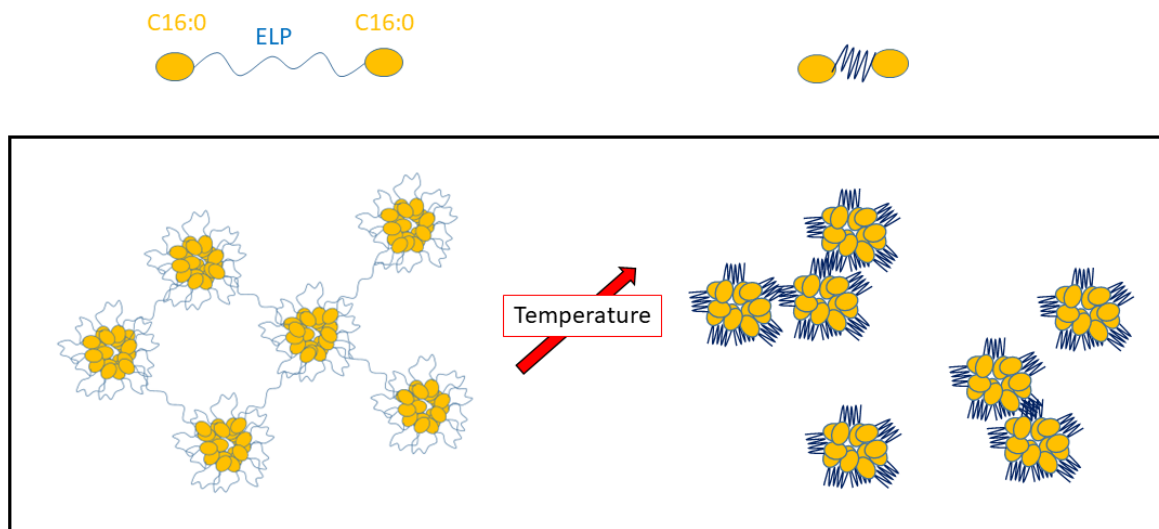


**Figure 28. Schematic representation of the effect of temperature on gel formation. The color change for the ELP from light blue to dark blue represents the change in hydrophobicity resulting from increasing temperature.**

To evaluate the validity of our finding, and to prove that it wasn't specific to the ELP M40C block, we performed identical experiments with another ELP previously built in our laboratory. This is a diblock ELP of formula  $MW[(VPGVG)(VPGMG)(VPGVG)_2]_{10}(VPGIG)_{20}C$ . The first hydrophilic block is therefore identical to M40, and the second block is hydrophobic owing to its content in Isoleucine residues. This diblock bears a cysteine residue at its C-terminus and therefore can dimerize after oxidation.

Using the same protocol as that used for M40C, we first oxidized M40I20C to obtain a majority of dimers, and then we grafted palmitic acid on both N-termini. The purified compound was then dissolved in water at a concentration of 5% and the corresponding hydrogel was analyzed by rheology (Fig. 29).

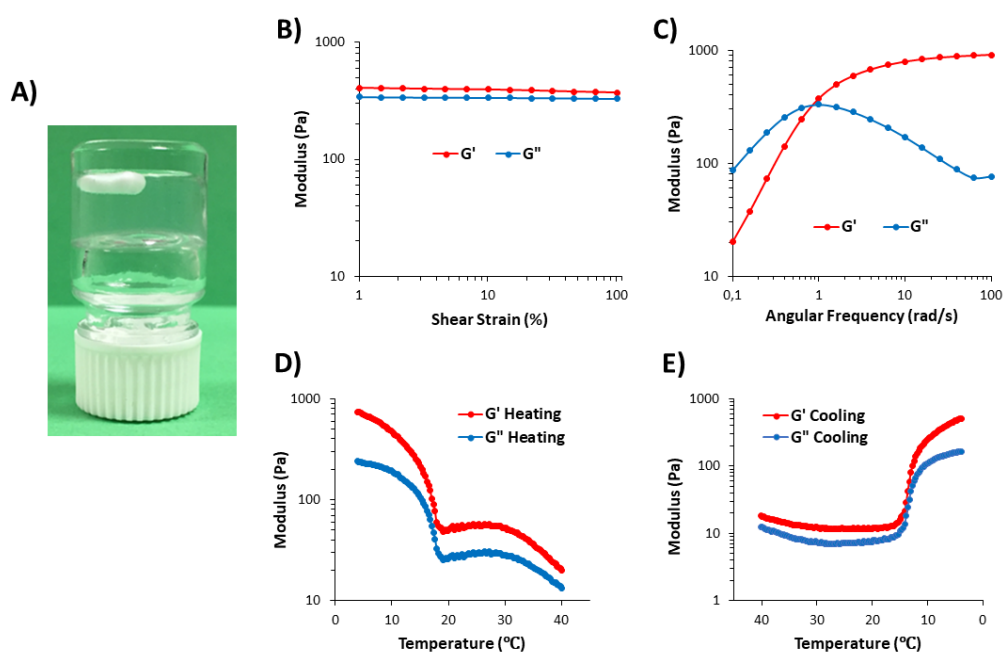


**Figure 29. Rheological parameters of palmitoylated M40I20C dimers. A) Picture of 5% hydrogel. B) Storage modulus ( $G'$ ) and loss modulus ( $G''$ ) versus shear strain at 1 rad/s and 4°C. C) Storage modulus ( $G'$ ) and loss modulus ( $G''$ ) versus frequency at 4°C. D) and E) Storage moduli ( $G'$ ) and loss moduli ( $G''$ ) of the aqueous solution of palmitoylated M40I20C dimers in water in response to temperature changes. D) heating ramp and E) cooling ramp. The polymer concentration was 5%. Angular frequency of set at 10 rad/s.**

The gel obtained with the palmitoylated M40I20C dimers was similar to that obtained with palmitoylated M40C dimers. It was highly transparent and heat sensitive, dissociating upon heating. The transition temperature was slightly lower ( $\sim 14$  °C) than that of the palmitoylated M40C dimers, most likely due to the higher hydrophobicity of the M40I20 diblock. The rheological parameters were also similar, with  $G'$  value  $\sim 700$  Pa at a frequency of 10 rad/s, and a relaxation time of 1 s. However, it seems that this network is more resistant to shear because the linear domain extended to 100%, whereas for the C16-M40C dimers, a destructuring has been observed from 40%.

### 4.3. Conclusions and perspectives

By using palmitoylated M40C dimers, or M40I20C, we succeeded in obtaining physical hydrogels with interesting intrinsic properties: (i) they are highly transparent, which is a sought-after characteristic for therapeutic applications such as intraocular implants; (ii) they have self-healing properties which may be of interest for tissue engineering; (iii) they can be dissociated either by incubation with a reducing agent which will break the disulfide bridges, and therefore generate micelles identical to those described for C16-M40, or by increasing the temperature.

The fact that the structure of our BAAB triblock relies on the formation of disulfide bridges can be an advantage as said above, but it complicates the approach. Indeed, the formation of dimers is obtained after incubation of the monomers with hydrogen peroxide, and this reaction is not 100% effective, leaving 10% of the product in monomeric form. Moreover, this reaction leads to undesirable side reactions such as oxidation of methionine, thus affecting the Tt of the ELP. This is why we started with the acylation of MxK-series ELPs, to obtain a monomeric ELP core flanked by two fatty acids. Unfortunately, our results showed that this type of BAB triblock did not allow the formation of good hydrogels. We don't have a definitive answer as to why C16-M80K-C16 and C16-M40C-CM40-C16 gave such different results, because their chemical structures are quite similar. We can only make two assumptions. The first is that the disulfide bond between the two ELPs gave a certain "freedom" to the molecule, being a little more flexible than a classic peptide bond. Thus, the FA fragments could come out of their micelle more easily to connect a neighboring micelle. However, we did not find in the literature data showing that the peptide bond is more "rigid" than a disulfide bond. We think that a second hypothesis is more likely. In the case of C16-M80K-C16, the palmitic acid grafted at the N-terminus of the ELP will be almost in the same axis as the polypeptide. On the contrary, the second palmitic acid will be at  $\sim 90^\circ$  from the ELP backbone, being grafted on the lateral chain of the lysine residue. Of course, this is a simplistic view because the ELP block is not a linear rod, and is flexible. This is illustrated in Figure 30.

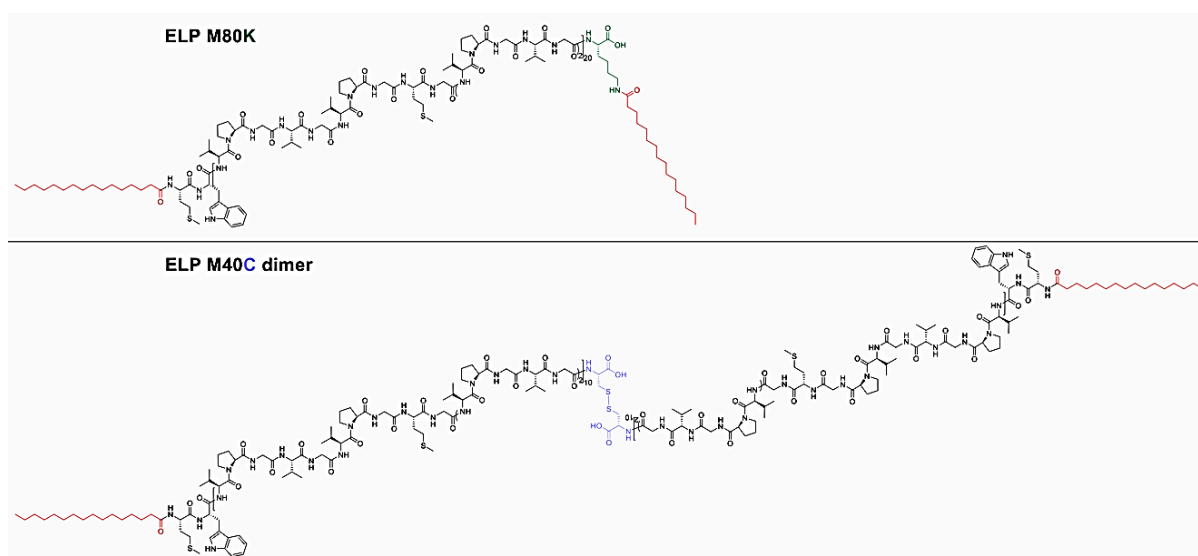


**Figure 30. Schematic representation of C16-M80K-C16 (top) and C16-M40C-CM40-C16 (bottom) copolymers. The structure of the ELP moiety is in black. Palmitic acid molecules are in red, lysine and cysteine residues respectively in blue and green.**

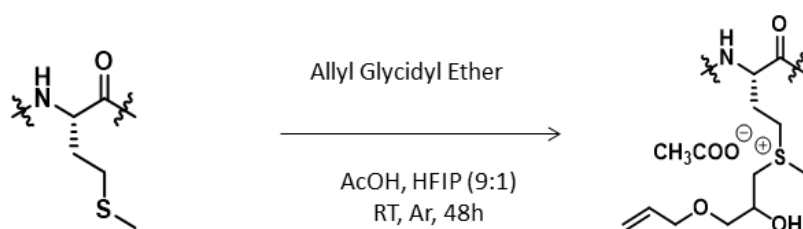
So, from this simplistic scheme, we can imagine that the connection between two micelles will be favored, or once established maybe more stable, in the case of C16-M40C-CM40-C16. To confirm this hypothesis, we could graft palmitic acids onto M80K using its primary amine from the N-terminus and its carboxyl from the C-terminus. As explained in the introduction, this will require two different chemical reactions. However, the final product will have the two fatty acids grafted in the same axis as the ELP segment, and we could evaluate if this new C16-M80K-C16 allows the assembly of hydrogels similar to those obtained with the acylated dimers of M40C.

Another way of improvement would be to modify the temperature at which the hydrogels dissociate. Indeed, the hydrogels obtained with C16-M40C-CM40-C16 and C16-M40I20C-CI20M40-C16 were stable up to temperatures of 18 and 12°C respectively. This will be a problem for biological applications where gel formation at a temperature above 37°C is desired. As discussed earlier, this dissociation temperature depends on the  $T_t$  of the ELP, and the question is how we could increase this temperature. One way would be to design new hydrophilic ELPs, with polar amino acids (serine, threonine, asparagine, glutamine) or even charged amino acids (glutamic acid or aspartic acid) as guest residues. Arginine and lysine are not an option because they contain a primary amine that can react with the activated fatty acid

during the grafting step, producing brush-like structures. This strategy is possible, but would require 6 to 9 months for the whole cloning procedure.

Another possibility would be to modify the Tt of the ELP used in our study. As shown in Chapter 3, methionine oxidation of M40 increases its Tt by nearly 20°C. Therefore, we could perform such oxidation either on the M40C before the acylation step, or directly on the C16-M40C-CM40-C16. Finally, to considerably increase the Tt of ELPs containing methionine, we could alkylate these residues as has already been successfully achieved in our lab<sup>22</sup>. The only downside to this approach is that the chemical modification introduces positive charges to each methionine in the ELP (Figure 31).

**A)**



**B)**

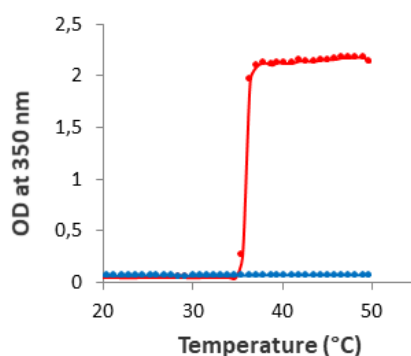


**Figure 31. Alkylation reaction of ELP M40. A) Diagram of the chemical reaction. B) Analysis by turbidimetry of solutions at 100  $\mu$ M in Tris buffer of M40 (red trace) and alkylated M40 (blue trace).**

Knowing that the prerequisite for the formation of the hydrogel is the contact of the micelles to allow connections by exchange of the fatty acid segment, the presence of charges on the surface of the ELP could prevent the interaction of the micelles by electrostatic repulsion. On the other hand, the presence of charges on the surface of the ELP segment could solve another problem which is the aggregation of FA-ELP-FA micelles in the presence of buffers containing salts, such as PBS. Indeed, if we want to use our hydrogel for therapeutic applications, it must

be stable in the presence of physiological salt concentration. Therefore, we believe that fine tuning of the charge on the surface of the ELP will be necessary to find the right balance that will allow gel formation under physiological conditions (salt concentration, T°).

A more direct biological application of our hydrogel could be the evaluation of their ability to encapsulate spheroids for long-term storage. These spheroids are aggregates of compact round cells often generated from cancer cell lines. They are widely used in oncology drug development processes and to better understand cancer biology<sup>23-25</sup>. These spheroids are usually stored for a short period, up to 3 days, in culture media at 4°C in oxygen-free conditions. A recent improvement in storage conditions has increased the shelf life of some spheroids to up to 7 days<sup>26</sup>. In the future, we will encapsulate spheroids in our physical hydrogel to assess its biocompatibility and see if this represents a good way to easily store these cellular aggregates.

## 4.4. Experimental section

### 4.4.1. Materials

Palmitic acid (Riedel-de-haenTM, 98%), Stearic acid (Sigma-Aldrich, 98.5%), O-(1H-6-Chlorobenzotriazole-1-yl)-1,1,3,3-tetramethyluronium hexafluorophosphate (HCTU, Novabiochem), N,N-Diisopropylethylamine (DIPEA, Sigma-Aldrich, 99.5%), N,N-Dimethylformamide (DMF, VWR chemicals, 99.9%), Diethyl ether (VWR international, 100%), Acetone (VWR international, 99%), Hydrogen peroxide (Acros organics, 35 wt.% solution in water), Phosphate Buffer Saline 10X, (PBS 10X, Euromedex) were used without further purification. Ultrapure water (18 MΩ cm) was obtained by passing in-house deionized water through a Millipore Milli-Q Biocel A10 purification unit. Bacto Tryptone (Sigma), Yeast extract (Sigma), Ampicillin (Sigma) and isopropyl β-D-thiogalactopyranoside (IPTG, VWR chemicals) were used for cell culture.

### 4.4.2 Construction of MxK clones

The *E. coli* clone containing the pUC19 plasmid with the ELP M40 sequence was grown overnight at 37°C in LB medium (composition) with 100 µg/mL ampicillin. The M40-pUC19 plasmid was then purified with the NucleoSpin® Plasmid kit (Macherey Nagel) according to the manufacturer's instructions. The concentration of the purified plasmid was measured by spectrophotometry at 260 nm using a Nanodrop ND 1000, and the identity of M40-pUC19 plasmid was confirmed by digestion with the restriction enzyme *Bam*HI (New England Biolabs) followed by agarose gel electrophoresis.

The insertion of a lysine codon (AAA) at the c-terminal end of the M40 sequence was performed by site directed mutagenesis using the InFusion kit (Takara). Briefly, a first PCR was performed using the M40-pUC19 plasmid as the matrix and the following primers: Forward primer ELP40MK : 5' CGTAGG**TAA**AATAACCTCATCGCTGGATCCTC 3', and Reverse primer ELP40MK : 5' GTTT**ATT**TACCTACGCCAGGTACGCC 3'. The Lysine codon is in bold. The PCR reaction was as follows: 3 cycles of denaturation at 98°C for 10 seconds, hybridization at 56°C for 15 seconds and elongation at 72°C for 20 seconds, and then 34 cycles of 98°C for 10 seconds, hybridization at 58°C for 15 seconds and elongation at 72°C

for 20 seconds. To separate the linear PCR product from the M40-pUC19 matrix, the product of the reaction was separated in 0.8% agarose gel and the band corresponding to the PCR product (3281 bp) was excised from the gel and purified using Monarch<sup>®</sup> DNA gel extraction kit (Biolabs). A second band, around 2980 bp was also purified for cloning, because its size corresponded to a M20K linear product. Then the linear PCR products were re-circularized using Fusion HD enzyme (Takara), and the M40K-pUC19 and M20K-pUC19 plasmids were transformed into *E. coli* competent Stellar Cells from Takara (F<sup>-</sup>, endA1, supE44, thi-1, recA1, relA1, gyrA96, phoA, Φ80d lacZΔ M15, Δ(lacZYA-argF) U169, Δ(mrr-hsdRMS-mcrBC), ΔmcrA, λ-]. Clones containing a pUC19 plasmid were selected on LB agar plates containing 100 µg/mL ampicillin, and analysed by PCR using One Taq Hot Start DNA polymerase (New England Biolabs) and the primers M13 forward (5' TGTA AACGACGGCCAGT 3') and M13 reverse (5' CAGGAAACAGCTATGACC 3'). PCR was as follows: cell lysis for 3 min at 94°C, and then 35 cycles 94°C for 15 sec, 50°C for 30 sec, and 68°C for 1 min. The PCR products were analyzed by 1.5% agarose gel electrophoresis. Plasmids from three PCR positive clones were purified with the NucleSpin<sup>®</sup> Plasmid kit, verified by double digestion with *Bam*HI and *Nde*I, and sent for sequence determination (Eurofins Genomics)

For subcloning in the expression vector pET44a M40K-pUC19 and M20K-pUC19 purified plasmids were digested by *Bam*HI and *Nde*I. The restriction products were separated in 1.2% agarose gel, and the band corresponding to the M40K insert (625 bp) and M20K insert (325 bp) were purified with the Monarch<sup>®</sup> DNA gel extraction kit. In parallel, the pET44a plasmid was double-digested with *Bam*HI and *Nde*I, and the linearized plasmid was purified by 0.8% agarose gel electrophoresis with Monarch<sup>®</sup> DNA gel extraction kit. Inserts and linearized pET44 plasmid were ligated using the Quick ligase Kit from New England Biolabs and a 3:1 insert/vector molar ratio. The final reaction volume was 20 µL. Then, 2.5 µL of the reaction was used to transform BLR(DE3) *E. coli* cells [F-ompT hsdSB(rB- mB-) gal lac ile dcm Δ(srI-recA)i306::Tn10 (tetR)(DE3)]. Cells were spread on LB agar plates containing 100 µg/mL ampicillin, and clones were screened by PCR using One Taq Hot Start DNA polymerase (New England Biolabs). The primer specific for pET44 were pET forward 5'-GTGAGCGGATAACAATTC CCC-3' and pET rev 5'-GTTATGCTAGTTATTGCTCAGCGG-3'. The PCR procedure was as follows: 94°C 3 min for cell lysis, and then 35 cycles 94°C 15 sec, 55°C 30 sec, 68°C 1 min. The PCR products were analyzed by 1.5% agarose gel electrophoresis in TAE buffer. The plasmids from positive

clones were purified with NucleoSpin® Plasmid kit, and their sequences verified (Eurofins genomics).

#### **4.4.3. Production of MxK and M40C**

A single bacterial colony was selected and cultured overnight at 37°C in a rotary shaker at 200 rpm in 15 mL of lysogeny broth (LB) medium (0.4% LB Lennox, 0.1% yeast extract) containing 100 µg/mL ampicillin. Thereafter, this seed culture was inoculated into 400 mL of LB medium supplemented with glycerol (1 g/L) and ampicillin (100 µg/mL) to obtain an initial OD<sub>600nm</sub> of 0.15. The culture was grown at 37°C and 200 rpm until the OD<sub>600nm</sub> reached a value close to 0.6. IPTG was added to a final concentration of 0.5 mM, and the temperature was decreased to 25°C. After 12 h of IPTG induction, the culture was harvested by centrifugation at 7500 g and 4°C for 15 min and the cell pellet was resuspended with 10 mL/g wet weight in deionized water. Thereafter the samples were incubated overnight at -80°C and slowly defrosted by incubation at 30°C. Total cell lysis was performed by sonication at 15°C with several 4-s pulses at 125 W 9 s apart for a total duration of 45 min. Insoluble debris were removed by centrifugation at 11 000 g for 15 min at 4°C. The cleared lysate (soluble fraction) was subjected to three successive cycles of inverse transition cycling (ITC). Briefly, ELP was precipitated at 30°C in the presence of salts and pelleted by centrifugation for 15 min at 7 000 g and 30°C. After elimination of the supernatant containing soluble proteins, and re-suspension of the pellet in cold water, the ELP was re-dissolved whereas insoluble proteins from *E. coli* were eliminated by centrifugation for 15 min at 11 000 g and 4°C. The supernatant containing the ELP was then processed through second and third ITC cycles. Before each “warm spin”, NaCl was added to both samples M40K and M20K at a final concentration of 2 M and 1.5 M for the first and second cycles. For the third cycle, NaCl concentrations were 0.5 M for the ELP M40K and 1M for M20K. Finally, the purified ELPs were dialyzed against ultrapure water and lyophilized.

#### 4.4.4. Acylation of the ELPs

The first step was the activation of the carboxylic acid of the palmitic acid. A solution prepared at 3 mM in anhydrous DMF was stirred for 1 h at RT. The activation of carboxylic acids was achieved by adding 7.4 mg (18  $\mu$ mol) of HCTU and 4.6  $\mu$ L (26  $\mu$ mol) of DIPEA to the solution containing 18  $\mu$ mol of FA, and performing the reaction for 15 min in the dark. The second step was the conjugation of the activated fatty acid with the primary amine of the ELP. To conjugate C16 on the two primary amines of the MxK and the M40C dimers, 3  $\mu$ mol of activated fatty acid was reacted with 1  $\mu$ mol of ELP for 12 h in the dark. The reaction product was precipitated by 10 volumes of acetone, collected by centrifugation for 5 min at 2 500 g and 20°C, and then re-suspended in DMF. After a second precipitation step using 10 volumes of diethyl ether, the pellets were recovered by centrifugation and washed three times with 10 volumes of diethyl ether. After drying for 2 h at room temperature, the product was dissolved in cold water, centrifuged at 2 500 g for 10 min at 4°C to remove insoluble impurities. The clear supernatant was dialyzed (1 kDa, Spectra/Por® membrane) against ultrapure water for 2 days at 4°C. The product was then lyophilized and stored at -20°C.

#### 4.4.5. Oxidization of M40C

80 mg (4.6  $\mu$ M) of M40C was dissolved in 4 mL of Tris buffer (Tris 10 mM, pH 8.8) at 4°C. Then, 1.5 mL of 0.05% H<sub>2</sub>O<sub>2</sub> (5 eq) were added for 30 min at 25°C. The oxidized ELP was dialyzed with 1 kDa cut off membrane for two days against water at 10°C, and then lyophilized. SDS page were performed to calculate the amounts of monomers and dimers in solution. NMR spectra were acquired in D<sub>2</sub>O at 10°C on a NMR 400 MHz cryoprobe Prodigy. Data processing was performed using Topspin software.

<sup>1</sup>H NMR (400 MHz, D<sub>2</sub>O):  $\delta$  6.94-7.38 ppm (8 H, proton on aromatic ring of Try),  $\delta$  4.10-4.57 ppm (180 H,  $\alpha$ CH Met +  $\alpha$ CH Val +  $\alpha$ CH Pro),  $\delta$  3.98 ppm (60 H,  $\alpha$ CH Val guest residue, as reference peak),  $\delta$  3.35-3.78 ppm (br m, 449 H,  $\delta$ CH<sub>2</sub> Pro +  $\alpha$ CH<sub>2</sub> Gly),  $\delta$  2.41 ppm (39 H,  $\gamma$ CH<sub>2</sub> Met),  $\delta$  1.79-2.14 (527 H = 60 H  $\epsilon$ CH<sub>3</sub> Met + 140 H  $\beta$ CH Val + 42 H  $\beta$ CH<sub>2</sub> Met + 160 H  $\beta$ CH<sub>2</sub> Pro + 160 H  $\gamma$ CH<sub>2</sub> Pro),  $\delta$  0.77 ppm (br m, 793 H,  $\gamma$ CH<sub>3</sub> Val).

#### 4.4.6. Methods

**Reversed-phase high performance liquid chromatography (RP-HPLC)** was performed using a Ultimate 3000 system (Thermo Scientific) instrument using a hydrophobic C18 stationary phase (ZORBAX Eclips Plus C18, 4.6 x 250 mm, 5  $\mu\text{m}$ , Agilent Technologies) and a gradient of solvent A ( $\text{H}_2\text{O} + 0.1\% \text{TFA}$ )/solvent B (methanol + 0.1% TFA). The flow rate was 1 mL/min. 35  $\mu\text{L}$  of samples (70  $\mu\text{M}$ ) were injected, and the absorbance at 230 nm was recorded with a diode array detector (Thermo Scientific). Data obtained by RP-HPLC were used to calculate the percentage of purity of the ELP-FA conjugates. This was achieved by integrating the area below the peak of the ELP-FA, and by subtracting the area under the peak, if any, of the unmodified ELP.

**Cloud point temperatures (T<sub>cp</sub>)** were determined by measuring the turbidity at 350 nm between 10 and 50°C at a 1 °C·min<sup>-1</sup> scan rate. Data were collected with a Cary 100 UV–vis spectrophotometer equipped with a multicell thermoelectric temperature controller from Agilent Technologies. The T<sub>cp</sub> is defined as the maximum of the first derivative of absorbance versus temperature.

**Dynamic light scattering (DLS)** analyses were performed using a Nano ZS instrument (Malvern U.K.) working at a 90° angle detection. All samples were filtrated through 0.45  $\mu\text{m}$  PVDF devices (Millex, Merck Millipore) just before measurement. The hydrodynamic radius (R<sub>H</sub>) and the polydispersity index (PDI) were derived from the autocorrelation functions using the cumulant method.

**For hydrogel formation** the triblock polymer was dissolved in water at a concentration of 5% or 10% (w/vol) by incubating under stirring at 4°C (below T<sub>cp</sub>). Gel formation occurred after 12 to 24 h of stirring.

**Rheological data** were obtained on an Anton Paar Rheometer with Peltier temperature controller. After setting the temperature to 4°C, the gel was loaded between standard steel plates (25 mm diameter) or conical plates (25 mm diameter, 2° angle) depending on the structure of the gel and the amount of material available. The linear domain was evaluated at 1 rad/s in the range 1-100%. The frequency sweep experiments were done from 100 rad/s to 0.1 or 0.01 rad/s depending of the sample. Temperature ramp experiments were performed between

4°C and 40°C at heating or cooling rates of 2°C/min. Data were recorded with the Anton Paar RheoCompass™ software.

## 4.5. References

- 1 B. P. dos Santos, B. Garbay, M. Fenelon, M. Rosselin, E. Garanger, S. Lecommandoux, H. Oliveira and J. Amédée, *Acta Biomaterialia*, 2019, **99**, 154-167.
- 2 D. W. Lim, D. L. Nettles, L. A. Setton and A. Chilkoti, *Biomacromolecules*, 2007, **8**, 1463-1470.
- 3 D. L. Nettles, K. Kitaoka, N. A. Hanson, C. M. Flahiff, B. A. Mata, E. W. Hsu, A. Chilkoti and L. A. Setton, *Tissue Eng Part A*, 2008, **14**, 1133-40.
- 4 M. K. McHale, L. A. Setton and A. Chilkoti, *Tissue Engineering*, 2006, **11**, 1768-1779.
- 5 K. Trabbic-carlson, L. A. Setton and A. Chilkoti, *Biomacromolecules*, 2003, **4**, 572-580.
- 6 K. Nagapudi, W. T. Brinkman, J. E. Leisen, L. Huang, R. A. McMillan, R. P. Apkarian, V. P. Conticello and E. L. Chaikof, *Macromolecules*, 2002, **35**, 1730-1737.
- 7 J. Lee, C. W. Macosko and D. W. Urry, *Macromolecules*, 2001, **34**, 5968-5974.
- 8 D. Xu, D. Asai, A. Chilkoti and S. L. Craig, *Biomacromolecules*, 2012, **13**, 2315-2321.
- 9 C. Chassenieux, T. Nicolai and L. Benyahia, *Current Opinion in Colloid & Interface Science*, 2011, **16**, 18-26.
- 10 M. A. Winnik and A. Yekta, *Current Opinion in Colloid & Interface Science*, 1997, **2**, 424-436.
- 11 E. R. Wright and V. P. Conticello, *Adv Drug Deliv Rev*, 2002, **54**, 1057-1073.
- 12 M. Dai, G. Goudounet, H. Zhao, B. Garbay, E. Garanger, G. Pecastaings, X. Schultze and S. Lecommandoux, *Macromolecules*, 2021, **54**, 327-340.
- 13 D. L. Elbert, *Acta Biomaterialia*, 2011, **7**, 31-56.

- 14 J. F. Berret, D. Calvet, A. Collet and M. Viguier, *Current Opinion in Colloid & Interface Science*, 2003, **8**, 296–306.
- 15 T. Annable, R. Buscall, R. Ettelaie and D. Whittlestone, *Journal of Rheology*, 1993, **37**, 695-735.
- 16 G. Fonnum, J. Bakke and F. K. Hansen, *Colloid and Polymer Science*, 1993, **271**, 380–389.
- 17 B. Xu, A. Yekta, L. Li, Z. Masoumi and M. A. Winnik, *Colloids and Surfaces A: Physicochemical and Engineering Aspects*, 1996, **112**, 239–250.
- 18 L. Cai, C. B. Dinh and S. C. Heilshorn, *Biomater Sci*, 2014, **2**, 757-765.
- 19 H. Wang, L. Cai, A. Paul, A. Enejder and S. C. Heilshorn, *Biomacromolecules*, 2014, **15**, 3421–3428.
- 20 D. Zhu, H. Wang, P. Trinh, S. C. Heilshorn and F. Yang, *Biomaterials*, 2017, **127**, 132–140.
- 21 P. Contessotto, D. Orbančić, M. da Costa, C. Jin, P. Owens, S. Chantepie, C. Chinello, J. Newell, F. Magni, D. Papy-Garcia, N. G. Karlsson, M. Kilcoyne, P. Dockery, J. C. Rodríguez-Cabello and A. Pandit, *Science Translational Medicine*, 2021, **13**, eaaz5380
- 22 J. R. Kramer, R. Petidemange, L. Bataille, K. Bathany, A.-L. Wirotius, B. Garbay, T. J. Deming, E. Garanger and S. Lecommandoux, *ACS Macro Letters*, 2015, **4**, 1283-1286.
- 23 N. E. Ryu, S. H. Lee and H. Park, *Cells*, 2019, **8**, 1620-1633.
- 24 M. Ravi, A. Ramesh and A. Pattabhi, *J Cell Physiol*, 2017, **232**, 2679–2697.
- 25 L. B. Weiswald, D. Bellet and V. Dangles-Marie, *Neoplasia*, 2015, **17**, 1-15.
- 26 A. Goisnard, C. Dubois, P. Daumar, C. Aubel, M. Depresle, J. Gauthier, B. Vidalinc, F. Penault-Llorca, E. Mounetou and M. Bamdad, *Cancers (Basel)*, 2021, **13**, 1945-1965



## Conclusions and perspectives

To conclude, we would like to summarize the advantages and disadvantages of using PELs to fabricate micelles for drug delivery or hydrogels for tissue engineering.

ELPs are biocompatible, biodegradable and not very immunogenic, even if this last point must be carefully assessed on a case-by-case basis. Moreover, they are monodispersed and can be chemically modified at specific sites to introduce sugars, lipids or cell signaling peptides such as RGD, IKVAV or YIGSR among others. This means that ELPs are not simply structural polymers, but that it is possible to graft biologically active groups onto them. This is therefore very different from chemically synthesized polymers which are more or less biodegradable, sometimes immunogenic, polydisperse and which cannot be easily modified to acquire biological functions such as cell adhesion properties.

An important characteristic of ELP is their thermosensitivity. Indeed, a few years ago many articles were published where ELPs made up of different blocks with different T<sub>ts</sub> were developed to obtain micelles or polymersomes, and physical hydrogels. However, the results obtained were not as good as expected. Indeed, the ELP diblocks form what are called "weak micelles", with a highly hydrated hydrophobic core which limits the encapsulation capacity of hydrophobic drugs. The ELP hydrogels had to be cross-linked using poorly biocompatible chemical reagents because the gels simply obtained after heating above the T<sub>cp</sub> point displayed poor rheological properties. According to several specialists in the field, these mixed results are explained by the fact that even if the ELP blocks can be designed to be more hydrophilic, by limiting the chain length and/or by using residues charged in guest position, or more hydrophobic by increasing the chain length and/or by using hydrophobic host residues (leucine, isoleucine), the hydrophobic/hydrophilic ratios obtained are not sufficient to obtain strong micelles or physical hydrogels. This is the reason why in more recent studies molecules that are very hydrophilic, such as sugars, or very hydrophobic, such as lipids, have been grafted onto ELP backbones to increase this hydrophobic/hydrophilic ratio. However, in these systems, the intrinsic thermosensitivity of the ELP can become a problem. Indeed, in our work we have shown that stable micelles obtained using ELP-FAs aggregate at a temperature above the T<sub>cp</sub>, and that the physical hydrogels lose their gel characteristics above this T<sub>cp</sub>. Our short-term objective will be therefore to increase these T<sub>cp</sub> above 40°C, for example by oxidizing the methionine residues of the M<sub>x</sub> series, or to eliminate this T<sub>cp</sub> by alkylation of the same

methionine residues. Hence the question: what is the point of using the ELP if the thermosensitivity is not useful for the intended application?

Finally, another disadvantage of ELPs, little mentioned in the scientific community but worrying for companies, comes from their production cost. Of course, this is not specific to ELPs but a general problem when it is desired to use recombinant proteins. Just a few facts. The production and purification of large batches of our leading ELP (M80) have been outsourced to a Spanish company (TPNBT) specializing in the production and purification of ELPs. This small contract manufacturing organization is a spin-off from the laboratory of José Cabello-Rodríguez, a recognized specialist in the field of ELPs. The cost of production in a 100-liter fermenter is 12,000 €, and the amount of purified ELP is around 20 g, with some variation from batch to batch. The average price is therefore approximately 600 €/g, and this does not take into account the investments made for the construction of the corresponding clone. Of course, economies of scale can be expected if the process is industrialized, but additional costs will be added to carry out production according to good manufacturing standards, which is mandatory for health authorities. Such high costs are bearable by the pharmaceutical industry for therapeutic proteins of high added value such as growth factors, cytokines, hormones or therapeutic antibodies. This is less true for recombinant proteins lacking intrinsic biological action like those used to encapsulate drugs or to produce hydrogels. Nevertheless, if the use of ELPs can be envisaged for therapeutic applications, their use in products with less added value such as those used in the cosmetics industry is not realistic in the near future. Indeed, when we spoke with people from L'Oréal, they explained to us that the target cost for a recombinant ELP should be close to 10 €/g, which is not possible today with the technologies available. Therefore, ELP will not replace soon hyaluronic acid in these applications.

So, if someone wants to design biocompatible materials based on polypeptide polymers, the question is: is there an alternative to ELPs today?

The answer is yes, but these alternatives have their own drawbacks. An alternative is to use collagen-based materials. This is now widely used to develop 3D cell culture matrices. The problem with collagen is that it is not produced recombinantly, due to the highly repeated sequences of three amino acids, which presents almost insurmountable difficulties for biotechnologists. There are recombinant collagen type polypeptides but they do not have the interesting properties of natural collagens. Current uses are therefore mainly limited to natural

collagen, but knowing that it is purified from dead animals, risks of contamination by viruses or prions cannot be ruled out. A second alternative would be to use recombinant polypeptide polymers inspired by resilin or spider silks. These polymers can be produced in bacteria or in eukaryotic cells with yields equivalent to those of ELPs, and they have intrinsic characteristics, such as the presence of alternating elastic blocks with crystalline blocks, which are very interesting in particular for hydrogels. However, the main disadvantage of these polymers is that they contain non-human peptide sequences, and can therefore trigger undesirable immunological reactions. To our knowledge, the assessment of this risk has not been analyzed experimentally.

Finally, ELP-based materials for therapeutic applications are a good choice, although some limitations exist and should be taken into account. Of course, their heat sensitivity could be the determining factor leading to their selection. However, when this property is not desired, or needs to be removed, they remain good candidates over existing alternatives. In addition, their thermosensitivity is important during the production process, their purification by ITC being simple and economical compared to the classic downstream process conventionally used for therapeutic recombinant proteins.

In this PhD research project, we showed the interest to conjugate ELPs to hydrophobic molecules to generate nanoparticles and micelles capable of encapsulating hydrophobic molecules, or of forming physical hydrogels. The properties of these nanoparticles and hydrogels can be adjusted by varying the size and composition of the ELP and/or the nature of the hydrophobic group (lipid, fatty acid, polyisoprene, etc.). Methods for the production of ELPs by the recombinant route are well established and could be industrialized if necessary. The coupling reactions that we used are relatively simple, in particular for the conjugation of fatty acids, which will also allow a scale-up for the production of ELP-FAs.

Future developments could be made in two directions. For the delivery of drugs, it would for example be interesting if the ELP-FA micelles could deliver their content to specific cell types. To introduce this specificity, one could imagine grafting a peptide or carbohydrate motif to one of the ends of the ELP which would bind to a given cell receptor. Regarding hydrogels, in addition to the development of compounds that will make it possible to obtain stable hydrogels under physiological conditions (temperature, salt concentrations, etc.), their biocompatibility and their ability to allow cell adhesion will have to be assessed. For this last point, we believe

that the very nature of our FA-ELP-FA triblocks will be favorable since the fatty acids which ensure the cohesion of the gel by making the connection between two micelles can also be inserted into the membrane of the environment cells and thus improve their adhesion.

## **Polypeptides de type élastine conjugués à des molécules hydrophobes : vers des nanoparticules et des hydrogels pour la biomédecine.**

L'objectif de cette thèse était d'utiliser des polypeptides inspirés de l'élastine, appelés « Elastin-like polypeptides » (ELPs) pour concevoir des systèmes de délivrance de médicaments et des hydrogels pour la thérapie cellulaire. Dans le but d'améliorer les performances des ELPs, nous leur avons greffé des molécules naturelles hydrophobes. Dans un premier temps, nous avons choisi le polyisoprène (PI) qui est un constituant majeur du caoutchouc naturel. Après avoir mis au point la synthèse des diblocs ELP-*b*-PI, nous les avons caractérisés, puis étudié leur association en milieu aqueux. Ces diblocs s'assemblent pour former des nanoparticules d'environ 40 nm de rayon qui sont capables d'encapsuler et de libérer des molécules hydrophobes. Nous avons ensuite greffé des acides gras (AG) sur différents ELPs pour étudier l'influence de la longueur de chaîne et du nombre d'insaturation sur l'autoassemblage de ces AG-ELPs. Nous avons montré qu'ils s'assemblent en micelles en milieu aqueux. Leur rayon hydrodynamique varie entre 9 et 22 nm selon la nature de l'AG et la taille de l'ELP. Nous avons également étudié leur capacité à encapsuler et à relarguer une molécule hydrophobe. Dans une dernière partie, nous avons évalué la possibilité d'obtenir des hydrogels physiques à partir d'un ELP comportant un AG à chacune de ses deux extrémités. Après synthèse et caractérisation de ces composés téléchéliques, nous avons montré que certains d'entre eux permettent d'obtenir des hydrogels autoréparants, ouvrant la voie à leur évaluation comme outils en ingénierie tissulaire.

**Mots clés :** Elastine, Polypeptides recombinants, Nanoparticules, Hydrogels

---

### **Elastin-like polypeptides conjugated to hydrophobic molecules: towards nanoparticles and hydrogels for biomedicine**

The objective of this thesis was to use Elastin-like polypeptides (ELPs) to design drug delivery systems and hydrogels for cell therapy. To improve the performance of the ELPs, we have grafted them with natural hydrophobic molecules. Initially, we chose polyisoprene (PI) which is a major constituent of natural rubber. After having developed the synthesis of ELP-*b*-PI diblocks, we characterized them and studied their self-assembly in aqueous medium. These diblocks form nanoparticles of approximately 40 nm in hydrodynamic radius capable of encapsulating and releasing hydrophobic molecules. We then grafted fatty acids (FA) on different ELPs to study the influence of the chain length and the number of unsaturations on the self-assembly of these ELP-FAs. We have shown that they assemble into micelles in an aqueous medium. Their hydrodynamic radius varies between 9 and 22 nm depending on the nature of the FAs and the size of the ELPs. We also studied their ability to encapsulate and release a hydrophobic molecule. In a last part, we evaluated the possibility of obtaining physical hydrogels from a ELP comprising an FA at each of its two ends. After synthesis and characterization of these telechelic compounds, we showed that some of them made it possible to obtain self-repairing hydrogels, paving the way for their evaluation as tools in tissue engineering.

**Keywords :** Elastin, Recombinant Polypeptides, Nanoparticles, Hydrogels

**Laboratoire de Chimie des Polymères Organiques**  
LCPO, UMR 5629, 16 AV Pey Berland Pessac